ISSN 2071-4726
2071-0305

Инженерно-строительный журнал

НАУЧНОЕ ИЗДАНИЕ

№2(86) 2019

Федеральное государственное автономное образовательное учреждение высшего образования
Санкт-Петербургский политехнический университет Петра Великого

ПОЛИТЕХ
Санкт-Петербургский политехнический университет Петра Великого

Инженерно-строительный институт
Центр дополнительных профессиональных программ

195251, г. Санкт-Петербург, Политехническая ул., 29,
тел/факс: 552-94-60, www.stroikursi.spbstu.ru,
stroikursi@mail.ru

Приглашает специалистов организаций, вступающих в СРО, на курсы повышения квалификации (72 часа)

Код	Наименование программы	Виды работ*
	Курсы по строительству	
БС-01-04	«Безопасность и качество выполнения общестроительных работ»	**п.1,2, 3, 5, 6, 7, 9, 10, 11, 12, 13, 14**
БС-01	«Безопасность и качество выполнения геодезических, подготовительных и земляных работ, устройства оснований и фундаментов»	**1,2,3,5**
БС-02	«Безопасность и качество возведения бетонных и железобетонных конструкций»	**6,7**
БС-03	«Безопасность и качество возведения металлических, каменных и деревянных конструкций»	**9,10,11**
БС-04	«Безопасность и качество выполнения фасадных работ, устройства кровель, защиты строительных конструкций, трубопроводов и оборудования»	**12,13,14**
БС-05	«Безопасность и качество устройства инженерных сетей и систем»	**15,16,17,18,19**
БС-06	«Безопасность и качество устройства электрических сетей и линий связи»	**20,21**
БС-08	«Безопасность и качество выполнения монтажных и пусконаладочных работ»	**23,24**
БС-12	«Безопасность и качество устройства мостов, эстакад и путепроводов»	**29**
БС-13	«Безопасность и качество выполнения гидротехнических, водолазных работ»	**30**
БС-14	«Безопасность и качество устройства промышленных печей и дымовых труб»	**31**
БС-15	«Осуществление строительного контроля»	**32**
БС-16	«Организация строительства, реконструкции и капитального ремонта. Выполнение функций технического заказчика и генерального подрядчика»	**33**
	Курсы по проектированию	
БП-01	«Разработка схемы планировочной организации земельного участка, архитектурных решений, мероприятий по обеспечению доступа маломобильных групп населения»	**1,2,11**
БП-02	«Разработка конструктивных и объемно-планировочных решений зданий и сооружений»	**3**
БП-03	«Проектирование внутренних сетей инженерно-технического обеспечения»	**4**
БП-04	«Проектирование наружных сетей инженерно-технического обеспечения»	**5**
БП-05	«Разработка технологических решений при проектировании зданий и сооружений»	**6**
БП-06	«Разработка специальных разделов проектной документации»	**7**
БП-07	«Разработка проектов организации строительства»	**8**
БП-08	«Проектные решения по охране окружающей среды»	**9**
БП-09	«Проектные решения по обеспечению пожарной безопасности»	**10**
БП-10	«Обследование строительных конструкций и грунтов основания зданий и сооружений»	**12**
БП-11	«Организация проектных работ. Выполнение функций генерального проектировщика»	**13**
Э-01	«Проведение энергетических обследований с целью повышения энергетической эффективности и энергосбережения»	
	Курсы по инженерным изысканиям	
И-01	«Инженерно-геодезические изыскания в строительстве»	**1**
И-02	«Инженерно-геологические изыскания в строительстве»	**2,5**
И-03	«Инженерно-гидрометеорологические изыскания в строительстве»	**3**
И-04	«Инженерно-экологические изыскания в строительстве»	**4**
И-05	«Организация работ по инженерным изысканиям»	**7**

***(согласно приказам Минрегионразвития РФ N 624 от 30 декабря 2009 г.)**

По окончании курса слушателю выдается удостоверение о краткосрочном повышении квалификации установленного образца (72 ак. часа)

Для регистрации на курс необходимо выслать заявку на участие, и копию диплома об образовании по телефону/факсу: 8(812) 552-94-60, 535-79-92, , e-mail: stroikursi@mail.ru.

Инженерно-строительный журнал
НАУЧНОЕ ИЗДАНИЕ

ISSN 2071-4726, 2071-0305

Свидетельство о государственной регистрации: ПИ №ФС77-38070, выдано Роскомнадзором

Специализированный научный журнал. Выходит с 09.2008.

Включен в Перечень ведущих периодических изданий ВАК РФ

Периодичность: 8 раз в год

Учредитель и издатель:

Санкт-Петербургский политехнический университет Петра Великого

Адрес редакции:

195251, СПб, ул. Политехническая, д. 29, Гидрокорпус-2, ауд. 245

Дата выхода: 14.06.2019

Содержание

Байджанов Д.О., Абдрахманова К.А., Кропачев П.А., Рахимова Г.М. Модифицированные бетоны для производства свайных фундаментов 3

Торопов А.С., Бызов В.Е., Мелехов В.И. Получение элементов строительных конструкций из круглых лесоматериалов с сердцевинной гнилью 11

Пайюнен С., Хаутала Дж., Хейнисуо М. Моделирование несущих ограждающих конструкций плоскими конечными элементами со свойствами метаматериала 20

Худаяров Б.А., Тураев Ф.Ж. Нелинейные колебания трубопроводов на вязкоупругом основании, транспортирующего жидкость 30

Билы П., Фладр Й., Хылик Р., Враблик Л., Хрбек В. Влияние процесса замещения цемента и гомогенизации на высокоэффективный бетон 46

Чао Г., Лу Ч. Морозное пучение котлованов в регионах сезонного промерзания грунтов 61

Лунёв А.А., Сиротюк В.В. Распределение напряжений в массиве из золошлаковой смеси 72

Джао Я., Ши Я., Янг Д. Растрескивание туннельного днища под влиянием углеродистого сланца 83

Морозов В.И., Опбул Э., Ван Фук Ф. Работа осесимметричных толстых плит, опертых по конической поверхности 92

Аршади Х., Хайруддин А. Феномен сдвигового запаздывания в трубчатых системах с вынесенными опорами и поясами фермам 105

Контакты:
E-mail: mce@spbstu.ru
Web: http://www.engstroy.spbstu.ru

Magazine of Civil Engineering
SCHOLAR JOURNAL

ISSN 2071-4726, 2071-0305

Peer-reviewed scientific journal

Start date: 2008/09

8 issues per year

Publisher:

Peter the Great St. Petersburg Polytechnic University

Indexing:

Scopus, Russian Science Citation Index (WoS), Compendex, DOAJ, EBSCO, Google Academia, Index Copernicus, ProQuest, Ulrich's Serials Analysis System

Corresponding address:

245 Hydro Building, 29 Polytechnicheskaya st., Saint-Petersburg, 195251, Russia

Date of issue: 14.06.2019

Contents

Baydjanov, D.O., Abdrakhmanova, K.A., Kropachev, P.A., Rakhimova G.M. Modified concrete for producing pile foundations 3

Toropov, A.S., Byzov, V.E., Melekhov, V.I. Manufacturing structural building components from round timber with heartwood rot 11

Pajunen, S., Hautala, J., Heinisuo, M. Modelling the stressed skin effect by using shell elements with meta-material model 20

Khudayarov, B.A., Turaev, F.Z. Nonlinear vibrations of fluid transporting pipelines on a viscoelastic foundation 30

Bily, P., Fladr, J., Chylik, R., Vrablik, L., Hrbek, V. The effect of cement replacement and homogenization procedure on concrete mechanical properties 46

Chao, G., Lu, Z. Frost heaving of foundation pit for seasonal permafrost areas 61

Lunev, A.A., Sirotyuk, V.V. Stress distribution in ash and slag mixtures 72

Zhao, Y., Shi, Y., Yang, J. Cracking of tunnel bottom structure influenced by carbonaceous slate stratum 83

Morozov, V.I., Opbul, E.K., Van Phuc, P. Behaviour of axisymmetric thick plates resting against conical surface 92

Arshadi, H., Kheyroddin, A. Shear lag phenomenon in the tubular systems with outriggers and belt trusses 105

E-mail: mce@spbstu.ru

Web: http://www.engstroy.spbstu.ru/eng/index.html

Magazine of Civil Engineering. 2019. 86(2). Pp. 3–10
Инженерно-строительный журнал. 2019. № 2(86). С. 3–10

Magazine of Civil Engineering

journal homepage: http://engstroy.spbstu.ru/

ISSN 2071-0305

DOI: 10.18720/MCE.86.1

Modified concrete for producing pile foundations

D.O. Baydjanov, K.A. Abdrakhmanova*, P.A. Kropachev, G.M. Rakhimova,
Karaganda State Technical University, Karaganda, Republic of Kazakhstan
** E-mail: kagaip@mail.ru*

Keywords: modified concrete; additives; reinforced concrete pile foundations; resistance to corrosive environments; sulfate corrosion; water-tightness; concrete durability; ground water.

Abstract. There are considered the issues of structural modification of heavy concrete with oligomer-polymer additives. It has been established that crystallization of the cement stone proceeds at macro- and micro-levels. Macro-pores are filled with products of crystallization of cement particles grafted on the surface of polyvinyl chloride (PVC) macromolecules. The migration of PVC macromolecules and oligomers of the waste of coke-chemical production (WCP) into defective zones is due to the occurrence of internal stresses during hardening and volumetric compression which causes the closure of macro- and micro-pores, as well as cracks and capillaries. Thus, for the complex of physical and mechanical properties, resistance to sulfate corrosion and frost resistance the studied concrete based on structurally modified concrete can be used for producing pile foundations arranged in conditions of highly saline soils. The presented results of experimental studies indicate sufficient corrosion resistance of the concrete under study.

1. Introduction

The destruction of reinforced concrete structures depends on characteristics of the raw materials that form concrete. Therefore, concrete resistance to corrosion can be increased by reducing the ratio between water and cement, as well as the use of various modifiers [1–5]. In the field of developing and using modifiers there has been widely used the method of regulating the structure of concrete in order to increase its strength, cement hardening speed, increasing resistance to various aggressive media, etc.

Structural modification leads to increasing strength characteristics of concrete density, reducing water absorption and, as a consequence, chemical resistance of cement stone

There are a number of classification systems for cement and concrete modifiers. P.A. Rebinder [6] proposed to classify additives of surfactants according to the mechanism of their action. As it is known, all surfactants are divided into ionic and non-ionic compounds according to their ability to form ions in a viscous medium.

At present by the functionality of the modifier there are distinguished regulators of cement hardening speed, water repellent agents and plasticizers [7–9].

To obtain concrete with given structural and technological properties it is required to determine the functional area of modifiers and regularities of their impact on the parameters of cement systems at the stage of forming the cement stone structure. In this connection the development of the concrete composition, the study of the mechanism of the functional modifiers effect during hydration are of great importance.

Durability of concrete for foundations is mainly determined by the chemical composition of soils in the region of erection. Soil salinity is a characteristic feature of the regions with the arid climate, where the processes of evaporation of water prevail over the processes of infiltration.

Baydjanov, D.O., Abdrakhmanova, K.A., Kropachev, P.A., Rakhimova G.M. Modified concrete for producing pile foundations. Magazine of Civil Engineering. 2019. 86(2). Pp. 3–10. DOI: 10.18720/MCE.86.1.

Байджанов Д.О., Абдрахманова К.А., Кропачев П.А., Рахимова Г.М. Модифицированные бетоны для производства свайных фундаментов // Инженерно-строительный журнал. 2019. № 2(86). С. 3–10. DOI: 10.18720/MCE.86.1

These regions include western regions of Kazakhstan (the Atyrau and Mangystau regions, especially the Caspian and Aral territories), where salinity reaches 100–150 mg/l. The maximum content of readily soluble salts in the Western region of Kazakhstan is 5–10 %, insoluble 65–70 % and carbonates up to 60 %.

Saline soils are found everywhere in Kazakhstan and occupy 65–70 % of its entire territory. Due to salinity of the soils of Central and Western Kazakhstan there is a need of increasing resistance of foundations to aggressive environments. In this regard pile foundations built in water-saturated, saline and problem ground conditions should be manufactured with high corrosion resistance, frost resistance and reliable experimental properties, taking into account characteristics of the water-aggressive operating environment [10–13].

Present day ideas of forming the structure of concrete and giving them the greatest resistance to aggressive media, as well as ways of increasing corrosion resistance of concrete were considered in [14–17].

The purpose of this work is obtaining structural modifiers of concrete that increase corrosion resistance of pile reinforced concrete foundations in conditions of saline soils.

There have been studied the mechanisms of cement stone structuring depending on the process of the structure formation, which takes place during cement hardening (forming the macro- and microstructure of concrete), the impact of structural modifiers on the concrete mixture and cured concrete properties.

The obtained materials are recommended for producing pile foundations and their operation in highly saline soils of Western and Central Kazakhstan [18–20].

2. Methods

It is well known that strength of concrete depends on various violations in the structure of cement stone that are due to the presence of pores and a defect that have arisen as a result of external force impacts. In this material internal stresses cause destructive processes of forming macro- and micro-cracks and ultra-pores. Due to defects in the crystalline structure of concrete when it is loaded there arise micro-cracks which formation is explained by the presence and movement of dislocations. When concrete is loaded, due to the difference in physical and mechanical properties, the size of the structural components and the presence of defects in the structure of the cement stone there arises the secondary stress field. The intensity of forming micro-cracks is greatly affected by the plasticity of the material in over-stressed micro-volumes.

One of the methods of protecting reinforced concrete structures from sulfate corrosion is strengthening the anticorrosive properties of concrete as a result of using special types of cement increasing the concrete density and introducing additives [21, 22].

At present corrosion resistance of concretes and structures in contact with a highly aggressive water-salt ground environment is provided by a combination of using special types of cement, volumetric water repellent agents, plasticizing additives and surfactants. At this the water-cement ratio decreases, the concrete density increases, while the deformation-strength properties, water resistance, sulfate resistance and resistance to cracking of reinforced concrete structures increase [23].

The present work deals with consideration of the issues related to the mechanisms of cement stone structuring depending on the structure formation that takes place during the cement hardening (forming the macro- and microstructure of concrete).

According to V.M. Moskvin, all three main types of corrosion are related to structuring during the concrete hardening, the concrete components dissolution, the exchange reactions between the components of the cement stone and the aggressive environment and developing internal stresses as a result of accumulation and crystallization of poorly soluble products with increasing the volume of the solid phase [24]. Destruction of concrete in the presence of all three types of corrosion is due to dissolution of hardened cement stone, mass-exchange processes between the cement stone and corrosive environment, the growth of crystals in the pores of concrete during avalanche development of cracks and capillaries during the cement stone hardening, as well as during operation with overlapping cyclic temperature and mechanical effects of the environment.

In this connection it is interesting to regulate the capillary-porous structure of the cement stone during hardening, and to reduce the level of macro-pore formation in the interphase layer of the cement-filler system and cement-reinforcement.

Experimental studies conducted in the laboratory of KSTU found that concrete with high ductility have improved resistance to multiple loads. Thus, resistance of concrete to dynamic loads is determined by the combination of elastic properties of the mortar and coarse aggregate.

So, increasing the mechanical strength of concrete is provided by modifiers that absorb the impact energy and optimize the structure of the cement stone.

3. Results and Discussion

In the work there is proposed a modification of the secondary structure of concrete by introducing oligomer-polymeric additives. The mechanism of structural modification is based on the theory of crystallization of organic polymers in the presence of fillers. It has been taken into account that crystallization of cement proceeds according to the similar mechanism of crystallization of organic polymers: nucleation, formation of a crystallizing systems gel, growing the degree of crystallization, solidification of a solid. Unlike crystallization of organic polymers, crystallization of cement proceeds with isolation of crystallization water from the volume of the cement stone, with formation of a large number of capillaries with the diameter of 2–20 nm that form micro-voids that reduce mechanical strength, frost resistance and aggressive resistance of concretes. By the method of mercury porosimetry it has been found that the volume of micro-pores in real concretes is up to 30 % of the total volume of concrete. According to S.V. Fedosov, the volume of micro- and macro-pores in concrete can be up to 40 %. According to Yu.M. Bazhenov, P.A. Rebinder, and others, formation of macro-pores with dimensions from several hundreds of microns to several mm is associated with the failure to comply with the technology of concrete production and cement properties, as well as the presence of large aggregates and fine fillers in the concrete composition with a high activity of their surface that participate in the forming the structure of cement stone and concrete.

In this regard the regulation of macro- and microstructure of concrete will produce concrete with high resistance to aggressive media, as well as with high strength properties.

Structural modification of concrete based on Portland cement has been performed by introducing structural modifiers into the composition of concrete at the stage of preparing a concrete mass. S.V. Fedosov and S.M. Bazanov [25] divide the process of hardening cement stone into three stages: the first stage is the beginning of hardening or nucleation, the second stage is coagulation or crystal growth and the third stage is formation of monolithic structure or achievement of operational strength. In our opinion, structural modifiers participate in the structure formation at all stages of macrostructure formation in concrete. At the second stages of forming the crystallization structure of the macromolecule of the organic silicon oligomer “Silor” SO, the PVC macromolecules with cement micro-particles are entrained into defective zones. This is due to the low molecular weight of the “Silor” SO and the low effective viscosity of the PVC + “Silor” SO coagulation system: $4–8\cdot10^{15}$ Pa·s (water+cement system $\eta = 10^{16}–10^{25}$ Pa·s.). The mobility of the “Silor” SO system manifests itself with the onset of internal hydrostatic pressure (P_{hst}) in the volume of the cement stone and increases with its increase (P_{hst} = 40–60 MPa). At the third stage, due to high internal stresses, the process of displacement of the structural modifier into macro- and micro-pores and capillaries continues. The process of migration of the structural modifier stops with the final filling of the defect volume with growing cement crystals which are formed by the general mechanism of crystallization of cement.

The regulation of macro and microstructure during formation of the concrete structure is performed by introducing into the composition powdered PVC with particle sizes of 100–150 μm and density of 0.5 g/cm^3 and industrial waste of coke-chemical production (WCP) with the density of 1.238–1.254 g/cm^3, the content of resinous substances 37.7–45.4 % and insoluble toluene 42.3–54.6 %, the ash content of which varies within the range of 0.5–4.3 %.

The samples for the study have been obtained by mixing grade 400 Portland cement of the Karaganda cement plant with the estimated amount of quartz sand within 10–15 min. in a ball mill. In the obtained mix there has been introduced 0.5–1.0 wt. % of powdered PVC and mixed within 10 minutes. At the same time there has been prepared the 60 % solution of WCP in water by mixing within 30 minutes at the rotor speed of 45–60 rpm. The sand-cement mix has been closed with water and at the same time there has been introduced the 60 % aqueous WCP solution in the amount of 3–5 mass % of the solid components. The composition was mixed within 20–25 minutes. The water-cement ratio was 0.2–0.3. Formulation of the compositions is shown in Table 1.

Table 1. Formulation of the concrete composition.

No	Concrete composition	Amount, mass %, W/C		
		I	II	III
1	G400 Portland cement	25	30	35
2	Sand	75	70	65
3	PVC	0.5	0.75	1.0
4	WCP	4.5	4.25	4.0
	Total	100	100	100
	W/C ratio	0.2 0.25 0.3	0.25 0.30 0.2	0.30 0.25 0.20

The kinetics of water absorption after aging the samples in the form of a cube of 100x100x100 mm is shown in Figure 1.

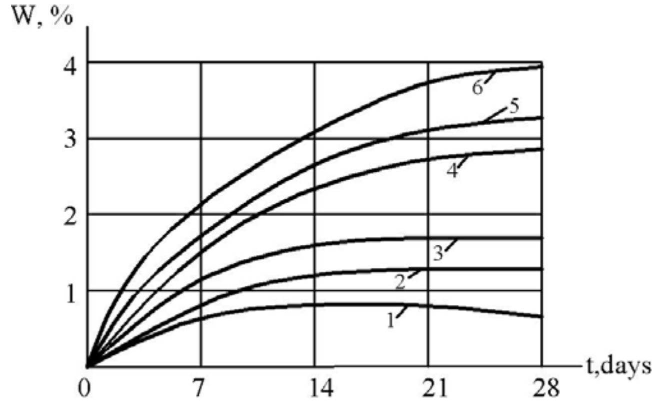

**Figure 1. Kinetics of concrete water absorption:
1, 2, 3 – Polyvinylchloride (PVC) content 0.5; 0.75; 1.0 and waste of coke-chemical production 4.5; 4.25; 4.0, respectively: 4, 5, 6 – without additives; W/C – 0.2; 0.25; 0.3, respectively**

As it can be seen from the presented data, the content of the complex additive leads to the 2.0–4.0 times reducing of water absorption which indicates decreasing porosity of the concrete. To determine the contribution to the .kinetics of water absorption, macro- and micro-pores there has been studied the structure of concrete on an optical electron microscope with resolution of x1000. The samples of the modified oligomer-polymeric additive did not contain macro-pores with sizes >200 μm as compared to the unmodified ones. The micro-pores of the modified concrete contained an oligomer additive. Macro-pores with sizes of 150–200 microns of concrete, as it has been supposed, at the stage of crystallization, are occupied by PVC macromolecules on which there are grafted Portland cement particles introduced with dry mixing of cement with PVC. After mixing with water, the cement particles grafted onto the PVC surface become new crystallization centers, and the crystal growth proceeds in the macro-pores volume. Migration of PVC macromolecules into macro-voids in the area of coverage of the filler (sand) contour is due to the difference in the PVC density and hardening concrete from the moment of coagulation to the formation of the crystallization structure. Apparently, the kinetics of crystallization of cement in the concrete mixture and in the macro-pores volume proceeds at different rates which explains the migration of WCP to the region of cracks and capillaries. The occupying of macro- and micro-pores of concrete by mobile molecules of the oligomer and polymer is also due to the development of internal stresses during formation of the crystallization structure of concrete. Unlike plasticizers and water repellents that envelop the aggregate particles and migrate to less crystallized regions, macromolecules of the oligomer and polymer under the impact of internal stresses participate in the structuring of the concrete. The processes of crystallization of cement particles grafted onto the surface of PVC macromolecules contribute to the formation of a micro-granular structure in defective areas of concrete. The mechanism of occupying defective zones by low-molecular products during crystallization (the doping effect) is known for crystallizing polymers. This indicates the formation of a fine-crystalline structure with optimal packing in the volume which causes increasing the deformation-strength characteristics of the material. Structural plasticization, i.e. occupation of the volume of submicrocracks by oligomers is also observed when both crystalline and amorphous oligomers are solidified. Thus, we assume that the crystal growth mechanism, both for organic and inorganic polymers, is similar. Migration to defective zones (pores, cracks, capillaries) of low-molecular and low-viscosity particles of WCP as a result of all-round compression during hardening of cement is confirmed by the parameters of the water absorption kinetics.

Figure 2 shows the results of testing concrete at the age of 28 days for compressive strength and frost resistance.

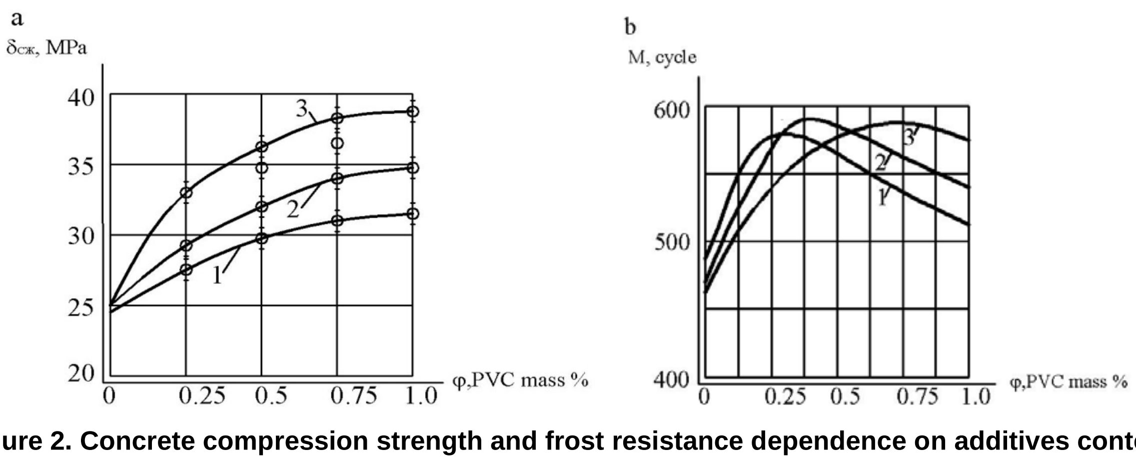

Figure 2. Concrete compression strength and frost resistance dependence on additives content: WCP content 1 – 3.0, mass %; 2 – 4.0 mass %; 3 – 5.0 mass %; formulation I, *W/C* = 0.25, to the effect of the 5 % water solution of sodium sulfate (Na_2SO_4).

The test results are shown in Table 2.

Table 2. Results of the studies.

Concrete	W/C	Concrete compression strength, t month		
		1 month	2 months	3 months.
I II III	0.2	27/25 31 35	27/18 30 35	25/12 29 32
I II III	0.25	27 31 35	22 27 30	20 23 26
I II III	0.3	27 31 35	20 25 27	18 19 21

Note. Denominator: indicators of concretes without additives.

The obtained results testify to the sufficient corrosion resistance of the studied concretes.

Thus, in the complex of physical and mechanical properties, resistance to sulfate corrosion and frost resistance, the studied concretes based on structurally modified concrete can be used for producing pile foundations arranged in conditions of highly saline soils.

4. Conclusions

1. The use of structural modifiers based on experimental data makes it possible to produce high quality concrete: strength higher by 20–30 %, corrosion resistance by 80–85 %.

2. The use of structural modifiers increases water-tightness to class W11–W12 and, as a result, reduces by 85–90 % capillary suction and water absorption which is caused by formation of the secondary crystallization structure of cement stone in defective areas of concrete;

3. Concretes modified with oligomer-polymeric additives exclude sulfate corrosion of concrete and anodic corrosion of metal reinforcement.

4. Adjusting the macro- and microstructure of concrete increases the structural uniformity of concrete which increases the speed of ultrasonic waves by an order of magnitude and in turn increases the continuity of the concrete.

5. Structural modification of concrete in the process of hydration of cement permits to increase the strength indicators of heavy concrete.

References

1. Sheynfeld, A.V. Organic mineral modifiers as a factor increasing the durability of reinforced concrete structures. Concrete and reinforced concrete. 2014. No. 3. Pp. 16–21. (rus)
2. Bogdanov, R.R., Ibragimov, R.A. Process of hydration and structure formation of the modified self-compacting concrete. Magazine of Civil Engineering. 2017. No. 73(5). Pp. 14–24. DOI: 10.18720/MCE.73.2
3. Selyaev, V.P., Oshkina, L.M., Seliayev, P.V., Sorokin, E.V. Studying the chemical resistance of cement-based concrete with regard to sulfate corrosion. Regional architecture and construction. 2013. No. 1. Pp. 4–11. (rus)
4. Rosenthal, N.K. Permeability and corrosion resistance of concrete. Industrial and Civil Construction. 2013. No. 1. Pp. 35–37. (rus)
5. Ibragimov, R. The influence of binder modification by means of the superplasticizer and mechanical activation on the mechanical properties of the high-density concrete. ZKG.: Zement – Kalk – Gips international. 2016. Vol. 69. No. 6. Pp. 34–39.
6. Rebinder, P.A. Surface-active substances. Moscow: Znaniye, 1961. 268 p. (rus)
7. Smirnova, O.M. Compatibility of portland cement and polycarboxylate-based superplasticizers in high-strength concrete for precast constructions. Magazine of Civil Engineering. 2016. 66(6). Pp. 12–22. DOI: 10.5862/MCE.66.2
8. Litvinova, T.A. Organo-mineral additives based on oil and gas complex waste to building materials. Magazine of Civil Engineering. 2016. 67(7). Pp. 13–21. DOI: 10.5862/MCE.67.2
9. Megat Johari, M.A., Brooks, J.J., Kabir, S., Rivard, P. Influence of supplementary cementitious materials on engineering properties of high strength concrete. Construction and Building Materials. 2011. Vol. 25. No. 5. Pp. 2639–2648
10. Vetrov, S.N., Yakovlev, S.V. Spetsifika obsledovaniya sostoyaniya zhelezobetonnykh konstruktsiy v usloviyakh agressivnogo vozdeystviya vody [The specifics of the study of the state of reinforced concrete structures in the conditions of aggressive air in water]. Magazine of Civil Engineering. 2010. 17(7). Pp. 35–40. (rus)
11. Bonakdar, A., Mobasher, B. Multi-parameter study of external sulfate attack in blended cement materials. Construction and Building Materials. 2010. Vol. 24. No. 1. Pp. 61–70.
12. Kotov, D.S. Deformatsii usadki betona, modifitsirovannogo khimicheskimi i tonkodispersnymi mineral'nymi napolnitelyami [Shrinkage deformations of concrete modified with chemical and fine mineral fillers]. Magazine of Civil Engineering. 2009. No. 7(9). Pp. 11–21. (rus)
13. Kirsanova, A.A., Kramar, L., Thiery, V. The effect of additives including metakaolin on the freeze resistance of concrete. Materials Science Forum. 2016. Vol. 843. Pp. 263–268.

14. Ibragimov, R.A., Pimenov, S.I. Influence of mechanochemical activation on the cement hydration features. Magazine of Civil Engineering. 2016. 62(2). Pp. 3–12. DOI: 10.5862/MCE.62.1
15. Prasad, J., Jain, D.K., Ahuja, A.K. Factors influencing the sulfate resistance of cement concrete and mortar. Asian Journal of civil engineering (building and housing). 2006. No. 7(3). Pp. 259–268.
16. Latypov, V.M., Latypova, T.V., Lutsyk, E.V., Fedorov, P.A. Durability of concrete and reinforced concrete in natural corrosive environments. Ufa: RIC USNTU. 2014. 288 p. (rus)
17. Mohebimoghaddam, B., Dianat, S.H. Evolution of the corrosion and strength of concrete exposed to sulfate solution. International Journal of Civil Engineering and Technology. 2012. Vol. 3. No. 2. Pp. 198–206.
18. Stevulova, N., Ondrejka Harbulakova, V., Luptakova, A., Repka, M. Study of sulphate corrosion simulations on concrete composites. International Journal of Energy and Environment. 2012. Vol. 6. No. 2. Pp. 276–283.
19. Brykov, A.S. Sulfate corrosion of Portland cement concretes. Cement and its Application. 2014. No. 6. Pp. 96–103. (rus)
20. Estemessova, A.S., Altayeva, Z.N., Esselbayeva, A.G. Modified concrete of new generation. Bulletin of the kazakh head architectural and construction academy. Science journla. JSC KazNIISA. 2015. No. 3 (57). Pp. 129–134. (rus)
21. Abdrakhmanova, K.A., Baydzhanov, D.O., Rakhimova, G.M., Mukhamedzhanova, A.T. Patent No. 33388 for an invention. Additive for concrete mixture. National Institute of Intellectual property RK. 2019.
22. Batrakov, V.G. Modifitsirovannye betony. Teoriya i praktika [Modified concretes. Theory and practice]. Moscow: Tekhnoproekt, 1998. 768 p.
23. Selyaev, V.P., Neverov, V.A., Selyaev, P.V., Sorokin, E.V., Yudina, O.A. Predicting the durability of concrete structures, including sulfate corrosion of concrete. Magazine of Civil Engineering. 2014. No. 1(45). Pp. 41–52. DOI: 10.5862/MCE.43.5 (rus)
24. Moskvin, V.I. Dolgovechnost betona i teoriya korrozii [The durability of concrete and the theory of corrosion]. Gidrotekhnicheskoe stroitelstvo. 1985. No. 8. Pp. 1–4. (rus)
25. Fedosov, S.V., Bazanov, S.M. Sulfatnaya korroziya betona [Sulphate corrosion of concrete]. Moscow: Izd-vo ACB, 2003. 191 p.

Contacts:

Djumageldy Baydjanov, +7(721)2569506; BDO3@yandex.ru
Kalamkas Abdrakhmanova, +7(701)5298782; kagaip@mail.ru
Pyotr Kropachev, +77021335710; kropachev-54@mail.ru
Galiya Rakhimova, +77014889480; galinrah@mail.ru

Инженерно-строительный журнал

ISSN 2071-0305

сайт журнала: http://engstroy.spbstu.ru/

DOI: 10.18720/MCE.85.13

Модифицированные бетоны для производства свайных фундаментов

Д.О. Байджанов, К.А. Абдрахманова*, П.А. Кропачев, Г.М. Рахимова,
Карагандинский государственный технический университет, г. Караганда, Республика Казахстан
** E-mail: kagaip@mail.ru*

Ключевые слова: модифицированные бетоны; добавки; железобетонные свайные фундаменты; стойкость к воздействию агрессивных сред; сульфатная коррозия; водонепроницаемость; долговечность бетона; грунтовые воды.

Аннотация. В работе рассмотрены вопросы структурной модификации тяжелых бетонов олигомер-полимерными добавками. Установлено, что кристаллизация цементного камня протекает на макро – и микроуровнях. Макропоры заполняются продуктами кристаллизации частичек цемента, привитых на поверхности макромолекул поливинилхлорида (ПВХ). Миграция макромолекул ПВХ и олигомеров отходов коксохимической промышленности (ОКП) в дефектные зоны протекает за счет возникновения внутренних напряжений в процессе твердения и объемного сжатия, что обуславливает закрытие макро и микропор, а также трещин и капилляров. Таким образом, по комплексу физико-механических свойств, стойкости к сульфатной коррозии и морозостойкости исследуемые бетоны на основе структурно-модифицированного бетона могут быть использованы для производства свайных фундаментов устраиваемых в условиях сильно засоленных грунтов. Представленные результаты экспериментальных исследований свидетельствуют о достаточной коррозионной стойкости исследуемых бетонов.

Литература

1. Шейнфельд А.В. Органоминеральные модификаторы как фактор, повышающий долговечность железобетонных конструкций // Бетон и железобетон. 2014. № 3. С. 16–21.
2. Богданов Р.Р., Ибрагимов Р.А. Процессы гидратации и структурообразования модифицированного самоуплотняющегося бетона // Инженерно-строительный журнал. 2017. № 5(73). С. 14–24. DOI: 10.18720/MCE.73.2
3. Селяев В.П., Ошкина Л.М., Селяев П.В., Сорокин Е.В. Исследование химической стойкости цементных бетонов с учетом сульфатной коррозии // Региональная архитектура и строительство. 2013. № 1. С. 4–11.
4. Розенталь Н.К. Проницаемость и коррозионная стойкость бетона // Промышленное и гражданское строительство. 2013. № 1. С. 35–37.
5. Ibragimov R. The influence of binder modification by means of the superplasticizer and mechanical activation on the mechanical properties of the high-density concrete. ZKG.: Zement-Kalk-Gips International. 2016. Vol. 69. No. 6. Pp. 34–39.
6. Ребиндер П.А. Поверхностно-активные вещества. М.: Знание, 1961. 268 с.
7. Смирнова О.М. Совместимость портландцемента и суперпластификаторов на поликарбоксилатной основе для получения высокопрочного бетона сборных конструкций // Инженерно-строительный журнал. 2016. № 6(66). С. 12–22. DOI: 10.5862/MCE.66.2
8. Литвинова Т.А. Органоминеральные добавки к строительным материалам на основе отходов газовой и нефтяной промышленности // Инженерно-строительный журнал. 2016. № 7(67). С. 13–21. DOI: 10.5862/MCE.67.2
9. Megat Johari M.A., Brooks J.J., Kabir S., Rivard P. Influence of supplementary cementitious materials on engineering properties of high strength concrete. Construction and Building Materials. 2011. Vol. 25. No. 5. Pp. 2639–2648.
10. Ветров С.Н., Яковлев С.В. Специфика обследования состояния железобетонных конструкций в условиях агрессивного воздействия воды // Инженерно-строительный журнал. 2010. № 7(17). С. 35–40.
11. Bonakdar A., Mobasher B. Multi-parameter study of external sulfate attack in blended cement materials. Construction and Building Materials. 2010. Vol. 24. No. 1. Pp. 61–70.
12. Котов Д.С. Деформации усадки бетона, модифицированного химическими и тонкодисперсными минеральными наполнителями // Инженерно-строительный журнал. 2009. № 7(9). С. 11–21.
13. Kirsanova A.A., Kramar L., Thiery V. The effect of additives including metakaolin on the freeze resistance of concrete. Materials Science Forum. 2016. Vol. 843. Pp. 263–268.

14. Ибрагимов Р.А., Пименов С.И. Влияние механохимической активации на особенности процессов гидратации цемента // Инженерно-строительный журнал. 2016. № 2(62). С. 3–12.
15. Prasad J., Jain D.K., Ahuja A.K. Factors influencing the sulfate resistance of cement concrete and mortar. Asian Journal of civil engineering (building and housing). 2006. No. 7(3). Pp. 259–268.
16. Латыпов В.М., Латыпова Т.В., Луцык Е.В., Федоров П.А. Долговечность бетона и железобетона в природных агрессивных средах. Уфа: РИЦ УГНТУ, 2014. 288 с.
17. Mohebimoghaddam B., Dianat S.H. Evolution of the corrosion and strength of concrete exposed to sulfate solution. International Journal of Civil Ingineering and Tehnology. 2012. Vol. 3. No. 2. Pp. 198–206.
18. Stevulova N., Ondrejka Harbulakova V., Luptakova A., Repka M. Study of sulphate corrosion simulations on concrete composites. International Journal of Energy and Environment. 2012. Vol. 6. No. 2. Pp. 276–283.
19. Брыков А.С. Сульфатная коррозия портландцементных бетонов // Цемент и его применение. 2014. № 6. С. 96–103.
20. Естемесова А.С., Алтаева З.Н., Есельбаева А.Г. Модифицированные бетоны нового поколения // Вестник Казахской головной архитектурно-строительной академии. Научный журнал. АО КазНИИСА. 2015. № 3(57). С. 129–134.
21. Абдрахманова К.А., Байджанов Д.О, Рахимова Г.М, Мухамеджанова А.Т. Патент № 33388 на изобретение Добавка в бетонную смесь // Национальный институт интеллектуальной собственности РК. 2019.
22. Батраков В.Г. Модифицированные бетоны. Теория и практика. М.: Технопроект, 1998. 768 с.
23. Селяев В.П., Неверов В.А., Селяев П.В., Сорокин Е.В., Юдина О.А. Прогнозирование долговечности железобетонных конструкций с учетом сульфатной коррозии бетона // Инженерно-строительный журнал. 2014. № 1(45). С. 41–52. DOI: 10.5862/MCE.43.5
24. Москвин В.И. Долговечность бетона и теория коррозии // Гидротехническое строительство. 1985. № 8. С. 1–4.
25. Федосов С.В., Базанов С.М. Сульфатная коррозия бетона. М.: Изд-во АСВ, 2003. 191 с.

Контактные данные:

Джумагельды Омарович Байджанов, +7(721)2569506; эл. почта: BDO3@yandex.ru
Каламкас Аманбековна Абдрахманова, +7(701)5298782; эл. почта: kagaip@mail.ru
Петр Александрович Кропачев, +77021335710; эл. почта: kropachev-54@mail.ru
Галия Мухамедиевна Рахимова, +77014889480; эл. почта: galinrah@mail.ru

Magazine of Civil Engineering. 2019. 86(2). Pp. 11–19
Инженерно-строительный журнал. 2019. № 2(86). С. 11–19

Magazine of Civil Engineering

ISSN 2071-0305

journal homepage: http://engstroy.spbstu.ru/

DOI: 10.18720/MCE.86.2

Manufacturing structural building components from round timber with heartwood rot

A.S. Toropov[a], V.E. Byzov[b]*, V.I. Melekhov[c],
[a] Saint Petersburg State Forest Technical University under name of S.M. Kirov, St. Petersburg, Russia
[b] St. Petersburg State University of Architecture and Civil Engineering, St. Petersburg, Russia
[c] Northern (Arctic) Federal University named after M.V. Lomonosov, Arkhangelsk, Russia
** E-mail: mapana@inbox.ru*

Keywords: round timber; heartwood rot; allometric growth equations; structural building components; the yield of T-section units.

Abstract. Coniferous sawn goods are widely used in construction industry. The quality of round timber deteriorates due to the presence of heartwood rot, which has to be removed in the manufacture of load-bearing structural units. As a rule, rot is removed during the round timber logging. At the same time, healthy sapwood is removed along with that impacted by rot. Therefore, large amounts of quality wood remain in forests. For qualitative ripping of round timber affected by heartwood rot, it is necessary to know the rot shape and size in trunks. The relationship between the round timber cross-sectional dimensions and heartwood rot size along the trunk length is quite accurately described by correlative (allometric) growth equations. As a result of the research, such interrelations were established. Based on the equations obtained, conditional ripping of round log was carried out. As a result, bars for manufacturing I-beams were obtained. They are widely used in low-rise wooden house construction. It was established that the recovery factor was high enough for structural units made of round timber affected by heartwood rot that makes it possible to propose this cutting method for industrial application.

1. Introduction

Coniferous sawn goods are widely used to manufacture load-bearing structural units. Requirements to timber intended for construction do not permit rot presence in it. However, dimensional and qualitative indicators deteriorate recently for raw materials intended for construction. Their average diameter becomes smaller, and saw logs with big diameter are affected by heartwood rot. It occurs due to the fact that trunks used for manufacturing timber assortments, become shorter, and the root parts of the logs with sufficient length and diameter are often affected by heartwood rot.

Crosscutting of such trunks into round logs involves removal of wood areas affected by rot due to difficulties in processing the wood injured with rot and high transportation costs. Therefore, significant amounts of wood are left in forests. Application of the existing technology results, first of all, in losing large amounts of raw wood since it contains high-quality sapwood (up to 70 % of the volume) along with the core injured by rot. Secondly, wood rotting spots are formed, which become sources of wood-destroying fungi and affect healthy timber stands. Therefore, the need appears to develop new ways of processing wood affected by heatwood rot.

Investigations to improve the quantitative and qualitative output of sawn goods from round wood affected by heartwood rot were carried out previously. In a number of studies, the sawn timber yield was compared when sawing low-quality coniferous raw materials through-and-through/ with log squaring at log

Toropov, A.S., Byzov, V.E., Melekhov, V.I. Manufacturing structural building components from round timber with heartwood rot. Magazine of Civil Engineering. 2019. 86(2). Pp. 11–19. DOI: 10.18720/MCE.86.2.

Торопов А.С., Бызов В.Е., Мелехов В.И. Получение элементов строительных конструкций из круглых лесоматериалов с сердцевинной гнилью // Инженерно-строительный журнал. 2019. № 2(86). С. 11–19. DOI: 10.18720/MCE.86.2

frames and individually in sleeper saw benches. The advantage of open-type sawing was established as compared to sawing at log frames. Studies, carried out by R.E. Kalitievsky showed that the volume yield of sawn goods increased when using bandsaw machines for logs affected by rot. A.N. Pesotskiy and many other researchers proposed to use a circular cutting method that allowed separation of the log rotten part and its exclusion from sawn goods. Having processed experimental data, V.S. Petrovsky established a correlation between recovery factor and the rot relative diameter. The resulting formulas were valid with regard to cutting bottom pinewood logs through-and-through into sawn timber. He proposed that each sawmill would determine the maximum allowable size of rot, depending on the raw material price, production costs and volume yield of sawn goods.

A.S. Toropov has developed cutting methods, protected by Russian Federation patents, for wood affected by heartwood rot, which made possible to efficiently use timber sapwood [1–3]. In particular, patent [3] provides longitudinal cutting of round timber into sections, from which the core zone is removed, for example, by shaping. Resulting blanks are straightened by steaming, bending and pressing. Then, sawn goods are produced by gluing. Other patents also provide efficient cutting of timber affected by rot and production of high-quality sawn goods.

Today, the volume of low-rise wooden house construction is growing significantly. During construction, various wooden beams are used. Beams made of I-shaped wood are of greatest demand. They are used to cover spans 2 m to 6 m long. Flanges are made of solid or glued wood. I-beam webs are made of plywood. In Canada, OSB-3 and OSB-4 material is used for web manufacturing, while in Russia LVL is used for beam webs production. The article [4] considers a method of I-beam units manufacturing from round timber with heart rot. Numerous studies are dedicated to strength characteristics of I-beams made of wood and wood materials with various connection types [5–18].

The accomplished paper review and assessment allows establishing the purpose and objectives of this study. The aim of the work is to improve the cutting method for round timber affected by heart rot to produce structural units, taking into account rot dimensions and location in assortments. Structural units are used in the low-rise wooden house construction. The goal requires to solve several tasks: to obtain dependences of the round timber shape and size; to establish correlation dependences between the heart rot diameter and the cross-sectional assortment diameter; to work out the way for balanced longitudinal cutting of round timber to obtain the maximum yield of structural units and to determine the yield of structural units from round timber with heartwood rot.

2. Methods

To efficiently cut round timber with heartwood rot, it is necessary to know the location of the rot in trunks. Therefore, let's consider the basic principles of tree trunk formation and the heartwood rot development in it. During the tree growth, its different organs develop simultaneously. It was found that the change in growth rates occurs synchronously during simultaneous growth of two or more organs. The growth rate ratio remains approximately constant. This ratio is well described by the formula:

$$y = C + ax^b, \tag{1}$$

where x and y are variable factors;

a and C are initial state constants;

b is the equilibrium constant that features the rate change of y relatively x.

To link the diameter of the heart rot in a random cross section and the diameter of the heartwood rot in the timber butt end, it is converted into an expression:

$$d_h = d_{h0} + al_h^b \ , \tag{2}$$

where d_h is the heartwood rot diameter in a random cross section, m;

d_{h0} is rot diameter in the round timber butt end, m;

l_h is the distance from the butt end to the heartwood rot distance,

m; a, b are initial state and equilibrium constants, correspondingly.

The diameters of the heardwood rot at the butt end of the timber and the diameter of heartwood rot and timber at a distance from the butt end was measured on 10 of the round timber with heartwood rot (Figure 1).

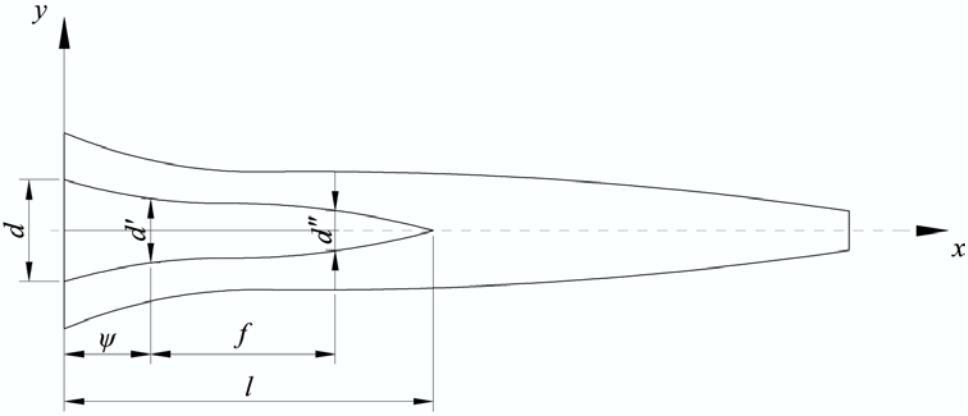

Figure 1. Computational model.

where d_{h0} is the rot diameter in the round timber butt end, m;

l_h is the distance from the butt end to the heartwood rot location, m;

$d_h^{'}, d_h^{''}$ is rot diameter in two locations of diameter measurement along the affected length l_h, correspondingly, m;

ψ and f are the x-coordinate of the location of the first measurement and the distance between the rot diameter measurement points, correspondingly, m.

Log and heartwood rot diameters were measured in meters per every meter of the length, as the length of a straight line that passes through the cross-section centre, perpendicular to the longitudinal axis of the log. Then, the average value was calculated for two measurements within one cross-section.

According to the program METHODS.EXE the values of the initial state constants a and equilibrium b. Values of the constants are calculated by formulas:

$$a = \left(\frac{1}{\psi}\right)^b \cdot \left(d_{h0} - d_h^{'}\right), \tag{3}$$

$$b = \ln\left[\left(d_{h0} - d_h^{''}\right) / \left(d_{h0} - d_h^{'}\right)\right] / \ln\left[\left(\psi + f\right) / \psi\right], \tag{4}$$

where d_h' and d_h'' are rot diameter in two measurement locations along the exposure length l_h, correspondingly, m;

ψ and f are the corresponding x-coordinate of the first measurement location and the distance between rot measurement points, m.

Applying the acquired values of the constants made the equation of when the rot diameter at an arbitrary cross section of the timber with the rot diameter at the butt end 10 of the round timber. Using the equations obtained, we calculated the diameters of the rot in the cross sections located 1 m along the length of the timber. The calculated rot diameters were compared with the actual values obtained as a result of measurements.

Round timber is conventionally cut in the logs with a length of 6 and 4 m. Logs were cut into squares with the maximum area in the log top part. Then, they were divided in half in a longitudinal direction. Each resulting part contained heart rot with different length. Rot dimensions were made based on the results of actual measurements, the rot at the round timber from which the logs are. The rot minimum size was in the square top, and the maximum one was in the butt end (Figure 2a).

To produce structural units from squares, rot was removed by conventional shaping and obtaining T-section units free from rot (Figure 2b).

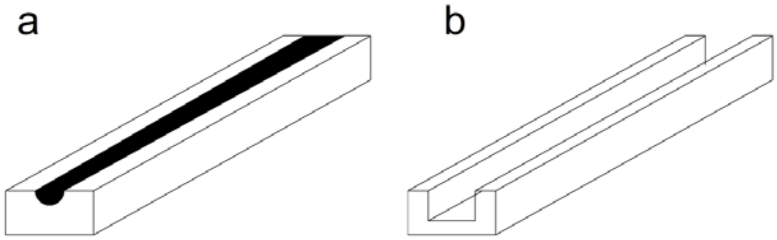

Figure 2. Shaping layout of the unit affected by rot
a – rot location diagram; b –T-section unit.

T-section units may be used to manufacture beam structures of different cross-sections. It is possible to use T-section units as I-beam flanges with plywood webs. Another application scheme involves connection of T-section units by a wide sawn face into an I-section beam. After conditional cutting and rot removal, the dimensions of T-section units were measured. The useful wood yield was defined for units made of round timber with rot.

3. Research results

According to the program METHODS.EXE the values of the initial state constants ***a*** and equilibrium ***b*** were calculated for the correlation equation of the rot diameter in an arbitrary section along the length with the rot diameter in the timber butt. For calculations, the results of measurements of rot diameters in sections located along the length of the lesion at the same distances from each other were used. The values of the distance from the butt of timber in the first section and the distances between the sections where the sections of rot were measured were applied. These values are based on the results of measurement of the heartwood rot size for ten pieces of pinewood round timber, in accordance with the computational model. Table 1 contains the computation results.

Table 1. Computation results.

Sec. No.	Heart rot diameter in a butt end, [m]	a	b
1	0.063	–0.012	0.658
2	0.082	–0.010	0.783
3	0.108	–0.032	0.512
4	0.097	–0.007	1.035
5	0.082	–0.029	0.387
6	0.093	–0.021	0.603
7	0.091	–0.013	0.759
8	0.076	–0.013	0.734
9	0.086	–0.029	0.344
10	0.076	–0.012	0.776

In an analytical form, dimensional dependence of the stump heartwood rot is as follows for the first trunk:

$$d_h = 0.063 - 0.012 l_h^{0.658}$$

The following diagrams were plotted based on the rot diameter computation data according to relative growth equations and measurement data of the heartwood rot diameter (Figures 3 to 5).

The data from the diagrams demonstrated good match of actual measurement results with the data calculated by relative growth equations.

Taking into account the heart rot shape and dimensions, we have worked out a cutting plan for round timber to produce structural units. Round timber rise has a significant impact on the final product output. Rise is the diameter decrease per one meter of the timber length from the butt end to the trunk top. Round timber was conditionally cut into 6 m long round logs with diameter of at least 20 cm at the top part. If the trunk length was insufficient for cutting into 6 m log, they were cut into 4 m long log. Log diameter was measured at their top and butt end. To exclude the effect of the near-root knar, butt-end diameter was measured at a distance one meter from the butt end. Rise values were calculated for round timber; the results are given in Table 2.

The data in Table 2 illustrated that the rise in round logs achieved 2.0 % to 2.3 %. According to research results presented in [19], rise value was about 1.4 cm/m for butt-end pinewood logs having diameter 26 cm. The higher rise in logs, which we obtained after trunk cutting, was caused by the fact that the biggest rise was typical for logs produced from the trunk butt portion. In this regard, the rise of sawn round timber is less than that for the logs with heartwood rot, which we obtained after conditional cutting.

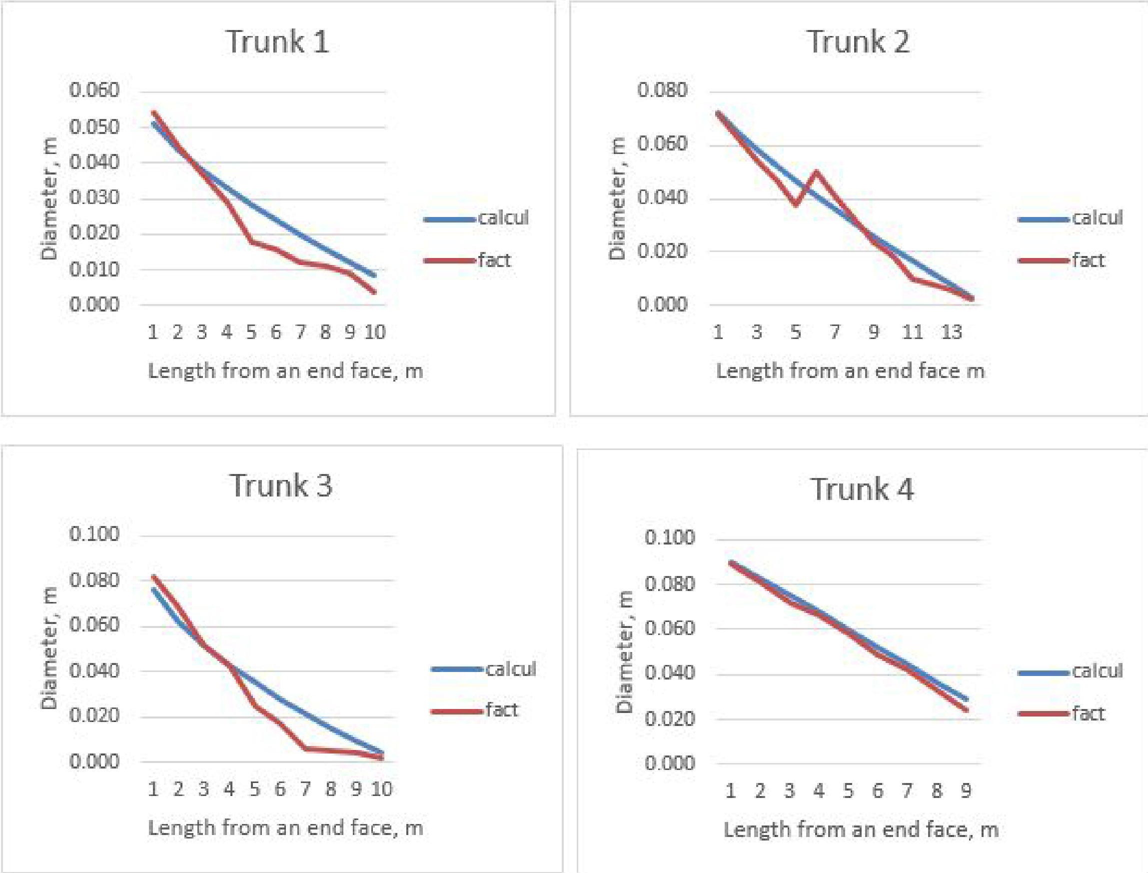

Figure 3. Actual heartwood rot diameters as compared with the calculation data (trunk 1 to 4).

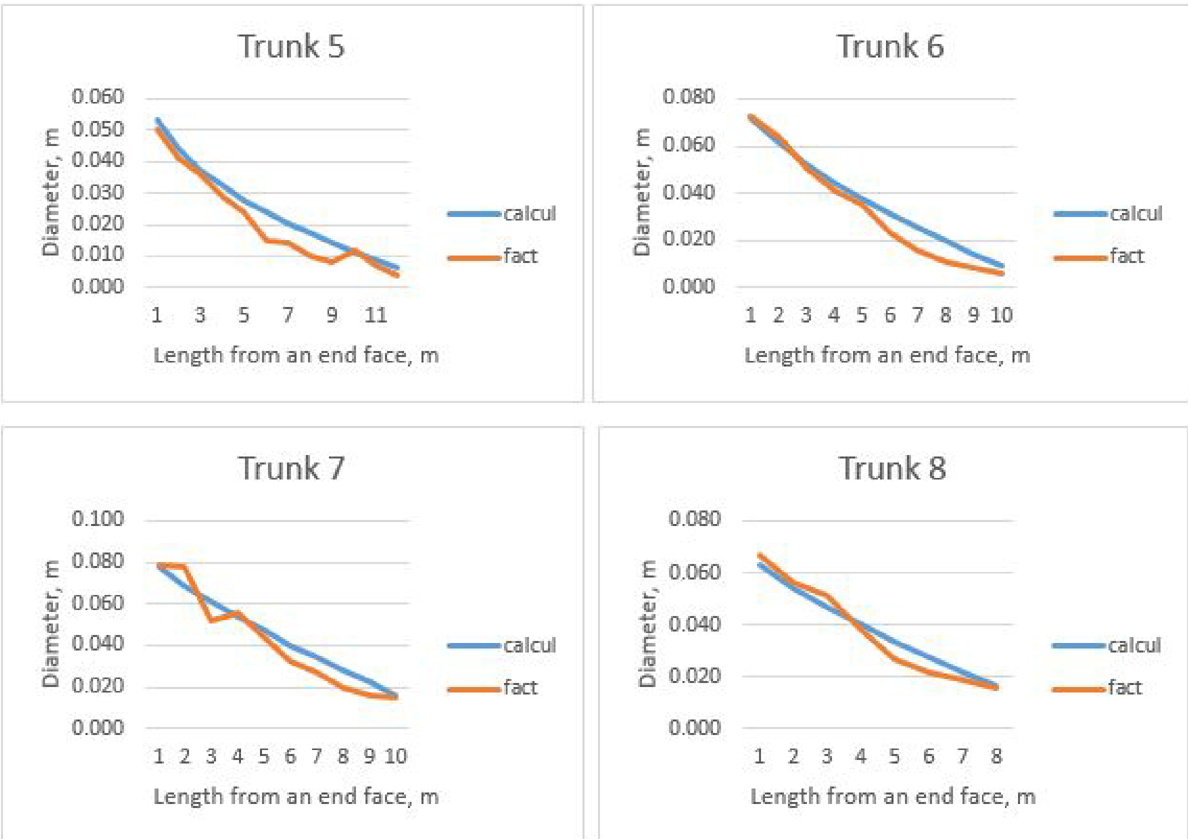

Figure 4. Actual heartwood rot diameters as compared with the calculation data (trunk 5 to 8).

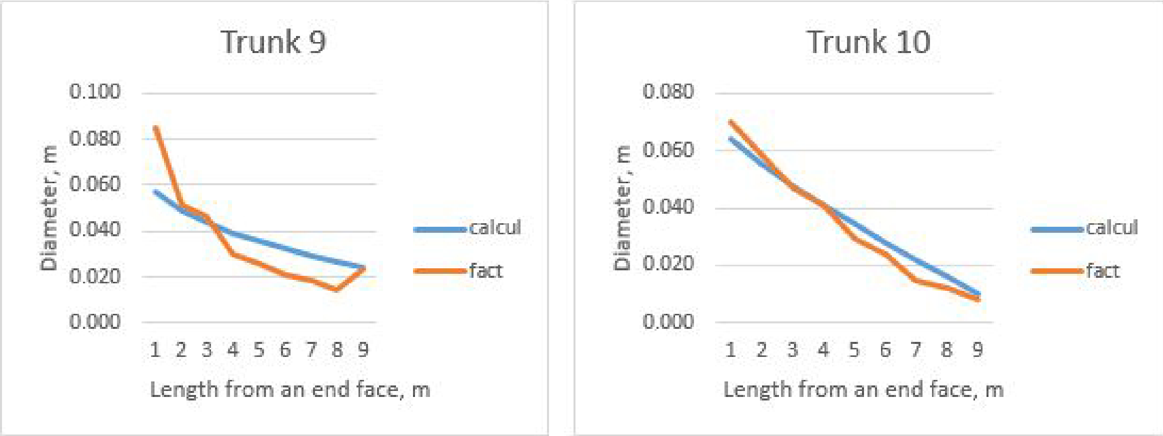

Figure 5. Actual diameter of heartwood rot as compared with the calculation data (trunk 9 to 10).

Table 2. Round log rise values.

Seq. No.	Round timber diameter, cm	Length, m	Round timber volume, m^3	Rise value, cm/m
1	24	6	0.330	0.9
2	24	6	0.330	2.0
3	20	6	0.230	2.1
4	26	6	0.390	1.4
5	22	4	0.178	2.3
6	24	6	0.330	2.0
7	22	4	0.178	0.9
8	22	4	0.178	2.3
9	20	6	0.230	1.3
10	20	4	0.147	1.0

Having performed a conditional timber cutting, we obtained the dimensions of T-section units. Then, we calculated the yield of T-section units from logs. Calculation results are given in Table 3.

Table 3. Yield of T-section units from round logs and unit dimensions.

Seq. No.	Round log diameter, mm	Length, m	Round log volume, m^3	Unit height, mm	Unit width, mm	Flange thickness, mm	Web thickness, mm	Unit volume, m^3	Yield of T-section units, %
1	24	6	0.330	175	85	55	55	0.155	47.0
2	24	6	0.330	175	85	51	51	0.149	45.1
3	20	6	0.230	150	72	20	20	0.061	26.5
4	26	6	0.390	175	85	51	51	0.149	38.2
5	22	4	0.178	150	72	30	30	0.056	31.6
6	24	6	0.330	175	85	41	41	0.129	39.2
7	22	4	0.178	150	72	30	30	0.083	46.4
8	22	4	0.178	150	72	37	37	0.064	36.2
9	20	6	0.230	150	72	32	32	0.087	38.0
10	20	4	0.147	150	72	36	36	0.064	43.5

The results shown in Table 2 indicate the possibility to produce structural units of 150 mm, 175 mm high and 4 m and 6 m long. The yield of bars for T-section units was about 40 % for round timber. The study performed [20] showed that, for example, the total timber yield from logs of 26 cm in diameter was about 57 %. It may be stated that the presence of rot in logs reduces the yield by 17 %. However, it should be kept in mind that approx. 40 % of the yield is made up by bars; and cutting will be performed for round timber, which is currently not allowed for manufacturing construction sawn goods; and wood remains in forests or is used to produce fuel chips at the best.

4. Conclusion

1. Application of allometric method during the trunk of the heartwood rot size permits to efficiently cut round timber.

2. It is possible to produce structural units from pinewood round timber affected by heartwood rot.

3. It is possible to use T-section structural units when manufacturing beam structures with different cross section. The most efficient way of their application is to use them as I-beam flanges or to connect directly into an I-beam.

4. Rise values for logs with heart stump rot significantly exceed the ones for the logs produced from trunk according to valid regulatory documents.

5. The yield of T-section structural unit from round timber with heartwood rot was approx. 40 %.

6. Application of round timber impacted by rot for manufacturing building structures increases wood resources for low-rise wooden house construction.

References

1. Patent 2051026 RF. Sposob pererabotki kruglyh lesomaterialov, imejushhih serdcevinnuju gnili [The method for processing round timber with heart rot]. A.S. Toropov, S.K. Tesljuk, S.A. Toropov; Marijskij politehnicheskij institut. No. 9301619815; zajav. 29.03.93; opubl. 27.12.95, Bjul. No. 36. (rus)
2. Patent 2399482 RF. Sposob raskroja kruglyh lesomaterialov, porazhjonnyh serdcevinnoj gnil'ju [The method of cutting round timber, affected by heart rot]. A.S. Toropov, S.A. Toropov, E.V. Mikrjukova. No. 200813768103; zajav. 19.09.2008; opubl. 20.09.2010. (rus)
3. Patent 2654720 RF. Sposob poluchenija konstrukcionnoj piloprodukcii iz kruglyh lesomaterialov, imejushhih serdcevinnuju gnili [The method of obtaining structural sawn timber from round timber with heart rot]. V.E. Byzov, A.S. Toropov, S.A. Toropov; Federal'noe gosudarstvennoe bjudzhetnoe obrazovatel'noe uchrezhdenie vysshego obrazovanija Sankt-Peterburgskij gosudarstvennyj arhitekturno-stroitel'nyj universitet. No. 2017131378; zajavl. 06.09.2017; opubl. 20.05.2018. (rus)
4. Byzov, V.E. Wooden I-Beams Made of Round Timber with a Core Rot. American Journal of Construction and Building Materials. 2018. No. 1. Pp. 16–21.
5. Karelskiy, A.V., Zhuravleva, T.P., Labudin, B.V. Load-to failure bending test of wood composite beams connected by gang nail. Magazine of Civil Engineering. 2015. 54(2). Pp. 77–127. DOI: 10.5862/MCE.54.9 (rus)
6. Ponomarev, A.N., Rassokhin, A.S. Hybrid wood-polymer composites in civil engineering. Magazine of Civil Engineering. 2016. 68(8). Pp. 45–47. DOI: 10.5862/MCE.68.5
7. Tusnin, A.R., Prokitch, M. Experimental research of I-beams under bending and torsion actions. Magazine of Civil Engineering. 2015. 53(1). Pp. 24–31. DOI: 10.5862/MCE.53.3 (rus)
8. Bryantsev, A.A., Absimetov, V.V. Effective application of I-beams with corrugated webs in the industrial building]. Construction of Unique Building and Structures. 2017. No. 3. Pp. 93–104. DOI: 10.18720/CUBS.54.8 (rus)
9. Ivanov, S.S. Foschi's method of strain calculation of the metal plate connectors compared to program complex APM Wood. Construction of Unique Building and Structures. 2016. No. 8. Pp. 31–46.
10. Benjeddou, O., Limam, O., Ouezdou, U. Experimental and theoretical study of a foldable composite beam. Engineerg Structures. 2012. No. 44. Pp. 312–321.
11. Challamel, N., Girhammar, U. Lateral-torsional buckling of vertically layered composite beams with interlayer slip under uniform moment. Engineering Structures. 2012. No. 34. Pp. 505–513.
12. Fernando, D., Frangi, A., Kobel, P. Behavior of basalt fiber reinforced polymer strengthened timber laminates under tensile load. Engineering Structures. 2016. No. 117. Pp. 437–456.
13. Khorsandnia, N., Valipour, H., Crews, K. Nonlinear finite element analysis of timber beams and joints using the layered approach and hypoelastic constitutive law. Engineering Structures. 2013. No. 46. Pp. 606–614.
14. Atavin, I.V., Melnikov, B.E., Semenov, A.S., Chernysheva, N.V., Yakovleva, E.L. Influence of stiffness of node on stability and strength of thin-walled structure. Magazine of Civil Engineering. 2018. No. 4(80). Pp. 48–61. DOI: 10.18720/MCE.80.5.
15. Harte, A., Baylor, G. Structural evaluation of castellated timber I-joists. Engineering Structures. 2011. Vol. 33. No. 12. Pp. 3748–3754.
16. Nekliudova, E.A., Semenov, A.S., Melnikov, B.E., Semenov, S.G. Experimental research and finite element analisis of elastic and strength properties of fiberglass composite material. Magazine of Civil Engineering. 2014. 47(3). Pp. 25–39. DOI: 10.5862/MCE.47.3
17. Rassokhin, A.S., Ponomarev, A.N., Figovsky, O.L. The formation of the seabed surface relief near the gravitational object. Magazine of Civil Engineering. 2018. 79(3). Pp. 132–139. DOI: 10.18720/MCE.79.14.
18. O'Loinsigh, C., Oudjene, M., Shotton, E., Pizzi, A., Fanning, P. Mechanical behavior and 3D stress analysis of multi-layered wooden beams made with welded-through wood dowels. Composite Structures. 2012. Vol. 94. No. 2. Pp. 313–321.
19. Vetsheva, V.F., Gerasimova, M.M. Issledovaniye resursoyemkosti sosnovykh i listvennichnykh pilovochnykh breven angaro-yeniseyskogo regiona [Study of the resource intensity of pine and larch sawn logs of the Angara-Yenisei region]. Vestnik KrasGAU. 2011. No. 10. Pp. 194–200. (rus)
20. Ogurtsov, V.V., Kargina, Ye.V., Matveyeva, I.S. Zavisimost obyema vykhoda pilomaterialov ot drobnosti sortirovki breven po tolshchine [The dependence of the volume of lumber output on the fractionality of sorting logs by thickness]. Khvoynyye borealnoy zony XXXI. 2013. No. 5–6. Pp. 71–75. (rus)

Contacts:

Aleksandr Toropov, +78126709369; Toropov_A_S@mail.ru
Viktor Byzov, +79811220539; mapana@inbox.ru
Vladimir Melekhov, +78182216149; lti@narfu.ru

Инженерно-строительный журнал

ISSN 2071-0305

сайт журнала: http://engstroy.spbstu.ru/

DOI: 10.18720/MCE.86.7

Получение элементов строительных конструкций из круглых лесоматериалов с сердцевинной гнилью

А.С. Торопов[a], В.Е. Бызов[b]*, В.И. Мелехов[c],

[a] Санкт-Петербургский государственный лесотехнический университет им. С.М. Кирова, Санкт-Петербург, Россия

[b] Санкт-Петербургский государственный архитектурно-строительный университет, Санкт-Петербург, Россия

[c] Северный (Арктический) федеральный университет им. М.В. Ломоносова, г. Архангельск, Россия

** E-mail: mapana@inbox.ru*

Ключевые слова: круглые лесоматериалы; сердцевинная ядровая гниль; уравнения аллометрического роста; элементы строительных конструкций; полезный выход.

Аннотация. В строительстве широко применяются пиломатериалы хвойных пород. Качество круглых лесоматериалов ухудшается. В них часто встречается ядровая гниль, которую приходиться удалять при изготовлении несущих строительных конструкций. Как правило удаление гнили происходит на этапе заготовки круглых лесоматериалов. При этом вместе с древесиной поражённой гнилью удаляется здоровая заболонная часть. Поэтому большое количество качественной древесины остаётся в лесу. Для качественного продольного раскроя круглых лесоматериалов с ядровой гнилью необходимо знать форму и размеры гнили в сортименте. Взаимосвязь размеров поперечного сечения круглых лесоматериалов и ядровой гнили по длине сортиментов достаточно точно описывается уравнениями соотносительного (аллометрического) роста. В результате проведения исследований были установлены такие связи. На основании полученных уравнений проведён условный продольный раскрой круглых сортиментов. В результате раскроя получали элементы для изготовления двутавровых балок. Такие балки находят широкое применение в малоэтажном деревянном домостроении. Установлено, что полезный выход элементов строительных конструкций из круглых лесоматериалов с сердцевинной ядровой гнилью достаточно высокий. Это даёт возможность предложить данный способ раскроя для промышленного применения.

Литература

1. Патент 2051026 РФ. Способ переработки круглых лесоматериалов, имеющих сердцевинную гниль / А.С. Торопов, С.К. Теслюк, С.А. Торопов; Марийский политехнический институт. – № 93016198/15; заяв. 29.03.93; опубл. 27.12.95, Бюл. № 36. 3 с.
2. Патент 2399482 РФ, МПК B27 B 1/00. Способ раскроя круглых лесоматериалов, поражённых сердцевинной гнилью / А.С. Торопов, С.А. Торопов, Е.В. Микрюкова. № 2008137681/03; заяв. 19.09.2008; опубл. 20.09.2010. 8 с.
3. Патент 2654720 РФ, МПК B27 B 1/00 Способ получения конструкционной пилопродукции из круглых лесоматериалов, имеющих сердцевинную гниль / В.Е. Бызов, А.С. Торопов, С.А. Торопов; Федеральное государственное бюджетное образовательное учреждение высшего образования «Санкт-Петербургский государственный архитектурно-строительный университет. № 2017131378; заявл. 06.09.2017; опубл. 20.05.2018. 10 с.
4. Byzov V.E. Wooden I-Beams Made of Round Timber with a Core Rot // American Journal of Construction and Building Materials. 2018. No. 1. Pp.16–21.
5. Карельский А.В., Журавлёва Т.П., Лабудин Б.В. Испытание на изгиб деревянных составных балок, соединённых металлическими зубчатыми пластинами, разрушающей нагрузкой // Инженерно-строительный журнал. 2015. № 2(54). С. 77–127. DOI: 10.5862/MCE.54.9
6. Пономарев А.Н., Рассохин А.С. Гибридные древесно-полимерные композиты в строительстве // Инженерно-строительный журнал. 2016. № 8(68). С. 45–57. DOI: 10.5862/MCE.68.5
7. Туснин А.Р., Прокич М. Экспериментальные исследования работы балок двутаврового сечения при действии изгиба и кручения // Инженерно-строительный журнал. 2015. № 1(53). С. 24–31. DOI: 10.5862/MCE.53.3
8. Брянцев А.А., Абсиметов В.В. Эффективность применения двутавров с гофрированными стенками в производственных зданиях // Строительство уникальных зданий и сооружений. 2017. № 3(54). С. 93–104. DOI: 10.18720/CUBS.54.8
9. Иванов С.С. Расчет соединений на металло-зубчатых пластинах методом Foschi и с использованием программного комплекса APM Wood // Строительство уникальных зданий и сооружений. 2016. № 8(47). С. 31–46.

10. Benjeddou O., Limam O., Ouezdou M. Experimental and theoretical study of a foldable composite beam // Engineering Structures. 2012. № 44. Pp. 312–321.
11. Challamel N., Girhammar U. Lateral-torsional buckling of vertically layered composite beams with interlayer slip under uniform moment // Engineering Structures. 2012. № 34. Pp. 505–513.
12. Fernando D., Frangi A., Kobel P. Behavior of basalt fiber reinforced polymer strengthened timber laminates under tensile load // Engineering Structures. 2016. № 117. Pp. 437–456.
13. Khorsandnia N., Valipour H., Crews K. Nonlinear finite element analysis of timber beams and joints using the layered approach and hypoelastic constitutive law // Engineering Structures. 2013. № 46. Pp. 606–614.
14. Атавин И.В., Мельников Б.Е., Семенов А.С., Чернышева Н.В., Яковлева Е.Л. Влияние жесткости узловых соединений на устойчивость и прочность тонкостенных конструкций // Инженерно-строительный журнал. 2018. № 4(80). С. 48–61. DOI: 10.18720/MCE.80.5.
15. Harte A., Baylor G. Structural evaluation of castellated timber I-joists // Engineering Structures. 2011. Vol. 33. No. 12. Pp. 3748–3754.
16. Неклюдова Е.А., Семенов А.С., Мельников Б.Е., Семенов С.Г. Экспериментальное исследование и конечно-элементный анализ упругих и прочностных свойств стекловолоконного композиционного материала // Инженерно-строительный журнал. 2014. №3(47). С. 25–39. DOI: 10.5862/MCE.47.3
17. Рассохин А.С., Пономарев А.Н., Фиговский О.Л. Сверхлегкие гибридные композитные древесно-полимерные конструкционные элементы в строительстве // Инженерно-строительный журнал. 2018. № 3(79). С. 132–139. DOI: 10.18720/MCE.79.14.
18. O'Loinsigh C., Oudjene M., Shotton E. et al. Mechanical behavior and 3D stress analysis of multi-layered wooden beams made with welded-through wood dowels // Composite Structures. 2012. Vol. 94. No. 2. Pp. 313–321.
19. Ветшева В.Ф., Герасимова М.М. Исследование ресурсоёмкости сосновых и лиственничных пиловочных брёвен ангаро-енисейского региона // Вестник КрасГАУ. 2011. № 10. С. 194–200.
20. Огурцов В.В., Каргина Е.В., Матвеева И.С. Зависимость объёма выхода пиломатериалов от дробности сортировки брёвен по толщине // Хвойные бореальной зоны XXXI. 2013. № 5–6. С. 71–75.

Контактные данные:

Александр Степанович Торопов, +78126709369; эл. почта: Toropov_A_S@mail.ru
Виктор Евгениевич Бызов, +79811220539; эл. почта: mapana@inbox.ru
Владимир Иванович Мелехов, +78182216149; эл. почта: lti@narfu.ru

Magazine of Civil Engineering. 2019. 86(2). Pp. 20–29
Инженерно-строительный журнал. 2019. № 2(86). С. 20–29

Magazine of Civil Engineering

ISSN 2071-0305

journal homepage: http://engstroy.spbstu.ru/

DOI: 10.18720/MCE.86.3

Modelling the stressed skin effect by using shell elements with meta-material model

S. Pajunen[a*], J. Hautala[a], M. Heinisuo[b]
[a] Tampere University, Tampere, Finland
[b] Sorvimo Optimointipalvelut Oy, Tampere, Finland
** E-mail: sami.pajunen@tuni.fi*

Keywords: stressed skin; diaphragm; corrugated sheet.

Abstract. It is a well-known fact that the so-called stressed skin design results in ca. 10–20 % mass and cost savings in a typical steel hall structures. The potential of this design method is however, too often disregarded due to e.g. rather complex and limited existing design rules and instructions. In this paper, a method for determination of generalized elastic parameters is proposed, so that the stressed skin can be modelled in the general finite element software using existing elements and material parameters. With the proposed method, structural designer can take advantage of the stressed skin design in the context of basic design tools as Autodesk Robot or RFEM.

1. Introduction

The stressed skin design fundamentals were established in Europe in the 1970s [1] as described in the comprehensive state-of-the-art review [2]. However, earlier applications were presented in which the bending panels were also carrying axial loads, see e.g. [3]. The stressed skin design method is based on the load-carrying capacity of wall or roof cladding which is typically built of either profiled sheets or cassettes and fastened to a steel frame. When adopted for roofs, the stressed skin action reduces the stresses in columns by transferring the horizontal loads to the gable end walls. In such applications, material cost savings due to stressed skin action is typically 10–20 %, but even higher cost reductions are reported as in [4, 5] and in [6] by adopting simulations and tests, respectively. The design method relies on remarkable way to various empirically obtained parameter values, which are then used to define the flexibility and load-carrying capacity of the designed structural system.

The stressed skin design method is prescribed in an ECCS TC7 report [7] dated to the mid 1990s. The design approach presented in the report is based on the research work established in [8]. A simpler approach for the stressed skin design is also presented, see e.g. [9]. Different aspect of these two approaches are discussed in [10]. The report [7] provides the design method itself, but also some generic rules for fastener and sheet flexibility and capacity calculations. The report does not, however, take into account all the aspects of the stressed skin design as pointed out in [2] and e.g. in [11]. Also the material and structural development would result in modified test results compared to those adopted in [7]. In order to make it possible to broaden the applicability area of the stressed skin design, comprehensive test series were carried out giving more information on non-standard structural cladding systems [12, 13].

The design principles for the stressed skin method are presented in detail e.g. in [8, 14, 15]. The design method ensures that the actual shear force acting in the sheet is less than the capacity of the structure taking into account seam shear force capacities and instability loads for local and global buckling as well as the end collapse. Fasteners are in the central role when defining the capacity and flexibility of the structure. The fasteners are used to connect sheets to each other and sheets to purlins, rafters and end gables as highlighted in Figure 1. In a typical well-designed case, the seam fastener capacity and profile's ability to restrain the

Pajunen, S., Hautala, J., Heinisuo, M. Modelling the stressed skin effect by using shell elements with meta-material model. Magazine of Civil Engineering. 2019. 86(2). Pp. 20–29. DOI: 10.18720/MCE.86.3.

Пайюнен С., Хаутала Дж., Хейнисуо М. Моделирование несущих ограждающих конструкций плоскими конечными элементами со свойствами метаматериала // Инженерно-строительный журнал. 2019. № 2(86). С. 20–29. DOI: 10.18720/MCE.86.3

distortion are the determining factors. The stressed skin action can be taken into account for corrugated sheet as well as cassette and sandwich panels. In the abovementioned conventional stressed skin design approach, the most severe drawback is, that the design rules [7] cannot be implemented to existing design modelling software as such, but they must be taken into account as separate calculations making the stressed skin design process complex and unattractive.

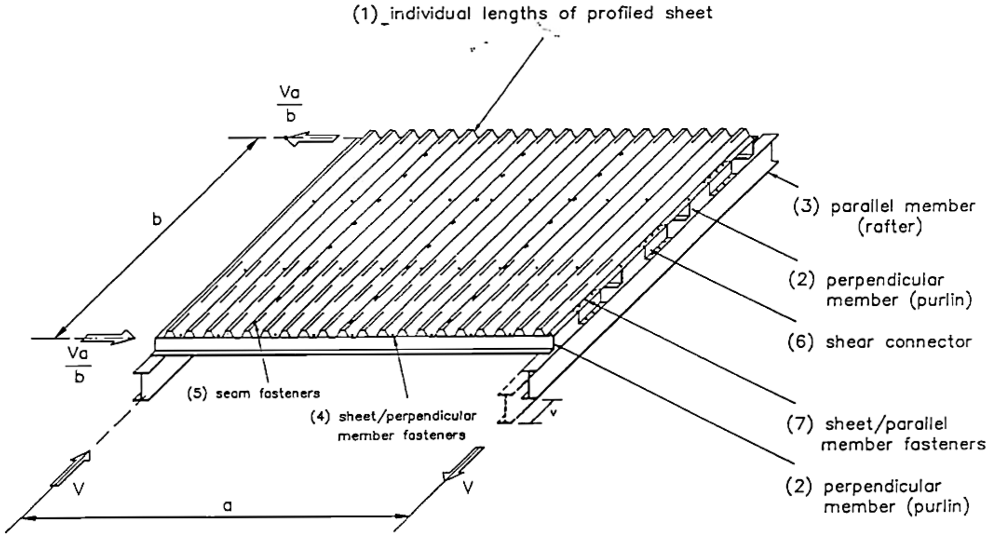

Figure 1. Typical shear panel according to [7].

This paper provides a simulation-driven point-of-view to the stressed skin design. The aim of the paper is to define an equivalent system of finite elements that can be used for the profiled sheet analysis and design instead of modelling the profiled sheet as complex folded plate. The paper discusses which generalized material parameters are needed for the system of elements. The FE-simulations and material definitions in this paper are carried out by using ANSYS, but a similar procedure can be derived for other platforms as well. The main benefits of the method is, that it provides an accurate and computationally efficient way to calculate shear force distribution in the sheet as well as the associated fastener forces.

The paper is organized in a way that the stressed skin principles are revisited in Chapter 2. The procedure for the generation of the proposed method is derived in Chapter 3 and the method usage is explained in detail in Chapter 4. Chapter 5 contains conclusions and further open research questions.

2. Methods

2.1. Stressed skin design principles

The stressed skin approach can be clarified by considering the frame structure augmented with a corrugated steel roof cladding depicted in Figure 2. When the roof is assumed to act as a diaphragm, it transverses part of the lateral load to foundations via shear stresses in the roof skin and via the diagonal bracing located to the end of the building. The roof is divided into shear panels and the stiffness and the shear capacity of each panel is defined according to the cladding and fastening by following the general rules given in [7]. Table 1 presents the ingredients from which the shear panel flexibility is calculated according to ECCS rules [7].

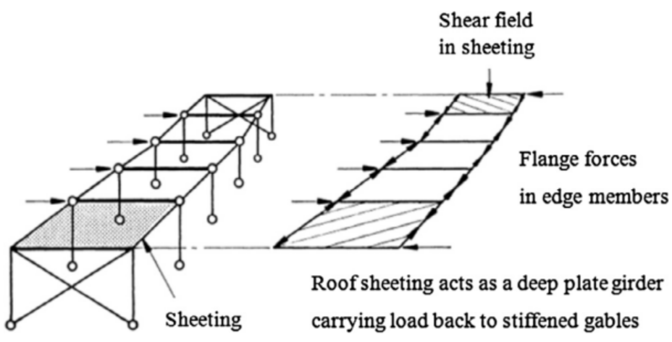

Figure 2. Structural model of the roof diaphragm [7].

In the design process, the lowest failure mode is assumed to be either seam/seam shear failure or seam/rafter shear failure. Depending on the sheeting properties and the number and the type of fasteners, the lower seam failure load is calculated. After this design shear force is calculated, the other failure modes associated with local and global shear buckling as well as profile sheet end distortion are checked. In a case where these instability phenomena become critical before the design shear load, the structure is modified. Otherwise the actual shear force is checked to be below the design shear load.

Being a rather simple design method, the stressed skin design approach is still not used too widely. The main reason for that is possibly the lack of knowledge of the method and the lack of easy-to-use stressed skin design tools. Moreover, the general design guide [7] contains many simplifications that reduce the full potential of the approach.

In order to get the method into more wide use, the finite element analysis and the stressed skin approach should be combined more closely and in a rather general way. That would enable the designer to get accurate distinct connector shear forces and a more realistic shear flow distribution field. Similarly, the actual failure mode could be identified, and its safety margin could be computed against both the true shear forces and the design seam shear capacities.

Table 1. An example of shear panel flexibility determination according to [7]. See the reference for detailed description of the components and other cases.

Shear flexibility due to:		shear flexibility mm/kN
sheet deformation	profile distortion	$c_{1.1}=\dfrac{ad^{2.5}\alpha_5 K}{Et^{2.5}b^2}$
	shear strain	$c_{1.2}=\dfrac{2a\left(1+v\right)\left(1+\dfrac{2h}{d}\right)}{Etb}$
fastener deformation	sheet to perpendicular member fastener	$c_{2.1}=\dfrac{2as_p p}{b^2}$
	seam fastener	$c_{2.2}=\dfrac{s_s s_p\left(n_{sh}-1\right)}{n_s s_p+\beta_1 s_s}$
	connections to edge members	$c_{2.3}=\dfrac{2s_{sc}}{n_{sc}}$
Total flexibility in true shear		$c'=\dfrac{b^2}{a^2}\left(c_{1.1}+c_{1.2}+c_{2.1}+c_{2.2}+c_{2.3}\right)$

2.2. Proposed method

By augmenting the finite element structural model with the stressed skin design principles, the designer can take into account the stiffening effect of the shear panels for arbitrary shaped roof structures. The finite element method can be undoubtedly used to model the actual shear panel and its connections to adjacent structures as Figure 4 depicts. The modelling and accuracy issues of such an approach are discussed in [16]. However, such an accurate modelling is not efficient due to extremely high number of degrees of freedom. Another, rather opposite, approach for taking into account the stressed skin effects is to model the structure using simple models as in [7], in which the Timoshenko beam theory is adopted for modelling the building roof with sheeting. Between these accurate but impractical and computationally inexpensive but inaccurate methods an intermediate numerical method is proposed. The proposed method is based on an assumption that the shear panel flexibility can be expressed as a sum of the sheet flexibility and the flexibility of the associated connections (sheet/rafter, sheet/edge beam, sheet/sheet). The connection flexibility includes the fastener flexibility as well as the flexibility of the surrounding sheet that can undergo buckling and yielding. The aforementioned flexibilities should be taken from test data. In this paper, such test data is not available and FE-modelling is used instead to get the required flexibilities for demonstrating purposes. The method can be implemented into the finite element method so that the sheet stiffness can be taken into account by using orthotropic material model with membrane element, and the connection stiffness's can be modelled as spring elements as depicted in Figure 3. With the proposed method, the stressed skin effect can be effectively implemented to existing structural model.

As mentioned earlier, the loading tests would be optimal way to obtain the flexibility data required by the method. Such data being unavailable, a global model with periodic boundary conditions depicted in Figure 5 is used to define the stiffness of the panel itself including the sheet-to-sheet seam fastener stiffnesses. In the model, periodic boundary conditions for both in-plane directions ensure that no boundary effects are mixed into the sheet stiffness. The FE-model depicted in Figure 5 is subjected to in-plane tensile unit load cases and to an in-plane shear unit load case as illustrated in Figure 6. Based on the deflections due to unit loads, the stiffness of the sheet including the stiffness of the sheet-to-sheet seams is obtained.

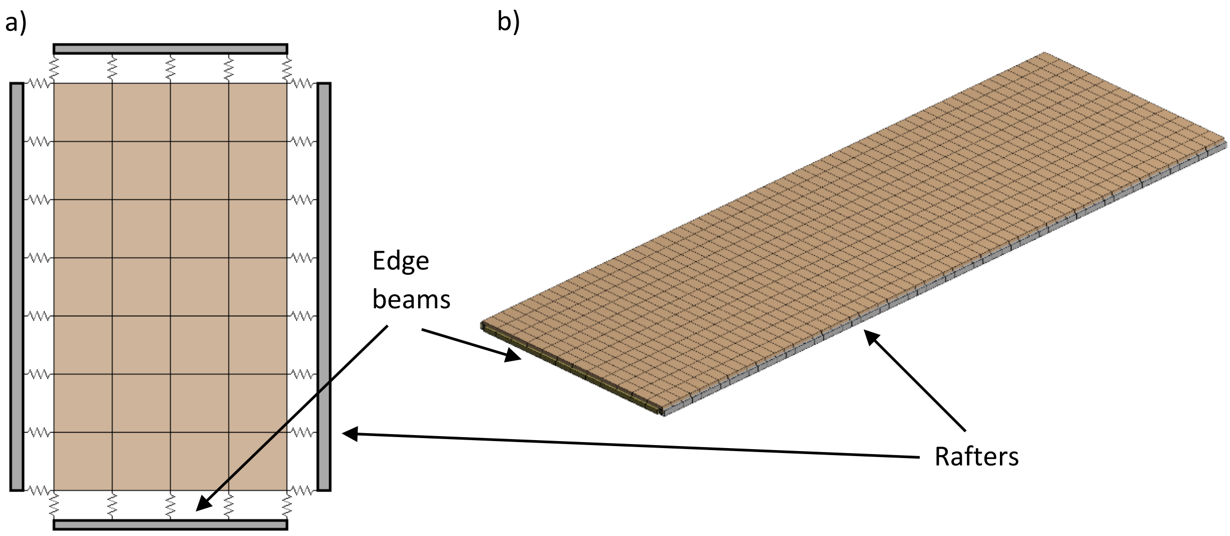

Figure 3. a) Schematic picture on the plate and adjacent rafters and end beams connected with fasteners and b) a simplified flat plate FE-model (counterpart of the accurate model depicted in Figure 4). Typical model 20m* 6m contains ca. 8000 degrees of freedom.

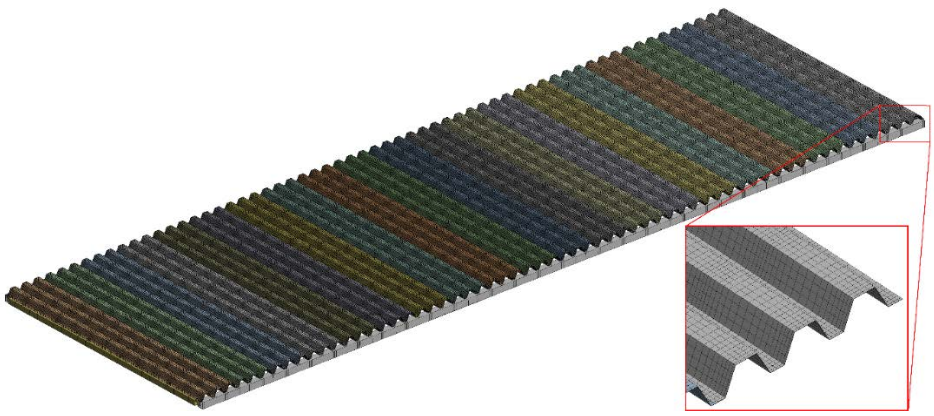

Figure 4. A FE-model of a corrugated sheet panel with accurate geometry modelling.
Typical model 20m* 6m contains ca. 4 million degrees of freedom.
Each sheet is highlighted by different colors.

Similarly, local FE-models are used to define the in-plane stiffness of the panel connection to the adjacent structures such as rafters, edge beams and end gables. An example of such a FE-model is shown in Figure 7 in which the connection between the sheet and rafter is modelled. In the FE-model, quadratic solid elements (SOLID186 in ANSYS) are used for the sheet and the rafter with two elements in through-the-thickness direction. Linear isotropic material model (E = 200 GPa, ν = 0.3) is used for the steel. The fastener connecting the sheet and the rafter is modelled also with the same quadratic solid elements with dense mesh. Exact geometry of the sheet profile is given in [21]. It should be noted, that the stiffness of the connection is dependent on the fastener stiffness itself but also on the sheet behavior in the vicinity of the connection. Again, such information could be also derived from tests and provided by the manufacturer. However, as discussed in [17], the fastener stiffness is of primary importance when the diaphragm action is taken into account and even multiple testing of the fastener provides no unique results. Thus, the adopting of the finite element method to the fastening modelling is also well-reasoned.

After the structural stiffnesses are defined for the panel and the connections, the corrugated sheet can be modelled as a simplified membrane with transversely isotropic material properties [18] according to

$$\begin{bmatrix} \sigma_{xx} \\ \sigma_{yy} \\ \sigma_{xy} \end{bmatrix} = \frac{1}{1-\nu_{xy}\nu_{yx}} \begin{bmatrix} E_x & \nu_{yx}E_x & 0 \\ \nu_{xy}E_y & E_y & 0 \\ 0 & 0 & G_{xy}(1-\nu_{xy}\nu_{yx}) \end{bmatrix} \begin{bmatrix} \varepsilon_{xx} \\ \varepsilon_{yy} \\ 2\varepsilon_{xy} \end{bmatrix}. \tag{1}$$

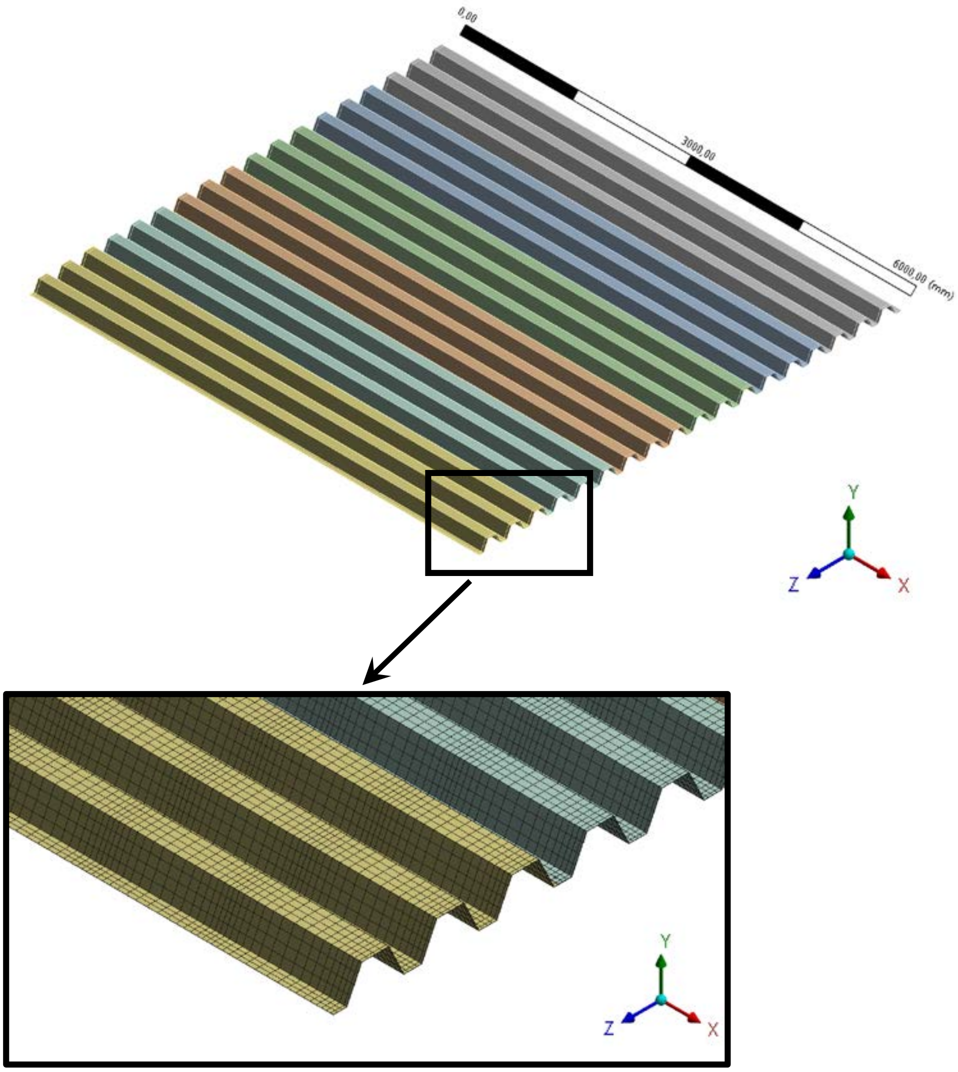

Figure 5. Stiffnesses of the corrugated panel including the sheet-to-sheet seams are obtained from a 6m*6m accurate FE-model with periodic boundary conditions. Sheets connections are included into the model.

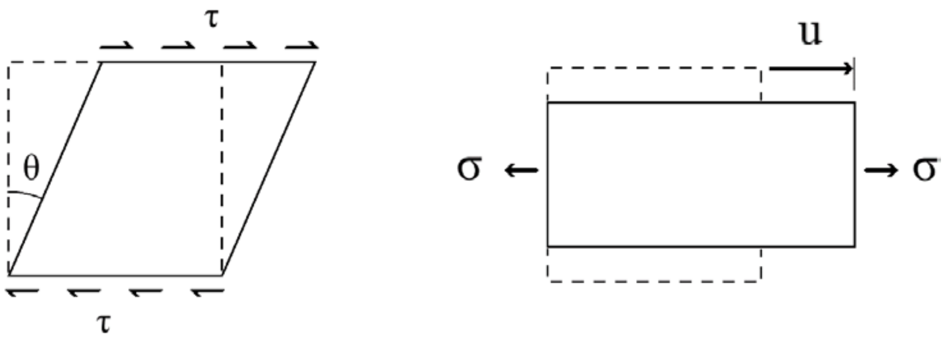

Figure 6. Unit load cases for determination of material properties: Young's moduli E_x, E_y, shear modulus G_{xy}, and Poisson's ratio E_{xy} and E_{yx}.

The membrane is connected to the surrounding skeleton model with joint elements as depicted in the Figure 3, in which four-node linear shell elements (SHELL181 in ANSYS) are used and the grid density in defined according to the fastener intervals. The FE analysis of the flat plate with distinct fasteners itself is trivial and similar simulations are carried out also for wood diaphragms and for hybrid structures in [19] and [20], respectively.

After the steps defined above, the simplified geometry model can be used in any finite element software to model the roof used as stressed skin. The size and shape of the structural entity can be arbitrary. The FE-model of the actual structure gives then results for panel shear forces as well as distinct fastener loads. It should be also noted, that all the previous steps for defining the stiffness's of various parts of the panel structure can be automated. Table 2 highlights the steps of the method.

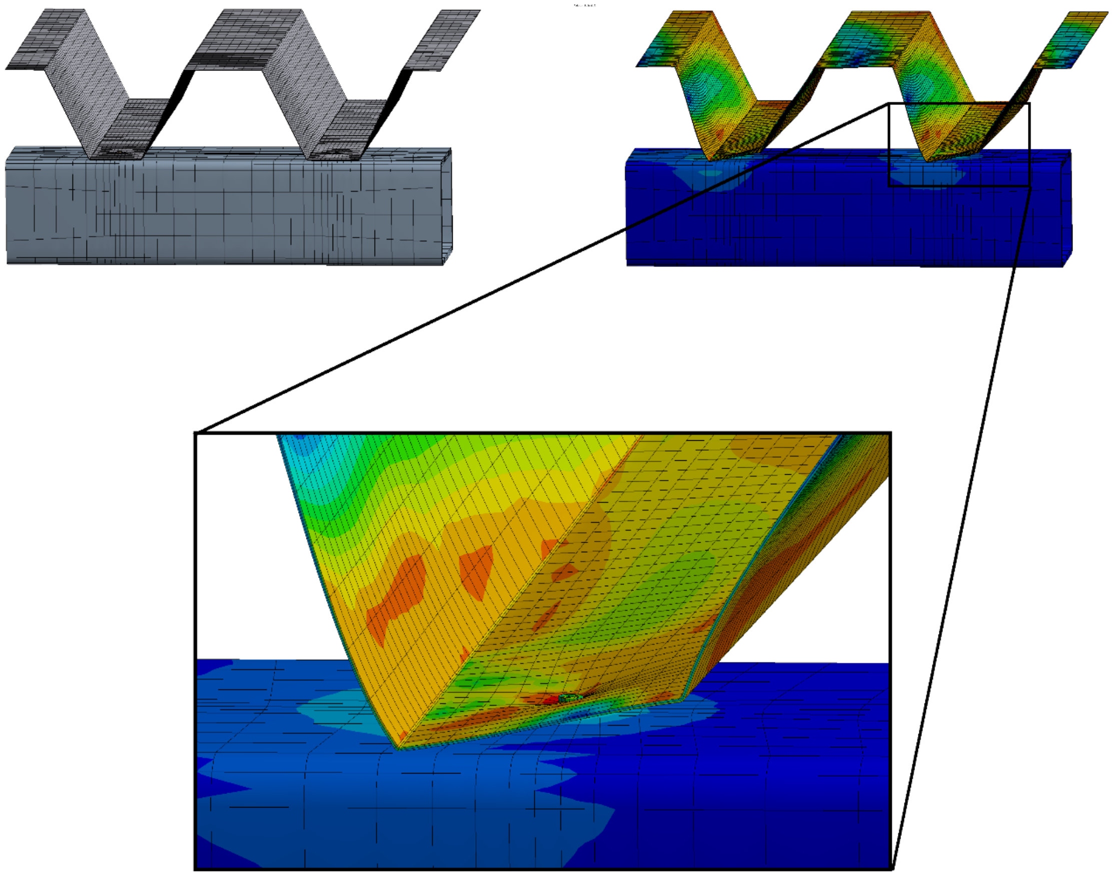

Figure 7. A local finite element model of the sheet-to-rafter connection. Fastening stiffness is influenced by the fastener itself and also by the local deformations of the sheet in the connection neighborhood.

Table 2. Main steps of the proposed method.

Step	Task	Note
#1	Define the sheet structure in-plane tensile and shear stiffnesses. This can be done either by tests or by FE simulations.	Sheet-to-sheet connections can be included in the material model of the sheet or modelled separately as in step #3.
#2	By using FEM, model the shear panel as a flat plate with transversely isotropic material properties defined in step #1	
#3	Define the stiffness for the connections between the sheet and adjacent structures	The stiffness is needed for each sheet/connector pairs
#4	Connect the flat plate into the structural model by using springs with the stiffness defined in step #3	

3. Results and Discussion

The major advantage of the proposed method is that arbitrary sheet panels can be easily attached to an existing skeleton model so that the stressed-skin effect is taken into account for the whole building. As a complementary benefit, the fastener forces are modelled accurately making the joint design more efficient and accurate. The challenges of the method are that the stiffness of each fastener-sheet pair must be defined either by a local FE-model as in this paper or by tests. However, the variety of the mostly used fasteners and sheets is limited making this challenge moderate. When the FE-modelling is used for corrugated sheet structures, numerical problems might appear due to significant difference in normal stiffness's in perpendicular directions. These numerical problems can be however circumvented by using adequate meshing.

In order to highlight the fastener force results, the proposed method is applied to a sheet structure depicted in Figure 8. The same configuration is also analyzed using the ECCS design rules [7] and using the FE-model with accurate geometry model to show the differences in the results. The considered shear panel has the material thickness of 1.0 mm and the total height of 130 mm. The detailed information of the panel can be found from [21]. Sheets are fastened at seams with 4.2 mm diameter screws at intervals of 500 mm. The sheet is attached to rafters (RHS 150×150×8) with 6.3 mm screws from each fold and to edge beams (RHS 120×120×4) with 6.3 mm at intervals of 500 mm.

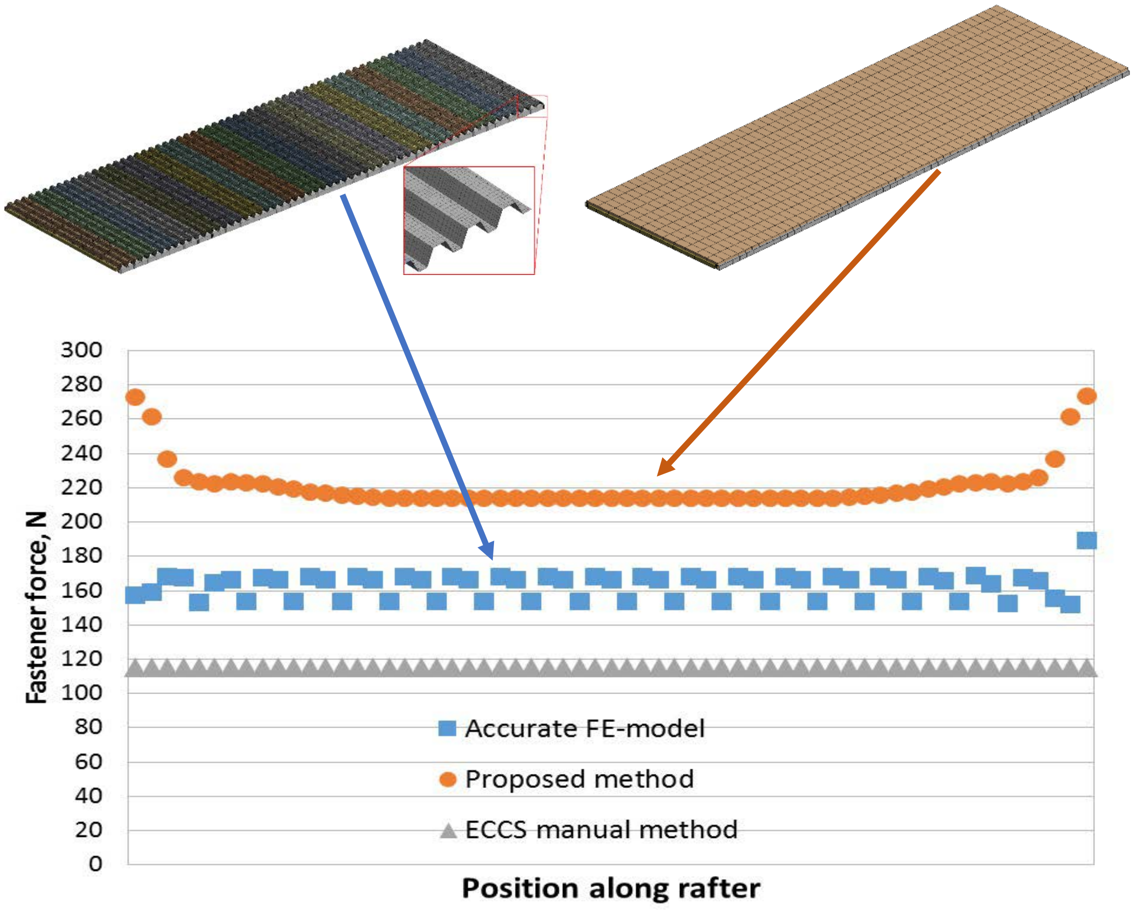

Figure 8. Fastener force distribution at the rafters according to the FE-models and ECCS design rules [7].

The results in the Figure 9 clearly show how the manual calculation according to [7] underestimates the fastener forces as expected due to the conservative nature of the manual design approach. Similarly, the fastener forces according to the proposed method are overestimated as expected. This is due to the general feature of the finite element method, that the structure becomes stiffer when less degrees of freedom are used in the model. However, the small margin between the accurate and simplified model results could be reduced by introducing a certain reduction parameter.

4. Conclusions

In the paper, a new method for the general use of the stressed skin action in the context of finite element modelling is presented. The method uses sheet stiffness's in the in-plane direction and sheet connection stiffness's as input. After defining these values, a simplified flat plate finite element model with transversely isotropic material properties can be used to model accurately any corrugated sheet panel. In this study, ANSYS was used, but any FE-package supporting orthotropic material model could be used, e.g. Autodesk Robot or RFEM. The method presents a potential remarkable competitive advantage to a material producer in a way that the producer can provide the sheet and fastener stiffness values to a FE software developer, after which a FE application could be defined for that product to be used in steel design taking the full advantage on the stressed skin action. The method lies between an accurate FE-modelling and simple hand calculations, as discussed in the Chapter 2. The work required by the method can be done before the actual design process, thus providing an efficient automated design tool.

When applied to corrugated sheet panels, the in-plane tensile structural stiffness's, with different order of magnitude, can produce potential numerical errors in the finite element method when defining the transversely isotropic material properties as discussed in Chapter 3. In the current research, only the in-plane loading is taken into account but in general, also the out-of-plane loading cases can be included into the analysis even if it is not the primary intention of the proposed method. The method is most beneficial when used instead of the conventional Timoshenko beam theory for the structural analysis and used together with the design principles in [7]. The proposed method gives also more accurate results when compared to the method in which the shear panel is modelled as diagonal bar, see e.g. [15]. In a further research, the exact material cost savings of the proposed method compared to the manual design method [7] will be studied. Such research results are needed when evaluating the economical beneficial of the method.

References

1. Bryan, E.R. The stressed skin design of steel buildings. Lockwood, 1973.
2. Davies, J.M. Developments in stressed skin design. Thin-Walled Structures. 2006. No. 44. Pp. 1250–1260.
3. Johnson, C.B. Light gage steel diaphragms in building construction, American Society of Civil Engineers meeting, Los Angeles, California, 1950.
4. Phan, D.T., Lim, J.B., Tanyimboh, T.T., Wrzesien, A.M., Sha, W., Lawson, R.M. Optimal design of cold-formed steel portal frames for stressed-skin action using genetic algorithm. Engineering Structures. 2015. No. 93. Pp. 36–49.
5. Nagy, Z., Pop, A., Moiș, I., Ballok, R. Stressed skin effect on the elastic buckling of pitched roof portal frames. Structures. 2016. Vol. 8. Pp. 227–244. Elsevier.
6. Wrzesien, A.M., Lim, J.B., Xu, Y., MacLeod, I.A., Lawson, R.M. Effect of stressed skin action on the behaviour of cold-formed steel portal frames. Engineering Structures. 2015. No. 105. Pp. 123–136.
7. European Recommendations for the application of metal sheeting acting as a diaphragm. European Convention for Constructional Steelwork. 1995. No. 88.
8. Davies, J.M., Bryan, E.R. Manual of stressed skin diaphragm design, Granada, 1982.
9. Schardt, R., Strehl, C. Theoretische Grundlagen für die Bestimmung der Schubsteifigkeit von Trapezblechscheiben–Vergleich mit anderen Berechnungsansätzen und Versuchsergebnissen. Stahlbau. 1976. No. 45(4). Pp. 97-108. (In German)
10. Misiek, T., Huck, G., Käpplein, S. The «combined approach» for the design of shear diaphragms made of trapezoidal profile sheeting. Steel Construction. 2018. No. 11(1). Pp. 16–23.
11. Lendvai, A., Joó, A.L. Development in calculation of stressed skin effect upon experimental and numerical research results. ce/papers. 2017. No. 1(2-3). Pp. 1812–1821.
12. Lendvai, A., Joó, A.L., Dunai, L. Experimental full-scale tests on steel portal frames for development of diaphragm action–Part I experimental results. Thin-Walled Structures, 2018.
13. Lendvai, A., Joó, A.L. Experimental full-scale tests on steel portal frames for development of diaphragm action–Part II Effect of structural components on shear flexibility. Thin-Walled Structures, 2018.
14. Höglund, T. Stabilisation by stressed skin diaphragm action. Stålbyggnadsinstitutet, 2002.
15. Dubina, D., Ungureanu, V., Landolfo, R. Design of cold-formed steel structures. ECCS and Ernst & Sohn, 2012.
16. Wright, H.D., Hossain, K.A. In-plane shear behaviour of profiled steel sheeting. Thin-walled structures. 1997. No. 29(1-4). P. 79–100.
17. Fan, L., Rondal, J., Cescotto, S. Finite element modelling of single lap screw connections in steel sheeting under static shear. Thin-Walled Structures. 1997. No. 27(2). Pp. 165–185.
18. Ding, H., Chen, W., Zhang, L. Elasticity of transversely isotropic materials. Springer Science & Business Media. 2006. Vol. 126.
19. Falk, R.H., Itani, R.Y. Finite element modeling of wood diaphragms. Journal of Structural Engineering. 1989. No. 115(3). Pp. 543–559.
20. Li, Z., He, M., Lam F., Li M., Ma R., Ma Z. Finite element modeling and parametric analysis of timber-steel hybrid structures. The Structural Design of Tall and Special Buildings. 2014. No. 23(14). Pp. 1045–1063.
21. Load-bearing sheet T130M-75L-930, accessed 25.2.2019 [Электронный ресурс]. URL: https://www.ruukki.com/b2b/products/load-bearing-profiles/load-bearing-sheets/load-bearing-sheets-details/load-bearing-sheet-t130m-75l-930

Contacts:

Sami Pajunen, +358408490571; sami.pajunen@tuni.fi
Janne Hautala, +358505710156; janne.hautala@tuni.fi
Markku Heinisuo, +358405965826; markku.heinisuo@tut.fi

Инженерно-строительный журнал

ISSN 2071-0305

сайт журнала: http://engstroy.spbstu.ru/

DOI: 10.18720/MCE.86.3

Моделирование несущих ограждающих конструкций плоскими конечными элементами со свойствами метаматериала

С. Пайюнен[a*], Дж. Хаутала[a], М. Хейнисуо[b]

[a] Технологический университет Тампере, г. Тампере, Финляндия

[b] Sorvimo Optimointipalvelut Oy, г. Тампере, Финляндия

** E-mail: sami.pajunen@tuni.fi*

Ключевые слова: несущая оболочка; диафрагма; профилированный лист.

Аннотация. Как известно, учет несущей способности ограждающих конструкций позволяет на 10–20 % уменьшить металлоемкость и стоимость строительства стальных пролетных сооружений. Тем не менее, преимущества данного подхода часто недооцениваются по причине сложности и ограниченности расчётных норм и рекомендаций. Данная статья предлагает метод определения общих упругих свойств материала, благодаря чему несущая ограждающая конструкция может быть смоделирована в обычном вычислительном комплексе с использованием имеющихся типов конечных элементов и свойств материалов. Данный метод дает возможность инженерам выполнять расчет несущей способности ограждающих конструкций с применением простых вычислительных комплексов, таких как Autodesk Robot или RFEM.

Список литературы

1. Bryan E.R. The stressed skin design of steel buildings. Lockwood, 1973.
2. Davies J.M. Developments in stressed skin design // Thin-Walled Structures. 2006. No. 44. Pp. 1250–1260.
3. Johnson C.B. Light gage steel diaphragms in building construction, American Society of Civil Engineers meeting, Los Angeles, California, 1950.
4. Phan D.T., Lim J.B., Tanyimboh T.T., Wrzesien A.M., Sha W., Lawson R.M. Optimal design of cold-formed steel portal frames for stressed-skin action using genetic algorithm // Engineering Structures. 2015. No. 93. Pp. 36–49.
5. Nagy Z., Pop A., Moiș I., Ballok R. Stressed skin effect on the elastic buckling of pitched roof portal frames // Structures. 2016. Vol. 8. Pp. 227–244. Elsevier.
6. Wrzesien A.M., Lim J.B., Xu Y., MacLeod I.A., Lawson R.M. Effect of stressed skin action on the behaviour of cold-formed steel portal frames // Engineering Structures. 2015. No. 105. Pp. 123–136.
7. European Recommendations for the application of metal sheeting acting as a diaphragm // European Convention for Constructional Steelwork. 1995. No. 88.
8. Davies J.M., Bryan E.R. Manual of stressed skin diaphragm design, Granada, 1982.
9. Schardt R., Strehl C. Theoretische Grundlagen für die Bestimmung der Schubsteifigkeit von Trapezblechscheiben–Vergleich mit anderen Berechnungsansätzen und Versuchsergebnissen // Stahlbau. 1976. No. 45(4). Pp. 97-108. (In German)
10. Misiek T., Huck G., Käpplein, S. The «combined approach» for the design of shear diaphragms made of trapezoidal profile sheeting // Steel Construction. 2018. No. 11(1). Pp. 16–23.
11. Lendvai A., Joó A.L. Development in calculation of stressed skin effect upon experimental and numerical research results // ce/papers. 2017. No. 1(2-3). Pp. 1812–1821.
12. Lendvai A., Joó A.L., Dunai L. Experimental full-scale tests on steel portal frames for development of diaphragm action–Part I experimental results. Thin-Walled Structures, 2018.
13. Lendvai A., Joó A.L. Experimental full-scale tests on steel portal frames for development of diaphragm action–Part II Effect of structural components on shear flexibility. Thin-Walled Structures, 2018.
14. Höglund T. Stabilisation by stressed skin diaphragm action. Stålbyggnadsinstitutet, 2002.
15. Dubina D., Ungureanu V., Landolfo R. Design of cold-formed steel structures. ECCS and Ernst & Sohn, 2012.
16. Wright H.D., Hossain K.A. In-plane shear behaviour of profiled steel sheeting // Thin-walled structures. 1997. No. 29(1-4). P. 79–100.
17. Fan L., Rondal J., Cescotto S. Finite element modelling of single lap screw connections in steel sheeting under static shear // Thin-Walled Structures. 1997. No. 27(2). Pp. 165–185.
18. Ding H., Chen W., Zhang L. Elasticity of transversely isotropic materials // Springer Science & Business Media. 2006. Vol. 126.

19. Falk R.H., Itani R.Y. Finite element modeling of wood diaphragms // Journal of Structural Engineering. 1989. No. 115(3). Pp. 543–559.
20. Li Z., He M., Lam F., Li M., Ma R., Ma Z. Finite element modeling and parametric analysis of timber-steel hybrid structures // The Structural Design of Tall and Special Buildings. 2014. No. 23(14). Pp. 1045–1063.
21. Load-bearing sheet T130M-75L-930, accessed 25.2.2019 [Электронный ресурс]. URL: https://www.ruukki.com/b2b/products/load-bearing-profiles/load-bearing-sheets/load-bearing-sheets-details/load-bearing-sheet-t130m-75l-930

Контактные данные:

Сами Пайюнен, +358408490571; эл. почта: sami.pajunen@tuni.fi
Джанне Хаутала, +358505710156; эл. почта: janne.hautala@tuni.fi
Маркку Хейнисуо, +358405965826; эл. почта: markku.heinisuo@tut.fi

Magazine of Civil Engineering. 2019. 86(2). Pp. 30–45
Инженерно-строительный журнал. 2019. № 2(86). С. 30–45

Magazine of Civil Engineering

ISSN 2071-0305

journal homepage: http://engstroy.spbstu.ru/

DOI: 10.18720/MCE.86.4

Nonlinear vibrations of fluid transporting pipelines on a viscoelastic foundation

B.A. Khudayarov*, F.Z. Turaev,
Tashkent institute of irrigation and agricultural mechanization engineers, Tashkent, Uzbekistan
** E-mail: bakht-flpo@yandex.ru*

Keywords: vibration process; foundation; pipeline; mathematical model; numerical algorithm; cylindrical shell

Abstract. The article presents the results of a study of vibration process in pipelines conveying fluid or gas. A mathematical model pipeline was used in the form of cylindrical shell and a viscoelastic foundation in the form of two-parameter model of the Pasternak. The hereditary Boltzmann-Volterra theory of viscoelasticity is used to describe viscoelastic properties. The effects of the parameters of the Pasternak foundations, the singularity in the heredity kernels and geometric parameters of the pipeline on vibrations of structures with viscoelastic properties are numerically investigated. It is found that an account of viscoelastic properties of the pipeline material leads to a decrease in the amplitude and frequency of vibrations by 20–40 %. It is shown that an account of viscoelastic properties of soil foundations leads to a damping of vibration process in pipeline.

1. Introduction

Pipeline systems provide a safe and uninterrupted operation of the objects in fuel and energy industry. The pipelines provide population with basic resources: fresh water, natural gas, oil, etc. Wide networks of pipelines, both domestically and abroad, support the vital functions of states, and are one of the main factors of economic development. The failure of even small sections of pipelines, often accompanied by explosions and fires, can cause serious consequences associated with the loss of the product, the high cost of repairs, and can lead to a significant pollution of the environment.

Currently, the objects of agriculture, oil and gas industry, housing and communal services and others face the problems of repair and restoration of metal pipelines due to the impact of various external factors. One of the ways to solve this problem is to use composite polymer material that has a number of advantages. Due to their characteristics, pipes made of composite materials have found wide application in such areas as housing and communal services, agriculture, oil production and energy industry. They are used in cold and hot water supply systems for pressure and pressure-free systems of domestic and industrial sewerage, in pipeline systems construction in irrigation and melioration, in engineering systems for hydroelectric power plants, etc.

Trunk pipelines for transportation of gas and oil products represent complex engineering structures. When designing underground and underwater pipelines the engineers should correctly evaluate the properties of pipe material and soil foundation.

At present, the problem of vibration processes of pipelines resting on elastic and viscoelastic foundation with a fluid flowing through it is of great theoretical and practical interest. To date, many approaches have been developed to solve these problems, but none of them is able to adequately reflect the real picture of a pipeline – underlying soil interaction. Basically, these approaches describe the individual stages of the processes occurring in the pipelines. There are a significant number of publications devoted to solving the

Khudayarov, B.A., Turaev, F.Z. Nonlinear vibrations of fluid transporting pipelines on a viscoelastic foundation. Magazine of Civil Engineering. 2019. 86(2). Pp. 30–45. DOI: 10.18720/MCE.86.4.

Худаяров Б.А., Тураев Ф.Ж. Нелинейные колебания трубопроводов на вязкоупругом основании, транспортирующего жидкость // Инженерно-строительный журнал. 2019. № 2(86). С. 30–45. DOI: 10.18720/MCE.86.4

problems of calculating the characteristics of elastic and viscoelastic thin-walled structures [1–19]. Results of the theory are compared in some cases with experimental data [6].

Pengyu Jia et al. [8] have studied the effects of crack geometries, pipe geometry, and material properties on the reference strain. An effective empirical formula is proposed to estimate the reference strain. Taolong Xu et al. [9] have conducted combined computational and analytical study to investigate the lateral impact behavior of pressurized pipelines. David Carrier III et al. [10] have analyzed the vibration of a pipeline using the nouniform Winkler soil model with randomized spring constants. W.Q. Chen et al. [11] have studied vibrations of thick beams resting on a Pasternak elastic base. The effects of Poisson's ratio and Pasternak foundation parameters on natural frequencies are analyzed. Deep beam-columns on two-parameter elastic foundation with account of the effect of shear strain, depth change and rotation inertia are analyzed in [12]. Results obtained on the basis of approximate theory are compared with the results obtained by the Timoshenko theory and the classical beam theory. Nonlinear responses of planar motions of fluid-conveying pipe are investigated with allowance for nonlinear elastic foundations [13]. Kameswara Rao Chellapilla [14] has derived an analytical expression for computation of critical velocity of a fluid flowing through a pipeline. The Pasternak two-parameter foundation is used to take into account the effect of foundation properties. The conclusions on the influence of foundation on the critical velocity of a fluid are presented. Haryadi Gunawan Tj et al. [15] have studied vibrations of cylindrical shells partially buried in elastic foundations. The effects of rigidity ratio of foundation and shell are analyzed as well as vibrations of shells on elastic foundations. I. Lottati and A. Kornecki [16] have studied the effect of an elastic foundation and dissipative forces on the stability of fluid-conveying pipes. Results of numerical calculations are compared to the results in previously published papers. The problem of stability of fluid-conveying carbon nanotubes embedded in an elastic medium is considered in [17]. For the critical flow velocity, taking into account the rigidity parameters of the Winkler and Pasternak foundation, analytical expressions are obtained. In [18] a synchronization phenomenon of two equivalent fluid-conveying pipes coupled by a nonlinear spring is studied. On the basis of the Bubnov-Galerkin method the discrete systems of equations are obtained.

At present, there are a number of approaches for improving mechanical model of soil foundation, but, apparently, the simplest mathematical statement of the problem (except for the Winkler model) is the development of the model of two-parametric viscoelastic Pasternak foundation. The model of two-parameter Pasternak foundation, on the one hand, makes it possible to take into account the distribution capacity of soil, and on the other hand it does not complicate the mathematical statement of the problem in comparison with the Winkler model.

From the above review, it can be concluded that the development of adequate models describing viscoelastic properties of structure material and accounting the work of the viscoelastic soil foundation is a rather complex and relevant research task that is directly solved in this paper, along with the construction of appropriate mathematical models.

The aim of this study is to create a mathematical model, a numerical algorithm and a computer program for solving the problem of nonlinear oscillations of viscoelastic thin-walled pipelines of large diameter on the basis of shell theory into account the two-parameter viscoelastic Pasternak foundation.

2. Methods

2.1. Governing equation

Consider the behavior of a thin circular viscoelastic cylindrical shell, with an ideal fluid flowing inside it at a constant velocity. The fluid velocity is U and its direction coincides with the direction of the Ox axis (Figure 1). The impact of external medium is described by the Pasternak model of two-parametric foundation (Figure 2). The Kirchhoff-Love conventional hypotheses are used under the assumption that the deflections are small in comparison with thickness.

Under the assumption in [20] and assuming that, $y = R\theta$, Marguerre equations with respect to displacements u, v, w can be written in the following form:

$$
\begin{gathered}
(1-R^*)\left\{\frac{\partial^2 u}{\partial x^2}+\frac{1-\mu}{2R^2}\frac{\partial^2 u}{\partial\theta^2}+\frac{1+\mu}{2R}\frac{\partial^2 v}{\partial x\partial\theta}+L_1(w)\right\}-\rho\frac{1-\mu^2}{E}\frac{\partial^2 u}{\partial t^2}=0,\\
\left(1-R^*\right)\left\{\frac{1}{R^2}\frac{\partial^2 v}{\partial\theta^2}+\frac{1-\mu}{2}\frac{\partial^2 v}{\partial x^2}+\frac{1+\mu}{2R}\frac{\partial^2 u}{\partial x\partial\theta}+L_2\left(w\right)\right\}-\rho\frac{1-\mu^2}{E}\frac{\partial^2 v}{\partial t^2}=0,\\
D(1-R^*)\nabla^4 w+L_3^*(u,v,w)+(1-R_1^*)\left\{k_1 w-k_2\frac{\partial^2 w}{\partial x^2}\right\}+\rho h\frac{\partial^2 w}{\partial t^2}=q,
\end{gathered}
\tag{1}
$$

where D is the cylindrical rigidity of the pipe,

μ is the Poisson's ratio of the pipe material,

E is the modulus of elasticity of the pipe material,

ρ is its density;

k_1, k_2 are the coefficients of the Pasternak's foundation, characterizing the properties of external environment; R is the radius of curvature of the middle surface;

h is the thickness of the pipe wall;

R^* and R_1^* are the integral operators with the Koltunov-Rzhanitsyn relaxation kernels, $R(t)$ and $R_1(t)$, respectively:

$$R(t) = A\cdot \exp(-\beta\cdot t)\cdot t^{\alpha-1};\quad R_1(t) = A_1\cdot \exp(-\beta_1\cdot t)\cdot t^{\alpha_1-1};$$

$A>0,\quad \beta>0,\quad 0<\alpha<1,\ \ A_1>0,\quad \beta_1>0,\quad 0<\alpha_1<1,\ \ A,\ A_1$ – the viscosity parameters;

β, β_1 are the attenuation parameters;

α, α_1 are the singularity parameter determined by experiment

$$R^*\varphi(t) = \int_0^t R(t-\tau)\varphi(\tau)d\tau;\quad R_1^*\varphi(t) = \int_0^t R_1(t-\tau)\varphi(\tau)d\tau,$$

where $R(t-\tau)$, $R_1(t-\tau)$ are relaxation kernel;

t is the time of observation;

τ is the time before observation;

$\varphi(\tau)$ is the functions to be determined; the operators $L_1(w),\ L_2(w),\ L_3^*(u,v,w)$ are:

$$L_1(w) = -\frac{\mu}{R}\frac{\partial w}{\partial x} + \frac{\partial w}{\partial x}\frac{\partial^2 w}{\partial x^2} + \frac{1+\mu}{2R^2}\frac{\partial w}{\partial\theta}\frac{\partial^2 w}{\partial x\partial\theta} + \frac{1-\mu}{2R^2}\frac{\partial w}{\partial x}\frac{\partial^2 w}{\partial\theta^2},$$

$$L_2(w) = -\frac{1}{R^2}\frac{\partial w}{\partial x} + \frac{\partial w}{\partial\theta}\frac{\partial^2 w}{\partial\theta^2} + \frac{1+\mu}{2R}\frac{\partial w}{\partial x}\frac{\partial^2 w}{\partial x\partial\theta} + \frac{1-\mu}{2R}\frac{\partial w}{\partial\theta}\frac{\partial^2 w}{\partial x^2},$$

$$\begin{aligned} L_3^*(u,v,w) = {}& (1-R^*)\frac{Eh}{1-\mu^2}\left\{-\frac{\mu}{R}\frac{\partial u}{\partial x} - \frac{1}{R^2}\frac{\partial v}{\partial\theta} + \frac{w}{R^2} - \frac{\mu}{2R}\left(\frac{\partial w}{\partial x}\right)^2 - \frac{1}{R^3}\left(\frac{\partial w}{\partial\theta}\right)^2\right\} - \\ & -\frac{Eh}{1-\mu^2}\frac{\partial}{\partial x}\left\{\frac{\partial w}{\partial x}(1-R^*)\left[\frac{\partial u}{\partial x} + \frac{\mu}{R}\frac{\partial v}{\partial\theta} - \frac{\mu w}{R}\right] + \frac{1-\mu}{2R}\frac{\partial w}{\partial\theta}(1-R^*)\left(\frac{1}{R}\frac{\partial u}{\partial\theta} + \frac{\partial v}{\partial x}\right)\right\} - \\ & -\frac{Eh}{1-\mu^2}\frac{1}{R}\frac{\partial}{\partial\theta}\left\{\frac{1}{R}\frac{\partial w}{\partial\theta}(1-R^*)\left[\mu\frac{\partial u}{\partial x} + \frac{1}{R}\frac{\partial v}{\partial\theta} - \frac{w}{R}\right] + \frac{(1-\mu)}{2}\frac{\partial w}{\partial x}(1-R^*)\left(\frac{1}{R}\frac{\partial u}{\partial\theta} + \frac{\partial v}{\partial x}\right)\right\}, \end{aligned} \tag{2}$$

q is a pressure of fluid on the pipeline wall [21]:

$$q = -\varphi_{\alpha m}^*\rho\left(\frac{\partial^2 w}{\partial t^2} + U^2\frac{\partial^2 w}{\partial x^2}\right). \tag{3}$$

where $-\varphi_{\alpha m}^*$ is an associated mass of fluid;

m is the number of waves formed along the circumference,

α is the wave number or the constant of phase propagation.

The boundary conditions have the form

$$x=0,\quad x=L:\quad w=0;\quad v=0;\quad N_x=0;\quad M_x=0. \tag{4}$$

Under bending in the middle surface, there arise normal and tangential forces:

$$N_x = \int_{-h/2}^{h/2} \sigma_x dz \quad (x \Leftrightarrow y), \quad N_{xy} = \int_{-h/2}^{h/2} \sigma_{xy} dz. \tag{5}$$

Physical dependence between stresses $\sigma_x, \sigma_y, \tau_{xy}$ and strains $\varepsilon_x, \varepsilon_y, \gamma_{xy}$ is taken in the form [20]:

$$\sigma_x = \frac{E}{1-\mu^2}\left(1-R^*\right)\left(\varepsilon_x + \mu\varepsilon_y\right), \ \sigma_y = \frac{E}{1-\mu^2}\left(1-R^*\right)\left(\varepsilon_y + \mu\varepsilon_y\right), \ \sigma_{xy} = \frac{E}{2\left(1+\mu\right)}\left(1-R^*\right)\varepsilon_{xy}. \tag{6}$$

Here ε_x, ε_y, ε_{xy} are the components of finite strain determined by:

$$\varepsilon_x = \frac{\partial u}{\partial x} - k_x w + \frac{1}{2}\left(\frac{\partial w}{\partial x}\right)^2, \quad \varepsilon_y = \frac{\partial v}{\partial y} - k_y w + \frac{1}{2}\left(\frac{\partial w}{\partial y}\right)^2, \quad \varepsilon_{xy} = \frac{\partial u}{\partial y} + \frac{\partial v}{\partial x} + \frac{\partial w}{\partial x}\frac{\partial w}{\partial y}, \tag{7}$$

where κ_x, κ_y are the curvature parameters.

Moments M_x, M_y and M_{xy} are determined through the deflection function w:

$$M_x = -D\left(1-R^*\right)\left(\frac{\partial^2 w}{\partial x^2} + \mu\frac{\partial^2 w}{\partial y^2}\right),$$

$$M_y = -D\left(1-R^*\right)\left(\frac{\partial^2 w}{\partial y^2} + \mu\frac{\partial^2 w}{\partial x^2}\right), \quad M_{xy} = D(1-\mu)\left(1-R^*\right)\frac{\partial^2 w}{\partial x \partial y}. \tag{8}$$

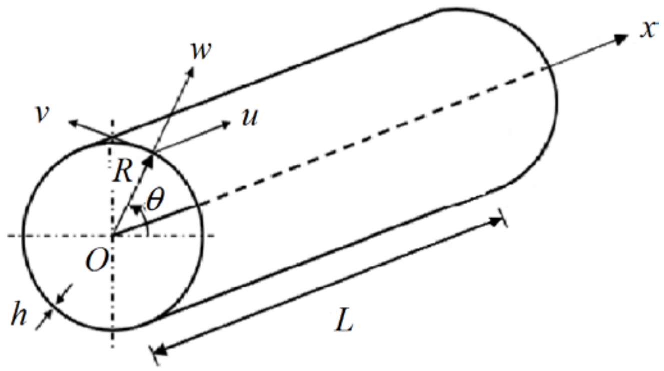

Figure 1. Geometry of the cylindrical shell.

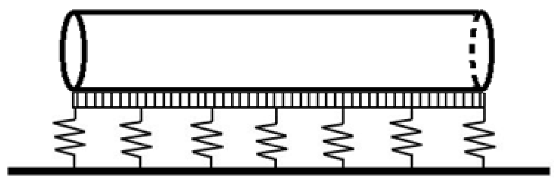

Figure 2. Pasternak's foundation.

2.2. Discret model

The solution of IDE systems in partial derivatives (1) under various boundary conditions and in the presence of singular heredity kernels represents a significant mathematical difficulty. Therefore, the natural way to solve these systems is to discretize them with respect to spatial variables and obtain a system of resolving nonlinear IDE with respect to time functions.

An approximate solution of system (1) is sought for in the form:

$$u\left(x,\theta,t\right) = \sum_{n=1}^{N}\sum_{m=1}^{M} u_{nm}\left(t\right) cos\frac{n\pi x}{L} sinm\theta,$$

$$v\left(x,\theta,t\right) = \sum_{n=1}^{N}\sum_{m=1}^{M} v_{nm}\left(t\right) sin\frac{n\pi x}{L} cosm\theta, \tag{9}$$

$$w\left(x,\theta,t\right) = \sum_{n=1}^{N}\sum_{m=1}^{M} w_{nm}\left(t\right) sin\frac{n\pi x}{L} sinm\theta,$$

where $u_{nm}\left(t\right), v_{nm}\left(t\right), w_{nm}\left(t\right)$ are the unknown time functions.

Substituting (9) in system **(**1**)** and applying the Bubnov-Galerkin method, the following system of integro-differential equations is obtained:

$$\ddot{u}_{kl}+\left(1-R^*\right)\left\{\left(k^2\pi^2\delta^2\gamma^2+\frac{1-\mu}{2}l^2\delta^2\right)u_{kl}-\frac{1-\mu}{2}kl\pi\gamma\delta^2 v_{kl}+\right.$$

$$+\mu\delta^2\gamma^2 k\pi w_{kl}+\sum_{n,i=1}^{N}\sum_{m,\ r=1}^{M}\left(\frac{ni^2\pi^2}{2}\gamma^3\delta+\frac{1-\mu}{2}\frac{nr^2}{2}\gamma\delta\right)\overline{\Delta}_{1klnmir}w_{nm}w_{ir}-$$

$$\left.-\frac{1+\mu}{2}\sum_{n,i=1}^{N}\sum_{m,r=1}^{M}\frac{imr}{2}\gamma\delta\overline{\Delta}_{2klnmir}w_{nm}w_{ir}\right\}=0\ ,$$

$$\ddot{v}_{kl}+\left(1-R^*\right)\left\{\left[\frac{1-\mu}{2}k^2\pi^2\delta^2\gamma^2+l^2\delta^2\right]v_{kl}-\frac{1+\mu}{2}kl\pi\gamma\delta^2 u_{kl}-l\delta^2 w_{kl}-\right.$$

$$-\sum_{n,i=1}^{N}\sum_{m,r=1}^{M}\frac{mr^2}{2\pi}\delta\overline{\Delta}_{3klnmir}w_{nm}w_{ir}+\frac{1+\mu}{2}\sum_{n,i=1}^{N}\sum_{m,r=1}^{M}\frac{inr\pi}{2}\gamma^2\delta\overline{\Delta}_{4klnmir}w_{nm}w_{ir}-$$

$$\left.-\frac{1-\mu}{2}\sum_{n,i=1}^{N}\sum_{m,r=1}^{M}\frac{i^2m\pi}{2}\gamma^2\delta\overline{\Delta}_{3klnmir}w_{nm}w_{ir}\right\}=0\ ,$$

$$\left(1+\varphi_{\alpha l}^*\right)\ddot{w}_{kl}+\left(1-R^*\right)\left\{\left(\frac{1}{12}\left[k^2\pi^2\gamma^2+l^2\right]^2+\delta^2\right)w_{kl}+\pi\mu\gamma\delta^2 ku_{kl}-l\delta^2 v_{kl}-\right.$$

$$\left.-\frac{\delta}{4\pi}\sum_{n,i=1}^{N}\sum_{m,r=1}^{M}mr\overline{\Delta}_{5klnmir}w_{nm}w_{ir}-\frac{\pi\mu\gamma^2\delta}{4}\sum_{n,i=1}^{N}\sum_{m,r=1}^{M}ni\overline{\Delta}_{6klnmir}w_{nm}w_{ir}\right\}+$$

$$+\frac{1-\mu}{4}\gamma\delta\sum_{n,i=1}^{N}\sum_{m,r=1}^{M}w_{nm}n\left(1-R^*\right)\left[\gamma\pi irv_{ir}-r^2u_{ir}\right]\overline{\Delta}_{6klnmir}+$$

$$+\frac{\delta}{2}\sum_{n,i=1}^{N}\sum_{m,r=1}^{M}mw_{nm}\left(1-R^*\right)\left[ir\mu\gamma u_{ir}-\frac{r^2}{\pi}v_{ir}+\frac{r}{\pi}w_{ir}\right]\overline{\Delta}_{5klnmir}+$$

$$+\frac{1-\mu}{4}\delta\sum_{n,i=1}^{N}\sum_{m,r=1}^{M}mw_{nm}\left(1-R^*\right)\left[ir\gamma u_{ir}-\gamma^2 i^2\pi v_{ir}\right]\overline{\Delta}_{5klnmir}-$$

$$-\frac{\delta}{2}\sum_{n,i=1}^{N}\sum_{m,r=1}^{M}nw_{nm}\left(1-R^*\right)\left[ir\mu\gamma^2\pi v_{ir}-i^2\gamma^3\pi^2u_{ir}-\mu\pi i\gamma^2 w_{ir}\right]\overline{\Delta}_{6klnmir}-$$

$$-\frac{1-\mu}{4}\delta\sum_{n,i=1}^{N}\sum_{m,r=1}^{M}nmw_{nm}\left(1-R^*\right)\left[r\gamma u_{ir}-i\gamma^2\pi v_{ir}\right]\overline{\Delta}_{7klnmir}-$$

$$-\sum_{n,i=1}^{N}\sum_{m,r=1}^{M}m^2w_{nm}\left(1-R^*\right)\left[i\mu\gamma u_{ir}-\frac{r}{\pi}v_{ir}+\frac{1}{\pi}w_{ir}\right]\frac{\delta}{2}\overline{\Delta}_{8klnmir}-$$

$$-\frac{1-\mu}{4}\delta\sum_{n,i=1}^{N}\sum_{m,r=1}^{M}nmw_{nm}\left(1-R^*\right)\left[r\gamma u_{ir}-i\gamma^2\pi v_{ir}\right]\overline{\Delta}_{7klnmir}-$$

$$-\frac{\delta}{2}\sum_{n,i=1}^{N}\sum_{m,r=1}^{M}n^2w_{nm}\left(1-R^*\right)\left[i\gamma^3\pi^2u_{ir}-\mu r\gamma^2\pi v_{ir}+\mu\gamma^2\pi w_{ir}\right]\vec{\Delta}_{8klnmir}-$$

$$-\delta^2M_1^2\gamma^2M_E^2k^2\pi^2w_{kl}+\delta^2\left(1-R_1^*\right)\left(\delta^2k_1+\pi^2k^2\gamma^2k_2\right)w_{kl}=0. \qquad (10)$$

$$u_{nm}\left(0\right)=u_{0nm},\quad \dot{u}_{\mathrm{nm}}(0)=\dot{u}_{0nm},\quad v_{nm}\left(0\right)=v_{0nm},\quad \dot{v}_{nm}(0)=\dot{v}_{0nm},$$

$$w_{nm}\left(0\right)=w_{0nm},\quad \dot{w}_{nm}(0)=\dot{w}_{0nm}.$$

Here $\delta=\frac{R}{h}$, $\gamma=\frac{R}{L}$, $M_1=\frac{U}{V_\infty}$, $M_E=\sqrt{\frac{E}{\rho V_\infty^2}}$, $V\infty$ is the sound speed $\overline{\Delta}_{1k\ln mir}$, $\overline{\Delta}_{2k\ln mir}$, $\overline{\Delta}_{3k\ln mir}$, $\overline{\Delta}_{4k\ln mir}$, $\overline{\Delta}_{5k\ln mir}$, $\overline{\Delta}_{6k\ln mir}$, $\overline{\Delta}_{7k\ln mir}$, $\overline{\Delta}_{8k\ln mir}$ are the dimensionless coefficients related to coordinate functions and their derivatives; dots over a variable denote the time derivatives of the corresponding order.

2.3. Computational algorithm

Solution of IDE (10) is sought for by a numerical method based on the use of quadrature formulas [22–27]. This method is based on various analytic transformations that make it possible to reduce the initial systems to the systems of integral equations with regular kernels and stable numerical integration ensuring the solution of problems with a high degree of accuracy. Since the integral entering system (10) has a weak Abel-type singularity, it is impossible to use a quadrature formula. Therefore, by changing the variables

$$t-\tau=z^{\frac{1}{\alpha}},\quad 0\le z\le t^{\alpha}\quad (0<\alpha<1) \tag{11}$$

the integral at the Koltunov-Rzhanitsyn kernel with singularity of the following form

$$A\int_0^t (t-\tau)^{\alpha-1}\exp(-\beta(t-\tau))w(\tau)d\tau \tag{12}$$

has the form

$$\frac{A}{\alpha}\int_0^{t^{\alpha}}\exp(-\beta\, z^{\frac{1}{\alpha}})w(t-z^{\frac{1}{\alpha}})dz. \tag{13}$$

Note that after the change of variables, the integrand with respect to z becomes regular. Assuming that $t=t_i$, $t_i=i\Delta t$, $I=1, 2, \ldots$ ($\Delta t=const$ – the integration step) and replacing the integrals by some quadrature formulas (in particular, the trapezoid one), we get

$$\frac{A}{\alpha}\sum_{k=0}^{i}B_k\exp(-\beta\, t_k)w_{i-k}, \tag{14}$$

where the coefficients are $B_0=\frac{\Delta t^{\alpha}}{2}$; $\quad B_i=\frac{\Delta t^{\alpha}(i^{\alpha}-(i-1)^{\alpha})}{2}$;

$$B_k=\frac{\Delta t^{\alpha}((k+1)^{\alpha}-(k-1)^{\alpha})}{2},\quad k=\overline{1,i-1}. \tag{15}$$

Based on this method, an algorithm for the numerical solution of system (10) is described. Integrating the system (10) twice with respect to t, it can be written in integral form; by rational transformation the singularities of the integral operators R^* and R_1^* are eliminated. Then, assuming that $t=t_i$, $t_i=i\cdot\Delta t$, $i=1,2,\ldots$ (Δt is the integration step) and replacing the integrals with quadrature trapezoid formulas for the computation of $u_{ikl}=u_{kl}(t_i)$, $v_{ikl}=v_{kl}(t_i)$ and $w_{ikl}=w_{kl}(t_i)$, we obtain the following recurrence formulas for the Koltunov-Rzhanitsyn kernel $\left(R(t)=A\cdot\exp(-\beta t)\cdot t^{\alpha-1},\ 0<\alpha<1\right)$:

$$u_{pkl}=u_{okl}+\dot{u}_{okl}\,t_p-\sum_{j=0}^{p-1}A_j\left(t_p-t_j\right)\left\{\varphi_{kl}\left(u_{jkl}-\frac{A}{\alpha}\sum_{s=0}^{j}B_s e^{-\beta t_s}u_{j-s,kl}\right)-\psi_{kl}\left(v_{kl}-\frac{A}{\alpha}\sum_{s=0}^{j}B_s e^{-\beta t_s}v_{j-s,kl}\right)+\right.$$

$$\left.+\,\omega_k\left(w_{jkl}-\frac{A}{\alpha}\sum_{s=0}^{j}B_s e^{-\beta t_s}w_{j-s,kl}\right)+\frac{\delta\gamma}{4}\sum_{n,i=1}\sum_{m,r=1}D_{klnmir}\left(w_{jnm}w_{jir}-\frac{A}{\alpha}\sum_{s=0}^{j}B_s e^{-\beta t_s}w_{j-s,nm}w_{j-s,ir}\right)\right\}$$

$$v_{pkl}=v_{okl}+\dot{v}_{okl}\,t_p-\sum_{j=0}^{p-1}A_j\left(t_p-t_j\right)\left\{\aleph_{kl}\left(v_{jkl}-\frac{A}{\alpha}\sum_{s=0}^{j}B_s e^{-\beta t_s}v_{j-s,kl}\right)-\psi_{kl}\left(u_{jkl}-\frac{A}{\alpha}\sum_{s=0}^{j}B_s e^{-\beta t_s}v_{j-s,kl}\right)-\right.$$

$$\left.-d_e\left(w_{jkl}-\frac{A}{\alpha}\sum_{s=0}^{j}B_s e^{-\beta t_s}w_{j-s,kl}\right)+\frac{\delta}{4}\sum_{n,i=1}^{N}\sum_{m,r=1}^{M}F_{klnmir}\left(w_{jnm}w_{jir}-\frac{A}{\alpha}\sum_{s=0}^{j}B_s e^{-\beta t_s}w_{j-s,nm}w_{j-s,ir}\right)\right\}$$

$$w_{pkl}=w_{okl}+\dot{w}_{okl}\,t_p-\frac{1}{1+\phi^*_{\alpha l}}\sum_{j=0}^{p-1}A_j\left(t_p-t_j\right)\left\{\Theta_{kl}\left(w_{jke}-\frac{A}{\alpha}\sum_{s=0}^{j}B_s e^{-\beta t_s}w_{j-s,kl}\right)+\right.$$

$$+\frac{\omega_k}{\gamma}\left(u_{jkl}-\frac{A}{\alpha}\sum_{s=0}^{j}B_s e^{-\beta t_s}u_{j-s,kl}\right)-d_e\left(v_{jkl}-\frac{A}{\alpha}\sum_{s=0}^{j}B_s e^{-\beta t_s}v_{j-s,kl}\right)-$$

$$-\frac{\delta}{4}\sum_{n,i=1}^{N}\sum_{m,r=1}^{M}G_{klnmir}\left(w_{jnm}w_{jir}-\frac{A}{\alpha}\sum_{s=0}^{j}B_s e^{-\beta t_s}w_{j-s,nm}w_{j-s,ir}\right)+ \qquad .(16)$$

$$+\frac{\delta}{4}\sum_{n,i=1}^{N}\sum_{m,r=1}^{M}w_{jnm}\left\langle H_{klnmir}\left(u_{jir}-\frac{A}{\alpha}\sum_{s=0}^{j}B_s e^{-\beta t_s}u_{j-s,ir}\right)+Z_{klnmir}\left(v_{jir}-\frac{A}{\alpha}\sum_{s=0}^{j}B_s e^{-\beta t_s}v_{j-s,ir}\right)+\right.$$

$$\left.\left.+C_{klnmir}\left(w_{jir}-\frac{A}{\alpha}\sum_{s=0}^{j}B_s e^{-\beta t_s}w_{j-s,ir}\right)\right\rangle-\eta_{kl}{}^2 w_{jkl}+\delta^2(\delta^2k_1+\pi^2k^2\gamma^2k_2)\left(w_{jkl}-\frac{A_1}{\alpha_1}\sum_{s=0}^{j}B_s e^{-\beta t_s}w_{j-s,kl}\right)\right\}$$

$$p=1,2,3,...;\quad k=1,2,...,N;\quad l=1,2,...,M.$$

Here A_j, B_s are the numerical coefficients that do not depend on the choice of integrands and acquire different values depending on the use of quadrature formulas; φ_{kl}, ψ_{kl}, $\aleph_{kl}$, Θ_{kl}, η_{kl}, ω_k, d_e, D_{klnmir}, G_{klnmir}, C_{klnmir}, F_{klnmir}, H_{klnmir}, Z_{klnmir} are the dimensionless coefficients related to the coordinate functions and their derivatives.

2.4. Example of Test Solutions

Verification of efficiency of the proposed numerical method and programs, based on the solution of test cases, is a necessary stage to confirm the reliability of research results obtained in solving specific problems. The problems for which an exact solution is known [22] have been considered as test cases. Table 1 show a satisfactory agreement of approximate solutions with exact ones; this shows the reliability and high accuracy of calculation results.

Consider a non-linear integro-differential equation of the form

$$\ddot{w}+\lambda_0\dot{w}+\omega^2w=q-\lambda_1\int_0^t R(t-\tau)w(\tau)d\tau-\lambda_2 w\int_0^t R(t-\tau)w(\tau)d\tau-\lambda_3\int_0^t R(t-\tau)w^2(\tau)d\tau;$$

$$w(0)=1,\quad \dot{w}(0)=-\beta, \qquad (17)$$

where

$$R(t)=A\exp(-\beta t)t^{\alpha-1},\quad 0<\alpha<1;$$

$$q=\left[\beta^2+\omega^2-\lambda_0\beta-\frac{At^\alpha}{\alpha}\left(\lambda_1+\left[\lambda_2+\lambda_3\right]\exp(-\beta t)\right)\right]\exp(-\beta t)$$

Equation (17) has an exact solution $w=\exp(-\beta t)$, which satisfies the initial conditions.

According to (16), the approximate values $w_n=w(t_n)$ ($t=t_n=n\Delta t$, $n=0, 1, 2, \dots$) are found from the relationships

$$w_n = \frac{1}{1+\lambda_0 A_n}\left\{ 1-(\beta-\lambda_0)t_n - \sum_{i=0}^{n-1} A_i \left\langle \lambda_0 w_i - (t_n - t_i)\left[q(t_i) - \omega^2 w_i + \frac{A\lambda_2}{\alpha} w_i \times \right.\right.\right.$$
$$\left.\left.\left. \times \sum_{s=0}^{i} B_s \exp(-\beta t_s) w_{i-s} + \frac{A}{\alpha}\sum_{s=0}^{i} B_s \exp(-\beta t_s) w_{i-s}\left(\lambda_1 + \lambda_3 \exp(-\beta\ t_s) w_{i-s}\right)\right] \right\rangle \right\} \tag{18}$$

$n = 1, 2, \ldots,$; where A_i, B_s are the coefficients of the quadrature formula of trapezoids.

Table 1 gives approximate results of calculations by formulas (18) within the interval from 0 to 1 with Δt = 0.01 step, and exact solutions. The following initial data have been used: λ_0 = 1.1; λ_1 = 1.2; λ_2 = 1.3; λ_3 = 1.4; A = 0.01; β = 0.03; α = 0.01. It follows from the table that the maximum error Δ of calculations performed by described method represents the value $const \cdot \Delta t^2$. The efficiency of this numerical method and programs is shown in other test cases as well.

From the table it follows that the error Δh of calculations performed by described method coincides with the error of the quadrature formulas used and has the same order of smallness relative to the interpolation step (for the trapezoid formula the error of the method with respect to the interpolation step is of second-order, for the Simpson formula – of third order, etc.).

Table 1. Comparison of exact and approximate solutions of IDE.

t	Solution		Δh
	Exact	Approximate	
0	1.000000	1.000000	–
1	0.970445	0.970373	$0.7 \cdot 10^{-4}$
2	0.941764	0.941622	$1.4 \cdot 10^{-4}$
3	0.913931	0.913644	$2.8 \cdot 10^{-4}$
4	0.886920	0.886569	$3.5 \cdot 10^{-4}$
5	0.860707	0.860271	$4.3 \cdot 10^{-4}$
6	0.835270	0.834855	$4.1 \cdot 10^{-4}$
7	0.810584	0.810278	$3 \cdot 10^{-4}$
8	0.786627	0.786113	$5.1 \cdot 10^{-4}$
9	0.763379	0.763126	$2.5 \cdot 10^{-4}$
10	0.740818	0.740509	$3 \cdot 10^{-4}$

3. Results and Discussion

Based on the developed algorithm, a package of applied computer programs in Delphi language has been created. Results of calculations are reflected by the graphs shown in Figures 3–10.

The influence of the viscoelastic properties of material on the vibration process of the pipeline on a two-parameter foundation was investigated (Figure 3, a, b, c). On the ordinate, displacements w (Figure 3, a), u (Figure 3, b), v (Figure 3, c) are plotted. On the abscissa, the parameter of dimensionless time is plotted. The first of these curves is constructed for elastic pipelines $A = 0.0(1)$, the second and the third curves reflect the effect of the viscosity parameter at the following values: $A = 0.05(2); A = 0.1(3)$. The following parameter values were used for calculations: μ = 0.3; V_∞ = 330 m/s; M_1 = 0.1; γ = 0.02; δ = 4; ρ = 7800 kg/cm^3; k_1 = 1; k_2 = 1; N = 5; M = 2.

As seen from the figure, the viscoelastic properties of material lead to a decrease in the amplitude and frequency of the pipeline vibration.

Figure 4 shows the effect of rheological parameter α on the vibration process. Calculations have been carried out at α = 0.05; 0.1 and 0.5. The pipeline data and flow parameters were as follows: A = 0.03;

β = 0.005; A_1 = 0.1; α_1 = 0.25; β_1 = 0.005; k_1 = 1; k_2 = 1; $\gamma = 0.02$; $\delta = 3$; $V_\infty = 330$ m/s; $\mu = 0.3$; $M_1 = 0.1$; $\rho = 7800$ kg/cm^3; $k_1 = 1$; $k_2 = 1$; $N = 5$; $M = 2$.

The figure shows that an increase in parameter α leads to an increase in the amplitude and frequency of vibrations. At t = 0,75, 1.5, 2.3 and 3.2 the amplitude of oscillations reaches a maximum value. At t = 1.2 the amplitude of vibrations becomes minimal. Further calculations show that the change in the third rheological viscosity parameter β $(0 < \beta < 1)$ does not have a significant effect on the pipeline vibration process; this confirms the unacceptability of application of exponential relaxation kernels in calculating the dynamic problems of viscoelastic systems. These conclusions and results fully agree with the conclusions and results obtained in [22, 28].

Figure 5 shows the curves corresponding to various values of viscosity parameter of the foundation A_1. On the ordinate the parameter of the pipeline deflection is plotted, on the abscissa – the time parameter. The curves are plotted for the pipeline at the following values of the viscosity parameter: $A_1 = 0$ (curve 1), $A_1 = 0.1$ (curve 2). The value of geometric and physical constants is assumed to be: A = 0.05; α = 0.25; β = 0.005; α_1 = 0.25; β_1 = 0.005; k_1 = 1; k_2 = 1; γ = 0.02; δ = 5; μ = 0.3; $V_\infty = 330$ m/s; $M_1 = 0.1$; $\rho = 7800$ kg/cm^3; $E = 2 \cdot 10^5$ MPa; $N = 5$; $M = 2$.

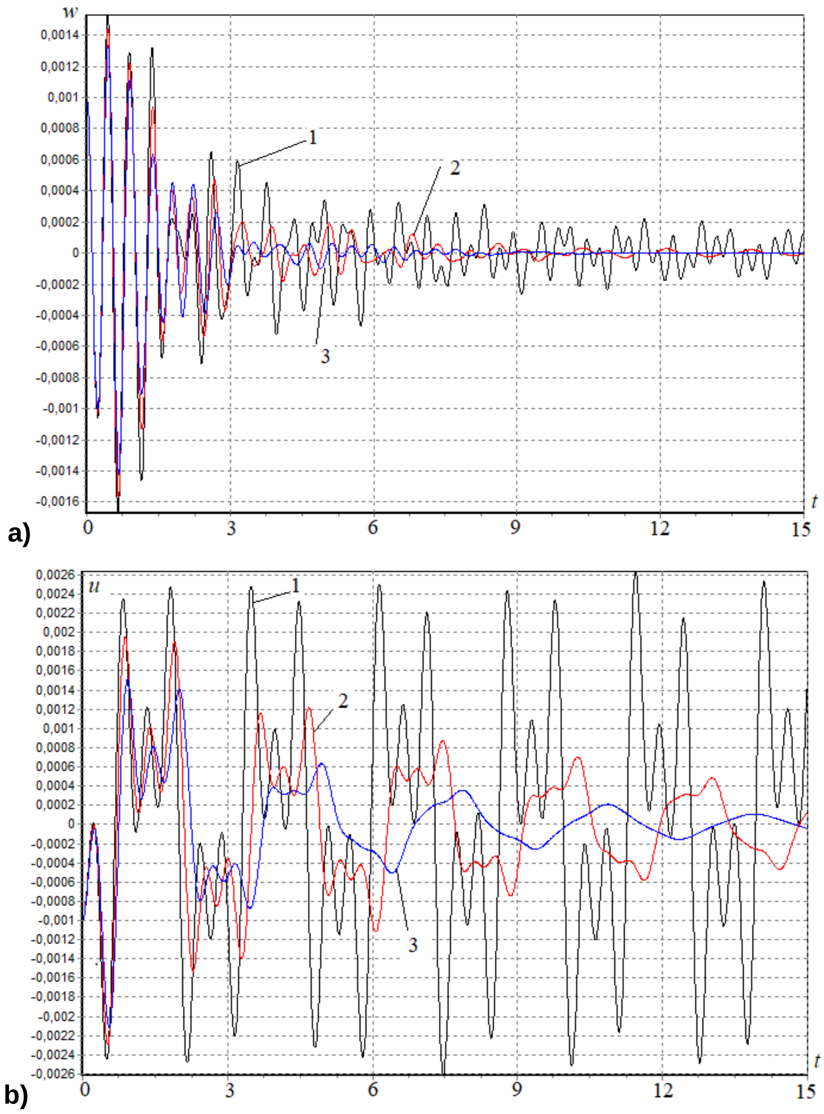

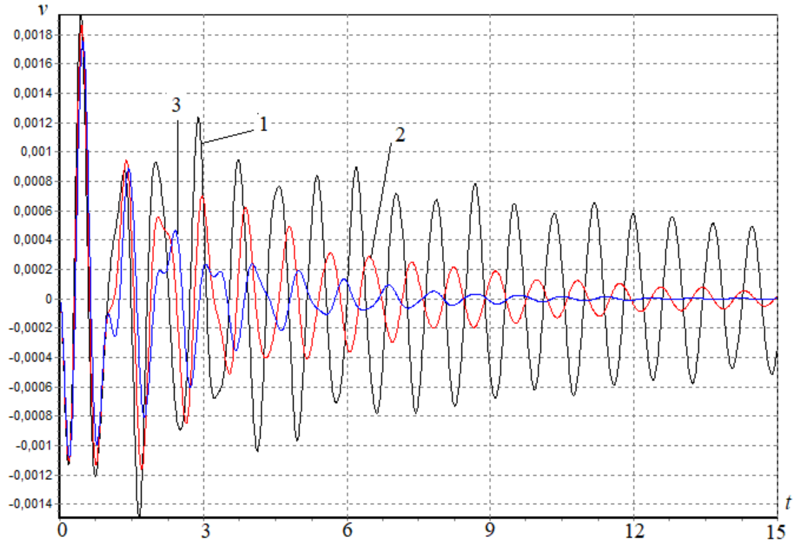

c)

Figure 3 (a, b, c). Displacements versus time at A = 0(1); 0.05(2) 0.1(3).

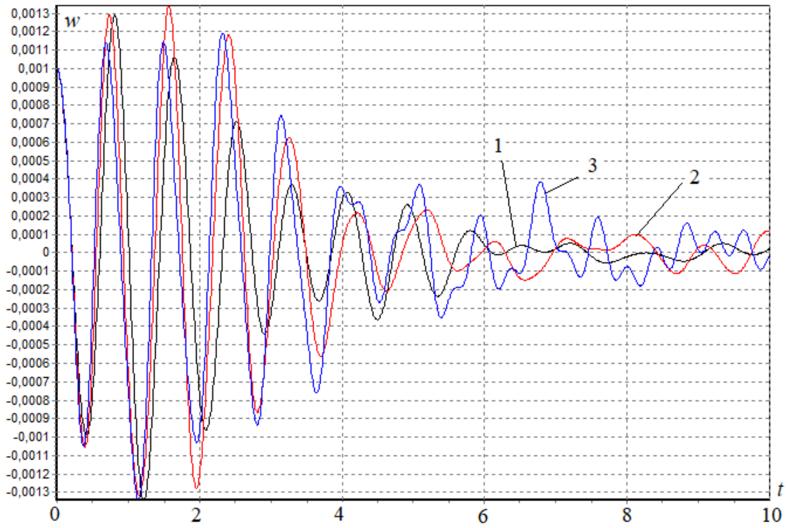

Figure 4. Deflection versus time at α = 0.05(1); 0.1(2); 0.5(3).

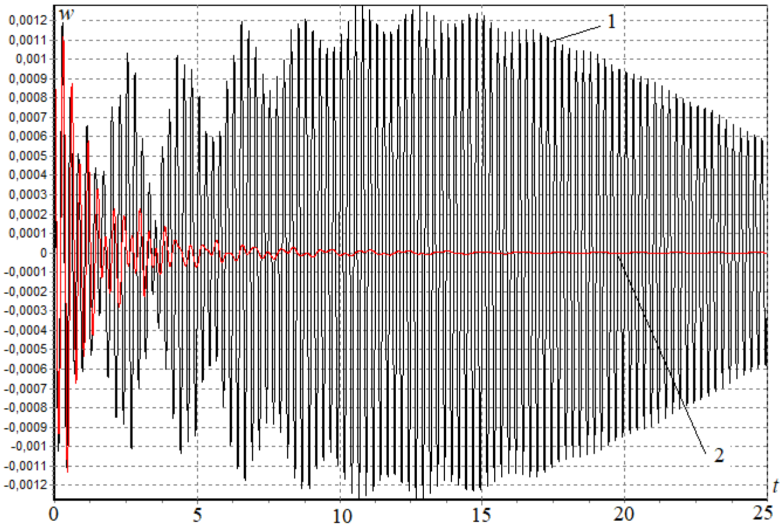

Figure 5. Deflection versus time at A_1 = 0(1); A_1 = 0.1(2).

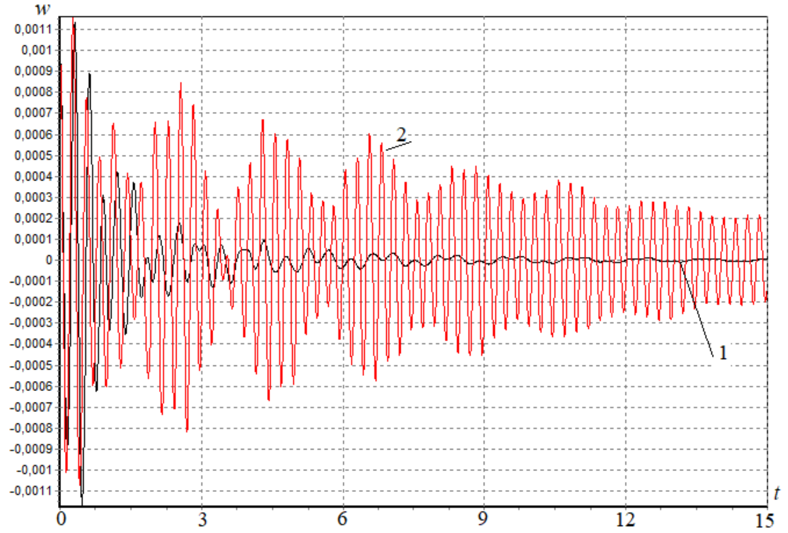

Figure 6. Deflection versus time at α_1 = 0.2 (1); α_2 = 0.75 (2).

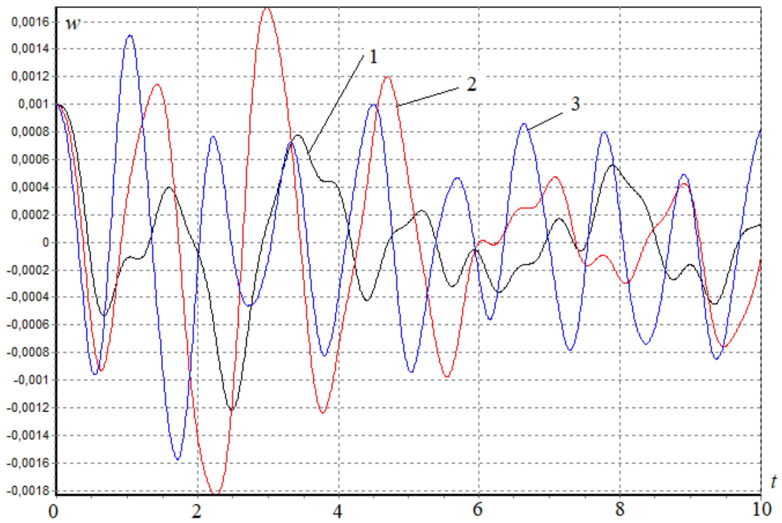

Figure 7. Deflection versus time at γ = 0.01(1); 0.06(2); 0.1(3).

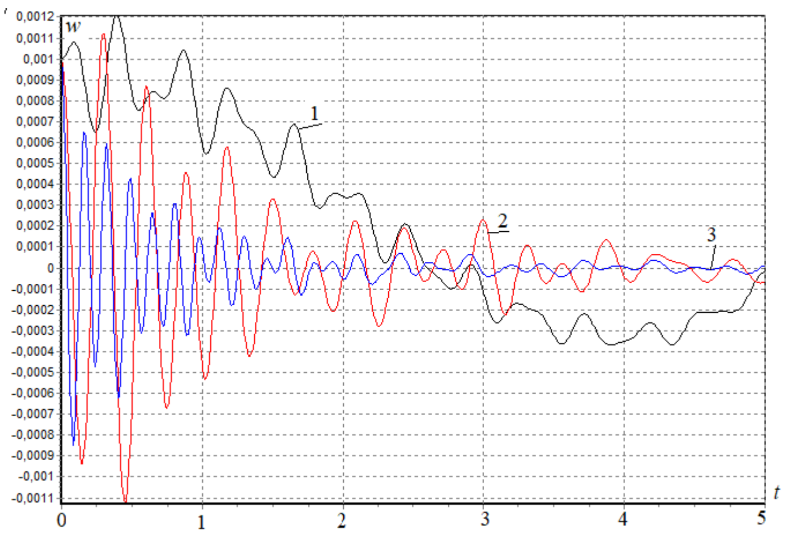

Figure 8. Deflection versus time at the values of k_1 and k_2:
k_1 = 0; k_2 = 0 (curve1); k_1 = 1; k_2 = 1 (curve 2); and k_1 = 3; k_2 = 3 (curve 3)

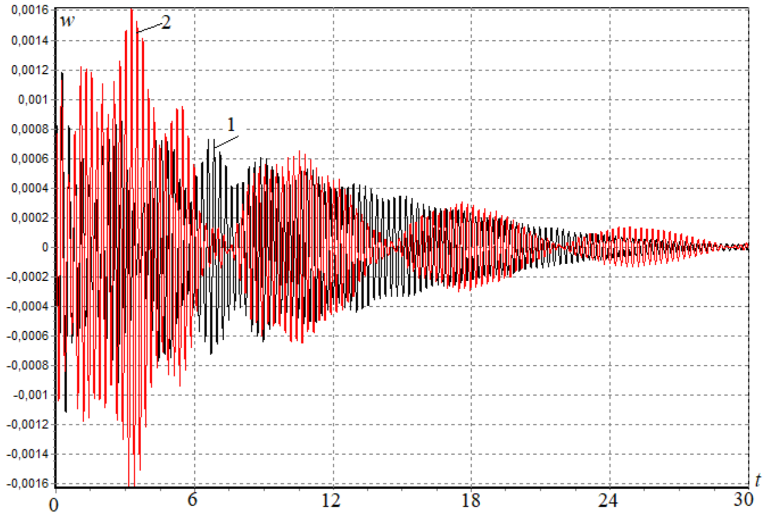

Figure 9. Deflection versus time at various values of M_1: 0.1(1); 1.8(2).

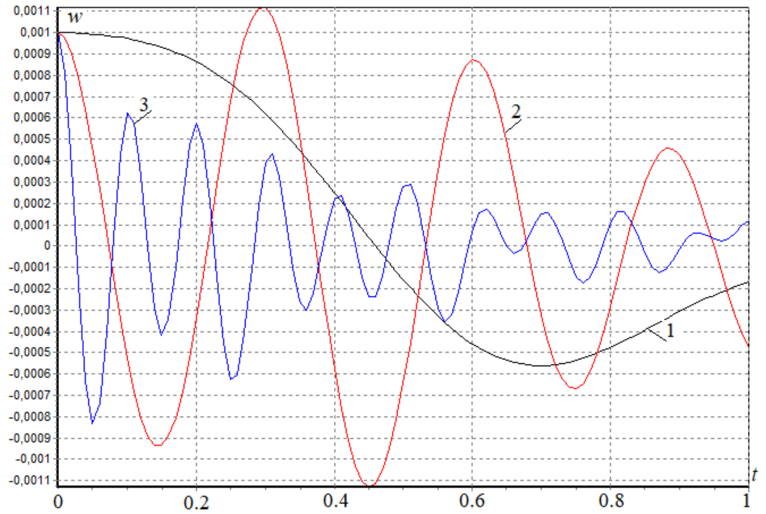

Figure 10. Deflection versus time at various values of δ parameter: 2 (curve 1); 5 (curve 2); 8 (curve 3).

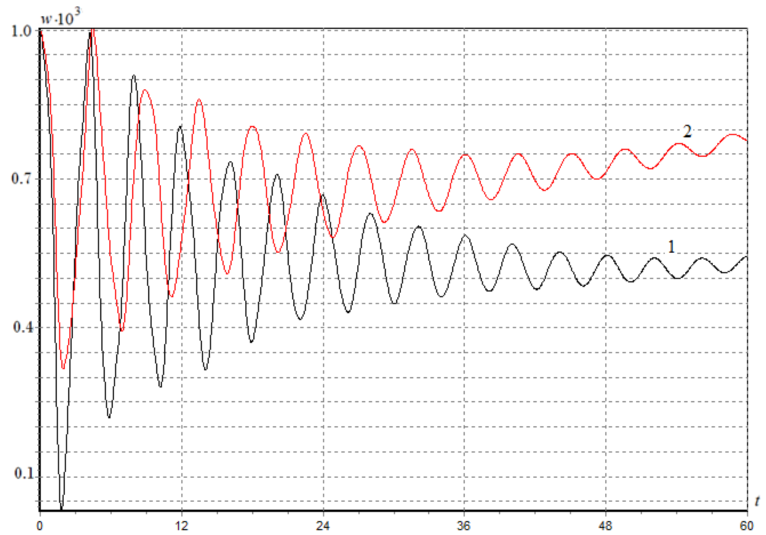

Figure 11. Linear theory (1); nonlinear theory (2).

As seen from Figure 5, an account of viscoelastic properties of soil foundation leads to the damping of vibration process. Though the solution of elastic and viscoelastic problems in the initial period of time differ little from each other, viscoelastic properties exert a significant influence over time. The amplitude of vibrations attenuates, and the vibration phase shifts to the right.

Figure 6 shows the nature of the pipeline motion under various rheological parameters of the foundation α_1. At $\alpha_1=0.2$; $\alpha_1=$ 0.75 the amplitude of pipeline vibration attenuates over time. An increase in rheological parameter $\alpha_1=$ 0.75 leads to an increase in the frequency and amplitude of pipeline vibrations. The following values of geometric and physical constants are used in calculation: $A=0.05$; $\alpha=0.25$; $\beta=0.005$; $A_1=0.1$; $\beta_1=0.005$; $k_1=1$; $k_2=1$; $\gamma=0.02$; $\delta=3$; $\mu=0.3$; $V_\infty=330$ m/s; $M_1=0.1$; $\rho=7800$ kg/cm^3; $E=2\cdot10^5$ MPa; $N=5$; $M=2$.

The influence of parameter γ, equal to the ratio of the radius and length of the pipeline is shown in Figure 7. The numbers indicate the results obtained at the following values of parameter γ: 1 – 0.01; 2 – 0.06; 3 – 0.1. An increase in parameter γ (which corresponds to an increase in the radius or a decrease in the length of the pipeline) causes an increase in the amplitude and frequency of vibrations of the pipeline.

Figure 8 shows the graphs of the function w(t) in time at different values of k_1 and k_2. Curves 1-3 correspond to the values $k_1=0$; $k_2=0$ (curve 1); $k_1=1$; $k_2=1$ (curve 2); and $k_1=3$; $k_2=3$ (curve 3). Analyzing the results obtained, it can be concluded that the presence of a viscoelastic foundation leads to a decrease in the amplitude of vibrations, and the frequency of vibrations increases. At $k_1=3$; $k_2=3$ (curve 3), the amplitude of vibrations rapidly decays.

The influence of the flow velocity M_1 on the vibration process of the pipelines is studied. Figure 9 shows the graphs of the function $w(t)$ in time at different values of M_1 not exceeding the critical value. The solution is obtained at the following values of physical and geometric coefficients: $A=0.05$; $\alpha=0.25$; $\beta=0.005$; $A_1=0.01$; $\alpha_1=$ 0.25; $\beta_1=0.005$; $k_1=1$; $k_2=1$; $\gamma=0.02$; $\delta=5$; $\mu=0.3$; $V_\infty=330$ m/s; $\rho=7800$ kg/cm^3; $E=2\cdot10^5$ MPa. Curves 1 and 2 correspond to the values $M_1=0.1$ (curve 1) and $M_1=1.8$ (curve 2). Note that with an increase in M_1 at the initial time, the amplitude and frequency of vibrations remain constant. At greater values of M_1 the vibration period increases with time.

Figure 10 shows the time variation of the deflection of the pipeline w at various values of the parameter δ: 2 (curve 1); 5 (curve 5); 8 (curve 3). As seen from the graph, the growth of the parameter δ contributes to a significant decrease in the amplitude of vibrations. An increase in the parameter δ makes it possible to significantly improve the stability of the pipeline.

Figure 11 shows the time variation of the displacement w of the midpoint of viscoelastic cylindrical shell, obtained from various theories: the linear theory (curve 1) and the nonlinear theory (curve 2). According to Figure 11, the results of linear and nonlinear theories differ significantly from each other. Although the solutions of the problems of linear and nonlinear theories differ little in the initial period of time, in the course of time the geometric nonlinearity exerts a significant influence on the solution.

4. Conclusions

It should be noted that the algorithm of the proposed method makes it possible to investigate in detail the influence of viscoelastic properties of structure material, geometric nonlinearities, and Pasternak two-parameter viscoelastic foundation on vibration processes of pipelines with fluid flowing inside.

When studying pipelines vibrations with a flowing fluid, a number of dynamic effects are obtained:

1. It has been established that an account of viscoelastic properties of the pipeline material leads to a decrease in the amplitude and frequency of vibrations by 20–40 %;

2. It is shown that an increase in the geometric parameter γ (which corresponds to an increase in the radius or a decrease in the length of the pipeline) and dimensionless flow velocity M_1 leads to an increase in the amplitude and frequency of vibration;

3. It has been established that an account of viscoelastic foundation leads to a decrease in the amplitude of vibrations, and the frequency of vibration increases.

The obtained results of numerical simulation may be implemented at the enterprises of oil and gas industry, agriculture, housing and communal services and design organizations.

5. Acknowledgement

The study was supported by the National Research Foundation of Uzbekistan (Grant QXA-13-001-2015).

References

1. Stojanović, V., Petković, M.D. Nonlinear dynamic analysis of damaged Reddy–Bickford beams supported on an elastic Pasternak foundation. Journal of Sound and Vibration. 2016. Vol. 385. No. 22. Pp. 239–266.
2. Lee, S.Y., Kes, H.Y. Free vibrations of non-uniform beams resting on non-uniform elastic foundation with general elastic end restraints. Computers and Structures. 1990. Vol. 34. No. 3. Pp. 421–429.
3. De Rosa, M.A. Free vibrations of Timoshenko beams on two-parameter elastic foundation. Computers and Structures. 1995. Vol. 57. Pp. 151–156.
4. Naidu, N.R., Rao, G.V. Vibrations of initially stressed uniform beams on two-parameter elastic foundation. Comput. Struct. 1995. Vol. 57. Pp. 941–943.
5. Ayvaz, Y., Özgan, K. Application of modified Vlasov model to free vibration analysis of beams resting on elastic foundations. J. Sound and Vib. 2002. Vol. 255. Pp. 111–127.
6. Bergant, A., Hou, Q., Keramat, A., Tijsseling, A.S. Water hammer tests in a long PVC pipeline with short steel end sections. Scientific professional Quarterly Spring. 2013. Vol. 1. No. 1. Pp. 23–34.
7. Wu, D., Jing, H., Xu, L., Zhao, L., Han, Y. Theoretical and numerical analysis of the creep crack initiation time considering the constraint effects for pressurized pipelines with axial surface cracks. International Journal of Mechanical Sciences. 2018. Vol. 141. Pp. 262–275.
8. Jia, P., Jing, H., Xu, L., Han, Y., Zhao, L. A modified reference strain method for engineering critical assessment of reeled pipelines. International Journal of Mechanical Sciences. 2016. Vol. 105. Pp. 23–31.
9. Xu, T., Yao, A., Jiang, H., Li, Y., Zeng, X. Dynamic response of buried gas pipeline under excavator loading: Experimental/numerical study. Engineering Failure Analysis. 2018. Vol. 89. Pp. 57–73.
10. Carrier III, W.D. Pipeline Supported on a Nonuniform Winkler Soil Model. Journal of Geotechnical and Geoenvironmental Engineering. 2005. Vol. 131. No. 10.
11. Chen, W.Q., Lü, C.F., Bian, Z.G. A mixed method for bending and free vibration of beams resting on a Pasternak elastic foundation. Applied Mathematical Modelling. 2004. Vol. 28. No. 10. Pp. 877–890.
12. Matsunaga, H. Vibration and buckling of deep beam-columns on two-parameter elastic foundations. Journal of Sound and Vibration. 1999. Vol. 228. No. 2. Pp. 359–376.
13. Qian, Q., Wang, L., Ni, Q. Nonlinear responses of a fluid-conveying pipe embedded in nonlinear elastic foundations. Acta Mechanica Solida Sinica. 2008. Vol. 21. No. 2. Pp. 170–176.
14. Chellapilla, K.R., Simha, H.S. Critical velocity of fluid-conveying pipes resting on two-parameter foundation. Journal of Sound and Vibration. 2007. Vol. 302. No. 1–2. Pp. 387–397.
15. Tj, H.G., Mikami, T., Kanie, S., Sato, M. Free vibration characteristics of cylindrical shells partially buried in elastic foundations. Journal of Sound and Vibration. 2006. Vol. 290. No. 3–5. Pp. 785–793.
16. Lottati, I., Kornecki, A. The effect of an elastic foundation and of dissipative forces on the stability of fluid-conveying pipes. Journal of Sound and Vibration. 1986. Vol. 109. No. 2. Pp. 327–338.
17. Rao, Ch.K., Rao, L.B. Critical velocities in fluid-conveying single-walled carbon nanotubes embedded in an elastic foundation. J. Appl. Mech. Tech. Phy. 2017. Vol. 58. Pp. 743–752.
18. Lü, L., Hu, Y., Wang, X. Dynamical bifurcation and synchronization of two nonlinearly coupled fluid-conveying pipes [Online]. Nonlinear Dynamics. 2015. Vol. 79. Pp. 2715–2734. URL: https://doi.org/10.1007/s11071-014-1842-y
19. Kozhaeva, K.V. Calculation of optimized methods of the river underwater pipeline backfill with the use of APMWinMachine 9.7. Magazine of Civil Engineering. 2016. No. 5. Pp. 42–66. doi: 10.5862/MCE.65.4
20. Grigolyuk, E.I., Mamay, V.I. Nelineynoye deformirovaniye tonkostennykh konstruktsiy [Nonlinear Deformation of Thin-walled Structures]. Moscow: Nauka. Fizmatlit, 1997. 272 p. (rus)
21. Vol'mir, A.S. Obolochki v potoke zhidkosti i gaza [Shell in the flow of liquid and gas]. Moscow: Nauka,1979. 320 p. (rus)
22. Badalov, F.B. Metody resheniya integral'nykh i integro-differentsial'nykh uravneniy nasledstvennoy teorii vyazkouprugosti [Methods for Solving Integral and Integro-differential Equations of the Hereditary Theory of Viscoelasticity]. Tashkent: Mekhnat, 1986. 269 p. (rus)
23. Khudayarov, B.A. Numerical Study of the Dependence of the Critical Flutter Velocity and Time of a Plate on Rheological Parameters. International Applied Mechanics. 2008. Vol. 44. No. 6. Pp. 676–682.
24. Khudayarov, B.A. Numerical Analysis of Nonlinear Flutter of Viscoelastic Plates. International Applied Mechanics. 2005. Vol. 41. No. 5. Pp. 538–542.
25. Khudayarov, B.A. Flutter of Viscoelastic Plate in a Supersonic Gas Flow. International Applied Mechanics. 2010. Vol. 46. No. 4. Pp. 455–460.
26. Badalov, F.B., Khudayarov, B.A., Abdukarimov, A. Effect of the Hereditary Kernel on the Solution of Linear and Nonlinear Dynamic Problems of Hereditary Deformable Systems. Journal of Machinery Manufacture and Reliability. 2007. Vol. 36. No. 4. Pp. 328–335.
27. Khudayarov, B.A., Bandurin, N.G. Nelineynyy flatter vyazkouprugikh ortotropnykh tsilindricheskikh paneley [Nonlinear Flutter of Viscoelastic Orthotropic Cylindrical Panels]. Matematicheskoye modelirovaniye. 2010. Vol. 17. No. 10. Pp. 79–86. (rus)
28. Il'in, V.P., Sokolov, V.G. O svobodnykh kolebaniyakh tsilindricheskikh obolochek s protekayushchey zhidkost'yu [On free oscillations of cylindrical shells with flowing fluid]. Proceedings of the universities: Series Construction and Architecture. 1979. No. 12. Pp. 26–31. (rus)

Contacts:

Bakhtiyar Khudayarov, +998712370986; bakht-flpo@yandex.ru
Fozil Turaev, +998977117666; t.fozil86@mail.ru

Инженерно-строительный журнал

ISSN
2071-0305

сайт журнала: http://engstroy.spbstu.ru/

DOI: 10.18720/MCE.86.4

Нелинейные колебания трубопроводов на вязкоупругом основании, транспортирующего жидкость

Б.А. Худаяров*, Ф.Ж. Тураев,
Ташкентский институт инженеров ирригации и механизации сельского хозяйства, г. Ташкент, Узбекистан
** E-mail: bakht-flpo@yandex.ru*

Ключевые слова: колебательный процесс; основания; трубопровод; математическая модель; численный алгоритм; цилиндрическая оболочка

Аннотация. В статье представлены результаты исследования процесса колебания трубопроводов, транспортирующих жидкость или газ. При исследовании колебаний трубопроводов с протекающей внутри газо-жидкостью используется моделью в виде цилиндрических оболочек и двухпараметрической модели вязкоупругого основания Пастернака. Для описания вязкоупругих свойств использована наследственная теория вязкоупругости Больцмана-Вольтерра. Численно исследованы влияния параметров оснований Пастернака, влияние сингулярности в ядрах наследственности и геометрических параметров трубопровода на колебания конструкций, обладающих вязкоупругими свойствами. Установлено, что учет вязкоупругих свойств материала трубопровода приводит к уменьшению амплитуды и частоты колебаний на 20–40 %. Показано, что учет вязкоупругих свойств оснований грунта приводит к затуханию колебательного процесса трубопровода.

Список литературы

1. Stojanović V., Petković M.D. Nonlinear dynamic analysis of damaged Reddy–Bickford beams supported on an elastic Pasternak foundation // Journal of Sound and Vibration. 2016. Vol. 385. № 22. Pp. 239–266.
2. Lee S.Y., Kes H.Y. Free vibrations of non-uniform beams resting on non-uniform elastic foundation with general elastic end restraints // Computers and Structures. 1990. Vol. 34. №. 3. Pp. 421–429.
3. De Rosa M.A. Free vibrations of Timoshenko beams on two-parameter elastic foundation // Computers and Structures. 1995. Vol. 57. Pp. 151–156.
4. Naidu N.R., Rao G.V. Vibrations of initially stressed uniform beams on two-parameter elastic foundation // Computers and Structures. 1995. Vol. 57. Pp. 941–943.
5. Ayvaz Y., Özgan K. Application of modified Vlasov model to free vibration analysis of beams resting on elastic foundations // J. Sound and Vib. 2002. Vol. 255. Pp. 111–127.
6. Bergant A., Hou Q., Keramat A., Tijsseling A.S. Water hammer tests in a long PVC pipeline with short steel end sections // Scientific professional Quarterly Spring. 2013. Vol. 1. № 1. Pp. 23–34.
7. Wu D., Jing H., Xu L., Zhao L., Han Y. Theoretical and numerical analysis of the creep crack initiation time considering the constraint effects for pressurized pipelines with axial surface cracks // International Journal of Mechanical Sciences. 2018. Vol. 141. Pp. 262–275.
8. Jia P., Jing H., Xu L., Han Y., Zhao L. A modified reference strain method for engineering critical assessment of reeled pipelines // International Journal of Mechanical Sciences. 2016. Vol. 105. Pp. 23–31.
9. Xu T., Yao A., Jiang H., Li Y., Zeng X. Dynamic response of buried gas pipeline under excavator loading: Experimental/numerical study // Engineering Failure Analysis. 2018. Vol. 89. Pp. 57–73.
10. Carrier III W.D. Pipeline Supported on a Nonuniform Winkler Soil Model // Journal of Geotechnical and Geoenvironmental Engineering. 2005. Vol. 131. No 10.
11. Chen W.Q., Lü C.F., Bian Z.G. A mixed method for bending and free vibration of beams resting on a Pasternak elastic foundation. // Applied Mathematical Modelling. 2004. Vol. 28. № 10. Pp. 877–890.
12. Matsunaga H. Vibration and buckling of deep beam-columns on two-parameter elastic foundations // Journal of Sound and Vibration. 1999. Vol. 228. № 2. Pp. 359–376.
13. Qian Q., Wang L., Ni Q. Nonlinear responses of a fluid-conveying pipe embedded in nonlinear elastic foundations // Acta Mechanica Solida Sinica. 2008. Vol. 21. № 2. Pp. 170-176.
14. Chellapilla K.R., Simha H.S. Critical velocity of fluid-conveying pipes resting on two-parameter foundation // Journal of Sound and Vibration. 2007. Vol. 302. № 1–2. Pp. 387–397.

15. Tj H.G., Mikami T., Kanie S., Sato M. Free vibration characteristics of cylindrical shells partially buried in elastic foundations // Journal of Sound and Vibration. 2006. Vol. 290. № 3–5. Pp. 785–793.
16. Lottati I., Kornecki A. The effect of an elastic foundation and of dissipative forces on the stability of fluid-conveying pipes // Journal of Sound and Vibration. 1986. Vol. 109. № 2. Pp. 327–338.
17. Rao Ch. K., Rao L. B. Critical velocities in fluid-conveying single-walled carbon nanotubes embedded in an elastic foundation // J. Appl. Mech. Tech. Phy. 2017. Vol. 58. Pp. 743–752.
18. Lü L., Hu Y., Wang X. Dynamical bifurcation and synchronization of two nonlinearly coupled fluid-conveying pipes [Online] // Nonlinear Dynamics. 2015. Vol. 79. Pp. 2715–2734. URL: https://doi.org/10.1007/s11071-014-1842-y
19. Kozhaeva K.V. Calculation of optimized methods of the river underwater pipeline backfill with the use of APMWinMachine 9.7 // Magazine of Civil Engineering. 2016. № 5. Pp. 42–66. doi: 10.5862/MCE.65.4
20. Григолюк Э.И., Мамай В.И. Нелинейное деформирование тонкостенных конструкций. М.: Наука. Физматлит, 1997. 272 с.
21. Вольмир А.С. Оболочки в потоке жидкости и газа. М.: Наука, 1979. 320 с.
22. Бадалов Ф.Б. Методы решения интегральных и интегро-дифференциальных уравнений наследственной теории вязкоупругости. Ташкент: Мехнат, 1986. 269 с.
23. Khudayarov B.A. Numerical Study of the Dependence of the Critical Flutter Velocity and Time of a Plate on Rheological Parameters // International Applied Mechanics. 2008. Vol. 44. № 6. Pp. 676–682.
24. Khudayarov B.A. Numerical Analysis of Nonlinear Flutter of Viscoelastic Plates. International Applied Mechanics. 2005. Vol. 41. № 5. Pp. 538–542.
25. Khudayarov B.A. Flutter of Viscoelastic Plate in a Supersonic Gas Flow // International Applied Mechanics. 2010. Vol. 46. № 4. Pp. 455–460.
26. Badalov F.B., Khudayarov B.A., Abdukarimov A. Effect of the Hereditary Kernel on the Solution of Linear and Nonlinear Dynamic Problems of Hereditary Deformable Systems // Journal of Machinery Manufacture and Reliability. 2007. Vol. 36. № 4. Pp. 328–335.
27. Худаяров Б.А., Бандурин Н.Г. Нелинейный флаттер вязкоупругих ортотропных цилиндрических панелей. Математическое моделирование. 2010. Т. 17. № 10. С. 79–86.
28. Ильин В.П., Соколов В.Г. О свободных колебаниях цилиндрических оболочек с протекающей жидкостью // Известия вузов: Серия строительство и архитектура. 1979. № 12. С. 26–31.

Контактные данные:

Бахтияр Алимович Худаяров, +998712370986; эл. почта: bakht-flpo@yandex.ru
Фозил Журакулович Тураев, +998977117666; эл. почта: t.fozil86@mail.ru

Magazine of Civil Engineering. 2019. 86(2).Pp. 46–60
Инженерно-строительный журнал. 2019. № 2(86). С. 46–60

Magazine of Civil Engineering

ISSN 2071-0305

journal homepage: http://engstroy.spbstu.ru/

DOI: 10.18720/MCE.86.5

The effect of cement replacement and homogenization procedure on concrete mechanical properties

P. Bily*, J. Fladr, R. Chylik, L. Vrablik, V. Hrbek,
Czech Technical University, Prague, Czech Republic
** E-mail: petr.bily@fsv.cvut.cz*

Keywords: high-performance concrete; supplementary cementitious materials; fly ash; microsilica; metakaolin

Abstract. Supplementary cementitious materials (SCM) are used in concrete for two main reasons – to reduce the amount of cement used and to improve material properties. A material that is more sustainable, durable, environmental friendly and economical compared to the traditional Portland cement concrete can be obtained. This paper investigates the effect of two important factors on mechanical properties of high-performance concrete (HPC) containing SCM. The first factor is the content of selected SCM, the second one is the homogenization procedure used for preparation of concrete. In the first part of the research program, 10 different mixtures were compared: reference mixture with no SCM and mixtures where 10 %, 20 % or 30 % of cement weight were replaced by microsilica, fly ash or metakaolin. In the second part, three mixtures with selected replacement levels were prepared by four different homogenization procedures and studied. Tests of bulk density, compressive strength, splitting tensile strength, flexural tensile strength, dynamic and static elastic modulus and depth of penetration of water under pressure were carried out for the tested mixtures. The best results were reached when cement was partially replaced by fly ash. Resistance of concrete to penetration of water under pressure was significantly improved by all SCM. The homogenization procedure in which the SCM was added to the mixture after water led to slightly better properties than the standard mixing technique in case of mixtures containing microsilica and metakaolin. The paper provides an extensive database that can serve as a benchmark for the design of HPC containing SCM.

1. Introduction

1.1. Object of study

The paper investigates the effect of two important factors on mechanical properties of high-performance concrete (HPC) containing supplementary cementitious materials (SCM). The first factor is the content of selected SCM, the second one is the homogenization procedure used for preparation of concrete. Ten different mixtures were compared (see table 2). The studied mechanical properties were compressive strength, splitting tensile strength, flexural tensile strength, dynamic and static elastic modulus and depth of penetration of water under pressure.

1.2. State of the art: Effect of SCM content on the properties of HPC

Comparable comprehensive work dealing with the influence of cement replacement by various SCM in various contents on various mechanical properties of high-performance concrete have not been found it the literature. However, some partial conclusions can be selected from the existing works as a reference for our research. Research works focused on similar materials (high-performance concretes with SCM without fibres, reaching compressive strength around 100 MPa and having water-to-binder ratio (w/b) between 0.20 and 0.30) have been selected. The values of the given characteristics at the age of 28 days are cited in all the cases.

Bily, P., Fladr, J., Chylik, R., Vrablik, L., Hrbek, V. The effect of cement replacement and homogenization procedure on concrete mechanical properties. Magazine of Civil Engineering. 2019. 86(2). Pp. 46–60. DOI: 10.18720/MCE.86.5.

Билы П., Фладр Й., Хылик Р., Враблик Л., Хрбек В. Влияние процесса замещения цемента и гомогенизации на высокоэффективный бетон // Инженерно-строительный журнал. 2019. № 2(86). С. 46–60. DOI: 10.18720/MCE.86.5

The most comprehensive study found is the work of Megat Johari et al. [1] who investigated the influence of SCM on compressive strength and elastic modulus of mixtures with $w/b = 0.28$. The used relatively low cement content of 450 kg/m^3 (OPC mixture) which was partially replaced by 5–15 % wt. of microsilica (SF5 – SF15 mixtures) or metakaolin (MK5 – MK15 mixtures) or 10–30 % wt. of fly ash (FA10 – FA30 mixtures). The results are summarized in table 1. In total, it can be stated that microsilica and metakaolin slightly improved the followed properties at all replacement levels, the use of fly ash led to mild deterioration with no clear dependence on the replacement amount.

Gesoglu et al. [2] studied the effect of microsilica and nanosilica addition on the properties of ultra-high performance concretes (UHPC). For mixtures without nanosilica (comparable with our study) they used 800 kg/m^3 of cement withoutmicrosilica first and then 720 kg/m^3 of cement with 80 kg/m^3 of microsilica (10 % replacement) at $w/b = 0.20$. The compressive strength was 115 MPa and 121 MPa respectively, the flexural tensile strength was 7.1 MPa and 7.9 MPa respectively. This means that cement replacement slightly improved the followed properties of concrete.

Zhang et al. [3] developed the artificial neural network model for estimation of strength of UHPC with SCM. They conducted a series of validation experiments. They focused on concretes with w/b =0.22 containing cement, fly ash and microsilica. The reference mix contained 875 kg/m^3 of cement and 44 kg/m^3 of microsilica. The other mixes contained 263 kg/m^3 of fly ash and a total of 656 kg/m^3 of cement and microsilica. The ratios of cement:microsilica differed from 14:1 to 3:1. For the reference concrete, 98 MPa compressive strength was reached. The strength of fly ash concretes varied between 85 and 108 MPa, almost linearly increasing with increasing microsilica content.

Table 1. Results of research of Megat Johari et al. [1].

Mixture	Compressive strength [MPa]	Static elastic modulus [GPa]	Dynamic elastic modulus [GPa]
OPC	86.7	44.6	50.0
SF5	105.7	46.1	53.5
SF10	113.9	47.1	54.2
SF15	117.5	48.3	55.0
FA10	85.7	43.7	49.6
FA20	84.3	43.1	48.8
FA30	82.1	42.4	48.2
MK5	91.5	45.7	52.9
MK10	103.7	45.5	51.8
MK15	103.4	46.3	52.2

Shi et al. [4] observed the influence of fly ash content and w/b on compressive strength, gas permeability and carbonation depth of HPC. The studied mixtures contained 550 kg/m^3 of cement with 0–60 % replacement by fly ash. For $w/b = 0.25$, the compressive strength increased from initial 81 MPa to 90 MPa at 30 % replacement and then decreased to 42 MPa at 60 % replacement. For $w/b = 0.30$, the strength uniformly decreased from 76 MPa to 40 MPa.

Poon et al. [5] developed HPC with high fly ash content, starting from the mixture containing 637 kg/m^3 of cement and further replacing 25 % and 45 % by the admixture at constant $w/b = 0.24$. The reference mixture reached 97 MPa compressive strength, which increased to 106 MPa at 25 % replacement and decreased to 89 MPa at 45 % replacement.

MuhdNorhasri et al. [6] dealt with the influence of standard metakaolin and nanometakaolin on UHPC properties. For mixes without nanometakaolin (comparable with our study) they used 800 kg/m^3 of cement without metakaolin and then 720 kg/m^3 of cement with 80 kg/m^3 of metakaolin (10 % replacement) at $w/b = 0.20$. The compressive strengths were 164 MPa and 168 MPa respectively, thus the effect of the admixture was negligible.

Tafraoui et al. [7] investigated UHPC with 20 % replacement of cement by microsilica and metakaolin. For 828 kg/m^3 of cement, 207 kg/m^3 of an admixture and $w/b = 0.22$ they reached the strengths of 98 MPa (microsilica) and 109 MPa (metakaolin).

In general, it can be said that cement replacements up to 30 % of cement weight have either positive or negligible effect on compressive strength of HPC. Higher replacements usually lead to unacceptable deterioration of mechanical properties.

1.3. State of the art: Effect of homogenization procedure on the properties of HPC

Research works focused on the effect of homogenization procedure on mechanical properties of HPC containing SCM are rather rare. Therefore, also works dealing with lower strength HPC (around 60 MPa) are cited in the following review.

Hiremath and Yaragal [8] focused on hardened properties of reactive powder concrete (900 kg/m^3 of cement, 180 kg/m^3 of silica fume, 180 kg/m^3 of quartz powder, w/b = 0.18). They experimented with the sequence of addition of compounds (microsilica before/after water, aggregate before/after water, water added in two or three steps), speed of mixing (25–150 rotations per minute – rpm) and mixing duration (10–30 min). Regarding the sequence of addition of compounds, the highest compressive strength of 128 MPa was reached when aggregate was added to wet mortar; the standard mixing procedure (adding water to dry mix of all constituents) led to 105 MPa. The study of mixing speed showed that 100 rpm was the most appropriate choice leading to 132 MPa strength; 117 MPa was obtained at 25 rpm, 121 MPa at 150 rpm. The most suitable mixing time was 15 min leading to 130 MPa compressive strength; 122 MPa was reached after 10 min of mixing and 109 MPa after 30 min. Further analysis has shown that excessively long or fast mixing can increase the percentage of pores in concrete, leading to reduced hardened properties.

Chang and Peng [9] studied the influence of sequence of addition of compounds and mixer type on properties of various HPC mixtures containing 300–600 kg/m^3 of cement and 80–160 kg/m^3 of fly ash (w/b = 0.4–0.5). Six different mixing procedures were compared. They obtained the best compressive strength (67 MPa) when the aggregate was added into the mix of cement with water and at the same time horizontal twin shaft mixer was used. However, almost the same result (66 MPa) was obtained when standard drum mixer and basic mixing method (first aggregate, then cement, then SCM, then all the water with superplasticizer at one moment) was used. Dividing the amount of waterwith superplasticizer in more doses did not have a positive effect.

Hemalatha et al. [10] investigated the effect of different types of mixers (ribbon type, pan, drum and Elrich) and the influence of time of addition of superplasticizer on properties of self-compacting HPC (various compositions, typically 450 kg/m^3 of cement, 100 kg/m^3 of fly ash, w/b = 0.38). The best compressive strength (67 MPa) was obtained with the use of Elrich mixer (forced action type mixer with variable speed), followed by standard pan mixer (58 MPa). No significant influence of time of addition of superplasticizer was noticed.

1.4. Study relevance

The reasons for the use of SCM in concrete are broadly known [11–13].By adding microsilica to concrete, fresh mix properties can be significantly improved. Bleeding of concrete can be avoided andpumpability is enhanced. The main advantages in case of hardened concrete are resistance to shrinkage, cracking, aggressive environmental conditions and penetration of water under pressure because of higher matrix density.

The main effect of fly ash is the deceleration of hydration of cement paste leading to lower hydration heat release and slower initial strength growth. Non-hydrated fly ash functions as microfiller, improving the density of cement matrix. It also improves the rheological properties of fresh concrete. It makes concrete more resistant to chemical aggressive agents. Concrete costs and carbon footprint reduction belong to other benefits of fly ash use.

Metakaolin contributes to the densification of structure and better rheology of concrete. It also improves compressive strength and resistance to deicing chemicals.

Considering the aforementioned effects, the design of high-performance concrete (HPC) mixture without the use of SCM is rather rare. In recent years, HPC became more common in civil engineering applications. Excellent compressive and tensile strength and exceptional durability are the main motivating factors for its exploitation in structural elements. However, the design of HPC mixtures is usually performed just based on the empirical experience, using trial-and-error method. Such an approach is lengthy, inefficient and expensive. To change the current practice and to proceed to modern controlled design methods, it is required to conduct a comprehensive and systematic research of the relations between the composition, homogenization process and properties of the material.

1.5. Objectives of the study

The objectives of the presented experimental program were:

- To quantify the effect of cement replacement by selected SCM – microsilica, fly ash and metakaolin – on a wide range of mechanical properties of HPC.
- To quantify the effect of changes in homogenization procedure on mechanical properties of HPC.
- To create an extensive database that could serve as a benchmark for further research works investigating this issue and as a guideline for concrete designers.

2. Methods

2.1. Investigated materials

The research was conducted for 10 different HPC mixtures. The reference mixture without SCM (labelled as REF in Table 2) and mixtures with 10 %, 20 % or 30 % cement replacement by three SCM – microsilica, fly ash or metakaolin (labelled as MIC, POP and MET with number denoting the replacement level in Table 2) – were produced. The selection of replacement levels was done based on the results of previous study [14] carried out on cement pastes that considered 0–80 % replacement levels. In accordance with the information found during the literature review, the study [14] showed that it was practically impossible to reach the mechanical parameters of HPC at replacements higher than 30 %. The workability of such mixtures was also very poor.

The composition of particular mixtures is given in Table 2. In all the cases, constant w/b = 0.26 was kept. The *k*-value concept was used to establish the required amount of water:

$$w/b = \frac{m_w}{m_c + k \cdot m_{SCM}} \tag{1}$$

Where m_w is the amount of water, m_c is the amount of cement and m_{SCM} is the amount of SCM in kg/m^3. The k-value was considered 2.0 for microsilica, 0.4 for fly ash and 1.0 for metakaolin in accordance with [15]. The following cementitious materials were used (for detailed specification please refer to Tables 3 and 4 and Figure 1):

- Portland cement CEM 42.5 R, Českomoravský cement company, plant Mokrá.
- MicrosilicaStachesil S.
- Fly ash ETU EN 450 from ČEZ company, Tušimice II power plant. The fly ash was mixed from two fractions P1 and P2 in 2:1 ratio.
- MetakaolinMefisto L05 from company Českélupkovézávody.

Table 2a Composition of the mixtures – part 1.

Compound	Specification	REF [kg/m^3]	MIC10 [kg/m^3]	MIC20 [kg/m^3]	MIC30 [kg/m^3]
cement	CEM I 42,5 R	800	720	640	560
admixture	microsilica	0	80	160	240
	fly ash	0	0	0	0
	metakaolin	0	0	0	0
water	-	210	231	252	273
w/b	-	0.26	0.26	0.26	0.26
aggregate (basalt)	8/16	320	320	320	320
	4/8	390	390	390	390
	0/4	730	730	730	730
SPF	Stachement	25.0	33.0	33.0	33.0
fibres	13 + 25 mm, 1:1	0	0	0	0

Table 2b. Composition of the mixtures – part 2.

Compound	Specification	POP10 [kg/m3]	POP20 [kg/m3]	POP30 [kg/m3]	MET10 [kg/m3]	MET20 [kg/m3]	MET30 [kg/m3]
cement	CEM I 42,5 R	720	640	560	720	640	560
admixture	microsilica	0	0	0	0	0	0
	flyash	80	160	240	0	0	0
	metakaolin	0	0	0	80	160	240
water	-	197.4	184.8	172.2	210	210	210
w/b	-	0.26	0.26	0.26	0.26	0.26	0.26
aggregate (basalt)	8/16	320	320	320	320	320	320
	4/8	390	390	390	390	390	390
	0/4	730	730	730	730	730	730
SPF	Stachement	34.0	32.0	30.0	30.0	30.0	30.0
fibres	13 + 25 mm, 1:1	0	0	0	0	0	0

Table 3. Chemical composition of cementitious materials [%].

Compound	CaO	SiO_2	Al_2O_3	Fe_2O_3	SO_3	MgO	K_2O	TiO_2
cement	64.2	19.5	4.7	3.2	3.2	1.3	-	-
microsilica	1.5	92.1	-	0.4	-	0.3	0.7	-
fly ash	4.2	48.8	24.2	12.5	1.2	0.7	1.4	1.4
metakaolin	-	54.1	40.1	1.1	-	-	0.8	1.8

Table 4. Additional characteristics of cementitious materials; x_{50} is median particle, x_{90} is 90 % quantile.

Compound	Specific surface area [m^2/g]	Bulk density [kg/m^3]	x_{50} [μm]	x_{90}[μm]
cement	0.37	3100	9.11	34.06
microsilica	15.0	2400	2.92	6.74
fly ash P1	-	-	40.41	183.84
fly ash P2	-	-	2.10	6.82
fly ash P1+P2 2:1	0.25	2000	5.89	124.35
metakaolin	12.7	2300	2.15	7.50

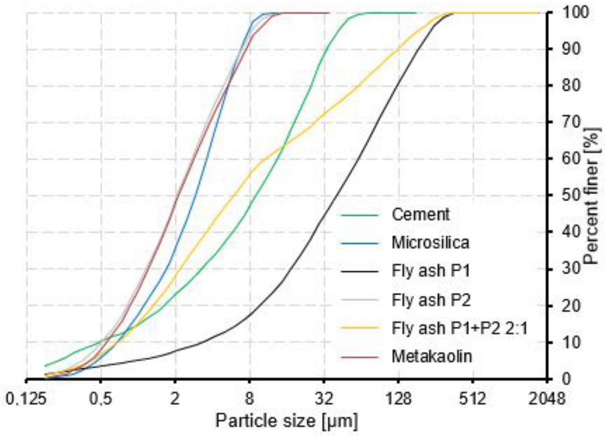

Figure 1. Particle size distribution curves of cementitious materials.

2.2. Homogenization procedures

The effect of homogenization procedure (namely the instant of addition of SCM into the mixer and the mixing time of SCM) was studied on three selected mixtures, namely MIC20, POP30 and MET20. All the mixes were prepared in standard pan laboratory mixer with centre shaft (pan fixed, scraper moving) and nominal volume of 80 litres at the speed of 30 rpm. For each mixture, four different mixing procedures were used:

- Procedure no. 1 (P1) was the standard one used for mixtures with different SCM content. At first, aggregate was homogenized, than cement was added, followed by silica fume and water with superplasticizer.
- In procedure no. 2 (P2), SCM was added before cement.
- In procedure no. 3 (P3), SCM was added as the last component (after the water with superplasticizer).
- Procedure no. 4 (P4) was the same as standard (P1), but the mixing time of SCM was increased from 180 s to 300 s.

Detailed schedule including mixing times is shown in Table 5. Before addition of each dry compound, the mixer was stopped. The water was added in the course of mixing.

Table5.Schedule of mixing procedures. The length of the step in seconds is given in the brackets.

Step no.	P1	P2	P3	P4
1	Aggregate 8/16+4/8 (20)	Aggregate 8/16+4/8 (20)	Aggregate 8/16+4/8 (20)	Aggregate 8/16+4/8 (20)
2	Aggregate 0/4 (20)	Aggregate 0/4 (20)	Aggregate 0/4 (20)	Aggregate 0/4 (20)
2	Cement (20)	SCM (180)	Cement (20)	Cement (20)
3	SCM (180)	Cement (20)	Water+SPF (60)	SCM (300)
4	Water+SPF (60)	Water+SPF (60)	SCM (180)	Water+SPF (60)

3. Results and Discussion

The tests of bulk density, compressive strength, splitting tensile strength, flexural tensile strength, dynamic and static elastic modulus and depth of penetration of water under pressure at the age of 28 days were carried out.

3.1. Bulk density

Bulk density was determined according to EN 12390-7 [16] on 100 mm cubes. Three values were measured for each mixture and averaged.

3.1.1 Effect of SCM content

Considering the high amount of fine compounds and the use of basaltic aggregate, the bulk densities are relatively high, slightly below 2500 kg/m^3. Lower values were reached for mixtures containing microsilica. In this case, the bulk density uniformly decreased with increasing admixture content. This was probably caused by the fact that water content increased with increasing admixture content as well, leading to increased porosity of hardened cement paste. For other mixtures, the bulk density was practically identical and independent on SCM content. The results are given in Table 6 and Figure 2.

Table6. Bulk density of mixtures with different SCM contents – results.

Mixture	Bulk density [kg/m^3]	Standard deviation[kg/m^3]
REF	2487	13.0
MIC10	2423	7.9
MIC20	2384	15.8
MIC30	2342	17.8
POP10	2489	26.4
POP20	2488	12.5
POP30	2468	9.5
MET10	2483	10.2
MET20	2507	18.0
MET30	2469	25.2

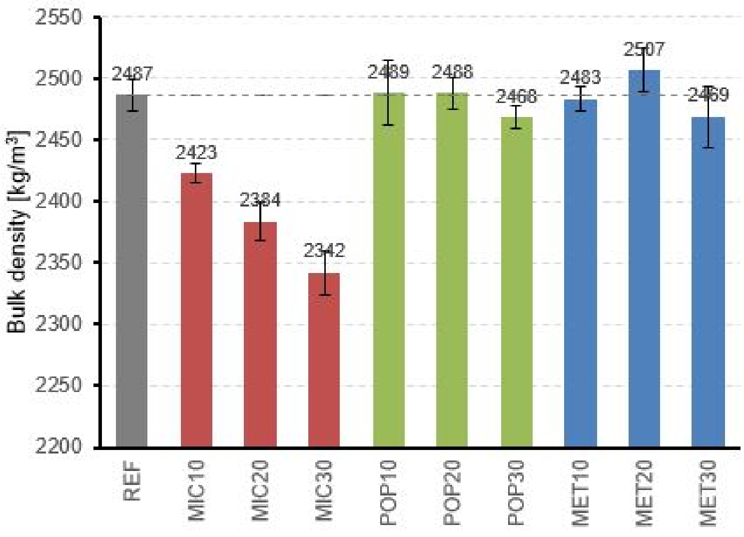

Figure 2. Bulk density of mixtures with different SCM contents – results.

3.1.2 Effect of homogenization procedure

It can be concluded that the bulk density was not influenced by the applied mixing procedure. The variations relative to procedure P1 did not exceed 2.5 %.The results are given in Table 7 and Figure 3 (for example, MIC20-3 is mixture MIC20 prepared by homogenization procedure P3).

Table7. Bulk density of mixtures with different homogenization procedures – results.

Mixture	Bulk density [kg/m³]	Standard deviation[kg/m³]
REF	2487	12.9
MIC20-1	2383	15.8
MIC20-2	2412	8.6
MIC20-3	2427	16.6
MIC20-4	2401	9.8
POP30-1	2468	9.6
POP30-2	2419	20.9
POP30-3	2472	10.3
POP30-4	2473	3.5
MET20-1	2507	18.1
MET20-2	2502	24.3
MET20-3	2524	17.2
MET20-4	2473	19.3

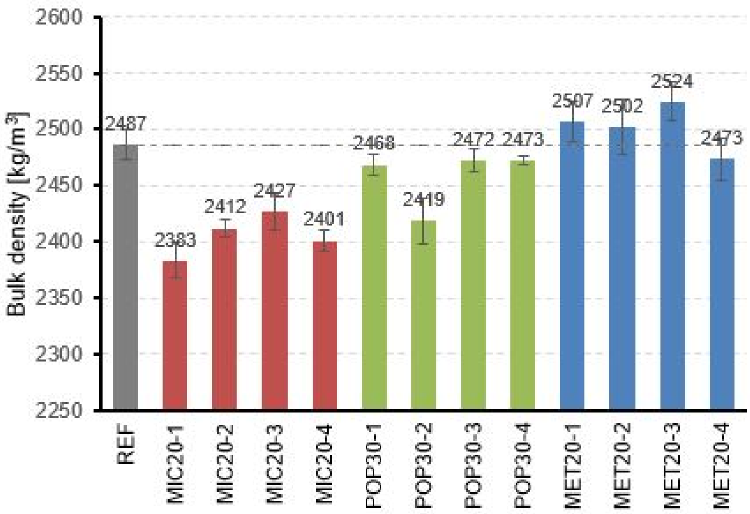

Figure 3. Bulk density of mixtures with different homogenization procedures – results.

3.2. Compressive strength

Compressive strength was determined according to EN 12390-3 [17] on 100 mm cubes. Six values were measured for each mixture and averaged.

3.2.1. Effect of SCM content

The reference mixture reached 105.9 MPa compressive strength. In case of microsilica use, the strength had decreasing tendency with increasing admixture content (corresponding to the decreasing trend of bulk density), but the measured values were very close to that of the reference mix. Replacement of cement by fly ash led to increase of strength above the reference value up to 125.3 MPa in case of POP30 mixture. Metakaolin did not affect the strength up to 20 % replacement, decrease was observed for 30 % replacement.The results are summarized in Table 8 and Figure 4.

Table8. Compressive strength of mixtures with different SCM contents – results.

Mixture	Strength [MPa]	Standard deviation[MPa]
REF	105.9	1.98
MIC10	109.3	2.84
MIC20	101.3	4.25
MIC30	97.7	6.77
POP10	106.6	7.85
POP20	120.8	1.25
POP30	125.3	2.39
MET10	108.9	2.92
MET20	110.3	4.50
MET30	96.7	4.04

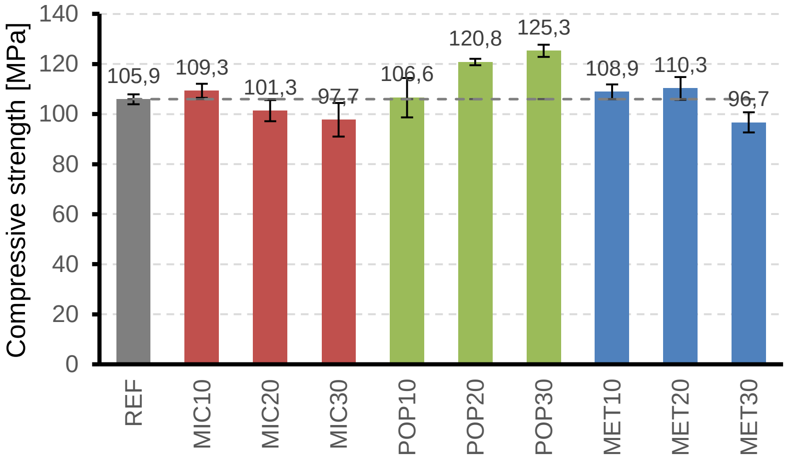

Figure 4 Compressive strength of mixtures with different SCM contents – results.

3.2.2 Effect of homogenization procedure.

Procedure P3 (SCM added after water with superplasticizer) gave better results than the other two alternative procedures (P2 and P4) for all types of SCM. It provided the highest strength of all the mixing procedures in case of microsilica and metakaolin. This can be attributed to the higher amount of water available for initial wetting of cement before the addition of SCM.

P2 (SCM added before cement) decreased the compressive strength of fly ash concrete by 30 MPa (25 %). Increase of mixing time (P4) led to 16 MPa (13 %) reduction. Microsilica and metakaolin concretes were practically unaffected by P2 and P4 mixing procedures. The results are given in Table 9 and Figure 5.

Table 9. Compressive strength of mixtures with different homogenization procedures – results.

Mixture	Strength [MPa]	Standard deviation [MPa]
REF	105.9	1.98
MIC20-1	101.3	4.25
MIC20-2	99.0	1.56
MIC20-3	113.8	6.81
MIC20-4	103.8	3.19
POP30-1	125.3	2.39
POP30-2	95.5	2.62
POP30-3	115.8	3.45
POP30-4	109.0	1.45
MET20-1	110.3	4.50
MET20-2	118.0	4.25
MET20-3	127.7	1.70
MET20-4	115.4	9.58

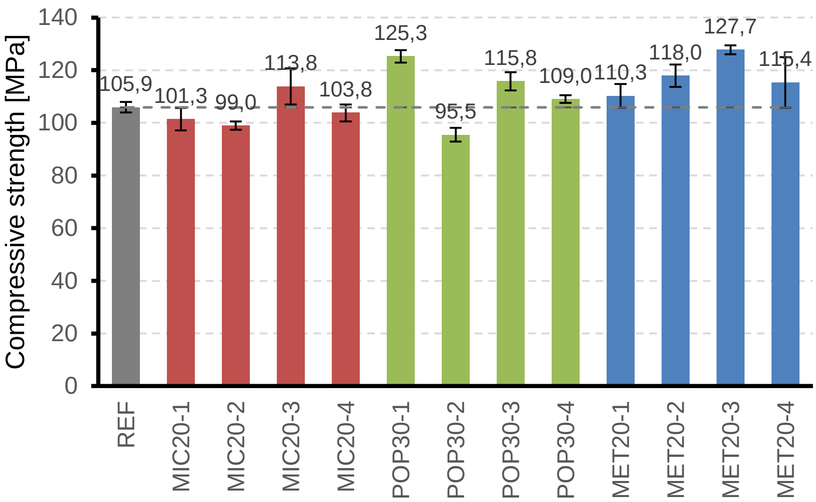

Figure 5 Compressive strength of mixtures with different homogenization procedures – results.

3.3. Tensile strength

Four-point flexural tensile strength was measured according to EN 12390-5 [18] on 100×100×400 mm prismatic samples for all the mixtures. Splitting tensile strength was measured according to EN 12390-6 [19] on 100 mm cubes for the mixtures with different SCM contents. Three values were measured for each mixture and each test and averaged.

3.3.1 Effect of SCM content

The tensile strengths measured by both types of tests were similar for most of the mixtures (with the exception of REF, MIC20 and MET20); the differences of average values did not exceed the size of the standard deviation. It is possible to say that the replacement of cement by microsilica or metakaolin led to overall decrease of tensile strengths compared to reference mixture, but no clear dependence on replacement percentage could be identified. In case of fly ash, the strength slightly increased with increasing replacement level.The results are summarized in Table 10 and Figure 6.

Table 10. Tensile strengths of mixtures with different SCM contents – results.

Mixture	Flexural t.s. $f_{ct,fl}$ [MPa]	Standard deviation [MPa]	Splitting t.s. $f_{ct,sp}$ [MPa]	Standard deviation [MPa]	Ratio $f_{ct,sp}/f_{ct,fl}$ [-]
REF	7.8	0.36	9.6	1.40	0.81
MIC10	6.7	0.43	7.5	1.22	0.89
MIC20	7.6	0.20	5.9	0.27	1.28
MIC30	6.5	0.29	5.8	0.68	1.12
POP10	8.6	0.18	8.2	0.70	1.04
POP20	8.5	0.36	8.8	0.96	0.96
POP30	9.1	0.43	8.6	0.16	1.06
MET10	7.5	0.59	7.3	0.52	1.03
MET20	6.5	0.91	9.1	0.45	0.71
MET30	7.9	0.38	7.9	0.34	1.01

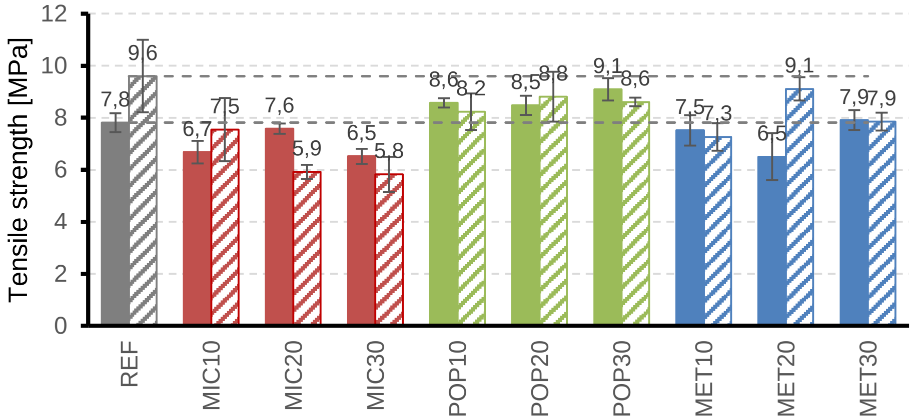

Figure 6. Tensile strength of mixtures with different SCM contents – results. Solid columns – flexural tensile strength, hatched columns – splitting tensile strength.

3.3.2 Effect of homogenization procedure

With the exception of MET20-1, the strength obtained for one type of SCM by various mixing procedures was practically identical. No clear dependence on homogenization procedure was identified for any SCM. The results are given in Table 11 and Figure 7.

Table 11. Flexural tensile strength of mixtures with different homogenization procedures– results.

Mixture	Strength [MPa]	Standard deviation [MPa]
REF	7.8	0.36
MIC20-1	7.6	0.20
MIC20-2	8.1	1.66
MIC20-3	7.3	0.12
MIC20-4	8.0	0.53
POP30-1	9.1	0.43
POP30-2	8.2	0.23
POP30-3	8.5	0.10
POP30-4	9.0	0.54
MET20-1	6.5	0.91
MET20-2	7.9	0.66
MET20-3	8.7	0.66
MET20-4	8.4	0.06

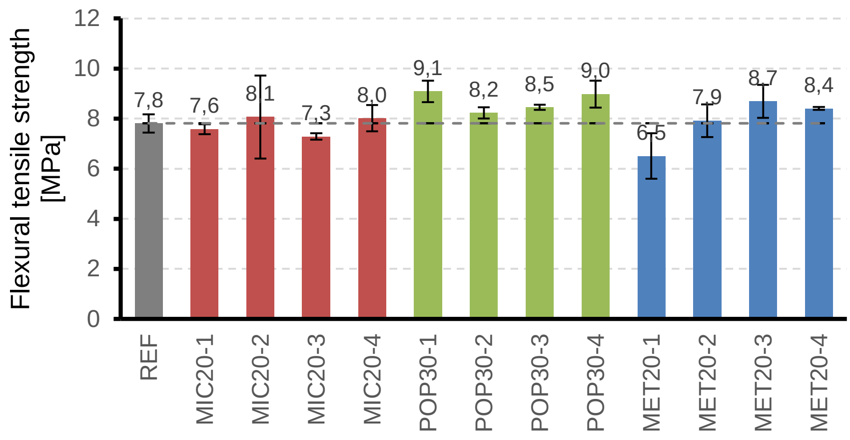

Figure 7. Flexural tensile strength of mixtures with different homogenization procedures – results.

3.4. Elastic modulus

Two types of elastic modulus were determined for each mixture with different SCM contents: dynamic one using the ultrasonic pulse method according to ČSN 73 1371 [20] and static one according to ISO 1920-10 [21]. Cylinders 100 mm in diameter and 200 mm in height were used for both tests. Only static modulus was measured for mixtures with different homogenization procedures. Three values were measured for each mixture and each test and averaged.

3.4.1 Effect of SCM content

The ratio between static and dynamic modulus varied between 0.8 and 0.9, the only exception being the reference mixture with 0.95 ratio. The static modulus of all the concretes with SCM was lower than that of the reference mixture. The dynamic modulus of concretes with metakaolin was lower that for the reference mixture; mixtures with microsilica and fly ash reached the values that were basically identical with the reference concrete. In case of microsilica and fly ash, the moduli increased with increasing replacement level; in case of metakaolin, they were practically constant.The results are summarized in Table 12 and Figure 8.

Table 12. Elastic modulus of mixtures with different SCM contents – results.

Mixture	Dynamic elastic modulus E_d [GPa]	Standard deviation [GPa]	Static elastic modulus E_s [GPa]	Standard deviation [GPa]	Ratio E_s/E_d [-]
REF	54.0	1.24	51.3	2.51	0.95
MIC10	51.3	2.57	42.2	3.12	0.82
MIC20	55.0	4.13	46.8	2.15	0.85
MIC30	55.9	1.23	48.1	3.56	0.86
POP10	51.3	3.65	46.2	2.08	0.90
POP20	55.0	2.97	49.5	1.34	0.90
POP30	55.9	1.73	49.8	3.39	0.89
MET10	48.7	3.46	39.0	2.03	0.80
MET20	51.2	1.94	41.9	2.22	0.82
MET30	47.9	1.87	39.7	1.31	0.83

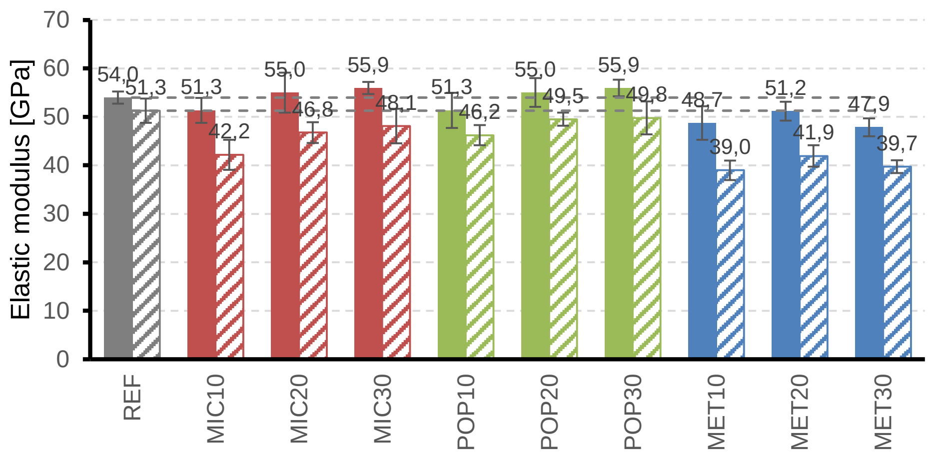

Figure 8. Elastic modulus of mixtures with different SCM contents – results.
Solid columns – dynamic modulus, hatched columns – static modulus.

3.4.2 Effect of homogenization procedure

Different tendencies were obtained for each type of SCM. In case of microsilica, the use of all alternative mixing procedures (P2, P3 and P4) lead to decrease of elastic modulus. No influence was observed in case of fly ash concrete. Metakaolin enriched mixtures prepared by any of the alternative procedures showed higher elastic modulus than the mixture prepared by standard procedure P1.The results are given in Table 13 and Figure 9.

Table 13. Static elastic modulus of mixtures with different homogenization procedure – results.

Mixture	Elastic modulus [GPa]	Standard deviation [GPa]
REF	51.3	2.51
MIC20-1	46.8	2.15
MIC20-2	39.8	3.49
MIC20-3	41.6	3.97
MIC20-4	40.7	2.70
POP30-1	49.8	3.39
POP30-2	49.5	2.90
POP30-3	51.0	3.97
POP30-4	50.4	3.22
MET20-1	41.9	2.22
MET20-2	52.9	2.30
MET20-3	52.5	2.77
MET20-4	45.5	3.19

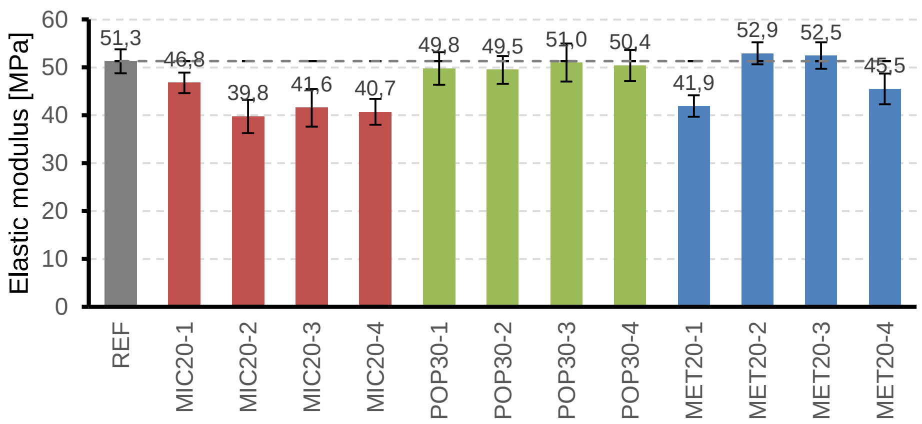

Figure 9. Static elastic modulus of mixtures with different homogenization procedures – results.

3.5. Depth of penetration of water under pressure

The test was performed only for mixtures with varied SCM content according to EN 12390-8 [22] on three 100 mm cubes for each mixture. Three values were measured for each mixture and averaged. Relatively high variance of results was experienced for some mixtures.

Reduction of the depth of penetration of water under pressure compared to the reference concrete was observed for all the mixtures with SCM, although it was quite negligible in case of MIC30 considering the size of the standard deviation. In case of microsilica and metakaolin, the depth of penetration increased with increasing admixture content. Fly ash appeared to be the most efficient admixture in this test; the depth of penetration significantly decreased with increasing cement replacement.The results are summarized in Table 14 and Figure 10.

Table 14 Depth of penetration of water under pressure of mixtures with different SCM contents – results.

Mixture	Depth of penetration [mm]	Standard deviation [mm]
REF	17.5	4.04
MIC10	10.5	1.73
MIC20	10.5	4.04
MIC30	17.0	1.15
POP10	9.0	5.77
POP20	3.0	1.15
POP30	0.8	0.29
MET10	6.0	1.15
MET20	7.0	2.31
MET30	10.0	1.15

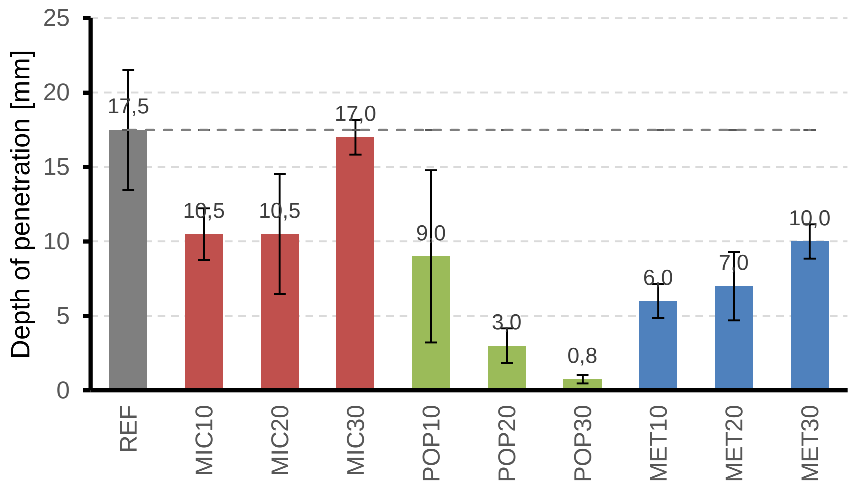

Figure 10 Depth of penetration of water under pressure of mixtures with different SCM contents – results.

4. Conclusions

The study provided a large database describing the changes of mechanical properties of the studied high-performance concretes containing supplementary cementitious materials. This database can be used for reference when designing and optimizing new HPC mixtures.

When varying the SCM content and using the standard homogenization procedure (P1), the best results were obtained when cement was partially replaced by fly ash. Compressive strength was improved by up to 18 % compared to reference concrete, flexural tensile strength increased by up to 16 % and the resistance to penetration of water under pressure was enhanced by up to 95 %. What is more, the beneficial influence of fly ash grew with increasing admixture content.

The most significant adverse effect of SCM was recorded in case of splitting tensile strength of microsilica mixtures, where the reduction reached 40 % compared to the reference concrete. However, this result was not fully confirmed by the flexural tensile strength measurement, which is generally considered more reliable. The decrease in this case was only up to 16 %. In case of cement replacement by metakaolin, static elastic modulus was reduced by up to 24 %, but again this was not confirmed by dynamic elastic modulus test that showed only 11 % reduction.

To sum up, it can be stated that partial replacement of cement by SCM up to 30 % cement weight did not affect the followed mechanical properties significantly. This is in accordance with the information found during the literature review. The only exception was the resistance to penetration of water under pressure that was improved by at least 40 % in all cases except MIC30 mixture.

After considering all the results obtained by different homogenization procedures, the most appropriate approach for mixtures containing microsilica and metakaolin seems to be P2, i.e. the addition of SCM into wet mix. Compressive strength was increased by this procedure; other properties were either increased or decreased by less than 10 %. Standard mixing procedure provided the best results for fly ash concretes. Increased mixing time did not lead to improvement of mechanical properties of HPC.

5. Acknowledgements

The paper was prepared thanks to the support of the Science Foundation of the Czech Republic (GAČR), project no. 17-19463S “Analysis of the relations between the microstructure and macroscopic properties of ultra-high performance concretes“.

References

1. Megat Johari, M.A., Brooks, J.J., Kabir, S., Rivard, P. Influence of supplementary cementitious materials on engineering properties of high strength concrete. Construction and Building Materials. 2011. 25. Pp. 2639–2648.
2. Gesoglu, M., Güneyisi, E., Asaad, D.S., Muhyaddin, G.F. Properties of low binder ultra-high performance cementitious composites: Comparison of nanosilica and microsilica. Construction and Building Materials. 2016. 102. Pp. 706–713.
3. Zhang, J., Zhao, Y., Li, H. Experimental Investigation and Prediction of Compressive Strength of Ultra-High Performance Concrete Containing Supplementary Cementitious Materials. Advances in Materials Science and Engineering. 2017. Vol. 2017. Article ID 4563164.
4. Shi, H., Xu, B., Zhou, X. Influence of mineral admixtures on compressive strength, gas permeability and carbonation of high performance concrete. Construction and Building Materials. 2009. 23. Pp. 1980–1985.

5. Poon, C.S., Lam, L., Wong, Y.L. A study on high strength concrete prepared with large volumes of low calcium fly ash. Cement and Concrete Research. 2000. 30. Pp. 447–455.
6. Muhd Norhasri, M.S., Hamidah, M.S., Mohd Fadzil, A., Megawati, O. Inclusion of nano metakaolin as additive in ultra high performance concrete (UHPC). Construction and Building Materials. 2016. 127. Pp. 167–175.
7. Tafraoui, A., Escadeillas, G., Lebaili, S., Vidal, T. Metakaolin in the formulation of UHPC. Construction and Building Materials. 2009. 23. Pp. 669–674.
8. Hiremath, P.N., Yaragal, S.C. Influence of mixing method, speed and duration on the fresh and hardened properties of Reactive Powder Concrete. Construction and Building Materials. 2017. 141. Pp. 271–288.
9. Chang, P.-K., Peng, Y.-N. Influence of mixing techniques on properties of high performance concrete. Cement and Concrete Research. 2001. 31. Pp. 87–95.
10. Hemalatha, T., Ram Sundar, K.R., Ramachandra Murthy, A., Iyer, N.R. Influence of mixing protocol on fresh and hardened properties of self-compacting concrete. Construction and Building Materials. 2015. 98. Pp. 119–127.
11. Aïtcin, P.-C. High-Performance Concrete. Informační centrum ČKAIT, Prague 2005.
12. Elahi, A., Basheer, P.A.M., Nanukuttan, S.V., Khan. Q.U.Z.: Mechanical and durability properties of high performance concretes containing supplementary cementitious materials. Construction and Building Materials. 2010. 24. Pp. 292–299.
13. Hela, R. Concrete admixtures. Beton TKS 2/2015. Pp. 4–10.
14. Chylík, R., Šeps, K. Influence of cement replacement by admixture on mechanical properties of concrete. Proceedings of the 12th fib PhD Symposium in Civil Engineering. 2018. Prague. Pp. 1267–1274.
15. ČSN EN 206+A1 Concrete – Specification, performance, production and conformity. ÚNMZ, Prague 2018.
16. ČSN EN 12390-7 Testing hardened concrete – Part 7: Density of hardened concrete. ÚNMZ, Prague 2009.
17. ČSN EN 12390-3 Testing hardened concrete – Part 3: Compressive strength of test specimens. ÚNMZ, Prague 2009.
18. ČSN EN 12390-5 Testing hardened concrete – Part 5: Flexural strength of test specimens. ÚNMZ, Prague 2009.
19. ČSN EN 12390-6 Testing hardened concrete – Part 6: Tensile splitting strength of test specimens. ÚNMZ, Prague 2010.
20. ČSN 73 1371 Non-destructive testing of concrete – Method of ultrasonic pulse testing of concrete. ÚNMZ, Prague 2011.
21. ČSN ISO 1920-10 Testing of concrete – Part 10: Determination of static modulus of elasticity in compression. ÚNMZ, Prague 2016.
22. ČSN EN 12390-8 Testing hardened concrete – Part 8: Depth of penetration of water under pressure. ÚNMZ, Prague 2009.

Contacts:

Petr Bily, +420737431835; petr.bily@fsv.cvut.cz
Josef Fladr, +420737431835; fladr@fsv.cvut.cz
Roman Chylik, +420737431835; chylik@fsv.cvut.cz
Lukas Vrablik, +420737431835; vrablik@fsv.cvut.cz
Vladimir Hrbek, +420737431835; hrbek@fsv.cvut.cz

Инженерно-строительный журнал

ISSN 2071-0305

сайт журнала: http://engstroy.spbstu.ru/

DOI: 10.18720/MCE.86.5

Влияние процесса замещения цемента и гомогенизации на высокоэффективный бетон

П. Билы*, Й. Фладр, Р. Хылик, Л. Враблик, В. Хрбек,
Чешский политехнический университет, Прага, Чехия
** E-mail: petr.bily@fsv.cvut.cz*

Ключевые слова: высокопрочный бетон; дополнительные вяжущие материалы; зольный унос; микрокремнезем; метакаолин.

Аннотация. Дополнительные вяжущие материалы (SCM) применяются при изготовлении бетонов по двум основным причинам – для уменьшения количества используемого цемента и улучшения их свойств. С их помощью возможно получить материал, являющийся более стойким, долговечным, экологически безопасным и экономичным по сравнению с традиционным портландцементным бетоном. В статье исследуется влияние двух важных факторов на механические свойства высокоэффективного бетона (HPC), содержащего SCM. Первым фактором является содержание выбранных дополнительных вяжущих материалов, вторым – вид процедуры гомогенизации, используемой при изготовлении бетона. В первой части исследования сравнивали 10 различных смесей: эталонная смесь без SCM, а также смеси, в которых 10, 20 или 30 % от массы цементы было заменено на микрокремнезем, летучую золу или метакаолин. Во второй части были изготовлены и изучены бетоны на основе трех смесей с различными уровнями замещения цемента дополнительными вяжущими материалами и четырех различных процедур гомогенизации. Для исследуемых составов определяли объемную плотность, прочности на сжатие, прочность на растяжение, динамический и статический модули упругости и глубину проникновения воды в бетон под давлением. Наилучшие результаты были достигнуты для смесей, в которых цемент частично был заменен на летучую золу. Устойчивость бетона к проникновению воды под давлением была значительно улучшена всеми SCM. Процедура гомогенизации, при которой SCM добавлялись к смеси после воды, позволила получить немного лучшие свойства бетонов, по сравнению со стандартной методикой смешивания применительно к смесям, содержащим микрокремнезем и метакаолин. В работе представлена обширная база данных, которая может служить эталоном для разработки HPC, содержащих SCM.

Список литературы

1. Megat Johari M.A., Brooks J.J., Kabir S., Rivard P. Influence of supplementary cementitious materials on engineering properties of high strength concrete // Construction and Building Materials. 2011. № 25. Pp. 2639–2648.
2. Gesoglu M., Güneyisi E., Asaad D.S., Muhyaddin G.F. Properties of low binder ultra-high performance cementitious composites: Comparison of nanosilica and microsilica // Construction and Building Materials. 2016. № 102. Pp. 706–713.
3. Zhang J., Zhao Y., Li H. Experimental Investigation and Prediction of Compressive Strength of Ultra-High Performance Concrete Containing Supplementary Cementitious Materials // Advances in Materials Science and Engineering. 2017. Vol. 2017. Article ID 4563164.
4. Shi H., Xu B., Zhou X. Influence of mineral admixtures on compressive strength, gas permeability and carbonation of high performance concrete. Construction and Building Materials. 2009. № 23. Pp. 1980–1985.
5. Poon C.S., Lam L., Wong Y.L. A study on high strength concrete prepared with large volumes of low calcium fly ash // Cement and Concrete Research. 2000. № 30. Pp. 447–455.
6. Muhd Norhasri M.S., Hamidah M.S., Mohd Fadzil A., Megawati O. Inclusion of nano metakaolin as additive in ultra high performance concrete (UHPC) // Construction and Building Materials. 2016. № 127. Pp. 167–175.
7. Tafraoui A., Escadeillas G., Lebaili S., Vidal T. Metakaolin in the formulation of UHPC // Construction and Building Materials. 2009. № 23. Pp. 669–674.
8. Hiremath P.N., Yaragal S.C. Influence of mixing method, speed and duration on the fresh and hardened properties of Reactive Powder Concrete // Construction and Building Materials. 2017. № 141. Pp. 271–288.
9. Chang P.-K., Peng Y.-N. Influence of mixing techniques on properties of high performance concrete // Cement and Concrete Research. 2001. № 31. Pp. 87–95.
10. Hemalatha T., Ram Sundar K.R., Ramachandra Murthy A., Iyer N.R. Influence of mixing protocol on fresh and hardened properties of self-compacting concrete // Construction and Building Materials. 2015. № 98. Pp. 119–127.

11. Aïtcin P.-C. High-Performance Concrete. Informační centrum ČKAIT, Prague 2005.
12. Elahi A., Basheer P.A.M., Nanukuttan S.V., Khan Q.U.Z.: Mechanical and durability properties of high performance concretes containing supplementary cementitious materials // Construction and Building Materials. 2010. № 24. Pp. 292–299.
13. Hela R. Concrete admixtures. Beton TKS 2/2015. Pp. 4–10.
14. Chylík R., Šeps K. Influence of cement replacement by admixture on mechanical properties of concrete. Proceedings of the 12th fib PhD Symposium in Civil Engineering. 2018. Prague. Pp. 1267–1274.
15. ČSN EN 206+A1 Concrete – Specification, performance, production and conformity. ÚNMZ, Prague 2018.
16. ČSN EN 12390-7 Testing hardened concrete – Part 7: Density of hardened concrete. ÚNMZ, Prague 2009.
17. ČSN EN 12390-3 Testing hardened concrete – Part 3: Compressive strength of test specimens. ÚNMZ, Prague 2009.
18. ČSN EN 12390-5 Testing hardened concrete – Part 5: Flexural strength of test specimens. ÚNMZ, Prague 2009.
19. ČSN EN 12390-6 Testing hardened concrete – Part 6: Tensile splitting strength of test specimens. ÚNMZ, Prague 2010.
20. ČSN 73 1371 Non-destructive testing of concrete – Method of ultrasonic pulse testing of concrete. ÚNMZ, Prague 2011.
21. ČSN ISO 1920-10 Testing of concrete – Part 10: Determination of static modulus of elasticity in compression. ÚNMZ, Prague 2016.
22. ČSN EN 12390-8 Testing hardened concrete – Part 8: Depth of penetration of water under pressure. ÚNMZ, Prague 2009.

Контактные данные:

Петр Билы, +420737431835; эл. почта: petr.bily@fsv.cvut.cz
Йосеф Фладр, +420737431835; эл. почта: fladr@fsv.cvut.cz
Роман Хылик, +420737431835; эл. почта: chylik@fsv.cvut.cz
Лукаш Враблик, +420737431835; эл. почта: vrablik@fsv.cvut.cz
Владимир Хрбек, +420737431835; эл. почта: hrbek@fsv.cvut.cz

Magazine of Civil Engineering. 2019. 85(1). Pp. 61–71
Инженерно-строительный журнал. 2019. № 1(85). С. 61–71

Magazine of Civil Engineering

ISSN 2071-0305

journal homepage:http://engstroy.spbstu.ru/

DOI: 10.18720/MCE.86.6

Frost heaving of foundation pit for seasonal permafrost areas

G. Chao*, Z. Lu,
Shenyang Jianzhu University, Shenyang City, Liaoning, China
** E-mail: guochaoglovel@126.com*

Keywords: frost heaving; foundation pit; temperature field; temperature stress.

Abstract. Frost heaving can cause support structures to crack and even instability of the foundation pit. This paper describes the frost heaving features of the steel pile pre-stressed tendon composite foundation pit support system (SPPTCFPSS). As a combined rigid–flexible support system during the overwintering stage in Northeast China, these systems were used to investigate the transient heat conduction and fixed boundary one-dimensional frost heaving stress equations. The axial force sensors of the tendons used for the in-situ test accurately recorded the changing values of the axial forces of the pre-stressed tendons during the integrated working period for the foundation pit frost-heaving effect. Practical support data for the frost heaving stress analysis of the system were thus provided. The thermo-physical properties were obtained from the soil experiments, including the coefficient of thermal conductivity, specific heat of the foundation soil, and thermal expansion factor, among others. Base on this, the fluid effective velocity, saturation, and temperature fields were received from the heat flow coupling analysis of finite element methods (FEM).The results show that the actual axial force applied to the SPPTCFPSS is approximately equal to the theoretical value of the pit frost-heaving force calculated for the one-dimensional fixed boundary conditions corrected by saturation index from FEM. The SPPTCFPSS can adapt to a large-scale frost-heaving deformation to enable a reasonable increase in adaptive capacity in a region that has seasonal periods of frozen soil.

1. Introduction

Figure 1. Map of the project.

Chao, G., Lu, Z. Frost heaving of foundation pit for seasonal permafrost areas. Magazine of Civil Engineering. 2019. 86(2). Pp. 61–71. DOI: 10.18720/MCE.86.6.

Чао Г., Лу Ч. Морозное пучение котлованов в регионах сезонного промерзания грунтов // Инженерно-строительный журнал. 2019. № 2(86). С. 61–71. DOI: 10.18720/MCE.86.6

The utility tunnel project between Shenben Industry Greet in Benxi city, Liaoning province, China, and Liangjia Bridge is an important part of the Weining utility tunnel and is of great significance for the environmental protection and social development of the Benxi region. The utility tunnel constructed parallel to the Taizi river traverses a 6.2 km length of seasonal frozen soil region at 41°N (latitude) and an altitude higher than 150 m, as shown in Figure 1; a region of the Changbai mountains that experiences a relatively cold environment compared to the same latitude in a plain with five months of winter presents challenges associated with the mechanical sensitivity of geotechnical engineering measures to temperature variation. Under conditions of a seasonal frozen region at the high latitudes, engineering structures are forced to consider the threat of subsidence resulting from frost heaving and deformation of the underlying frozen soil foundation [1-4]. In response to such threats, lowering the deformation of the frozen foundation soils seems, in most cases, to present an effective approach for increasing the stability of the foundation pit in the seasonal frost region [5–8].

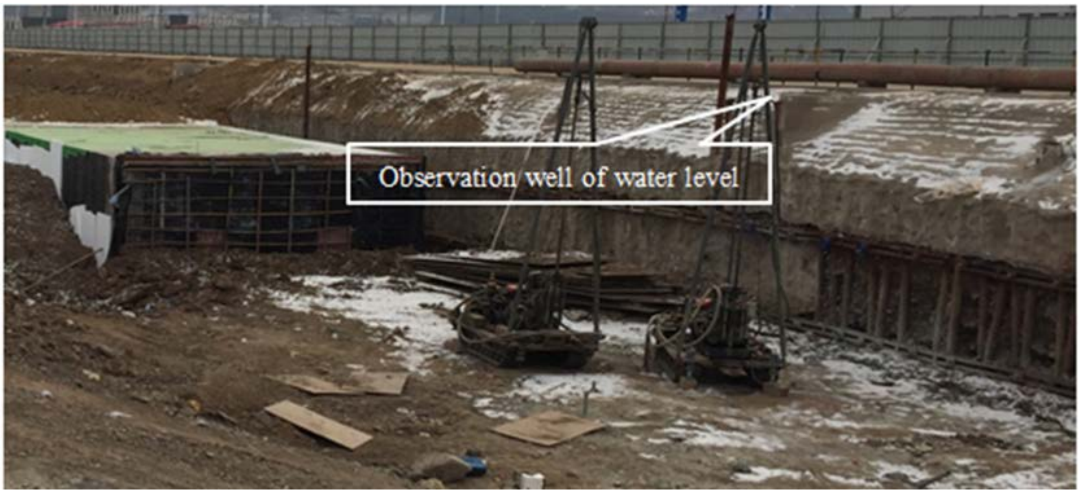

Figure 2. In-situ observation.

The foundation pit is located 50 m away from the south bank of the Taizi River; the depth of the pit is about 7 m, and the bottom elevation is 5 m below the water level. The soil layer formation shows that soil at a depth of 0–5 m is silt, 5–10 m is clay, and 10–12.5 m is gravel permeable layer. From this soil foundation information and observation well of water level, as shown in Figure 2, the capillary ascent zone (CAZ) or saturated frost zone (SFZ) is located between the capillary head and saturation lines, and the Taizi river provides the water resource for the freezing front of the foundation pit.

Many engineering measures have been proposed to protect foundation pits during the overwintering stages that underlie engineering infrastructures, and the effectiveness of some of these measures has been previously verified through field applications [9-13]. Among these, steel pipe piles with pre-stressed tendons that constitute a rigid-flexible composite supporting system, are considered one of the most efficient measures, as shown in Figure 3.

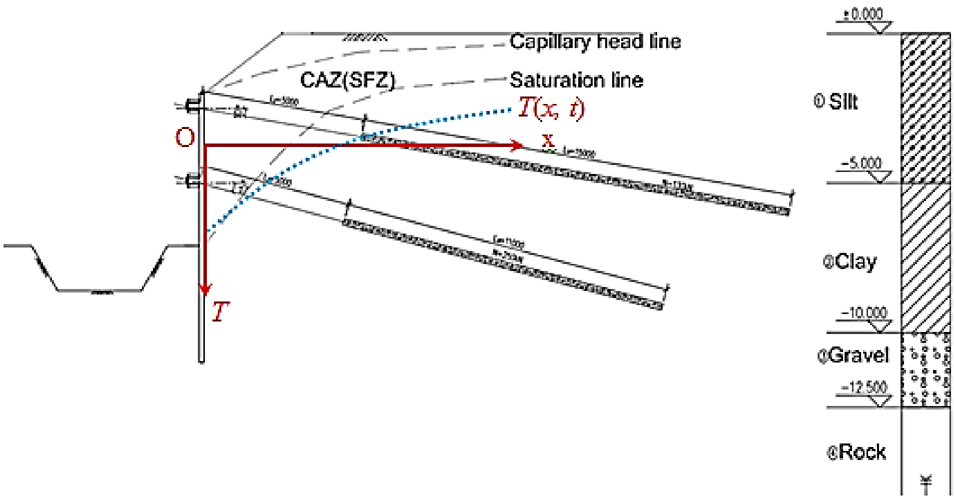

Figure 3. Profile of SPPTCFPSS.

Owing to the greater ability of steel to adapt to deformation than concrete, a steel pile pre-stressed tendon composite foundation pit support system (SPPTCFPSS) can adapt better to deflections from the frost heaving of the soils and synchronously maintain the stability of the foundation pit, while requiring no additional equipment and being easily realizable in construction projects. The existing protection measures for overwintering foundation pits include straw bags, extruded Expanded Polystyrene heat-preservation boards, granulated foam-glass ceramics [14–15], and other passive heat insulation measures, or heating tropics, hot water pipes, and other active heat insulation measures. However, all these insulation measures increase project costs and carbon emissions. A rigid–flexible composite supporting system has the advantages of low carbon emission and environmental friendliness for adapting to frost heaving deformations of foundation pits in winter.

Once the winter season has passed, this composite support system can return to the initial displacement state automatically. However, this system requires foundation pit over-digging, so predictions of the deflection of the support system are required in advance.

2. Methods

The precondition of foundation pit frost heaving analysis is to determine the location of the CAZ and SFZ accurately, in order to determine the saturated and unsaturated areas in the foundation pit. In this analysis, the finite element method (FEM) with ABAQUS was first used to analyze and calculate the seepage field in the foundation pit. The results are shown in Figures 4 and 5. The physical parameters of the soil sample are summarized in Table 1.

Table 1. Physical parameters of soil sample.

w	n	s_w	w_l	w_p	c	ø	k
%	%	%	%	%	kPa	°	m/s
34.5	41.86	98	40	18	24.7	11	1×10^{-6}

In Table 1, w is the water content of soil, n is the porosity, s_w is the saturation, w_l is the liquid limit moisture content, w_p is the plastic limit moisture content, c is the cohesion, ø is the internal friction angle, and k is the permeability coefficient.

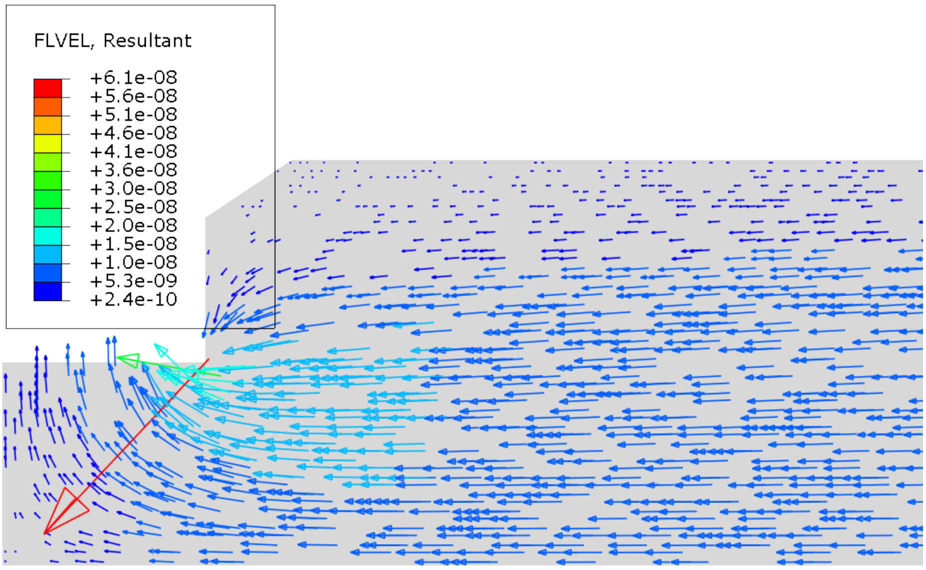

Figure 4. FLVEL of foundation pit.

In Figure 4, FLVEL denotes the current magnitude and components of the pore fluid effective velocity vector. The maximum value is 6.1×10^{-8} m/s, which occurs at the corner of the foundation pit. At the wall of the foundation pit, the direction of most velocity vectors is downward, while at the bottom of the foundation pit, the vectors' direction is upward. The comparison between Figures 4, 2, and 3 shows that the FEM results are consistent with the field foundation pit water level monitoring results. Because Taizi River is located 50 m outside the pit, the water level difference between the pit bottom and the river is 5 m, the hydraulic gradient is 0.1, and the permeability coefficient is small, the seepage water can be drained through the precipitation in the pit to ensure that the pit bottom is dry.

In Figure 5, SAT denotes the saturation of the foundation pit soil; the variation ranges from 1.0 to 0.33. The saturation curve is basically the line between the corner of the foundation pit and the river water level. The unsaturated curve is essentially parallel to the saturated curve, showing a linear decreasing trend, decreasing to the minimum value of 0.33 at the highest point, and the average value at the pit wall position is 0.68.

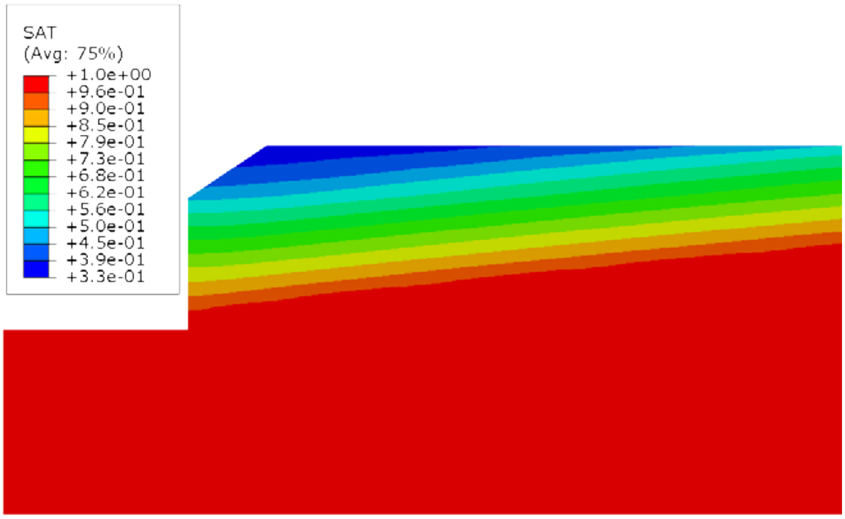

Figure 5. SAT of foundation pit.

The SPPTCFPSS is used in the natural environment during winter, so it is influenced by solar radiation and atmospheric temperature. Heat is generally transferred from the surface of the foundation to the depth, and converted with air. Therefore, it is necessary to analyze the temperature field of the system. The basic principle of the effect of temperature on a foundation pit is illustrated in Figure 3. The horizontal direction of the section shown is set as the x-axis and the vertical downward direction is the T-axis. The temperature field of the system was then obtained by the following equation [16, 17]:

$$\frac{\partial T}{\partial t} = a \cdot \left(\frac{\partial^2 T}{\partial x^2} \right), \tag{1}$$

where $T(x,t)$ is the temperature distribution function of the system, t is a temporal variable, and a is the temperature coefficient of the soil.

$$a = \frac{\lambda}{c_v}, \tag{2}$$

where λ is the heat conductivity coefficient and c_v is the volumetric heat capacity of the soil.

Substituting (2) into (1), we get

$$q_\Sigma = q_{sr}(t) - q_{ti}(t) + q_{hc}(t) = \lambda \frac{\partial T}{\partial x}, \tag{3}$$

where q_Σ is the sum of the heat flux of the foundation surface including solar radiation (SR) $q_{sr}(t)$, thermal irradiation $q_{ti}(t)$, and heat convection (HC) $q_{hc}(t)$, and λ is the coefficient of heat conductivity (CHC) in the present system, defined by

$$\lambda = \lambda_s - n\left[\lambda_s - s_w \lambda_i - (1 - s_w)\lambda_g\right], \tag{4}$$

where λ_s = 1.8 W/(m·K), λ_i= 2.2 W/(m·K), and λ_g= 0.02 W/(m·K) are the soil, water, and gas heat-conductivity coefficients, respectively, and λ = 1.92 W/(m·K) by equation (4) .

SR is considered the short-wave energy propagated to Earth from the Sun, and the amount of energy absorbed by the pit surface depends on its thermal properties and color

$$q_{sr}(t) = q_{sr0} \cos m\omega(t - 12) \quad 12 - \frac{c}{2} \le t \le 12 + \frac{c}{2}, \tag{5}$$

where q_{sr0} is the peak SR during daytime (q_{sr0}= 0.131 mQ), Q = 2.7×10^6(J/m^2) is the total SR during the day of winter, m = 12/c = 2 (c is the actual effective sunshine hours in a day, which is 6 h for winter), ω = 2π/24 (rad) is the earth's self-rotation frequency, and q_{sr0} = 0.707×10^6(J/m^2).

$$q_{sr}(t) = q_{sr0} \cos \frac{\pi}{6}(t - 12) \quad 9 \le t \le 15. \tag{6}$$

The thermal irradiation q_{ti} of the present system consists of long-wave heat flux between the foundation pit surfaces and the sky. The total irradiation is thus considered in accordance with the Stefan–Boltzmann law as follows:

$$q_{ti} = \gamma\varsigma[(T_1|_{x=0})^4 - (T_a)^4], \tag{7}$$

where $T_1|_{x=0}$ is the foundation pit surface temperature, ς = 5.6697×10⁻⁸ W/(m²·K⁴) is the Stefan–Boltzmann constant, and γ = 0.6 is the surface emissivity of the foundation pit surface.

The heat convection on the foundation pit surface is given by

$$q_{hc} = h_{hc}(T_a - T_s), \tag{8}$$

where $h_{hc}$is the convection coefficient, W/(m²·K), T_a is the air temperature (AT), and it is measured in-situ with a thermometer as shown in Figure 4. T_s is the surface temperature of the foundation pit.

The AT measurement curves during the winter months of December, January, and Februaryin the project area are shown in Figure 6.

It can be seen from Figure 6 that, in December 2017, the highest AT is 277 K, lowest AT is 254 K, and daily variation is approximately 15 K. The highest temperature is 275 K in January 2018, lowest temperature is 246 K, and daily variation is approximately 12 K. February 2018 has a maximum temperature of 278 K, minimum temperature of 250 K, and daily variation of approximately 12 K.

At the beginning of December, the ground temperature dropped to 273 K, and the shallow groundwater began to freeze. The lowest temperature in winter occurs from late January to early February, the temperature starts to rise by mid-February, and rises to 273 K by the end of February.

Because foundation pit freezing is mainly caused by low temperature accumulation, the above daily temperature change curves need to be converted into an accumulated temperature curve, and the results are as shown in Figures 7–9.

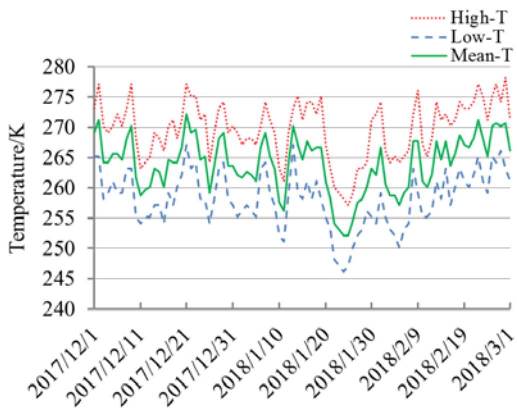

Figure 6. Air temperature.

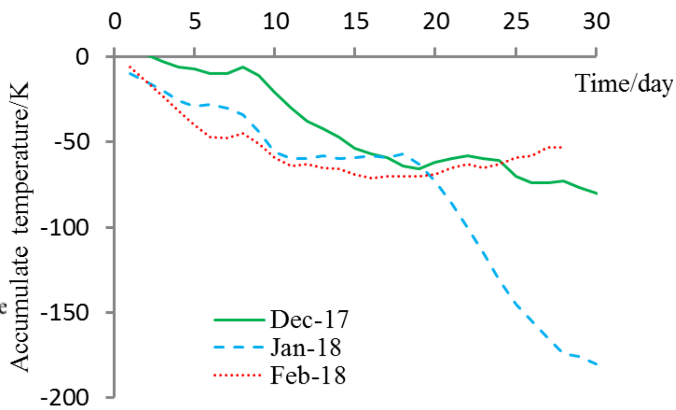

Figure 7. Daily highest temperature accumulation curves.

As seen in Figure 7, for December 2017 to January 2018, the daily highest temperature accumulation curves gradually fell; the temperature dropped dramatically in late January, with −50 K to −200 K change at this time for the wintering period, to the detriment of the foundation pit. By the middle of February, the temperatures began to rise, and the cumulative temperature curve rose gradually.

As seen in Figure 8, for December 2017 to January 2018, the daily lowest temperature accumulation curves gradually fell, with −400 K to −600 K change, and by the middle of February, the temperatures began to rise as the cumulative temperature curve rose gradually.

From Figure 9, the daily mean temperature accumulation curve trends are seen to be somewhere in between the maximum and minimum values, with −200 K to −380 K change. Therefore, the lowest temperature in January 2018 had the maximum influence on the foundation-pit temperature field; it was thus selected as the external temperature condition in this seasonal permafrost foundation temperature-field analysis.

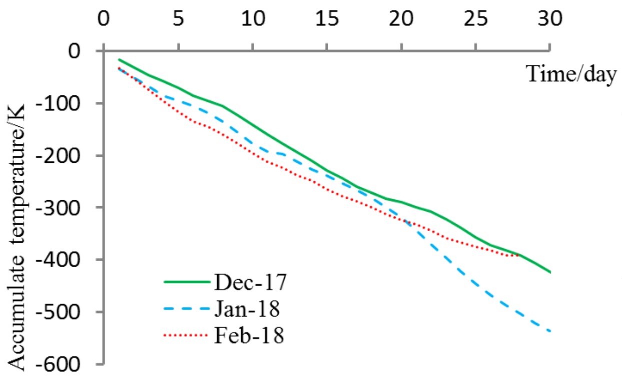

Figure 8. Daily lowest temperature accumulation curves.

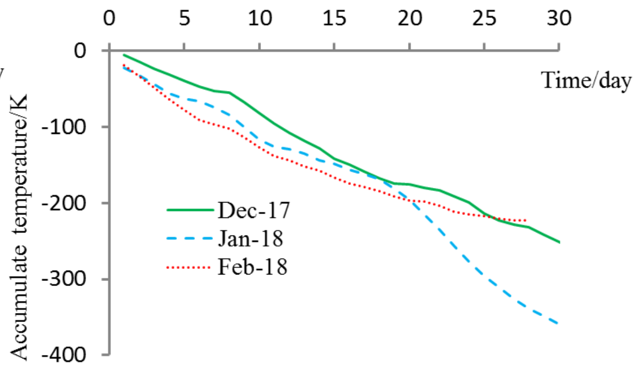

Figure 9. Daily mean temperature accumulation curves.

The parameter $h_{hc}$is a function of the local Reynolds number Re, thermal conductivity of air K_{air}, W/(m·K), Prandtl number Pr of air, and characteristic length of the medium on which the wind acts. According to the traditional heat-transfer theory, h_{hc} has two components, namely, free and forced convections. In this study, the Blasius solution was modified by combining the heat convection coefficients with the free and forced convections. The resultant heat-convection relationship can be expressed as

$$h_{hc} = 5.6 + 0.332\sqrt{\mathrm{Re}} \cdot \sqrt[3]{\mathrm{Pr}} \cdot \frac{K_{air}}{L}, \tag{9}$$

where K_{air}= 0.027 and Pr for air is 0.7. For airflow over an infinitely long flat plate, L = 0.15 m. The Reynolds number Re is given by

$$\mathrm{Re} = vL/\upsilon, \tag{10}$$

where v = 6 m/sis the local wind velocity, υ (m²/s) is the kinematic viscosity of air, which is usually 16.01×10^{-6}, and Re = 56214, h_{hc} = 18 W/(m²·K).

Owing to the effect of SR, AT varies periodically. The lowest temperature during the day usually occurs at 4–6 a.m., whereas the highest temperature usually occurs approximately 2 h after peak SR. Hence, in a duration of less than 10 h, AT increases from its lowest to the highest value, but subsequently requires more than 14 h to return to the lowest value. A single sine function is used to simulate this daily AT variation:

$$T_a = \overline{T}_a \sin\omega\left(t - t_0\right), \tag{11}$$

where $\overline{T}_a$ is the daily temperature variation amplitude and t_0 is the time between the occurrences of the highest SR and highest AT plus 7 h. The time between the highest SR and highest AT can generally be set to 2 h, so that t_0 = 9 h.

Substituting equations (6), (7), and (8) into equation (3), we get

$$T = \frac{2\overline{T}_a}{r} e^{-x\beta} \sin\left(\omega t + x\beta - \theta\right), \tag{12}$$

where r, β, θ, ψ_1, ψ_2, and S_t are the calculated parameters.

$$r = \sqrt{\psi_1^2 + \psi_2^2}; \tag{13}$$

$$\beta = \sqrt{\omega/2a}; \tag{14}$$

$$\theta = arctg\left(\frac{\psi_2}{\psi_1}\right); \tag{15}$$

$$\psi_1 = \left(1 + S_t\right)\cos\left(2\beta x\right) - \xi \cdot \sin\left(2\beta x\right); \tag{16}$$

$$\psi_2 = \xi \cdot \cos\left(2\beta x\right) + \left(1 + \xi\right)\sin\left(2\beta x\right); \tag{17}$$

$$\xi = \frac{\lambda}{h_{hc}} \sqrt{\frac{\omega}{2a}}\,; \tag{18}$$

$$S_t = \frac{\lambda}{h_{hc}} \sqrt{\frac{w}{2a}}\,. \tag{19}$$

When the temperature decreases, the pore water in the soil freezes and forms a freezing front; as water flow continues to be replenished, the freezing fronts shift, and even the pore water is blocked to form ice lenses in the soil. After water turns to ice, volume expansion occurs with gradual decrease in temperature. When the boundary conditions are constrained, temperature stress is generated. Thus far, there have been many methods to calculate the frost heaving stress [18–21]. The principle of a one-dimensional compressive stress is as follows: the one-dimensional frost heave force under saturated conduction is calculated as

$$\sigma = \alpha \cdot E \cdot \Delta T\,, \tag{20}$$

where α is the coefficient of thermal expansion (CTE) of the foundation soil, E is the elastic modulus of the frozen soil, and ΔT is the magnitude of temperature change of the soil.

For the unsaturated soil, frost heaving is relatively complex. This study uses the saturation $s_w$of the foundation pit soil to correct the above formula, and the results are as follows：

$$\sigma_{sw} = S_w \cdot \alpha \cdot E \cdot \Delta T\,. \tag{21}$$

The CTE in the present system is defined by

$$\alpha = \frac{1}{L_0} \cdot \frac{dL}{dT} = \frac{d\varepsilon}{dT}\,, \tag{22}$$

where L_0 is the orienting length of the soil specimen under some special temperature, $dL/dT = d\varepsilon$,and ε is the strain.

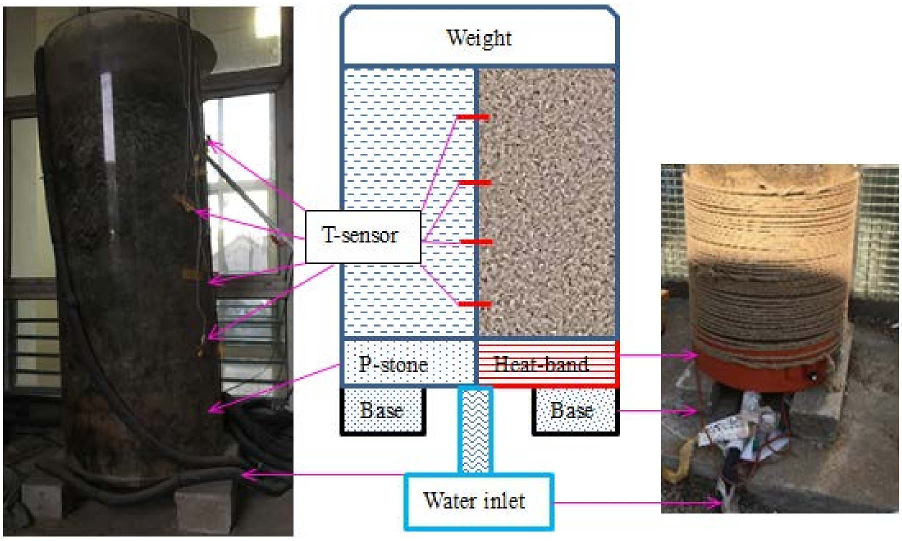

Figure 10. CTE and *E* test.

As shown in Figure 10, in this study, CTE and E were determined by an in-house test device. Refrigeration was used to ensure utilization of the natural winter environment in the project area, and the soil samples for the test were placed in an acrylic bucket with a diameter of 0.8 m, height of 2 m, and wall thickness of 1 cm. An inlet pipe, with electric and tropical packages to ensure the liquid state of the water, was arranged at the bottom of the bucket. A permeable stone was arranged between the water inlet pipe and the soil sample. The outer cylinder of the permeable stone enclosed an electric heating belt to prevent water from freezing at the site. The upper part of the permeable stone was filled with soil samples, and temperature sensors were embedded in the soil samples. A weight was set on top of the soil sample, and a deformation meter was set on top of the weight to observe the frost heave deformation.

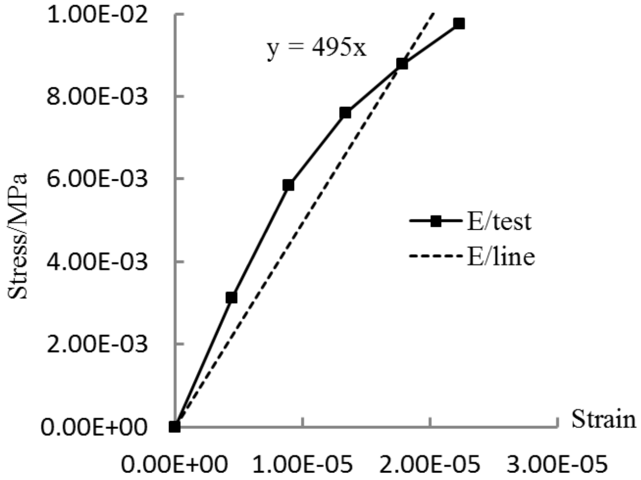

Figure 11. Elastic modulus E of frozen soil.

First, the surface elevation (dL) of the soil sample under the natural environmental condition in winter was observed; when dL stabilizes, it stops supplying liquid water, and CTE is calculated by formula (21). The temperature changes (dT) were measured with thermal sensors simultaneously. Then, the vertical deformation of the soil sample under the gravity of the weight was measured by stacking weights on the soil surface in order to calculate the value of E. The results are shown in Figure 11, the elastic modulus E = 495 MPa of frozen soil, measured with the in-house test device shown in Figure 10.

Assuming that all the frost heaving force is borne by the pre-stressed tendon, the axial force of the tendon is calculated as follows:

$$F = \int_0^D \sigma_{sw} \cdot S dx \,, \tag{23}$$

where S is the area of temperature stress assumed by each tendon and D is the depth of the freezing front of the foundation.

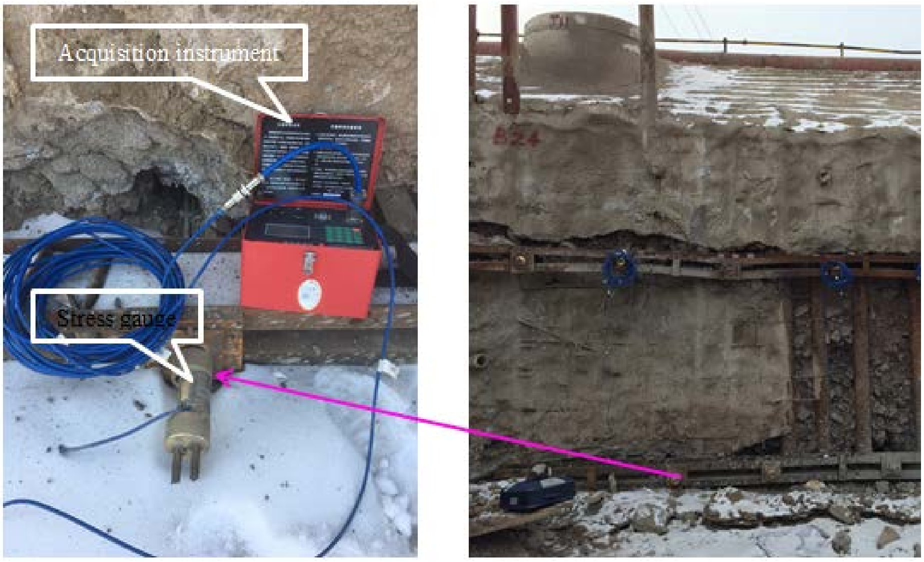

Figure 12. Tendon axle force test.

As shown in Figure 12, the axial force variations of pre-stressed tendons for the temperature stresses of foundation soils were measured using vibrating wire tendon stress gauges (JMZX3102HAT) with a range of 200 kN, sensitivity of 0.1 kN, and accuracy of 0.4 kN. Internally installed semiconductor temperature sensors were used for automatic temperature correction, and the data acquisition instrument (JMZX-3006) produced by Kingmach Measurement & Monitoring Technology Co., Ltd, was used to gather data.

The pre-stressed tendons are two stranded wires, each with a diameter of 15.2 mm and tensile strength of 1860 MPa, with a transverse spacing of 1.2 m and vertical spacing of 2 m. Each pre-stressed tendon resists a foundation pit compressive stress of 2.4 m^2.

The monitoring period of axial force of the pre-stressed tendon was from October 21, 2017 to March 14, 2018, when the initial tension of the anchor cable began. The monitoring frequency was once a week.

3. Results and Discussion

The thermo-physical parameters are summarized in Table 2.

Table 2. Thermo-physical parameters.

λ	c_v	E	ρ	h_{hc}	α
W/(m·K)	J/(kg·m^3)	MPa	kg/m^3	W/(m·K)	1/ K
1.92	1364	495	1.7×10^3	21	21×10^{-6}

The temperature field results of SPPTCFPSS are analyzed using equation (12) and FEM on ABAQUS for relative material variables and boundaries, and the results are shown in Figures 13 and 14.

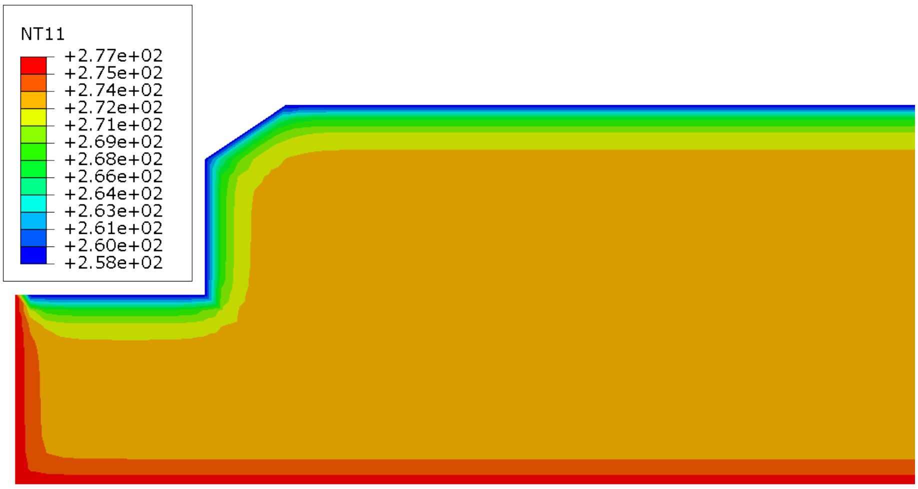

Figure 13. Temperature field in January 2018.

As can be seen from Figure 13, in January 2018, the temperature field of the foundation pit system gradually decreases from 258 K to 277 K along the outer boundary of the foundation to the distance. The boundary temperature is the same as the AT of 258 K, and the severe impact temperature area is within the range of 2 m near the foundation pit boundary, where the temperature quickly dropped to the freezing point of 273 K.

As can be seen from Figure 14, the temperature of the foundation pit system gradually decreases with the increase in depth, and the freezing depth ranges from 1.4 m to 2 m. The above freezing depth level is nonlinear; the freezing depth temperature is also nonlinear. December and January temperatures (accumulated) decrease, the minimum being 258 K, and recovery happens in February, with the lowest temperature being 269 K. As AT drops to zero in November, ground surface temperature from the surface to freezing front gradually decreases; the surface temperature in December fell to 263 K, the frozen depth was 1.8 m, and after that the earth's surface temperature fell down to 258 K in January, and the frozen depth was 2.0 m, simultaneously. At the beginning of February, with the increase in AT, the ground surface temperature increases too, but due to the heat capacity of the foundation, the curve of temperature distribution along the direction of depth exhibits a reverse bending change, showing a trend that the temperature change in the foundation lags behind the temperature change. The changing characteristics of the above temperature space-time curve scientifically reflect the influence of the temperature accumulation effect on the ground temperature field. The ground temperature below the freezing front gradually recovered from zero to 277 K and remained constant.

Temperature stresses according to the theoretically calculated value by equation (21) are shown in Figure 15. They gradually decrease to zero as the freezing front place is reached. The temperature stresses and temperature-field change rule are synergistic from December 2017 to January 2018, and increase gradually, then gradually decrease in February 2018; the maximum value occurs in January with 98 kPa. The above temperature stresses, on the conditions of the foundation pit with semi-infinite fully controlled one-dimensional boundary space, are the premise of the theoretical calculation results. However, as the scheme used here is to allow proper deformation of the support system, the actual temperature fields do not produce so much of the temperature stresses, and the axial force of pre-stressed tendons in the in-situ test and the ideal value from equation (23) are all shown in Figure 16.

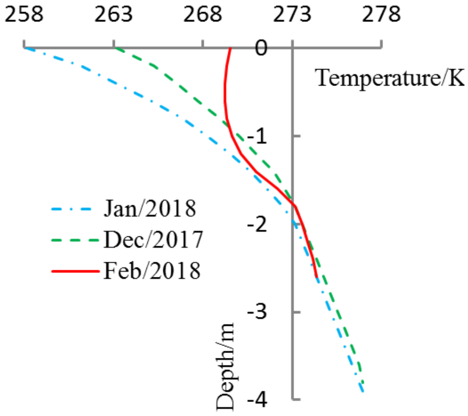

Figure 14. Temperature field.

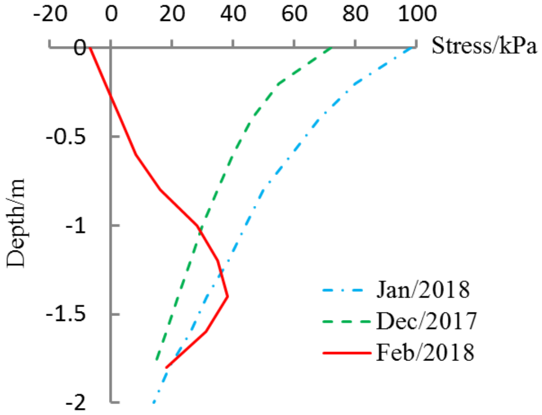

Figure 15. Temperature stresses.

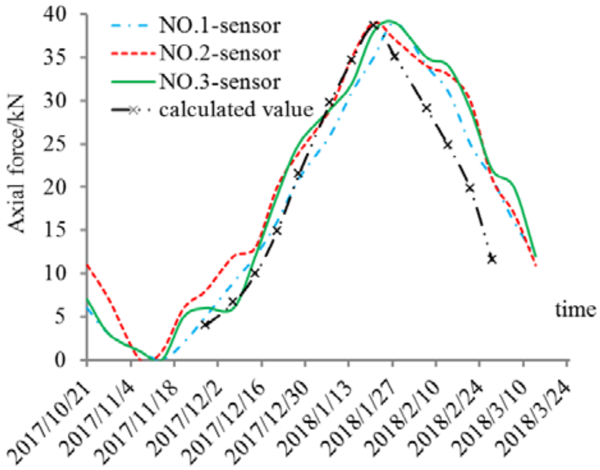

Figure 16. Axial force of pre-stressed tendons in-situ.

The axial force test results show that the three pre-stressed tendons are locked on October 21, 2017. Because of the relaxation of steel strands and anchorage segment of soil consolidation effect, the axial force of pre-stressed tendons fell by 8 kN in mid-November. The frost heaving of the foundation makes the axial force increase gradually in late January 2018 to a peak of 38 kN, with recovery in the middle of March 2018 to 12 kN, as shown in Figure 13. However, according to equation (23), which is used to calculate the frost heaving force value, each pre-stressed tendon gives an axial force of 39 kN, and the actual measured value is 38 kN. Thus, an agreement with theoretical calculation is seen. The temperature stress of the foundation pit soil based on one-dimensional fixed boundary calculation is corrected by the saturation index of soil. Because the foundation soil above the infiltration line is in an unsaturated state after foundation pit dewatering, the effect of saturation on frost heave force should be taken into account when calculating soil frost heave.

4. Conclusions

1. The seepage field including CAZ and SFZ, which is the precondition of foundation pit frost heaving analysis, was analyzed accurately by FEM. Based on the transient heat conduction equation and indoor and outdoor thermo-physical tests, the temperature field of the foundation pit in a seasonal frozen soil area can be accurately calculated. The theoretical calculation of temperature stress based on one-dimensional fixed boundary conditions corrected by saturation index is accurate.

2. The rigid and flexible composite support system composed of pre-stressed tendons and steel pipe piles can effectively resist part of the temperature stress. The deformation of the foundation pit can be partially recovered under the action of pre-stressed tendons when the temperature rises, so this kind of supporting structure is suitable for the foundation pit in a seasonal frozen area.

3. The engineering in-situ monitoring temperature stress data applied to the SPPTCFPSS is approximately equal to the theoretical value of the pit temperature stress, which is calculated based on the one-dimensional fixed boundary conditions and corrected by the saturation index of the unsaturated zone in the foundation pit. Therefore, the calculated value based on the one-dimensional fixed boundary temperature stress can be taken as the design value for the foundation pit support system.

References

1. Ivanov, K.S. Granulated foam-glass ceramics for ground protection against freezing. Magazine of Civil Engineering. 2018. 79(3). Pp. 95–102. DOI: 10.18720/MCE.79.10
2. Zhussupbekov, A., Shakhmov, Z., Tleulenova, G. Geotechnical problems on freezing ground soil and experimental investigation in Kazakhstan. Sciences in Cold and Arid Regions. 2017. No. 3(9). Pp. 331–334.
3. Guo, L., Zhang, Z., Wang, X., Yu, Q., You, Y, Yuan, C., Xie, Y., Gou, T. Stability analysis of transmission tower foundations in permafrost equipped with thermosiphons and vegetation cover on the Qinghai-Tibet Plateau. International Journal of Heat and Mass Transfer. 2018. No. 121. Pp. 367–376.
4. Yu, Q., Ji, Y., Zhang, Z., Wen, Z., Feng, C. Design and research of high voltage transmission lines on the Qinghai–Tibet Plateau–A Special Issue on the Permafrost Power Lines. Cold Regions Science and Technology. 2016. No. 121. Pp. 179–186.
5. Rui, D., Deng, H., Nakamura, D., Yamashita, S., Suzuki, T., Zhao, H. Full-scale model test on prevention of frost heave of L-type retaining wall. Cold Regions Science and Technology. 2016. No. 132. Pp. 89–104.
6. Tretyakova, O.V., Yushkov, B.S. Inverted-cone piles for transport constructions in seasonally freezing soils. Soil Mechanics and Foundation Engineering.2017. No. 3. Pp. 18–21.
7. Zhenya, Liu, Jiankun, Liu, Xu, Li. Experimental study on the volume and strength change of an unsaturated silty clay upon freezing. Cold Regions Science and Technology. 2019.No. 157. Pp. 1–12.
8. Zhang, S., Sheng, D., Zhao, G. Analysis of frost heave mechanisms in a high-speed railway embankment. Canadian Geotechnical Journal. 2016. No. 53. Pp. 520–529.
9. Batenipour, H., Alfaro, M., Kurz, D. Deformations and ground temperatures at a road embankment in northern Canada. Canadian Geotechnical Journal. 2014. No. 51. Pp. 260–271.
10. Zheng, H., Kanie, S., Niu, F. The thermal regime evaluation of high-speed railway foundation by mixed hybrid FEM. Cold Regions Science and Technology. 2018. No. 155.Pp. 333–342.
11. Nishimura, S., Gens, A., Olivella, S. THM-coupled finite element analysis of frozen soil: formulation and application. Ge´otechnique. 2009. 59(3). Pp. 159–171.
12. Lackner, R., Amon, A., Lagger, H. Artificial ground freezing of fully saturated soil: thermal problem. Journal of Engineering Mechanics. 2005. 131(2). Pp. 211–220.
13. Kong, Q., Wang, R., Song, G. Monitoring the soil freeze-thaw process using piezoceramic-based smart aggregate. Journal of Cold Regions Engineering. 2014. 28(2). Pp. 1–16.
14. Crandell, J.H. Below-ground performance of rigid polystyrene foam insulation: review of effective thermal resistivity values used in ASCE standard 32-01–design and construction of frost-protected shallow foundations. Journal of Cold Regions Engineering. 2010. 24(2). Pp. 35–53.
15. Liu, Z., Yu, X., Sun, Y. Formulation and characterization of freezing saturated soils. Journal of Cold Regions Engineering. 2013. 27(2). Pp. 94–107.
16. Zhang, M., Guo, C., Yu, B., etc. CTCP temperature fields and stresses. International Journal of Pavement Research and Technology. 2017. No. 3(3). Pp.553–562.
17. Chen, J.-Q., Li, L., Zhao, L.-H., Dan, H.-C., Yao, H. Solution of pavement temperature field in “Environment-Surface” system through Green’s function. Journal of Central South University. 2014. 21(5). Pp. 2108–2116.
18. Tretiakova, O.V. Normal stresses of frost heaving as function of excess moisture. Magazine of Civil Engineering. 2017. 76(8). Pp. 130–139. DOI: 10.18720/MCE.76.12
19. Ghoreishian Amiri, S.A., Grimstad, G., Kadivar, M. Constitutive model for rate-independent behavior of saturated frozen soils. Canadian Geotechnical Journal. 2016. No. 53. Pp. 95–102.
20. Scott Crowther, G. Lateral pile analysis frozen soil strength criteria. Journal of Cold Regions Engineering. 2015. 29(2). Pp. 11–23.
21. Shelman, A., Tantalla, J., Sritharan, S. Characterization of seasonally frozen soils for seismic design of foundations. Journal of Geotechnical and Geoenvironmental Engineering. 2014. No. 140(7). Pp. 1–11.

Contacts:

Guo Chao, 86-24-24692693; guochaoglovel@126.com
Zhengran Lu, 86-24-24692693; luzhengranglovel@126.com

Magazine of Civil Engineering. 2019. 86(2). Pp. 72–82
Инженерно-строительный журнал. 2019. № 2(86). С. 72–82

Magazine of Civil Engineering

ISSN 2071-0305

journal homepage: http://engstroy.spbstu.ru/

DOI: 10.18720/MCE.86.7

Stress distribution in ash and slag mixtures

A.A. Lunev*, V.V. Sirotyuk,
Siberian State Automobile and Highway University, Omsk, Russia
** E-mail: lunev.al.al@gmail.com*

Keywords: construction; coal ash; ash and slag mixture (ASM); mathematical modeling.

Abstract. In the design of roads, a number of engineering tasks that requires determining the stress state of the road structure are solved: estimating the stability of the embankment, calculating the load resistance, predicting deformations, determining the loads affecting on the culverts and communication lines in the body of the roadbed, etc. The solution of these tasks in the design of ash and slag mixture embankments cannot be performed due to the insufficient knowledge of the stress state formation mechanisms in similar solids. The article reviews and compares theoretical solutions for predicting stresses in a continuous and granular environment arising in the body under the flat plate effect on its surface. The tests were carried out on a solid with a compaction coefficient (0.95), with five values of humidity (from 22 to 38 % by weight). The results of experimental studies on the change in pressure arising in the ASM at different depths, when exposed to the vertical load from the stamp, are presented. The value of the shear resistance to increase by 21 % with an increase in moisture content from 22 % to 28 %, and with further growth returned to almost the original values without any visible effect on the stress distribution. Conclusions about the insignificant effect of humidity on the stress distribution in the ASM were drawn (at least under the chosen experimental conditions). Estimates of mathematical models for stress prediction in relation to the bulk body from the ash and slag mixture are given. To determine the distribution environment coefficient in the Fröhlich model, a correlation dependence between the CBR and the modulus of elasticity was derived. This correlation allowed us to link the theoretical solutions of Gonzalez and earlier experiments on the evaluation of the modulus of elasticity of embankments from ASM at different humidity with the stresses distribution.

1. Introduction

When designing roads, a number of engineering tasks are solved that requires determining the stress state of the road structure: estimating the stability of the embankment, calculating the load stability, predicting deformations, determining the loads acting on the culverts and communication lines in the embankment body, etc. In Russia and abroad, the use of man-made soils, industrial wastes and coal ash from the dumps of thermal power plants for the construction of embankments, in particular, planning embankments, etc. is becoming increasingly important. However, the verification of the stability of such structures cannot be performed with adequate accuracy due to the insufficient knowledge of the formation mechanisms of the stress state in such solids.

The studies in the field of stress state prediction have been carried out by a number of researchers, but mainly they relate to natural soils or abstract granular materials. Therefore, the solution of these tasks is complicated due to the insufficient knowledge of the mechanical characteristics of ash and slag mixture and the formation mechanism of the stress state in similar solids with a special structure, significantly different from natural soils.

In contrast to the first classical solutions for predicting the stressed soil state under the influence of an external load (Boussinesq, Flaman, Mitchell, Das, etc.) [1–3], modern concepts of the stressed

Lunev, A.A., Sirotyuk, V.V. Stress distribution in ash and slag mixtures. Magazine of Civil Engineering. 2019. 86(2). Pp. 72–82. DOI: 10.18720/MCE.86.7.

Лунёв А.А., Сиротюк В.В. Распределение напряжений в массиве из золошлаковой смеси // Инженерно-строительный журнал. 2019. № 2(86). С. 72–82. DOI: 10.18720/MCE.86.7

state formation take into account the difference in the structure of different soil types and the body state influence on stress distribution (structure influence is confirmed Beringer′s, Santamarine′s, Tadanaga′s Clarke′s experiments) [4–7]. Depending on the soil type, solutions of continuum mechanics or mechanics of granular materials are usually applied. In both cases, taking into account the different soil behavior, either distributive environment capacity coefficients are introduced into the solution, which is a numerical stress distribution characteristic, or the difference in mechanical parameters is taken into account.

In the continuous environment mechanics, the solutions involving distribution Fröhlich′s environment capacity coefficients are mainly used for stress prediction [8, 9]. Also, within structural mechanics framework, engineering approximations and theories based on certain angle presence of the environment distributive capacity (Piskunov, Timoshenko, Matveev, Klein) are sometimes used [10–14]. These theories are mostly developed to describe the quasi-flat environment behavior (soils with a finely dispersed structure), which, fine-grained ash and slag mixture can be attributed to (according to the granulometric composition analysis) [15, 16].

I.I. Kandaurov developed mechanics of granular materials (MGM) in contrast to the continuous environment mechanics, where individual particles are the object of investigation, the interaction between which is predicted on the basis of probability theory methods [17]. Unlike the basic formulas for continuous environment mechanics, the MGM initially took into account the difference in particles interaction by the environment coefficient distribution (Kandaurov). A priori, we believe that the granular environment mechanics laws can also be applied to the ash and slag mixture, since the shape and features of the contact pressure transfer between the ash and slag mixture particles are similar to the fine sands that are the description object of the MGM [17–19].

The use of the distribution environment coefficients allows application of the same solutions for different soils by changing this coefficient value. The distribution environment coefficients, as a rule, should be determined from stress-strain experiments, but such studies are complex and expensive. Therefore, a number of researchers (Alexandrov, Gonzalez, Muller, Matveev, and others) attempted to relate the stress distribution mechanism to soil parameters determined in the laboratory [9, 11, 20].

So Gonzalez linked Frohlich′s parameter and the main parameter used for the road structures design in Western countries – the California bearing ratio (CBR). Empirical relationships connecting these quantities are presented in the form of formulas:

$$n = 2 \cdot \left(\frac{CBR}{6}\right)^{0.337}, \quad n = 2 \cdot \left(\frac{CBR}{6}\right)^{0.1912}, \tag{1, 2}$$

where n is the stress distribution coefficient introduced by Fröhlich;

CBR is the California bearing capacity rate, %.

Analyzing Kandaurov′s work and developing them, Muller found a relationship between the coefficient of lateral pressure ζ and the coefficient of the distributive environment capacity v_p:

$$\xi = \frac{1}{8 \cdot v_p}. \tag{3}$$

In soil mechanics, lateral pressure coefficient determination, as a rule, requires complex tests. At the same time, there are dependencies deduced for the lateral pressure coefficient calculating through the internal friction angle φ. We also know our own solutions for determining the distribution environment coefficient. A number of mathematical models are presented in Table 1 [21–25].

The presented formulas make it possible to determine the environment distributional capacity coefficient based on the material parameters, but there is no data on the applicability of any solution for the entire variety of man-made soils (for example, for the ash and slag mixture) in the sources. It is not known which of the formulas for a solid or granular environment gives greater accuracy when estimating the stress state in the ash and slag mixture body. For this reason, the article conducts experimental verification of existing solutions.

Table 1. Formulas associated with the internal friction angle.

Authors	Determining coefficient formula	
	lateral pressure	Environment distribution capacity
J. Biarez and co-authors	$\xi = \dfrac{1-\sin\varphi}{1+\sin\varphi}$	$\nu_p = \dfrac{1+\sin\varphi}{8(1-\sin\varphi)}$
M.D. Bolton	$\xi = \dfrac{1-\sin(\varphi-11.5)}{1+\sin(\varphi-11.5)}$	$\nu_p = \dfrac{1+\sin(\varphi-11.5)}{8-8\sin(\varphi-11.5)}$
Brooker-Ireland	$\xi = 0.95-\sin\varphi$	$\nu_p = \dfrac{1}{7.6-8\sin\varphi}$
R.Ya. Popilsky and co-authors	$\xi = \mathrm{tg}^2\left[\dfrac{\pi}{4}-\dfrac{\varphi}{2}\right]$	$\nu_p = \left(8\,\mathrm{tg}^2\left[\dfrac{\pi}{4}-\dfrac{\varphi}{2}\right]\right)^{-1}$
Mayne-Kulhawy	$\xi = 1-0.998\sin\varphi$	$\nu_p = \left(8(1-0.998\sin\varphi)\right)^{-1}$
G.I. Pokrovsky	$\xi = 1-0.74\,\mathrm{tg}\varphi$	$\nu_p = \left(8(1-0.74\sin\varphi)\right)^{-1}$
Badanin and co-authors	–	$\nu_p = \mathrm{ctg}(\varphi+45°)$

2. Methods

To evaluate the most adequately describing the stress ash and slag mixture body state mathematical models, experimental studies were performed using original strain gauges located at different body depths. Body pressure along the flat plate axis is measured by vertical load. The prediction of the stresses values at the sensor position depth was carried out according to the coupling formulas presented above, based on the ash and slag mixture parameters, given in the paper [26].

An analogue of pressure sensors (pressure cells) constructed on the basis of liquid level sensors Piezus APZ 2422 (Figure 1) was used to determine the stresses (pressure measurements).

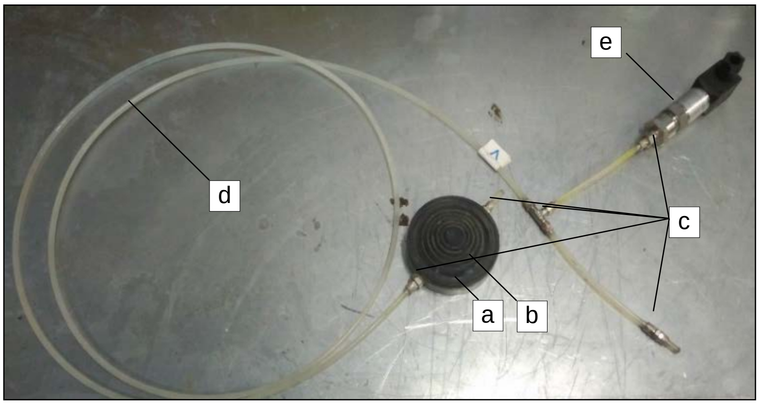

Figure 1. Soil pressure sensor (pressure cell) based on a Piezus APZ 2422 level sensor: a – metal chamber; b – rubber membrane; c – fittings made of nickel-plated brass; d – polyamide tubes; e – liquid level sensor Piezus APZ 2422.

Each pressure sensor is a closed system, filled with multigrade oil hydraulic thickened consisting of the following elements: an all-metal chamber with diameter of 82 mm, height of 18 mm; membrane Rm-L-Nd82 mm made of oil-resistant rubber (used to transfer pressures in ultra-sensitive environment separators); fittings with union nut for hydraulic systems of nickel-plated brass; tubes with an inner diameter of 3 mm and a wall thickness of 1 mm made of polyamide PA 12 Rilsan for transferring pressures up to 40 Bar; level sensor Piezus APZ 2422 with a measuring limit of 6 bar. The connection between the membrane and the chamber is carried out using a mixture for cold cure NILOS TL-T70 TOPGUM.

To obtain readings from the sensors (output signal 4–20 mA), the TRM-1-SHCH11.U.I. measuring instrument-regulator with built-in 12 V power supply, necessary for level sensors, was used. Before installation in the body, the sensors were calibrated in a universal test machine IR 5081-5.

To carry out the experiment, the laboratory tray was filled with the ash and slag mixture in layers, moistened to optimum moisture and compacted to a seal factor of 0.95. The lower layer had thickness of 15 cm. The subsequent layers were stacked according to the same algorithm, but with thickness of 7–8 cm. After preparing each layer, a laser level was set on it, which was directed along the marks to the design sensor position. The sensor positioning is shown in Figure 2.

Figure 2. Sensor positioning in the ash and slag mixture body.

The height sensor position was monitored using a level. In the center of the sensor, a rack was installed and a height mark was taken relative to the reference point. After that, a manual backfill was carried out with the tamping of the ash and slag mixture around the sensor. Three pressure sensors were laid in depth. The pressure was created by means of a hydraulic press stamp with diameter of 33 cm. The force produced by the plate was measured by an electronic dynamometer. Stamping to the installation site (along the sensor axis) was carried out using the laser level, which was used for sensor stacking (Figure 3).

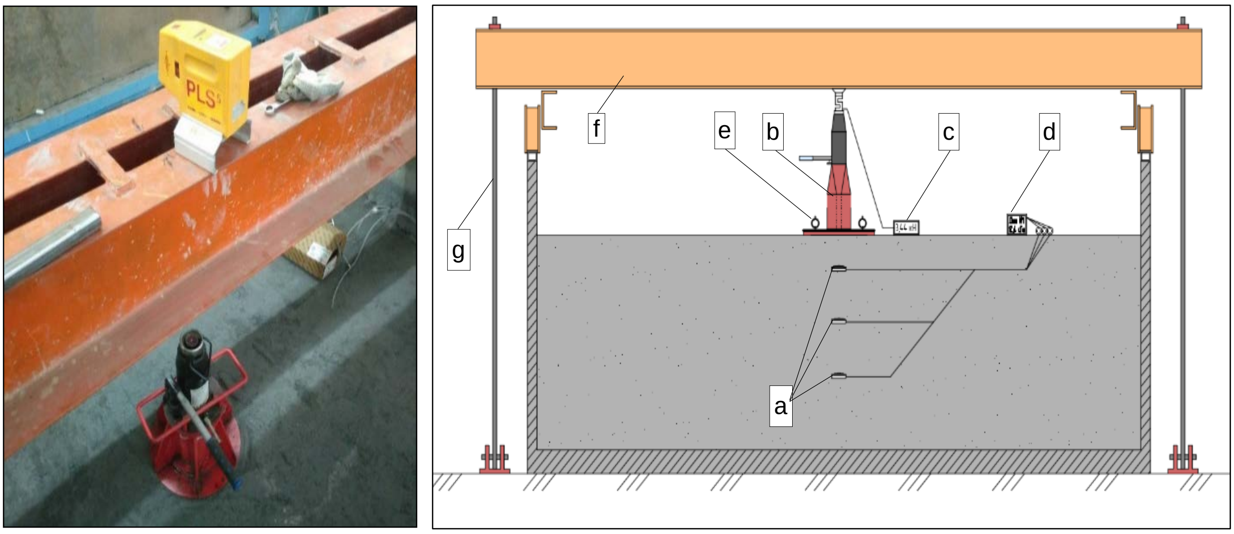

Figure 3. Placement of measuring equipment and a test stamp:
on the left – stamp positioning; on the right – equipment layout.
a – pressure sensors; b – press stamp; c – force gauge; d – measuring instrument-regulator;
e – displacement indicators; f – resistant system; g – anchor rod.

The rigid plate was successively loaded to a pressure of 50, 100, 150 and 200 kPa. The choice of the maximum pressure of 200 kPa is assigned to the known maximum voltage transmitted to the subgrade surface. After reaching the required pressure, a cascade plate discharge was carried out to 100, 50 and 1 kPa. Further, the stamp was re-loaded and unloaded, similarly to the first cycle. During the tests at each stage, movements along the displacement indicators mounted on the opposite edges of the stamp and the forces created by loading the die were measured.

After the test cycle, the body was hydrated, the calculated humidification step was 3 % for mom in the first three points and 5 % for the last two. Water was distributed through a watering gun with the function of watering can. The amount of water supplied to the ash and slag mixture body was monitored by the electronic digital water meter. Additional moisture control was carried out by sampling in layers along the body depth.

A number of test cycles were performed at a moisture content of 22 %, 25 %, 28 %, 33 % and 38 % by mass (corresponding to relative humidity values of 0.58, 0.68, 0.74, 0.87, 1.00).

In addition to the stressed state study, after each test cycle, the modulus of elasticity at different ash and slag mixture humidity was calculated. The need to determine the elasticity modulus is due to the fact that this indicator is the main parameter for the roadbed and road clothes bearing capacity calculating in the Russian Federation. In addition, according to research by Heukelom and C.R. Foster, W. Heukelom and A.J.G. Klomp Green and Hall, Witczak and Powell et. al Putri et. al, the elasticity modulus and CBR have a direct functional connection. This mathematical connection was established by us for fine-grained ash and slag mixture for the first time [27, 30].

To compare to the experimental data, theoretical solutions for determining the main maximum stresses along the circular plate axis are chosen: Kandaurov, Harr, Olson, Timoshenko, Piskunov and Matveev (Table 2).

Table 2. theoretical solutions for main maximum stresses determining along round plate axis.

Authors	*Determining formula*
I.I. Kandaurov	$\sigma_z = p\left[1-\exp\left(\frac{-R^2}{2z^2\nu}\right)\right]$
M. Harr	$\sigma_z = p\left[1-\exp\left(\frac{-4R^2\nu_p}{z^2}\right)\right]$
R. Olson	$\sigma_z = p\left[1-\frac{a^n}{\left(1+a^2\right)^{n/2}}\right], \quad \sigma_z = p\cdot\left[1-\left(\frac{z^n}{R^2+z^2}\right)^{\frac{n}{2}}\right]$
V.G. Piskunov, N.N. Ivanov	$\sigma_z = B\cdot\exp\left(-\gamma z\right)$
G.K. Klein	$\sigma_z = p\cdot\left(1+\frac{2\cdot z}{D_o}\cdot\mathrm{tg}\ f(\varphi)\right)^{-2}$
S.A. Matveyev (modified)	$\sigma_z = p\cdot\left[\exp\left(\nu\left\{1-\gamma z\right\}\right)\right]^{(1-\nu)}$
where p is pressure value on circular punch sole, MPa; z is point depth along stamp axis where the stress is determined, m; R is plate radius, m; λ is Kandaurov′s environment distribution capacity coefficient λ is Hara′s environment distribution coefficient; γ is attenuation coefficient; n is Frohlich′s environment distribution coefficient; D_o is plate diameter, m; $f(\varphi)$ is internal friction angle function, numerically equal to natural slope angle, deg.	

To compare the experimental and theoretical data, Gonzalez′s formulas were used to determine Frohlich′s distribution environment coefficient, which is part of Olson′s formula. The transition to CBR was carried out through the previously obtained empirical formula:

$$CBR = 0.57\cdot E^{0,922}, \tag{4}$$

where CBR is the California bearing capacity rate, %;

E is elasticity modulus, MPa.

An analysis using the mechanics of granular materials formulas (Kandaurov, Harr) was carried out using Muller′s formula to determine Hara′s distribution environment coefficient through the lateral pressure coefficient. The lateral pressure coefficient was determined through the internal friction angle according to the dependences developed by Biares, Bolton, Jaky, and others (Table 1) [21–25].

Comparison of the experimental data and the values predicted on Piskunov′s approximation basis was carried out by using the same dependences for lateral pressure coefficient determining (the attenuation coefficient is related to the lateral pressure coefficient) as for mechanics of granular materials solutions (Table 2).

Comparison with *Klein's* formula was conditional, since there is no data on the friction angle function form in his formula. For this reason, the comparison was carried out only to evaluate the possibility of stress shape and values describing when selecting this function value.

3. Results and Discussion

According to the provisions given earlier, and formulas (4), CBR variation patterns and elasticity modulus from humidity have similar values. Consequently, in stress state prediction using Olson′s formula with Fröhlich′s environment distribution capacity coefficient, found on Gonzalez′s theory basis, elasticity modulus has a significant effect. Elasticity modulus dependence on humidity is shown in Figure 4 [26].

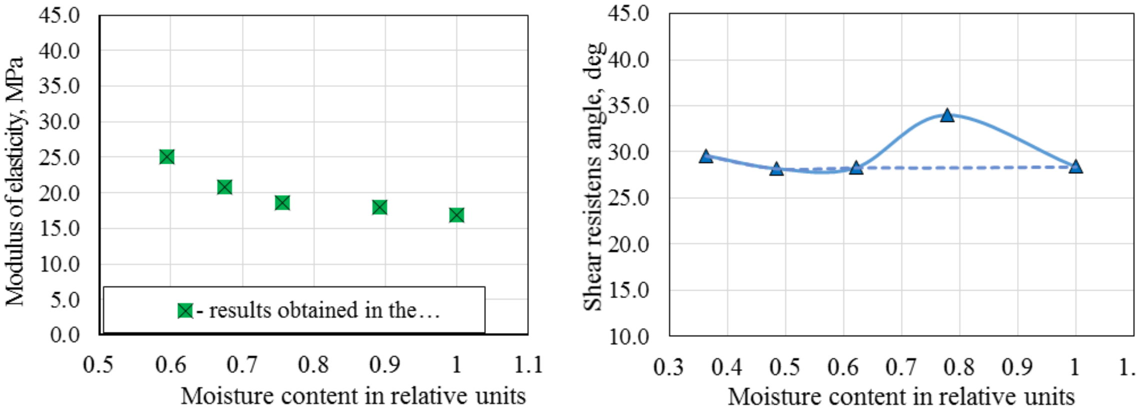

Figure 4. Ash and slag mixture parameters changing with humidity change.

You can notice a significant decrease in elasticity modulus when the body is moistened, which should seriously affect the stress distribution according to *Gonzalez's* theory. However, almost identical stress distributions were noted for almost all ash and slag mixture moisture content values in an experimental study (Figure 5).

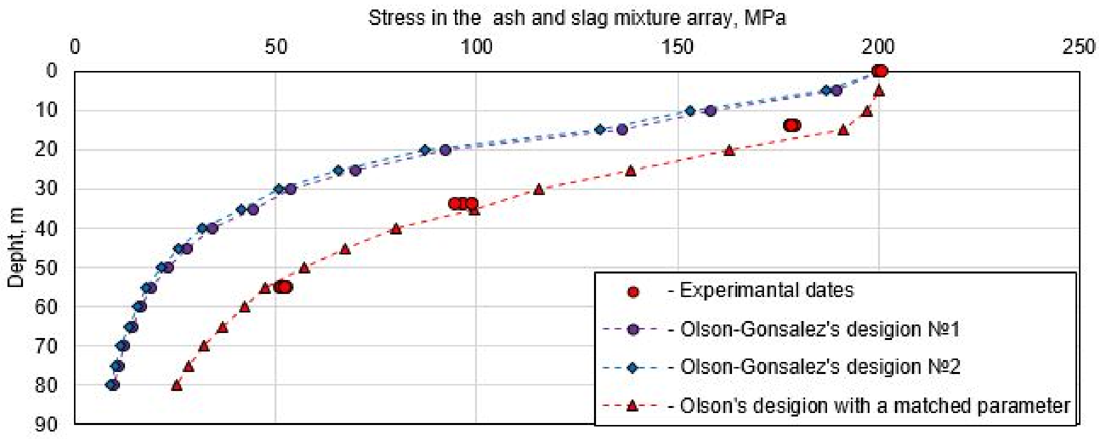

Figure 5. Stress distribution comparison according to Olson's formula and experimental data.

An attempt to describe the stress distribution using Olson's solution, formulas (1) and (2), showed the unsuitability (the approximation error amounted to 26.2 % and 27.8 %, respectively). In the rest, Olson's formula, when selecting the parameter (n = 6.5), describes the experimental data with an average approximation error (3.7 %). At the same time, when predicting a stress state according to mechanics of granular materials theory and Klein's formula, the stress distribution mainly depends on internal friction angle. Internal friction angle for the ash and slag mixture investigation basically depends on compaction degree and much less on the moisture material content.

Although in Figure 4 there is a significant increase in resistance angle to shear (internal friction angle), it is not a true physical friction angle. Apparently, its increase at the optimum humidity is caused by an increase in water films retention forces (capillary connectivity effect), which even more increased the shear resistance with increasing vertical load and particles approaching.

In the range of humidity values chosen for the experiment, internal friction angle (if the effect of the retaining water films was not taken into account) varied by only 1 %. That practically does not affect stress values arising in the body.

Among the dependencies presented above (see Table 2), there are those in which relationship forms between the parameters have already been proposed (Matveev), or are unclear (Piskunov), or are not completely defined (Klein). However, it is also relevant to evaluate stress distribution form in them and to compare it with the experimental data. Engineering methods comparison with experimental data is presented in Figure 6.

The analysis showed with the greatest approximation, by choosing the damping parameter, Piskunov's solution gave an error of approximation of 5.8 %. Function value choice for proposed by Klein dependence, namely $f(x)$, gave the approximation error of 3.7 % with the best approximation, as was Olson′s solution in Fröhlich′s modification. Matveev's solution (modified), when calculated with lateral pressure coefficient substitution from the experimental data [26], gives an error of 4.9 % approximation.

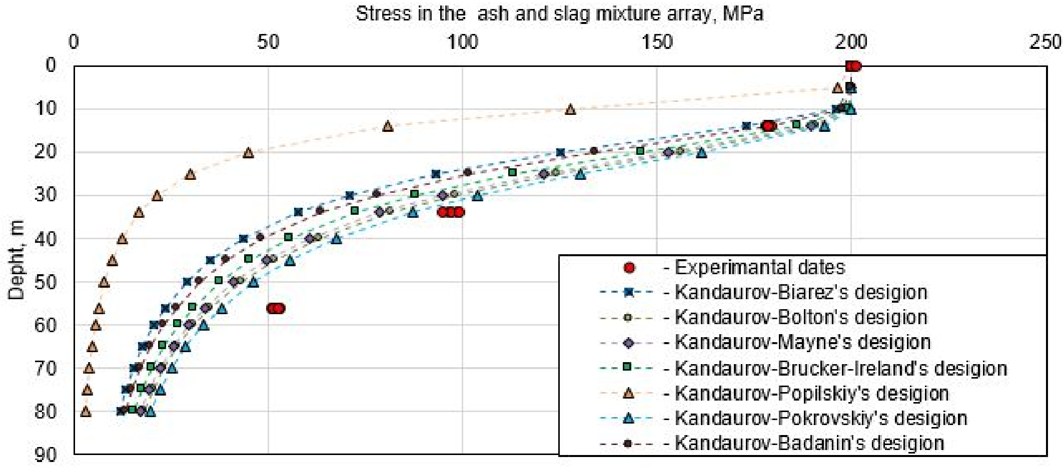

Figure 6. Stress distribution comparison by engineering solutions and experimental data

Experimental data comparison was carried out the same with mechanics of granular materials solutions. Comparison with Kandaurov's decision, in which environment distribution capacity coefficient determination was carried out through internal friction angle based on the dependencies of Table 1, is shown in Figure 7.

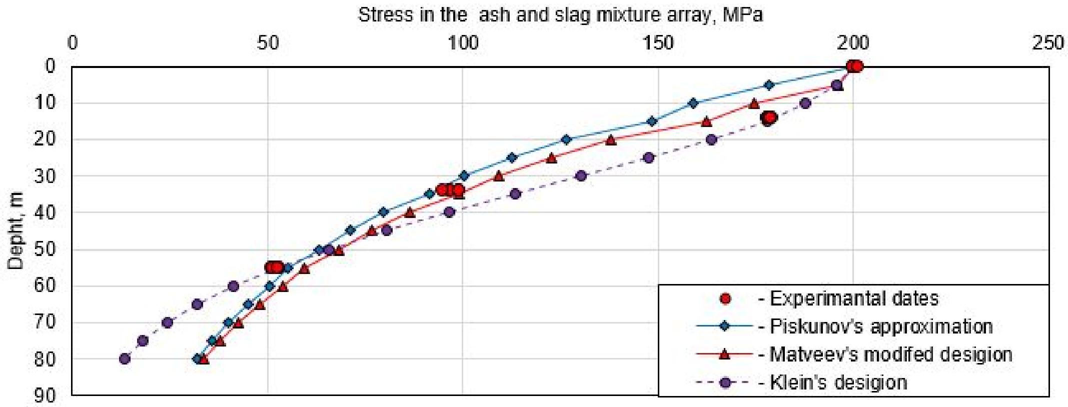

Figure 7. Stress distribution in the ash and slag mixture body by MGM solutions and experimental data.

The greatest approximation in comparison with the experimental data was given by the formula for determining Pokrovsky′s distribution ability coefficient, the approximation error for it was 9.2 %. Popilsky's dependence has the lowest accuracy, the approximation error for which was 45.1 %. All other dependencies are between the error values of 11 % to 20 %.

Kandaurov′s solution greatest accuracy, achieved when selecting environment distribution capacity parameter (0.15) is 5.3 %. Although Kandaurov's solution can describe the stress distribution in the ash and slag mixture, it has less accuracy than Olson's solution. Moreover, when using the Muller′s formula for the transition to Hara′s distribution environment coefficient, distribution values turn out to be identical to the Kandaurov′s solution.

4. Conclusion

The following learning points emerged from the findings of the study.

1. Stress distribution in the body from the investigated ash and slag mixture (at the boundary experiment values) is almost independent of this technogenic soil humidity.

2. The formulas proposed by Gonzalez to determine Frohlich′s distribution environment coefficient proved to be unsuitable for predicting stress distribution in fine-grained ash and slag mixture body.

3. It is established that the solution, expressed for a continuous environment (Olson) by selecting Frohlich′s parameter, gives the most accurate results for stress state prediction in the ash and slag mixture body among all the investigated dependencies (3.7 % approximation error). However, due to the limited data, it is not possible to identify the relationship between the ash and slag mixture parameters and the value of the Fröhlich′s parameter (at this stage of the study).

4. Engineering approximations of the experimental data (Piskunov, Matveev) gave satisfactory results, but even when substituting the lateral pressure coefficient obtained from laboratory tests, their accuracy was less than Olson's solution.

5. The formula proposed by Klein (as well as the Olson′s solution) gives a high approximation accuracy, but, unlike continuous environment mechanics solution, it allows us to predict only the maximum values of the principal stresses under circular plate axis.

6. Mechanics of granular materials solutions (using Jaky′s, Bolton′s, Brucker-Ireland′s, Mayne-Kulhawy′s, Popilsky′s and Pokrovsky′s dependencies) showed a lower accuracy of forecasts than the continuous environment mechanics solutions with parameter selection. However, when choosing a parameter, experimental values approximation by Kandurov's solution gives quite acceptable results with an average error of 5.3 %.

In future, it is planned to conduct a series of similar studies with different solid densities of ash and slag mixture. It will help to predict the stress state in the layers of solids and embankments made of the man-made soils more exact.

References

1. Podio-Guidugli, P., Favata, A. The Boussinesq Problem. Elasticity for Geotechnicians. 2014. Vol. 204. Pp. 79–114. DOI: https://doi.org/10.1007/978-3-319-01258-2_5
2. Ding, D. General model for the approximate calculation of elastic-bed settlements. Soil Mechanics and Foundation Engineering. 1995. Vol. 32. No. 2. Pp. 47–52. DOI: https://doi.org/10.1007/BF02336387
3. Szeidl, G., Van, Gemert D. On Mitchell conditions for plane problems in elastostatics. Acta Mechanica. 1992. Vol. 93. No. 1–4. Pp. 99–118. DOI: https://doi.org/10.1007/BF01182576
4. Behringer, R.P. Jamming in granular materials. Comptes Rendus Physique. 2015. Vol. 16. Pp. 10–25. DOI: 10.1016/j.crhy.2015.02.001
5. Santamarina, J.C. Soil Behavior at the Microscale: Particle Forces. Proc. Symp. Soil Behavior and Soft Ground Construction, in honor of Charles C. Ladd, Boston, USA. 2001. Pp. 1–32. DOI: https://doi.org/10.1061/40659(2003)2
6. Tadanaga, T., Clark, A.H., Majmudar, T., Kondic, L. Granular response to impact: Topology of the force networks. Phys. Rev. 2018. Vol. E 97. No. 012906. DOI: 10.1103/PhysRevE.97.012906.
7. Clark, A.H., Petersen, A.J., Kondic, L., Behringer, R.P. Nonlinear Force Propagation During Granular Impact. Phys. Rev. Lett. 2015. Vol. 114. No. 144502. DOI: https://doi.org/10.1103/PhysRevLett.114.144502
8. Bianchini, A. Fröhlich Theory-Based Approach for Analysis of Stress Distribution in a Layered System: case Study. Transportation Research Record Journal of the Transportation Research Board. 2014. Vol. 2462. Pp. 61–67. DOI: https://doi.org/10.3141/2462-08
9. Aleksandrov, A.S., Dolgikh, G.V., Kalinin, A.L. Improvement of shear strength design of a road structure. Part 2. Modified models to calculate the principal and shear stresses. Magazine of Civil Engineering. 2016. No. 2. Pp. 51–68. DOI: 10.5862/MCE.62.6
10. Shapiro, D.M. Analiticheskij i chislennyj linejnye raschety osnovanij fundamentov melkogo zalozheniya [Analytical and numerical linear calculations of shallow foundations bases]. PNRPU Mechanics Bulletin. 2015. No. 4. Pp. 5–18. DOI: 10.15593/2224-9826/2015.4.01 (rus)
11. Matveev, S.A. Litvinov, N.N. Petrov, R.E. Regularites of tension distribution in the interaeconomic highways soil base. Vestnik Omskogo GAU. 2017. Vol. 28. No. 4. Pp. 233–239. (rus)
12. Proshunin, Y.E. Calculation of stress field in immovable layer of loose material. Journal of Mining Science. 2004. Vol. 40. No. 5. Pp. 482–489. DOI: https://doi.org/10.1007/s10913-005-0033-0
13. Bajare, D., Bumanis, G., Upeniece, L. Coal Combustion Bottom Ash as Microfiller with Pozzolanic Properties for Traditional Concrete. Procedia Engineering. 2013. Vol. 57. Pp. 149–158 DOI: https://doi.org/10.1016/j.proeng.2013.04.022
14. Aleksandrov, A.S., Kalinin, A.L., Tsyguleva, M.V. Distribution capacity of sandy soils reinforced with geosynthetics. Magazine of Civil Engineering. 2016. No. 6. Pp. 35–48. DOI: 10.5862/MCE.66.4
15. Lanzerstorfer, C. Fly ash from coal combustion: Dependence of the concentration of various elements on the particle size. Fuel. 2018. Vol. 228. Pp. 263–271. DOI: https://doi.org/10.1016/j.egyr.2018.10.010
16. Vatin, N.I., Petrosov, D.V., Kalachev, A.I., Lahtinen, P. Use of ashes and ash-and-slag wastes in construction. Magazine of Civil Engineering. 2011. 22(4). Pp. 16–21. DOI: 10.5862/MCE.22.2 (rus)
17. Moshenzhal, A.V. Account of Irregularity in the Stress Distribution along Wood and Concrete Sleepers from a Perspective of Granular Media Mechanics. Procedia Engineering. 2017. Vol. 189. Pp. 637–642. DOI: 10.1016/j.proeng.2017.05.101
18. Beakawi, H.H.M., Baghabra, A.O.S. A review on the angle of repose of granular materials. Powder Technology. 2018. Vol. 330. Pp. 397–417. DOI: https://doi.org/10.1016/j.powtec.2018.02.003
19. Lynn, C.J., Ghataora, G.S., Dhir, R.K. O. Municipal incinerated bottom ash (MIBA) characteristics and potential for use in road pavements. International Journal of Pavement Research and Technology. 2017. Vol. 10. Pp. 185–201. DOI: https://doi.org/10.1016/j.ijprt.2016.12.003
20. Gonzales, C.R. Implementation of a New Flexible Pavement Design Procedure for U.S. Military Airports. Fourth LACCEI International Latin American and Caribbean Conference for Engineering and Technology, Mayagüez, Puerto Rico. 2006. Pp. 1–10.
21. Lee, J., Yun, T.S., Lee, D., Lee, J. Assessment of K0 correlation to strength for granular materials. Soils and Foundations. 2013. Vol. 53. No. 4. Pp. 584–595. DOI: https://doi.org/10.1016/j.sandf.2013.06.009
22. Federico, A., Elia, G. At-rest earth pressure coefficient and Poisson’s ratio in normally consolidated soils. Proceedings of the 17th International Conference on Soil Mechanics and Geotechnical Engineering, Alexandria, Egypt. 2009. Pp. 7–10. DOI: 10.3233/978-1-60750-031-5-7.
23. Brooker, E.W., Ireland, H.O. Earth Pressures at Rest Related to Stress History. Canadian Geotechnical Journal. 1965. No. 2(1). Pp. 1–15. DOI: https://doi.org/10.1139/t65-001
24. Mayne, P.W., Kulhawy, F.H. K0–OCR relationships in soil. Journal of the Geotechnical Engineering Division. 1982. No. 6. Pp. 851–872. DOI: 10.1016/0148-9062(83)91623-6

25. Badanin, A.N., Bugrov, A.K., Krotov, A.V. The determination of the first critical load on particulate medium of sandy loam foundation. Magazine of Civil Engineering. 2012. 35(9). Pp. 29–34. DOI: 10.5862/MCE.35.4. (rus)

26. Sirotyuk, V.V., Lunev, A.A. Strength and deformation characteristics of ash and slag mixture. Magazine of Civil Engineering. 2017. 74(6). Pp. 3–16. DOI: 10.18720/MCE.74.1.

27. Dione, A., Fall, M., Bertraud, Y., Benboudjema, F., Michou, A. Implementation of Resilient Modulus – CBR relationship in Mechanistic Empirical (M. -E) Pavement Design. Cames. 2014. Vol. 1. Pp. 65–71 [Online]. URL: http://publication.lecames.org/index.php/ing/article/view/358/240 (Accessed: 24.01.2019).

28. Zapata, C., Matthew, W., Witczak, W., Palanivelu, T.P. Evaluation of the Federal Aviation Administration methodology for characterizing the nonlinear behavior of granular base and subbase materials. Transportation Geotechnics. 2017. Vol. 13. Pp. 13–27. DOI: https://doi.org/10.1016/j.trgeo.2017.06.004

29. Pereira, P., Pais, J. Main flexible pavement and mix design methods in Europe and challenges for the development of an European method. Journal of Traffic and Transportation Engineering. 2017. Vol. 4. No. 4. Pp. 316–346. DOI: https://doi.org/10.1016/j.jtte.2017.06.001.

30. Putri, E.E., Kameswara, N.S.V.R., Mannan, M.A. Evaluation of Modulus of Elasticity and Modulus of Subgrade Reaction of Soils Using CBR Test. Journal of Civil Engineering Research. 2012. No. 2. Pp. 34–40. DOI: 10.5923/j.jce.20120201.05

Contacts:

Aleksandr Lunev, +79994533930; lunev.al.al@gmail.com
Victor Sirotyuk, +79659800004; sirvv@yandex.ru

Инженерно-строительный журнал

ISSN 2071-0305

сайт журнала: http://engstroy.spbstu.ru/

DOI: 10.18720/MCE.86.7

Распределение напряжений в массиве из золошлаковой смеси

А.А. Лунёв*, В.В. Сиротюк,
Сибирский государственный автомобильно-дорожный университет, г. Омск, Россия
** E-mail: lunev.al.al@gmail.com*

Ключевые слова: строительство; золошлаковая смесь; распределение напряжений; математическое моделирование.

Аннотация. При проектировании автомобильных дорог решается ряд инженерных задач, требующих определения напряженного состояния дорожной конструкции: оценка устойчивости насыпи, расчет сдвигоустойчивости, прогнозирование деформаций, определение нагрузок, действующих на водопропускные сооружения и коммуникации в теле земляного полотна и т. д. Решение этих задач при проектировании насыпей земляного полотна из золошлаковой смеси (ЗШС) не могут выполняться в связи со слабой изученностью механизмов формирования напряженного состояния в подобных массивах. В статье проводится обзор и оценка теоретических решений для прогнозирования напряжений в сплошной и зернистой среде, возникающих в массиве из ЗШС от воздействия на его поверхность нагрузки в виде плоского штампа. Испытания проводили на массиве с коэффициентом уплотнения (0,95), при пяти значениях влажности (от 22 до 38 % по массе). Представлены результаты экспериментальных исследований по изменению давлений, возникающих в ЗШС на разной глубине, при воздействии вертикальной нагрузки от штампа. Величина сопротивления сдвигу возрастала на 21 % при увеличении влажности от 22 % до 28 %, и при дальнейшем росте возвращалась практически до исходных значений без видимого влияния на распределение напряжений. Поэтому сделан выводы о незначительном влиянии влажности на распределение напряжений в ЗШС (по крайней мере при выбранных условиях эксперимента). Даны оценки существующих математических моделей для прогнозирования напряжений применительно к насыпному уплотнённому массиву из ЗШС. Для определения параметров распределительной среды в модели Фрелиха, была выведена корреляционная зависимость между CBR и модулем упругости, которая позволила связать теоретические решения Гонзалеза и более ранние опыты по оценке модуля упругости ЗШС при разной влажности с распределением напряжений.

Литература

1. Podio-Guidugli P., Favata A. The Boussinesq Problem // Elasticity for Geotechnicians. 2014. Vol. 204. Pp. 79–114. DOI: https://doi.org/10.1007/978-3-319-01258-2_5
2. Ding D. General model for the approximate calculation of elastic-bed settlements // Soil Mechanics and Foundation Engineering. 1995. Vol. 32. № 2. Pp. 47–52. DOI: https://doi.org/10.1007/BF02336387
3. Szeidl G., Van Gemert D. On Mitchell conditions for plane problems in elastostatics // Acta Mechanica. 1992. Vol. 93. № 1–4. Pp. 99–118. DOI: https://doi.org/10.1007/BF01182576
4. Behringer R.P. Jamming in granular materials // Comptes Rendus Physique. 2015. Vol. 16. Pp. 10–25. DOI: 10.1016/j.crhy.2015.02.001
5. Santamarina J.C. Soil Behavior at the Microscale: Particle Forces // Proc. Symp. Soil Behavior and Soft Ground Construction, in honor of Charles C. Ladd, Boston, USA. 2001. Pp. 1–32. DOI: https://doi.org/10.1061/40659(2003)2
6. Tadanaga T., Clark A.H., Majmudar T., Kondic L. Granular response to impact: Topology of the force networks // Phys. Rev. 2018. Vol. E 97. No. 012906. DOI: 10.1103/PhysRevE.97.012906.
7. Clark A.H., Petersen A.J., Kondic L., Behringer R.P. Nonlinear Force Propagation During Granular Impact // Phys. Rev. Lett. 2015. Vol. 114. No. 144502. DOI: https://doi.org/10.1103/PhysRevLett.114.144502
8. Bianchini A. Fröhlich Theory-Based Approach for Analysis of Stress Distribution in a Layered System: case Study // Transportation Research Record Journal of the Transportation Research Board. 2014. Vol. 2462. Pp. 61–67. DOI: https://doi.org/10.3141/2462-08
9. Александров А.С., Долгих Г.А., Калинин А.Л. Совершенствование расчета дорожных конструкций по сопротивлению сдвигу. Часть 2. Модифицированные модели расчета главных и касательных напряжений // Инженерно-строительный журнал. 2016. № 2. С. 51–68. DOI: 10.5862/MCE.62.6
10. Шапиро Д.М. Аналитический и численный линейные расчеты оснований фундаментов мелкого заложения // Вестник ПНИПУ. 2015. № 4. С. 5–18. DOI: 10.15593/2224-9826/2015.4.01 УДК 624.131
11. Матвеев С.А., Литвинов Н.Н., Петров Р.Е. Закономерности распределения напряжений в грунтовых основаниях внутрихозяйственных автомобильных дорог // Вестник Омского ГАУ. 2017. № 4. С. 233–239.

12. Proshunin, Y.E. Calculation of stress field in immovable layer of loose material // Journal of Mining Science. 2004. Vol. 40. № 5. Pp. 482–489. DOI: https://doi.org/10.1007/s10913-005-0033-0
13. Bajare D., Bumanis G., Upeniece L. Coal Combustion Bottom Ash as Microfiller with Pozzolanic Properties for Traditional Concrete // Procedia Engineering. 2013. Vol. 57. Pp. 149–158. DOI: https://doi.org/10.1016/j.proeng.2013.04.022
14. Александров А.С., Калинин А.Л., Цыгулева М.В. Распределяющая способность песчаных грунтов, армированных геосинтетикой // Инженерно-строительный журнал. 2016. № 6(66). С. 35–48. DOI: 10.5862/MCE.66.4
15. Lanzerstorfer C. Fly ash from coal combustion: Dependence of the concentration of various elements on the particle size // Fuel. 2018. Vol. 228. Pp. 263–271. DOI: https://doi.org/10.1016/j.egyr.2018.10.010
16. Ватин Н.И., Петросов Д.В., Калачев А.И., Лахтинен П. Применение зол и золошлаковых отходов в строительстве // Инженерно-строительный журнал. 2011. № 4. С. 16–21. DOI: 10.5862/MCE.22.2
17. Moshenzhal A.V. Account of Irregularity in the Stress Distribution along Wood and Concrete Sleepers from a Perspective of Granular Media Mechanics // Procedia Engineering. 2017. Vol. 189. Pp. 637–642. DOI: 10.1016/j.proeng.2017.05.101
18. Beakawi H.H.M., Baghabra A.O.S. A review on the angle of repose of granular materials // Powder Technology. 2018. Vol. 330. Pp. 397–417. DOI: https://doi.org/10.1016/j.powtec.2018.02.003
19. Lynn C.J., Ghataora G.S., Dhir R.K. O. Municipal incinerated bottom ash (MIBA) characteristics and potential for use in road pavements // International Journal of Pavement Research and Technology. 2017. Vol. 10. Pp. 185–201. DOI: https://doi.org/10.1016/j.ijprt.2016.12.003
20. Gonzales C.R. Implementation of a New Flexible Pavement Design Procedure for U.S. Military Airports // Fourth LACCEI International Latin American and Caribbean Conference for Engineering and Technology, Mayagüez, Puerto Rico. 2006. Pp. 1–10.
21. Lee J., Yun T.S., Lee D., Lee J. Assessment of K0 correlation to strength for granular materials // Soils and Foundations. 2013. Vol. 53. № 4. Pp. 584–595. DOI: https://doi.org/10.1016/j.sandf.2013.06.009
22. Federico A., Elia G. At-rest earth pressure coefficient and Poisson's ratio in normally consolidated soils // Proceedings of the 17th International Conference on Soil Mechanics and Geotechnical Engineering, Alexandria, Egypt. 2009. Pp. 7–10. DOI: 10.3233/978-1-60750-031-5-7.
23. Brooker E.W., Ireland H.O. Earth Pressures at Rest Related to Stress History // Canadian Geotechnical Journal. 1965. No. 2(1). Pp. 1–15. DOI: https://doi.org/10.1139/t65-001
24. Mayne P.W., Kulhawy F.H. K0–OCR relationships in soil // Journal of the Geotechnical Engineering Division. 1982. No. 6. Pp. 851–872. DOI: 10.1016/0148-9062(83)91623-6
25. Баданин А.Н., Бугров А.К., Кротов А.В. Обоснование первой критической нагрузки на зернистую среду супесчаного основания // Инженерно-строительный журнал. 2012. № 9 (35). С. 29–34. DOI: 10.5862/MCE.35.4
26. Сиротюк В.В., Лунёв А.А. Прочностные и деформационные характеристики золошлаковой смеси // Инженерно-строительный журнал. 2017. № 6(74). С. 3–16. DOI: 10.18720/MCE.74.1.
27. Dione A., Fall M., Bertraud Y., Benboudjema F., Michou A. Implementation of Resilient Modulus – CBR relationship in Mechanistic Empirical (M. -E) Pavement Design // Cames. 2014. Vol. 1. Pp. 65–71 [Электронный ресурс]. URL: http://publication.lecames.org/index.php/ing/article/view/358/240 (дата обращения: 24.01.2019).
28. Zapata C., Matthew W., Witczak W., Palanivelu T.P. Evaluation of the Federal Aviation Administration methodology for characterizing the nonlinear behavior of granular base and subbase materials // Transportation Geotechnics. 2017. Vol. 13. Pp. 13–27. DOI: https://doi.org/10.1016/j.trgeo.2017.06.004
29. Pereira P., Pais J. Main flexible pavement and mix design methods in Europe and challenges for the development of an European method // Journal of Traffic and Transportation Engineering. 2017. Vol. 4. Issue 4. Pp. 316–346. DOI: https://doi.org/10.1016/j.jtte.2017.06.001.
30. Putri E.E., Kameswara N.S.V.R., Mannan M.A. Evaluation of Modulus of Elasticity and Modulus of Subgrade Reaction of Soils Using CBR Test // Journal of Civil Engineering Research. 2012. No. 2. Pp. 34–40. DOI: 10.5923/j.jce.20120201.05

Контактные данные:

Александр Александрович Лунёв, +7(999)4533930; эл. почта: lunev.al.al@gmail.com
Виктор Владимирович Сиротюк, +7(965)9800004; эл. почта: sirvv@yandex.ru

Magazine of Civil Engineering. 2019. 86(2). Pp. 83–91
Инженерно-строительный журнал. 2019. № 2(86). С. 83–91

Magazine of Civil Engineering

ISSN 2071-0305

journal homepage: http://engstroy.spbstu.ru/

DOI: 10.18720/MCE.86.8

Cracking of tunnel bottom structure influenced by carbonaceous slate stratum

Y. Zhao[a*], Y. Shi[b], J. Yang[a],
[a] Central South University, Changsha City, Hunan Province
[b] Cccc WuHan Harbour Engineering Design And Research Co.Ltd, Wuhan, China
** E-mail: zhaoyiding89@126.com*

Keywords: carbonaceous slate; cracking; tunnel bottom structure; numerical analysis.

Abstract. Constructing tunnel is a difficult and expensive process which deserves special attention. In this article, cracking behavior in a highway tunnel structure during construction period is researched, including figuring out the causes and evolution of crack. Large deformation of rock mass is the major inducement of the damaging behavior, which is obtained from the field investigation. The layers of the ground were monitored with the displacement of tunnel while the numerical analysis was realized with extended finite element method. The results highlight the regions of cracking on tunnel bottom structure, which emphasizes the accuracy of model and the influence of poor geological condition. This work demonstrates that the carbonaceous slate stratum plays an important role in the stability of tunnel structure, which leads to the phenomenon of stress concentration in tunnel bottom region. Moreover, the implemented numerical model also simulates the process of the damaging behaviors of tunnel structure induced by the poor geological condition, which is similar to the results from field investigation and provides the design basis for maintenance work.

1. Introduction

Tunnel is an essential and special underground structure in transportation industry such as highway and railway. Complicated geological condition always brings serious challenges to tunnelling work in the mountainous area [1–2], such as landslide, mud gushing, rock burst, collapse of tunnel face and so on. As reported in previously published literatures, these hazards always lead to instability even failure of the tunnel structure. Especially, cracking is a basic form of lining failure [3–6] from construction period to operational period in tunnel, which is usually caused by different causes [7,8] such as geological conditions [9–13], adjacent structure and other natural factor [14–17]. Among them, the large deformation caused by geological condition becomes a hot issue in the construction of mountain tunnel [18, 19]. The large deformation of the surrounding rock is the typical representation in the carbonaceous slate stratum, such as the maximum accumulated settlement of a specific tunnel reaches 1.7 m [20]. Carbonaceous slate has characteristics of low shear strength, joint developed, high sensitivity to vibration, easy to be softened and collapsed [21]. For ensuring the stability and safety of tunnel, field investigation [22–24], numerical simulation [25–28] and model tests [29] are always used to considering the damaging behavior of structure. Nevertheless, few studies focused on the cracking behavior of the tunnel in carbonaceous slate stratum.

Consequently, further study of carbonaceous slate related to damaging behavior is required, which can provide an accurate basis for precaution or maintenance works of the tunnel. In this paper, lining cracking phenomenon of bottom region in a tunnel is presented not only by field investigation and laboratory test but also using numerical analysis, which is aimed at finding out the influence of tunnel structure damaging behaviors due to carbonaceous slate stratum.

Zhao, Y., Shi, Y., Yang, J. Cracking of tunnel bottom structure influenced by carbonaceous slate stratum. Magazine of Civil Engineering. 2019. 86(2). Pp. 83–91. DOI: 10.18720/MCE.86.8.

Джао Я., Ши Я., Янг Д. Растрескивание туннельного днища под влиянием углеродистого сланца // Инженерно-строительный журнал. 2019. № 2(86). С. 83–91. DOI: 10.18720/MCE.86.8

2. Methods

Figure 1 shows the geological condition around the tunnel, in which the longitudinal length is 2262 m and maximum burial depth is 461 m. The stratum around tunnel is comprised of strong or medium weathered carbonaceous slate with thin layer and fracture structure. The integral degree of rock mass is poor and local groundwater is rich, and the surrounding rock is weakened when encountering water and easy to be crushed by hand. Additionally, there is no obvious seismicity around tunnel site.

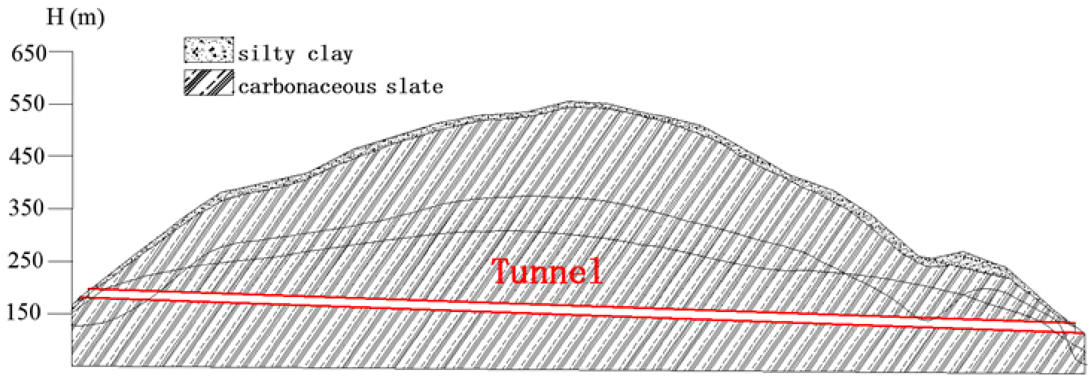

Figure 1. Geological condition of the tunnel.

During the excavation process, it can be observed that exposed surrounding rocks are mainly composed of strongly weathered slate with 0.06–0.2 m thickness. Large deformations of surrounding rock happened frequently during the construction period.

Monitoring displacement of the structure [30] is usually used as an effective method for evaluating construction stability. Figure 2 shows 17-days monitoring results of a cross-section, which includes vertical settlement and horizontal convergence by 5 measuring points as shown in illustrations, which illustrates the total displacements of the shotcrete before supporting secondary lining. The results demonstrate large initial deformation rate, long duration, large deformation and spatial asymmetry of deformation are the deformation characteristics of the tunnel in carbonaceous slate stratum.

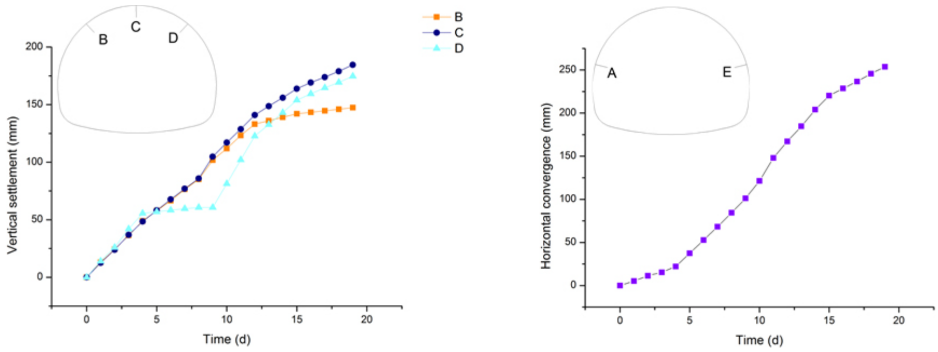

(a) (b)

Figure 2. Monitoring results.

A field investigation was implemented according to the large deformation phenomenon, several damaging behaviors were observed during the construction period. The typical damages are shown in Figure 3, which includes: (a) concrete cracking on the ground surface; (b) large deformation of shotcrete; (c) collapse of tunnel surface; (d) cracking of shotcrete; (e) cracking of secondary lining. The aforementioned damaging behaviors have great influences on the schedule, safety and quality of tunnel construction.

Especially, lining cracking was a common phenomenon in this tunnel, which had been already observed in 38.2 % of the construction regions. Figure 4(a) and (b) show two similar cracks at bottom of the tunnel. The burial depths of the cracking regions are almost from 40 m to 50 m, and the cracks at the middle surface of bottom region along with axial direction of the tunnel. The cracks would not only affect the safety of structure but also lead the potential hazard to further traffic. For this reason, the inducement and mechanism of cracks in the bottom region should be analyzed and discussed in this paper.

The surrounding rock (Figure 5) shows typical soft rock properties with characteristic of softening and argillation when contacting water, which might be the cause of large deformation. It is important to figure out the characteristics and compositions of the rock mass, finding out the relationship between carbonaceous slate and large deformation. Thus, X-ray fluorescence spectrum method was used to analyze the material compositions.

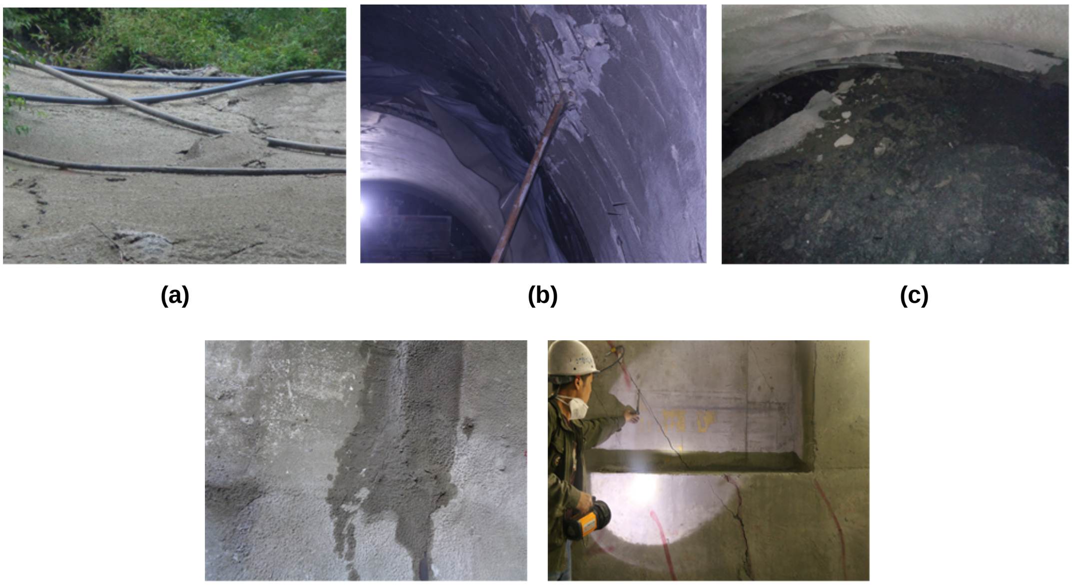

(a) (b) (c)

(d) (e)

Figure 3. Typical damages influenced by large deformation.

(a) (b)

Figure 4. Cracking at the bottom of tunnel.

Figure 5. Surrounding rocks around tunnel face.

It can be obtained from the results of the test report that the surrounding rocks are composed of quartz, muscovite, chlorite, albite, calcite, and dolomite as shown in Figure 6. Among them, the content of quartz, chlorite and white mica accounts for 81.3 % in the whole test block. Clay mineral such as chlorite is easily softened with water, resulting in reduced strength of surrounding rocks over time. The deformation of clinochlore has obvious creep properties [31], and volume will expand by 10 % to 30 %. Additionally, the hydrolysis products of calcite contain kaolin as shown in Equation 1, which is also a clay mineral.

$$4\mathrm{AISi_3O_8} + 6\mathrm{H_2O} = \mathrm{AI_4[Si_4O_{10}]\left(OH\right)_8} + 8\mathrm{SiO_2} + 4\mathrm{H_4SiO_4}, \tag{1}$$

where, $\mathrm{AISi_3O_8}$ is albite, $\mathrm{H_2O}$ is water, $\mathrm{AI_4[Si_4O_{10}]\left(OH\right)_8}$ is kaolin, $\mathrm{SiO_2}$ is quartz and $\mathrm{H_4SiO_4}$ is orthosilicic acid. Calcite and dolomite are the typical carbonate minerals with the capacity of hydrolysis reaction as show in Equation 2, and the surrounding rock with the characteristic of hydrophilic expansion usually contains similar carbonate minerals.

$$\mathrm{CO_3}^{2-} + \mathrm{H_2O} \leftrightarrow \mathrm{HCO_3}^{-} + \mathrm{OH}^{-}, \tag{2}$$

where, $\mathrm{CO_3}^{2-}$ is the carbonate ion, $\mathrm{H_2O}$ is water, $\mathrm{HCO_3}^{-}$ is the bicarbonate ions and OH^{-} is the hydroxyl ion. When the rock is saturated with saturated water, the strength will be reduced. The water will immerse along the joint fractures and weaken the bonding forces between the mineral particles and the rock, for which shear strength and compressive strength are reduced.

Chlorite, albite, calcite, and dolomite account for 37.3 % of the whole test block. Moreover, the degradation, softening, dilatability of these minerals discussed as above should be causes of large deformation. In order to verify the geological condition is the main factor inducing crack, numerical simulation based on ABAQUS [32] is used as an effective method.

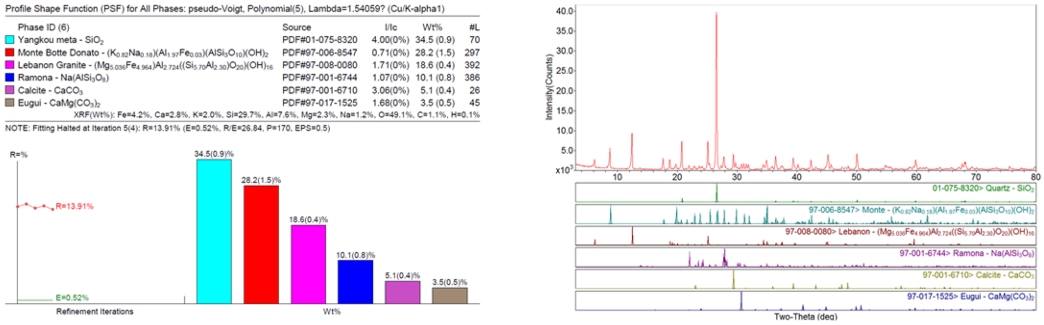

(a) **(b)**

Figure 6. X-ray fluorescence spectrum results.

The qualitative and quantitative analysis of carbonaceous slate can give a reasonable explanation of the rock characteristics around this tunnel. Consequently, the selection of a suitable model for the surrounding rock is the key to establish a reliable numerical model. The rock parameters obtained from geological exploration cannot reflect the realistic characteristics of surrounding rock in the process of simulating, considering of the softening and expansibility of carbonaceous slate. Drucker-Prager yield criterion performances well in simulating the mechanical response of soft rock such as carbonaceous slate [33, 34]. In this work, Drucker-Prager yield criterion is used to reflect carbonaceous slate and the main parameters can be calculated by the following Equations,

$$\sin\varphi = \frac{\tan\beta\sqrt{27-3\tan^2\psi}}{9-\tan\psi\tan\beta}, \tag{3}$$

$$c\cos\varphi = \frac{\sqrt{27-3\tan^2\psi}}{9-\tan\psi\tan\beta}d, \tag{4}$$

where β is the internal friction angle in the Drucker-Prager model, ψ is the dilation angle. Especially, associated flow rule is applied in the calculation, which means the dilation angle ψ is equal to β and flow stress ration k is 1. Moreover, c is the cohesive force and φ is the internal friction angle.

$$\beta = \arctan\frac{\sqrt{3}\sin\varphi}{\sqrt{1+\frac{1}{2}\sin^2\varphi}}, \tag{5}$$

$$\sigma_c^0 = \frac{1}{1-\frac{1}{3}\tan\beta}d, \tag{6}$$

where σ_c^0 is the calculated yield stress under compression behavior for Durcker-Prager Hardening.

After ensuring the reasonability of simulating rock mass, the cracking behavior also needs to be considered. For this reason, the affection of damaging in concrete lining induced by carbonaceous slate must be investigated visually, from which the extended finite element method (XFEM) is adopted in numerical simulation to reflect the crack propagation. XFEM allows local enrichment functions to be easily incorporated into a finite element approximation, which does not require the match of geometry discontinuities and mesh. Therefore, XFEM is a very superduper and effective method to simulate initiation and propagation of a discrete crack along an arbitrary, solution-dependent path without remeshing. The core of XFEM is that it improves the traditional finite element shape function based on the concept of partition of unity method, which is raised by Melenk and Babuska. XFEM allows for the existence of discontinuity in the elements, which can be used to enrich the degree of freedom by special displacement functions.

For the purpose of fracture analysis, the enrichment functions typically consist of the near-tip asymptotic functions that capture the singularity around the crack tip and a discontinuous function that represents the jump in displacement across the crack surfaces as shown in Figure 7 [32]. The approximation for a displacement vector function u with the partition of unity enrichment is

$$u = \sum_I^N N_I(\mathrm{x})[N_I + H(\mathrm{x})\alpha_I + \sum_{\alpha=1}^4 F_\alpha(\mathrm{x})b_I^\alpha]. \tag{7}$$

The discontinuous jump function across the crack surfaces, $H(\mathrm{x})$, which is given by

$$H(\mathrm{x}) = \begin{cases} 1 & \text{if}\,(\mathrm{x} - \mathrm{x}^*),\ \mathrm{n} \ge 0, \\ -1 & \text{otherwise} \end{cases} \tag{8}$$

where x is a sample (Gauss) point, x^* is the point on the crack closest to x, and n is the unit outward normal to the crack at x^*. $F_\alpha(\mathrm{x})$, which are given by

$$F_\alpha(\mathrm{x}) = \left[\sqrt{r}\sin\frac{\theta}{2}, \sqrt{r}\cos\frac{\theta}{2}, \sqrt{r}\sin\theta\sin\frac{\theta}{2}, \sqrt{r}\sin\theta\cos\frac{\theta}{2}\right], \tag{9}$$

where (r, θ) is a polar coordinate system with its origin at the crack tip and $\theta = 0$ is tangent to the crack at the tip.

The maximum principal stress criterion can be used to simulate the damaging behavior of secondary lining, which can be represented as,

$$f = \left\{ \frac{\langle \sigma_{\max} \rangle}{\sigma_{\max}^o} \right\} \tag{10}$$

Here, $\sigma_{\max}^o$ represents the maximum allowable principal stress. The symbol $< >$ represents the Macaulay bracket with the usual interpretation (i.e., $\langle \sigma_{\max} \rangle = 0$ if $\sigma_{\max} < 0$ and $\langle \sigma_{\max} \rangle = \sigma_{\max}$ if $\sigma_{\max} \ge 0$. The Macaulay brackets are used to signify that a purely compressive stress state does not initiate damage. Damage is assumed to initiate when the maximum principal stress ratio (as defined in the expression above) reaches a value of one.

Once the Drucker-Prager yield criterion and XFEM are confirmed to be used in the numerical model, the simulation process can be advanced. The numerical model and boundary conditions of a typical cross-section are shown in Figure 8, in which the longitudinal calculation range of the numerical model is 112 m, and the vertical calculation ranges of both lateral sides are 50 m, including vertical range of 43 m from tunnel top to the upper boundary. The surrounding rocks and concrete lining in the numerical model are simulated using solid elements in ABAQUS with 2D model considering the stress state of plane strain. Moreover, some assumptions are adopted for the boundary conditions of the numerical model, in which the displacements of the lower boundary are constrained in both longitudinal and vertical directions, those of both lateral boundaries are only restricted in the longitudinal direction, whereas those of upper boundary is free in both longitudinal and vertical directions.

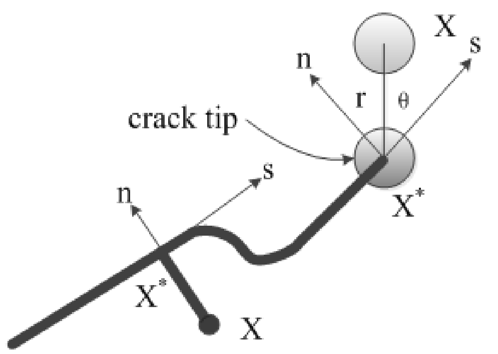

Figure 7. Normal and tangential coordinates of crack.

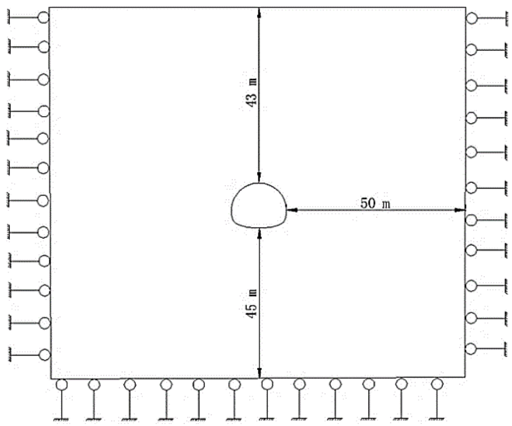

Figure 8. Numerical model and boundary condition.

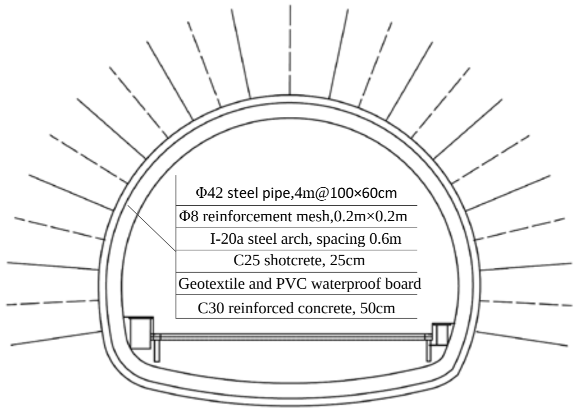

Figure 9. Transverse section of the tunnel structure (unit: m).

In the stage of establishing tunnel structure, Figure 9 shows the typical cross-section of the highway tunnel with 9.2 m height and 12 m width. Shotcrete with 0.25 m thickness and steel mesh with 0.2 m×0.2 m spacing are adopted in the primary lining. For the steel mesh, round bars with 8 mm diameters are both used in longitudinal and circumferential directions. In the anchor system, the 25 mm diameter hollow grouting anchor rod and 22 mm diameter mortar anchor rod with 1 m length and 1.2 m circumferential spacing are respectively fixed at arch part and side wall of surrounding rocks, and 42 mm steel pipes are fixed along longitudinal direction of surrounding rocks before excavating tunnel face. Moreover, the arch vault and side wall as well as inverted arch have 0.5 m thicknesses in the secondary lining.

The secondary lining is considered as ideal elastic material to use XFEM to simulate the process of crack. The damage criterion for traction-separation laws is used for lining damaging evolution, which is according to ultimate tensile strength of concrete with 1.42 MPa. Moreover, the effect of steel arch in primary lining is converted to shotcrete in primary lining by following Equation [35]:

$$E' = E_0 + S_g \cdot E_g / S_c, \tag{11}$$

where E' is equivalent Young's modulus;

E_0 and E_g are Young's modulus of shotcrete and reinforcement respectively;

S_g and S_c are section area of steel arch and shotcrete respectively.

The physical properties of composite lining and surrounding rock are listed in Table 1 as follows. From which, E is elastic modulus, ρ is bulk density, f_c' is compressive strength of concrete, f_t is tension strength of concrete, μ is Poisson's ratio, β is frictional angle (Drucker-Prager yield criterion), k is flow stress ration, ψ is dilation angle.

Table 1. Physical properties.

Material	Physical and mechanical parameters
Surrounding rock	E = 800 MPa, ρ = 2200 kg/m^3, μ = 0.32, β = 35º, k = 1, ψ = 35°
Primary lining concrete	E = 26 GPa, ρ = 2500 kg/m^3, f_c' = 9 MPa, f_t = 1.0 MPa, μ = 0.23
Secondary lining concrete	E = 31.5 GPa, ρ = 2500 kg/m^3, f_c' = 11 MPa, f_t = 1.42 MPa, μ = 0.2

The cracks were observed several months after finishing the construction of secondary lining, and the tunnel face is almost 80 m away from the cracking region. Thus, full-face excavation of the tunnel is adopted in the simulation process without considering any construction factor [36]. The numerical calculation is implemented as the following stages, 1) establishment of geometric model of stratum and lining systems, adding materials properties and generating mesh; 2) initial step for balance of ground stress; 3) simulation of tunnel excavation and initial support by model change function; 4) Establishment of secondary lining and simulation of the crack influenced by surrounding rock pressure. For simulating the large deformation of rock mass, plane strain elements CPE4R (4-node bilinear, reduced integration with hourglass control) are used in the numerical model.

3. Results and Discussion

The contour of true strain of lining is shown as Figure 10(b), which demonstrates that the dominant strains are distributed within the tunnel bottom regions. The maximum tensile strains in dominant regions exceed the ultimate value of concrete, which means that lining structure is already damaged at these regions. The results are similar to the illustrated lining failure forms as aforementioned, and which proves the effectiveness of the numerical analysis considering impacts of surrounding rock conditions. Moreover, the evolution of crack can be presented visually through the iso-surface for the signed distance function PHILSM by XFEM, and the outcomes of numerical calculation are shown in Figure 10(a). It can be clearly obtained that there is a tensile type crack generated and cracking is similar to the field conditions, and that confirms the numerical model can simulate the damaging process excellently.

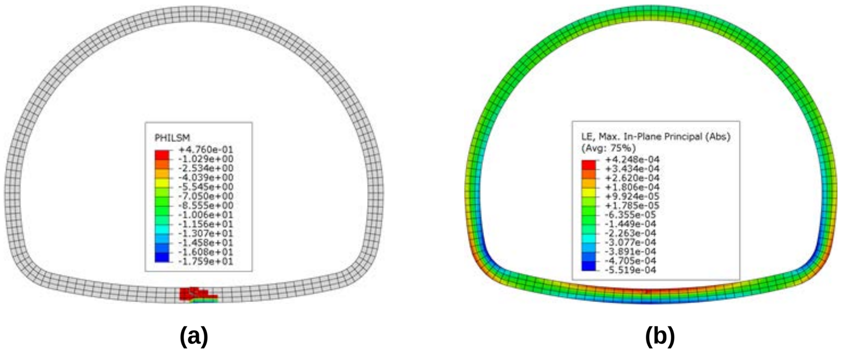

Figure 10. Results of numerical model.

From the partial enlarged view in Figure 11, it can be obtained that the crack generates along the vertical direction on lining surface. The evolution of the force characteristics can be also obtained, in which the traces indicate the movements of bottom structure influenced by the rock mass. Generally, the crack at bottom region is induced by deformation of structure under the tensile stress, which leads to the cracking behaviors and affects the stability of tunnel structure.

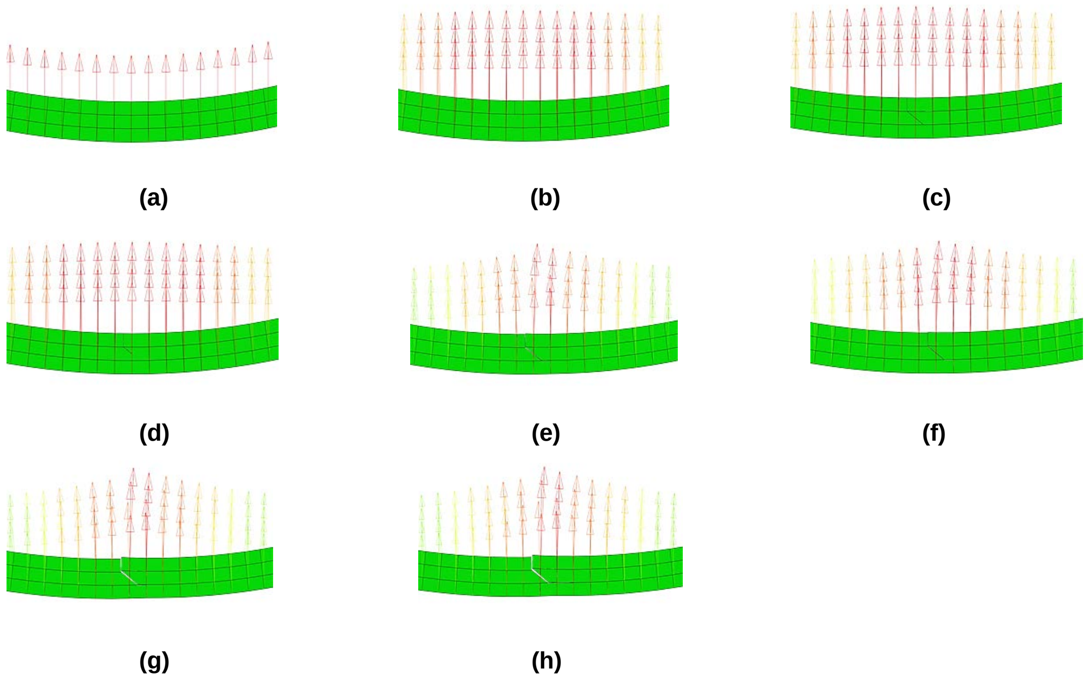

Figure 11. Evolution process of cracking.

Contours of displacements are shown in Figure 12(a) and (b), and the deformation analysis is helpful to confirm the reason for cracking. The results of displacement are similar to the distribution of maximum strain and the maximum total vertical displacement of the tunnel is 0.21 m in the middle region of tunnel bottom, besides, the maximum total horizontal displacement is 0.06 m around two side wall regions. It can be obtained from the numerical results that the geological condition of surrounding rock is the major inducement of cracks in tunnel, which leads to the bottom region becoming the most disadvantaged position of the whole structure. The displacements of the structure verify the reasonability of Drucker-Prager yield criterion for reflecting large deformation of carbonaceous slate. Consequently, strengthening the tunnel structure at bottom region or improving the surrounding rocks conditions are the necessary methods for preventing cracks in subsequent construction or similar engineering projects located in this area.

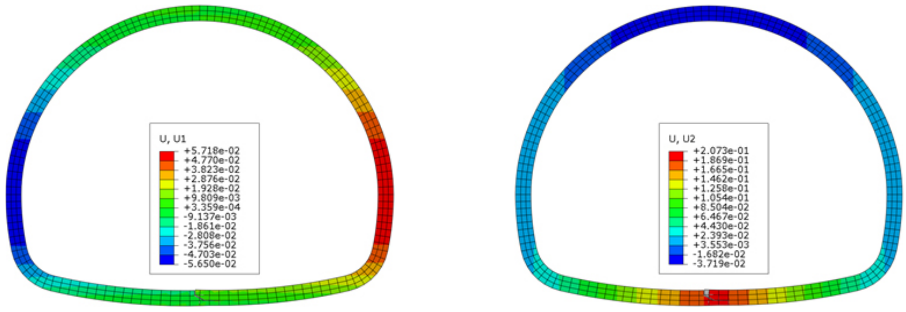

(a) (b)

Figure 12. Displacements of tunnel structure.

The outputs of the simulation demonstrate the propagation of the crack and the dangerous region of tunnel. Strengthened design of invert arch, bolting and grouting can be used to avoid the lining cracking of tunnel bottom, and it must be noticed that water should be drained away before the refilling work of inverted arch during the construction period.

4. Conclusion

Field investigation and laboratory test are conducted to identify the inducement of cracks during the construction period. It can be concluded that the geological condition is the major inducement for cracking of tunnel bottom without considering construction factors. In this instance, crack in this tunnel structure is simulated by finite element software to verify if this inducement is reasonable. The following points can be outlined as outcomes of the study,

- Tunnelling in carbonaceous slate stratum may be confronted with difficult construction caused by large deformation of surrounding rock, which has characteristics with high initial deformation rate, long duration, and large deformation. In addition, the large deformation of rock mass will lead to various damaging behaviors, especially cracking of the bottom region.

- The degradation, softening and dilatability of carbonaceous slate influenced by certain minerals should be the direct inducements of the large deformation, which was related to the underground water and inevitable construction water.

- Drucker-Prager yield criterion and XFEM is verified as an effective approach in simulating lining cracking of tunnel bottom in carbonaceous slate stratum. The results show that greater displacement and tensile strain of the bottom region can be obtained than other regions. Moreover, the generation of crack is similar to the realistic damaging behavior in field, which also can verify the cause of crack.

- The contours of total displacement of the secondary lining can also demonstrate that there is an obvious uplift phenomenon of the bottom region, which makes the tunnel bottom become the most disadvantageous part of the whole structure. Thus, necessary measures like strengthened design of tunnel structure need to be implemented in carbonaceous slate stratum. Moreover, water should be drained away before the refilling work of inverted arch.

References

1. Li, S.C., Liu, B., Nie, L.C., Liu, Z.Y, Tian, M.Z., Wang, S.R., Su, M.X., Guo, Q. Detecting and monitoring of water inrush in tunnels and coal mines using direct current resistivity method: a review. Journal of Rock Mechanics and Geotechnical Engineering. 2015. Vol. 7. No. 18. Pp. 469–478.
2. Zhao, Y., Li, P.F., Tian, S.M. Prevention and treatment technologies of railway tunnel water inrush and mud gushing in China. Journal of Rock Mechanics and Geotechnical Engineering. 2013. Vol. 5. No. 6. Pp. 468–477.
3. Federal Highway Administration. Highway and rail transit tunnel inspection manual. 2005. No. 3(4).
4. Sandrone, F., Labiouse, V. Identification and analysis of swiss national road tunnels pathologies. Tunnelling and Underground Space Technology. 2011. Vol. 26. No. 2. Pp. 374–390.
5. Asakura, T., Kojima, Y. Tunnel maintenance in japan. Tunnelling and Underground Space Technology. 2003. Vol. 18. No. 2. Pp. 161–169.
6. Huang, H.W., Liu, D.J., Xue, Y.D., Wang, P.R., Yin, L. Numerical analysis of cracking of tunnel linings based on extended finite element. Chinese Journal of Geotechnical Engineering. 2013. Vol. 35. No. 2. Pp. 266–275.
7. Yamada, T., Sano, N., Baba, K., Yoshitake, I., Nakagawa, K., Nishimura, K. A quantitative criterion for evaluation of tunnel lining concrete. Doboku Gakkai Ronbunshuu F. 2007. Vol. 63. No. 1. Pp. 86–96.
8. Jiang, Y., Tanabashi, Y., Fujii, M., Zhao, X., Idenaga, S. Database development for road tunnel maintenance and management by using geographical information system (new technology for maintenance/retrofit and renewal works in geotechnical engineering: tunnels, underground structures and antiquities). Soil Mechanics and Foundation Engineering. 2004. Vol. 52. Pp. 25–27.
9. Wang, T.T. Characterizing crack patterns on tunnel linings associated with shear deformation induced by instability of neighboring slopes. Engineering Geology. 2010. Vol. 115. No. 1–2. Pp. 80–95.

10. Zhang, Y.X., Shi, Y.F., Zhao, Y.D., Fu, L.L., Yang, J.S. Determining the cause of damages in a multiarch tunnel structure through field investigation and numerical analysis. Journal of Performance of Constructed Facilities. 2017. Vol. 31. No. 3. Pp. 1–7.
11. Lai, H., Song, W., Liu, Y., Chen, R. Influence of flooded loessial overburden on the tunnel lining: case study. Journal of Performance of Constructed Facilities. 2017. Vol. 31. No. 6. Pp. 1–11.
12. He, W., Wu, Z., Kojima, Y., Asakura, T. Failure mechanism of deformed concrete tunnels subject to diagonally concentrated loads. Computer-aided Civil and Infrastructure Engineering. 2009. Vol. 24. No. 6. Pp. 416–431.
13. Bukhartsev, V.N., Volkov, E.N. Influence of discontinuities on the rock mass stress-strain state around excavation. Magazine of Civil Engineering. 2013. 39(4). Pp. 3–11. DOI: 10.5862/MCE.39.1
14. Roy, N., Sarkar, R. A review of seismic damage of mountain tunnels and probable failure mechanisms. Geotechnical and Geological Engineering. 2017. Vol. 35. No. 1. Pp. 1–28.
15. Mohamad, H., Bennett, P.J., Soga, K., Mair, R.J., Bowers, K. Behaviour of an old masonry tunnel due to tunnelling-induced ground settlement. Géotechnique. 2015. Vol. 60. No. 12. Pp. 927–938.
16. Bian, K., Liu, J., Xiao, M., Liu, Z. Cause investigation and verification of lining cracking of bifurcation tunnel at Huizhou Pumped Storage Power Station. Tunnelling and Underground Space Technology. 2016. Vol. 54, No. 27, Pp. 123–134.
17. Tan, Y., Smith, J.V., Li, C.Q., Currell, M., Wu, Y. Predicting external water pressure and cracking of a tunnel lining by measuring water inflow rate. Tunnelling and Underground Space Technology. 2018. Vol. 71. Pp. 115–125.
18. Wang, B., Li, T.B., He, C., Zhou, Y. Analysis of failure properties and formatting mechanism of soft rock tunnel in meizoseismal areas. Chinese Journal of Rock Mechanics and Engineering. 2012. Vol. 31. No. 5. Pp. 928–936.
19. Lei, J., Zhang, J.Z., Lin, C.N. Analysis of stress and deformation site-monitoring infault zone of Wushaoling tunnel under complex geological conditions. Rock and Soil Mechanics. 2008. Vol. 29. No. 5. Pp. 1367–1371.
20. Wu, J.G., Liu, X.X., Wang, W.X. Deformation control technology during the construction of large section carbonaceous slate formation tunnel. Modern Tunnelling Technology. 2011. Vol. 46. No. 2. Pp. 68–72.
21. Wang, W.L., Wang, T.T., Su, J.J., Lin, C.H., Seng, C.R., Huang, T.H. Assessment of damage in mountain tunnels due to the taiwan chi-chi earthquake. Tunnelling and Underground Space Technology. 2001. Vol. 16. No. 3. Pp. 133–150.
22. Kontogianni, V.A., Stiros, S.C. Induced deformation during tunnel excavation: evidence from geodetic monitoring. Engineering Geology. 2005. Vol. 79. No. 1–2. Pp. 115–126.
23. Lai, J., Fan, H., Chen, J., Qiu, J.X., Wang, K. Blasting vibration monitoring of undercrossing railway tunnel using wireless sensor network. International Journal of Distributed Sensor Networks. 2015. No. 6. Pp. 1–7.
24. Gao, Y., Xu, F., Zhang, Q., He, P., Qin, Z. Geotechnical monitoring and analyses on the stability and health of a large cross-section railway tunnel constructed in a seismic area. Measurement. 2018. No. 122. Pp. 620–629.
25. Zhao, Y.D., Shi, Y., Yang, J.S. Study of the influence of train vibration loading on adjacent damaged tunnel. Shock and Vibration. 2019. Vol. 2019. Pp. 1–8.
26. Geniş, M. Assessment of the dynamic stability of the portals of the Dorukhan tunnelusing numerical analysis. International Journal of Rock Mechanics and Mining Sciences. 2011. Vol. 47. No. 8. Pp. 1231–1241.
27. Fang, Y., Xu, C., Cui, G., Kenneally, B. Scale model test of highway tunnel construction underlying mined-out thin coal seam. Tunnelling and Underground Space Technology. 2016. Vol. 56. Pp. 105–116.
28. Ivanes, T.V., Kavkazskiy, V.N., Shidakov, M.I. Geomechanical tasks solving in modelling of temporary support parameters in Sochi tunnels. Procedia Engineering. 2017. Vol. 189. Pp. 227–231.
29. Idinger, G., Aklik, P., Wu, W., Borja, R.I. Centrifuge model test on the face stability of shallow tunnel. Acta Geotechnica. 2011. Vol. 6. No. 2. Pp. 105–117.
30. Benin, A., Konkov, A., Kavkazskiy, V., Novikov, A., Vatin, N. Evaluation of deformations of foundation pit structures and surrounding buildings during the construction of the second scene of the state academic mariinsky theatre in saint-petersburg considering stage-by-stage nature of construction process. Procedia Engineering. 2016. Vol. 165. Pp. 1483–1489.
31. Yu, D.H., Peng, J.B. Experimental study of mechanical properties of chlorite schist with water under triaxial compression. Chinese Journal of Rock Mechanics and Engineering. 2009. Vol. 28. No. 1. Pp. 205–211.
32. Dassault Simulia International Inc. ABAQUS v 6.4. 2004.
33. Wang, W.M., Zhao, Z.H., Wang, L. Safety analysis for soft rock tunnel floor destruction based on different yield criterions. Chinese Journal of Rock Mechanics and Engineering. 2012, Vol. 31. No. S2. Pp. 3920–3927.
34. Deng, C.J., He, G.J., Zheng, Y.R. Studies on Drucker-Prager yield criterions based on M-C yield criterion and application in geotechnical engineering. Chinese Journal of Geotechnical Engineering. 2006. Vol. 28. No. 6. Pp.735–739.
35. Zhao, Y.D., Liu, C., Zhang, Y.X., Yang, J.S., Feng, T.G. Damaging behavior investigation of an operational tunnel structure. Engineering Failure Analysis. 2019. No. 47. Pp. 25–33.
36. Abdullayev, G.I., Velichkin, V.Z., Soldatenko, T.N. The organizational and technological reliability improvement in construction by using failure prediction method. Magazine of Civil Engineering. 2013. 38(3). Pp. 43–50. DOI: 10.5862/MCE.38.6

Contacts:

Yiding Zhao, +008618118686057; zhaoyiding89@126.com
Yao Shi, +008615861927700; 734169065@qq.com
Junsheng Yang, +8618075154205; 1797935162@qq.com

Magazine of Civil Engineering. 2019. 86(2). Pp. 92–104
Инженерно-строительный журнал. 2019. № 2(86). С. 92–104

Magazine of Civil Engineering

journal homepage: http://engstroy.spbstu.ru/

ISSN 2071-0305

DOI: 10.18720/MCE.86.9

Behaviour of axisymmetric thick plates resting against conical surface

V.I. Morozov*, E.K. Opbul, P. Van Phuc,
St. Petersburg State University of Architecture and Civil Engineering, St. Petersburg, Russia
** E-mail: morozov@spbgasu.ru*

Keywords: high-pressure casing; end element; axisymmetric plate; bearings; walls (structural partitions); internal pressure; loads (forces); key; conical surface.

Abstract. The present article is dedicated to analytical and numerical investigation of behavior of end elements of high-pressure casings for nuclear reactors. Nuclear energy generated inside the high-pressure casings will become an actual power-related choice of the human kind in the very near future. In this respect, development of methodology for proper calculation of axisymmetric plates resting against conical surface and bearing the evenly distributed load is becoming state of the art issue. In order to perform analytical calculation the authors used established concrete strength criteria and prerequisites assumed, while ANSYS WORKBENCH software package was applied to calculate the ultimate load value and stress state. Calculations were made considering a keyed connection between thick plate and load-bearing wall of the high-pressure casing and referring to considerably high, in one case, and low (variable), in the other case, plate stiffness. The article presents comparative analysis of calculation results that demonstrates calculation methods adequacy. The authors developed original methods of analytical and numerical calculations allowing to investigate stress state of end elements designed in the form of axisymmetric plates resting against conical surfaces. End elements behavior in load condition is characterized by formation of spheric vault where stress condition typical for concrete three-dimensional compression state occurs. Investigations presented show that sudden disintegration does not occur when concrete end elements are affected by cracks in the stretched area; instead, the spheric vault is formed. Strength of such spheric vault occurring in the element is rather depending upon load bearing wall stiffness, i.e. the lower the stiffness the smaller the strength and vice versa. The following scientific results have been obtained: – end elements shaped as thick axisymmetric plates in condition of ultimate load are characterized by spheric vault formation; -authors, based on assumptions and guided by approximate procedure have obtained the formula for spheric vault thickness calculation; – authors obtained original methods of analytical and numerical calculation to evaluate stress condition of high-pressure casings' end elements shaped as thick axisymmetric plates resting against conical surface; – comparison of calculation results displays minor discepancies between analytical and numerical calculation models.

1. Introduction

Problems associated with experimental-theoretical investigation of buildings and facilities locating hazardous production cycles are still regarded as topical issues which are represented by a wide range of design solutions. Alongside with [1–5], a particular place is held by nuclear reactor high pressure casings – special units in which the process is characterized by high internal pressure, temperature and radiation impacts.

It is a well-known fact [6–10], that NR steel casings have small active zone area dimensions and low parameters of reactor heat carrier, besides, they are very complicated in manufacturing which can be accomplished only in factory conditions. At that, in order to manufacture the casing it is required to prepare a number of ingots made of high-quality electric furnace (pearlitic) steel.

Morozov, V.I., Opbul, E.K., Van Phuc, P. Behaviour of axisymmetric thick plates resting against conical surface. Magazine of Civil Engineering. 2019. 86(2). Pp. 92–104. DOI: 10.18720/MCE.86.9.

Морозов В.И., Опбул Э., Ван Фук Ф. Работа осесимметричных толстых плит, опертых по конической поверхности // Инженерно-строительный журнал. 2019. № 2(86). С. 92–104. DOI: 10.18720/MCE.86.9

In 1959, in France, first nuclear reactors designed in the form pre-stressed concrete structure with active casing in the form of thick-walled (3 meters) horizontal (20 meters diameter) cylinder were built. End elements were made in the form of concave hemispheres to avoid any tension zones caused by internal pressure while lateral pressure, longitudinal and ring tensions were withstood by hooped and longitudinal pre-stressed reinforcements. Steel 3 cm thick leak proof cladding was installed inside the casing.

Despite the fact that pre-stressed reinforced concrete is known to be rather reliable it is necessary to underline that pre-stressing technology is becoming more and more complicated due to technical complexity of structures under design, structures and elements atypicality etc. [11–15].

High-pressure casings of structural solution under design and investigation is a complicated multi-component facility (refer to Figure 1) which includes load-bearing walls made of heavy armored cement [16], plug-type end elements protected from displacement by means of special keys and other structural components which are not covered by this article.

Heavy armored cement is fiber reinforced concrete with large (20 % volume and over)content of small diameter reinforcement rods. First heavy armored cement was invented in 1970s [16, 17].

This article is addressing behavior of axisymmetric thick plates resting against conical surface and bearing the evenly distributed load.

As it is known [17] thick plates may be used in the end parts of high-pressure casings. They are generally known as end elements.

Purpose of this article is to investigate behavior of end elements affected by evenly distributed load with reference to (i) resting state and (ii) stiffness of the casing load bearing wall. Where analytical problem was solved on the basis of classic theory of plastic behavior we made use of “Mathcad 15” software package while numerical computation required ANSYS WorkBench R18.1 software package.

Purpose of this article is (i) to create analytical and numerical methods of assessment of stress-strain behavior (SSB) and (ii) to determine the ultimate load value.

As it is known [16], cracked thick axisymmetric plate being in volumetric strain condition, at loads near to ultimate, is affected by considerably high area of omnidirectional compression, i.e. by a kind of “dome”. If you imagine the thick axisymmetric plate being in plane deformation state it means that the compressed spacial “dome” will take the shape of plane spheric “vault” which will cause “arcuated” behavior of the structure.

2. Methods

Figure 1 presents original structure of cylindrical high-pressure casing made of heavy armored cement [16, 17], in which special key is provided with a purpose to avoid plate displacement against the load-bearing wall.

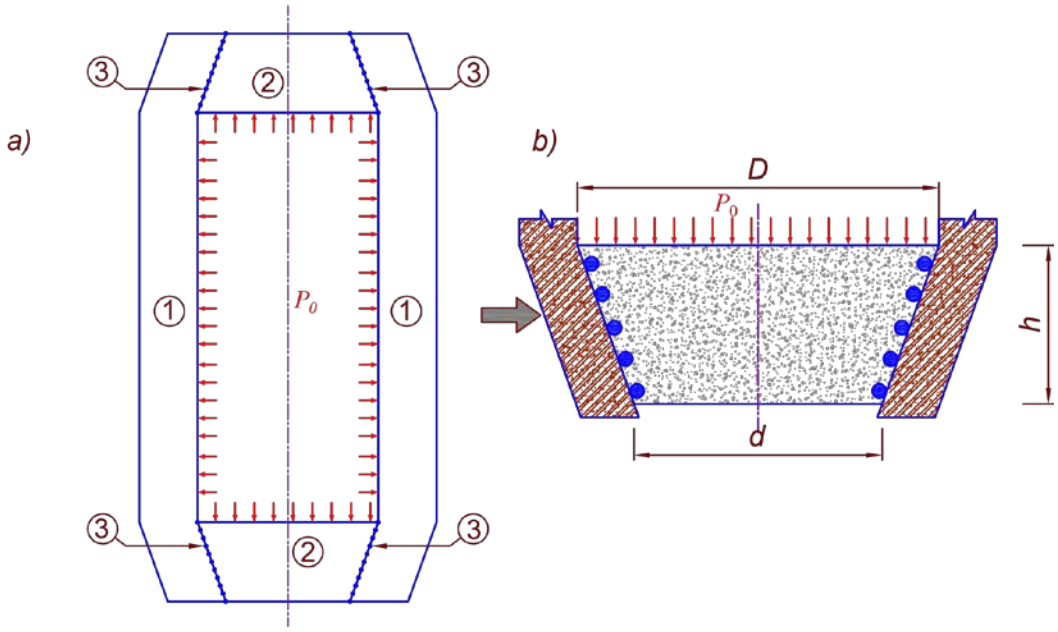

Figure 1. Structural layouts:
a) High-pressure casing: 1 is load bearing wall made of heavy armored cement, 2 is end element, 3 is keys, P_0 is evenly distributed load; b) end elements designed in the form of thick plate: D is largest diameter of the end elements, d is smallest diameter of the end elements, h is height of the end elements.

Below presented are several models of end elements calculation for the case where connection with high-pressure casing made of heavy armored cement is provided by means of the key, inter alia, calculation models depending on wall stiffness.

At the first stage we analyzed axisymmetric concrete thick plate abutting with load bearing wall through the key; at that, it was conditionally assumed that load bearing wall had rather high stiffness. Taking into account the accepted key-type connection between structural elements and casing load-bearing wall – calculation model of the end elements (for plane deformation state) may be viewed from Figure 2.

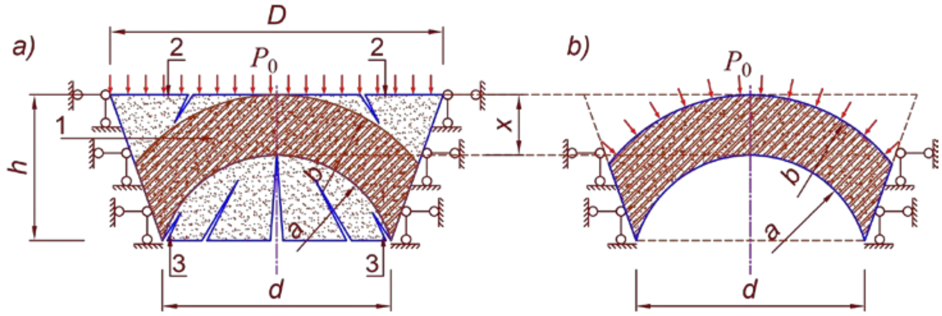

Figure 2. Calculation model for concrete end element with load bearing wall having high stiffness: a) during crack formation stage: 1 is spheric vault, 2 is tension are near supports, 3 is cracks, a is internal diameter of the vault, b is external diameter of the vault, b) during spheric vault crack formation stage.

Obviously, there are practically no radial displacements where load bearing wall is stiff. However, it may be admitted that prior to crack formation the thick wall is operating according to beam pattern.

For thick wall, prior to first cracks formation in plane deformation state, in order to calculate height of compression area it is necessary to assume the following allowances:

- thick concrete element (prior to crack formation) is operating according to beam pattern;
- flat cross-section hypothesis is valid;
- tension area is in the stage of plastic deformations, and ultimate value of plastic deformation is $\varepsilon_{bt2} = 15 \cdot 10^{-5}$;
- compression area is within the elastic behavior zone.

With consideration of accepted assumptions, Figure 3 presents calculation model of thick concrete element prior to first crack formation.

With provision for equilibrium conditions ΣX = 0 we obtain:

$$R_{bt}(h-x) - \frac{1}{2}\sigma_b x = 0. \tag{1}$$

From relations balance $\dfrac{\varepsilon_b}{\varepsilon_{bt}} = \dfrac{x}{h-x}$ we obtain

$$\varepsilon_b = \frac{\varepsilon_{bt} x}{h-x}. \tag{2}$$

Using Hooke's law for elastic cross-section zone $\sigma_b = \varepsilon_b E_b$, and taking into account (2) we obtain

$$\sigma_b = \frac{\varepsilon_{bt} x}{h-x} E_b. \tag{3}$$

Jointly solving equations (1) and (3) we obtain formula enabling compression area height (vault thickness) determination:

$$x = \frac{h - \sqrt{h^2 - h^2\left(1 - \dfrac{\varepsilon_{bt} E_b}{2R_{bt}}\right)}}{1 - \dfrac{\varepsilon_{bt} E_b}{2R_{bt}}}. \tag{4}$$

Figure 4 presents end elements pattern designed in the form of conic-shape thick plate limited by points *ABCD*, where $GE = x$ – thickness or height of the vault determined by formula (4).

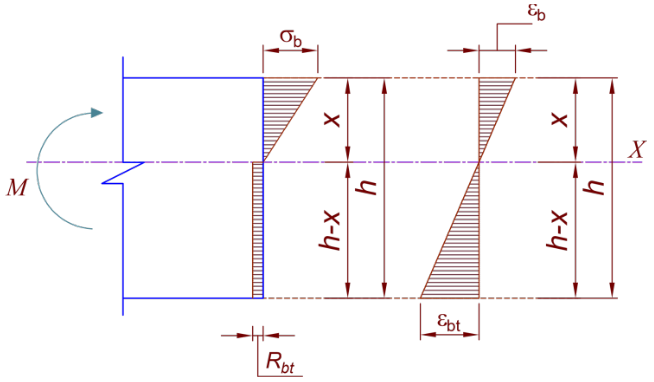

Figure 3. Model of calculation of thick element standard cross-section.
***M* is bending momentum, *h* is height of thick element, *x* is height of compressed zone, R_{bt} is concrete ultimate strength in condition of uniaxial tension, σ_b is normal stress in compression zone.**

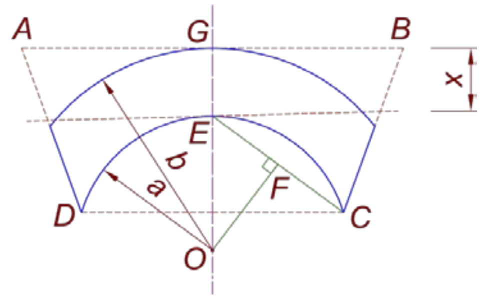

Figure 4. Graphical determination of parameters *a*&*b*.

In order to determine numerical values of thick vault inner a and outer b radii it is easy to use to use the model of graphical determination which, due to its demonstrativeness, is practically avoiding occurrence of mistakes (refer to Figure 4).

In [18–20], when analyzing structural strength parameters with account to complex stress state, it was determined that concrete disintegration (in axial compression condition) may occur along the inclined plane. In this case, crack formation begins near the lateral surface supports (Figure 5) with further occurrence of inclined cracks. Further load increase and cracks formation is leading to spherical vault formation.

Experimental investigations of glass and concrete [15, 16] conical elements carried out in late 1970's showed that from the moment of load application and with further load increase the process of crack formation was initiated and continued to spread in upper corner zones of the specimen, near the supports (Figure 2a). With further load increase, performance of the test specimen acquires a different character while stress-strain state transforms to some other qualitative condition. The process of crack formation is shifting from upper corner zones to the lower stretched area of the plate. Evidently, here the supporting sections of the conical element begin to perform in accordance with console-type deformation and it is not useful to take into account their resistance to active loads.

Let us admit that thick plate, prior to crack formation in the lower stretched zone, is performing as a beam, and, as cracks occur and begin spreading, the beam-type behavior is transformed into arc-type (Figure 3) which is characteristic of thick plates.

As it is known [16] – cracked thick axisymmetric plates in spacial deformation state at loads close to ultimate are characterized by formation of considerably large all-round compression area – a peculiar kind of "dome". If we assume the axisymmetric plate in plain deformation state, so the compressed spacial "dome" will transform into a kind of spherical "vault" in which the structure performs as an arc. Therefore, in order to perform analytical calculation of end elements represented by thick plates with consideration of cracked end element's plastic-behavior stage we admit the calculation scheme represented by Figure 5.

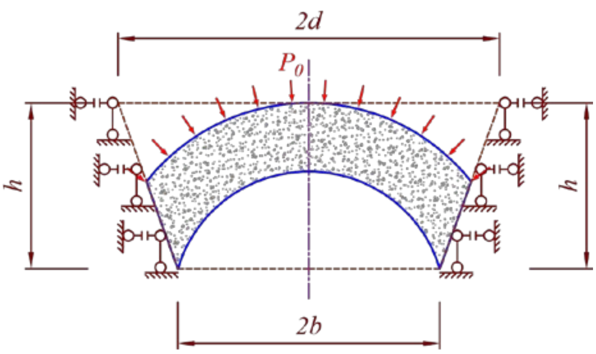

Figure 5. Calculation model for concrete end element.

It is necessary to note that similar model was used for experimental investigation of axisymmetric plate [16], where processes occurring during three-dimensional stress state were expectedly observed.

In the second case, we, tentatively, have relatively small stiffness of the load-bearing wall (Figure 6) where, with increasing operating load, the end elements begin to bias away or to expand the wall in radial direction. At a certain moment, crack formation in lower stretched area of the end elements will begin; at that, it will begin with formation of standard crack in the middle of element's span (Figure 6a) due to evidently low stiffness of the load bearing wall. At that, thickness of the vault (in comparison with first case) will considerably differ to the smaller size, at that (Figure 6b).

Thus, with low stiffness of the load bearing wall we have low bearing capacity of the end elements.

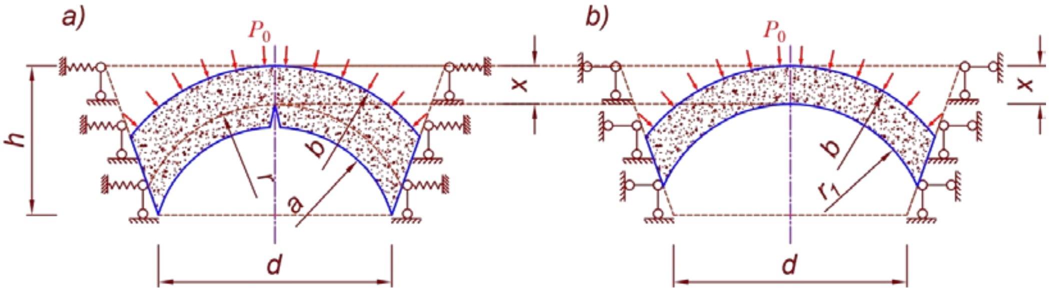

Figure 6. Calculation model for concrete end element with load bearing wall having very low stiffness: a) stage of the normal crack formation and development: *r* is radius of neutral axis b) final stage of formation of spheric vault having small thickness: *r*₁ is new position of the neutral axis corresponding to static state.

Third case. In order to ensure effective behavior of low-stiffness end elements it is required to use reinforcement (Figure 7*a*). At that, when end elements have sufficient amount of reinforcement metal we can assume that radial displacements may be neglected. Therefore, we can admit (like in the first case) formation of similar stress-strain behavior in the element according to which we will obtain respective calculation model presented in Figure 7b.

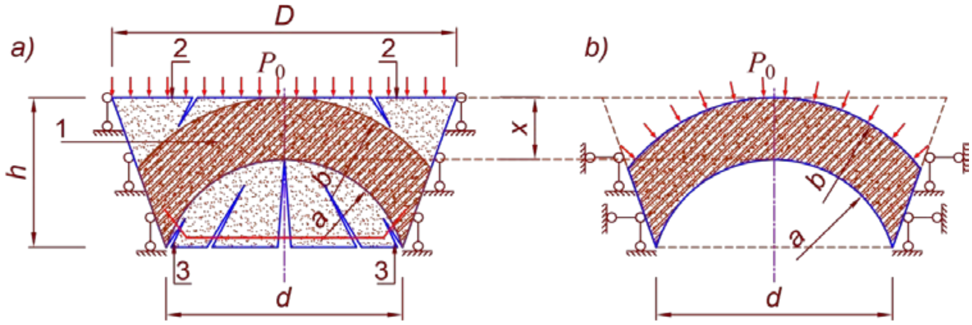

Figure 7. Calculation model. Reinforced concrete end elements with standard load-bearing wall: a) crack formation stage, b) spheric vault formation stage.

It is possible to admit that in this case typical processes (crack occurrence and propagation, formation of vault etc.) will obviously depend on stretched reinforcement behavior under load.

Concrete stiffness [ac. to Balandin] is presented as follows [22]:

$$\sigma_1^2+\sigma_2^2+\sigma_3^2-(\sigma_1\sigma_2+\sigma_2\sigma_3+\sigma_3\sigma_1)-(R_b-R_{bt})(\sigma_1+\sigma_2+\sigma_3)=R_bR_{bt}. \quad (5)$$

Taking into account $\sigma_1=\sigma_2=\sigma_\theta;\ \sigma_3=\sigma_r$ from (5) we obtain

$$(\sigma_1-\sigma_3)^2-(R_b-R_{bt})(2\sigma_1+\sigma_3)=R_bR_{bt}, \quad (6)$$

where σ_1, σ_1, σ_3 are main stresses,

σ_θ, σ_r are accordingly, circumferential and radial stresses,

R_b, R_{bt} are accordingly, concrete ultimate strength in uniaxial compression and tension states.

Differential equation of equilibrium in spherical coordinate system with regard to problem under consideration as per [22]:

$$\frac{d\sigma_r}{dr}+2\frac{\sigma_r-\sigma_\theta}{r}=0. \quad (7)$$

With account to expressions (6) & (7) we obtain

$$\frac{d\sigma_r}{dr}=\frac{1}{r}\cdot\left(2\cdot M+2\cdot\sqrt{M^2+3\cdot M\cdot\sigma_r+N}\right), \quad (8)$$

where $M = R_b - R_{bt}$; $N = R_b R_{bt}$.

We obtain the following boundary conditions for the sphere: at $r = a$, $\sigma_r = 0$ and at $r = b$, $\sigma_r = P_0$.

Further, using “MathCad 15” software quipped with decision function “Odesolve” decision function, with account to admitted boundary conditions and expression (8) we obtain the values of end elements ultimate load and stressed state.

To illustrate usage of dependencies obtained, below given is calculation example.

3. Results and Discussion

Initial data regarding end elements for B40 class concrete [16, 18]: R_b = 22 MPa, R_{bt} = 1.4 MPa, d = 1174 mm, h = 750 mm

We can graphically determine design parameters of the vault: (Figure 4): a = 612 mm; b = 922 mm.

Results of practical calculations are given in Table 1 and demonstrated in Figure 8.

Obtained calculated value of maximum stress: P_0 = 51 MPa.

Figure 8 shows «stress-radius» dependency on the axis of symmetry of the vault.

Table 1. Radial and circumferential stresses depending on radius r.

r, mm	612	643	674	705	736	767	798	829	860	891	922
σ_r, MPa	0	–4	–9	–14	–19	–24	–30	–35	–40	–46	–51
σ_θ, MPa	–42	–52	–62	–71	–80	–89	–98	–107	–115	–124	–132

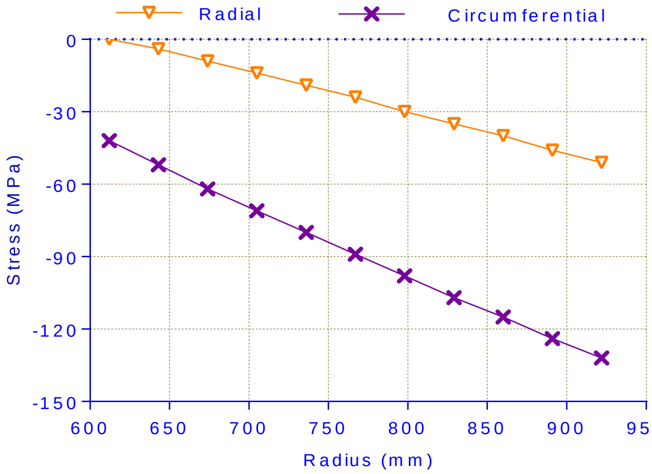

Figure 8. “Stress – radius” dependency diagram.

Development of end elements numerical calculation model with ANSYS WorkBench R18.1 software package [23, 24] will be based on results of analytical calculations made with the use of MathCad 15 software package.

Initial data regarding end elements for B40 class concrete [25]: R_b = 22 MPa, R_{bt} = 1.4 MPa, d = 1174 mm, h = 750 mm, E_b = 36000 MPa, Poison's ratio υ = 0.18.

In numerical calculation model we tried to take into account effect of biaxial compression on concrete strength. In this case, under the character of quantitative result evidencing the fact of concrete strength improvement in the state of biaxial compression we assumed the proposal set forth by [19], according to which we obtain the value $R_b^{''}$ = 35 MPa for B40 class concrete.

To build a 3D model of a concrete element at which three-axis compression occurs in the program ANSYS Workbench V18.1, we can use one of the following models:

1. Cam-Clay
2. Drucker-Prager
3. Joined Rock

4. Mohr-Coulomb

5. Porous Elasticity

In this article, the Drucker-Prager model for concrete under three-axis compression is chosen for the calculation.

At that, in order to calculate end elements with consideration of load bearing wall made of heavy armored cement, according to [16] let us assume the following initial parameters:

E_r = 44600 MPa, E_θ = 5980 MPa, E_z = 49900 MPa, $\nu_{\theta r}$ = 0.1, $\nu_{\theta z}$ = 0.2, ν_{zr} = 0.28, G = 15600 MPa.

Therefore, for numerical calculation of end elements we used calculation schemes represented by Figure 2, 2a – for vault thickness check, 2b – for stress state check.

Since structure under consideration is axisymmetric and active load is evenly distributed it means that ANSYS numerical method makes use of ¼ 3D-model [26–28]. At that, tangential stresses are represented by "Y"– direction while radial stresses – accordingly by "X" – direction [29–31]. Below given are some results of calculation made with consideration of concrete physical non-linearity.

Figure 9 shows isofields of stresses only in direction "Y" by which it is possible to determine the vault thickness. "+" means stretching, «–» means compression. Stretched zone, in such case, is not covered by calculation

Figure 10 shows tangential stresses in axis of symmetry of the end elements in the following load values: 10 MPa, 20 MPa, 25 MPa, 30 MPa. Please note that height of compressed zone, with increasing external load, is changing rather slightly.

Table 2 gives values of tangential stresses in axis of symmetry of end elements cross sections with reference to various loads and distance. Distance equal to 0 is an outermost fiber of the lower zone, 750 mm – outermost fiber of the upper zone.

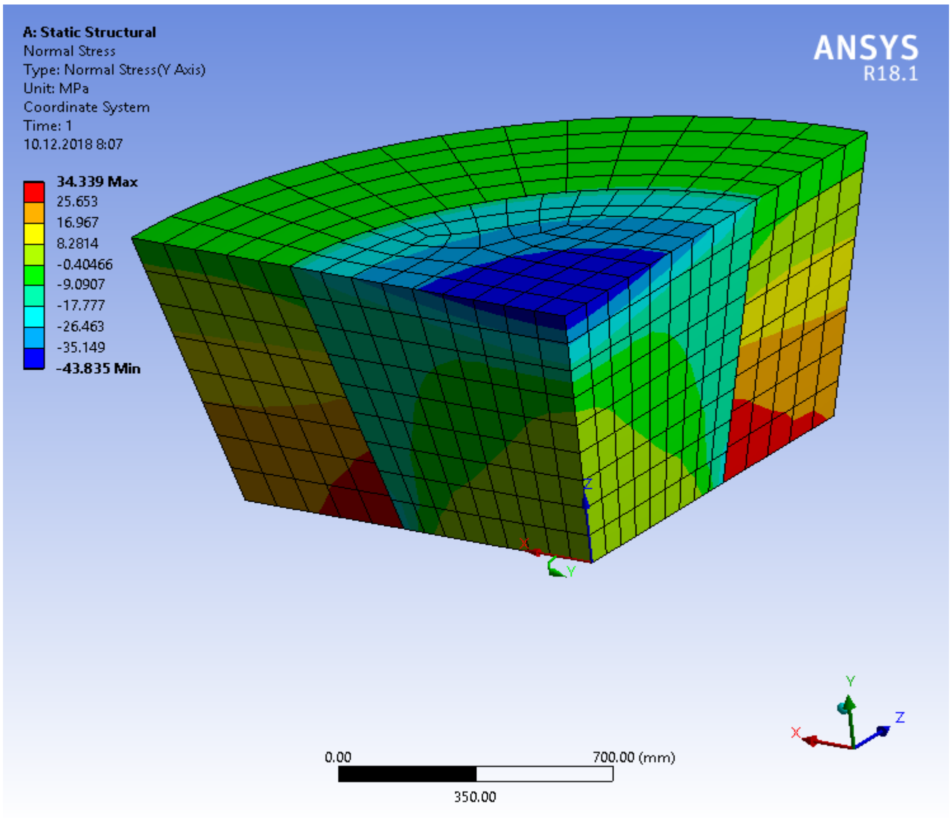

Figure 9. Isofields of stresses in axis "Y"

Table 2. Tangential stresses with reference to load and distance.

Distance,	0	75	150	225	300	375	450	525	600	675	750
10 MPa	1.0	1.0	0.9	0.9	0.9	0.9	0.3	–1.6	–5.1	–8.5	–12.8
20 MPa	1.0	1.0	0.9	0.9	0.9	0.9	0.8	–1.9	–9.9	–18.1	–28.4
25 MPa	1.0	1.0	0.9	0.9	0.9	0.8	0.7	–2.9	–13.0	–23.1	–35.8
30 MPa	0.9	0.9	0.9	0.9	0.9	0.8	–0.2	–5.5	–17.3	–29.1	–43.7

Figures 11, 12 and Tables 3, 4 represent comparison of accordingly radial and tangential stresses for analytical and numerical calculation of the end elements without consideration of the stretched zone.

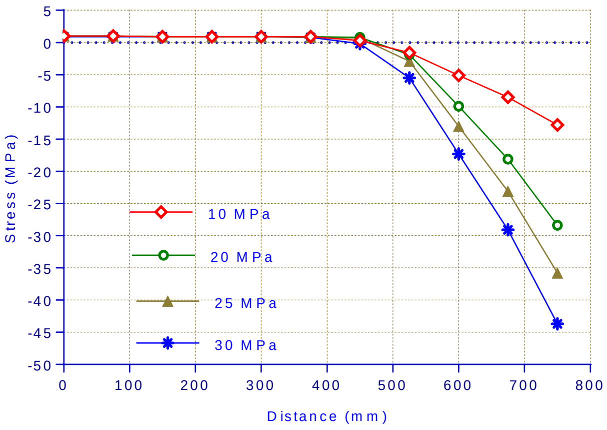

Figure 10. Tangential stresses in symmetry axis of the end elements according to ANSYS.

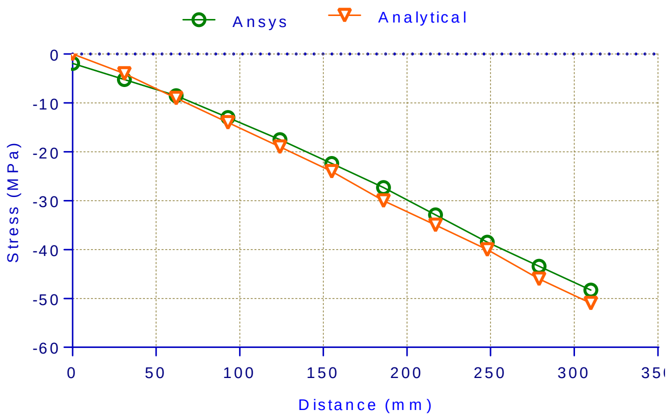

Figure 11. Comparison of radial stresses.

Table 3. Radial stresses in end elements compressed zone.

Distance, mm	0	31	62	93	124	155	186	217	248	279	310
Analytical, MPa	–0	–4	–9	–14	–19	–24	–30	–35	–40	–46	–51
Ansys, MPa	–1.9	–5.2	–8.5	–13.0	–17.5	–22.4	–27.3	–32.9	–38.5	–43.4	–48.3

Table 4. Circumferential stresses in end elements compressed zone.

r, mm	0	31	62	93	124	155	186	217	248	279	310
Analytical, MPa	–42	–52	–62	–71	–80	–89	–98	–107	–115	–124	–132
Ansys, MPa	–35.3	–42.6	–50.0	–60.0	–70.0	–80.9	–91.9	–104.4	–116.8	–127.7	–138.6

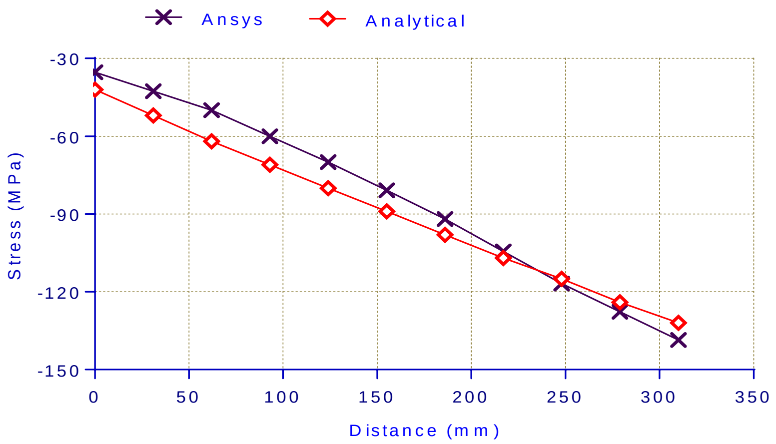

Figure 12. Comparison of circumferential stresses.

Comparison between analytical and numerical calculation models is displaying an essentially reasonable agreement. Moreover, analytical and numerical calculations of the spheric vault formed in the bottom in the course of works give no evident disagreements. Results of comparison between (i) results of analytical calculation of thick sphere and (ii) results of end elements behaviour calculated using ANSYS are unsurprising, i.e. it gives a predicted discrepancy reaching 19 %. This case is stipulated by ANSYS capabilities allowing to consider a more adequate geometrical pattern and, inter alia, to better consider concrete areas which are not made account to in analytical calculation model.

Investigations presented show that concrete end elements affected by cracks occurrence in the stretched area are subjected not to the sudden disintegration but to compressed spheric vault formation. At that, strength of element's spherical vault is more likely depending upon stiffness of load bearing wall – i.e. the lower its stiffness the lower its strength is and vice versa.

Let us note that from Tables 1, 2, 3 and 4 and Figures 11 and 12 we can view that difference between analytical and numerical calculation results is negligeable. Findings obtained cannot deplete the entire scope of issues associated with calculation and designing of this type of structures, however, enable the developer to determine overall dimensions, form and type of reinforcement at the stage of front end engineering design.

4. Conclusions

1. For concrete end elements of the high-pressure casings designed in the form of axisymmetric thick plates affected by ultimate loads and elements naturally affected by triaxial compression are characterized by spheric vault formation.

2. In virtue of assumed allowances and using proximal approach methodology we obtained spheric vault thickness determination formula.

3. Thus, we obtained original models of analytical and numerical calculations allowing to investigate stress state of end elements of high pressure casings designed in the form of axisymmetric thick plates resting on conical surface.

4. Comparison of calculation results obtained with the use of aforesaid methodology shows minor discrepancies (19 %) between analytical and numerical calculation models.

5. Results obtained may be used in design practice – at the stage of high pressure casing front end engineering design.

References

1. Serpik, I.N., Alekseytsev, A.V. Optimization of flat steel frame and foundation posts system. Magazine of Civil Engineering. 2016. 61(1). Pp. 14–24. DOI: 10.5862/MCE.61.2
2. Serpik, I.N., Alekseytsev, A.V., Balabin, P.Yu., Kurchenko, N.S. Flat rod systems: optimization with overall stability control. Magazine of Civil Engineering. 2017. 76(8). Pp. 181–192. DOI: 10.18720/MCE.76.16
3. Rybakov, V.A., Ananeva, I.A., Rodicheva, A.O., Ogidan, O.T. Stress-strain state of composite reinforced concrete slab elements under fire activity. Magazine of Civil Engineering. 2017. 74(6). Pp. 161–174. DOI: 10.18720/MCE.74.13.
4. Alekseytsev, A.V., Kurchenko, N.S. Deformations of steel roof trusses under shock emergency action. Magazine of Civil Engineering. 2017. 73(5). Pp. 3–13. DOI: 10.18720/MCE.73.1
5. Tusnina, O.A., Danilov, A.I. The stiffness of rigid joints of beam with hollow section column. Magazine of Civil Engineering. 2016. 64(4). Pp. 43–55. DOI: 10.5862/MCE.64.4
6. Zinkle, S.J., Busby, T.J. Structural materials for fission & fusion energy. Materials Today. 2009. No. 11(12). Pp. 12–19. DOI: 10.1016/S1369-7021(09)70294-9
7. Klueh, R.L. Reduced-activation bainitic and martensitic steels for nuclear fusion applications. Current Opinion in Solid State Materials Science. 2004. No. 3-4(8). Pp. 239–250. DOI: 10.1016/j.cossms.2004.09.004
8. Klueh, R.L., Hashimoto, N., Maziasz, P. New nano-particle-strengthened ferritic/martensitic steels by conventional thermo-mechanical treatment. Journal of Nuclear Materials. 2007. No. 367–370. Pp. 48–53.
9. Kohyama, A. The development of ferritic steels for DEMO blanket. Fusion Engineering and Design. 1998. No. 41. Pp. 1–6.
10. Blagoeva, D.T., Debarberis, L., Jong, M., Ten Pierick, P. Stability of ferritic steel to higher doses: Survey of reactor pressure vessel steel data and comparison with candidate materials for future nuclear systems. International Journal of Pressure Vessels and Piping. 2014. No. 122. Pp. 1–5. DOI: 10.1016/j.ijpvp.2014.06.001
11. Wang, S. Analytical evaluation of the dome-cylinder interface of nuclear concrete containment subjected to internal pressure and thermal load. Engineering Structures. 2018. 161. Pp. 1–7. DOI: 10.1016/j.engstruct.2018.01.063
12. Bílý, P., Kohoutková, A. Sensitivity analysis of numerical model of prestressed concrete containment. Nuclear Engineering and Design. 2015. No. 295. Pp. 204–214. DOI: 10.1016/j.nucengdes.2015.09.027
13. Hu, H.-T., Lin, J.-X. Ultimate analysis of PWR prestressed concrete containment under long-term prestressing loss. Annals of Nuclear Energy. 2016. No. 87. Part 2. Pp. 500–510. DOI: 10.1016/j.anucene.2015.10.005
14. Becker, G., Steffen, G., Notheisen, C. The design of the prestressed concrete reactor vessel for gas-cooled heating reactors. Nuclear Engineering and Design. 1989. No. 117. Pp. 333–340.
15. Bangash, Y. Safety and reliability of prestressed concrete reactor vessels. Nuclear Engineering and Design. 1979. No. 3(51). Pp. 473–486.
16. Morozov, V.I., Opbul, Eh.K., Van Phuc, P. To the calculation of thick plates of conical plates on the action of uniformly distributed load. Bulletin of Civil Engineers. 2017. No. 2(67). Pp. 66–73. DOI: 10.23968/1999-5571-2018-15-2-66-73
17. Morozov, V.I., Jurij, P. Nuclear Reactor Shell of Heavy Ferrocement. World Applied Sciences Journal. No. 23 (Problems of Architecture and Construction). 2013. Pp. 31–36. DOI: 10.5829/idosi.wasj.2013.23.pac.90007
18. Pukharenko, Yu., Aubakirova, I. Structural features of nanomodified cement stone. Architecture and Engineering. 2016. No. 1(1). Pp. 66–70. DOI: 10.23968/2500-0055-2016-1-1-66-70
19. Rybakov, V.A., Al Ali, M., Panteleev, A.P., Fedotova, K.A., Smirnov, A.V. Bearing capacity of rafter systems made of steel thin-walled structures in attic roofs. Magazine of Civil Engineering. 2017. No. 8. Pp. 28–39. DOI: 10.18720/MCE.76.3.
20. Jiang, J.-F., Xiao, P.-C., Li, B.-B. True-triaxial compressive behaviour of concrete under passive confinement. Construction and Building Materialsr. 2017. No. 156. Pp. 584–598. DOI: 10.1016/j.conbuildmat.2017.08.143
21. Matveeva, L., Efremova, M., Baranets, I. Studies of the morphology of waterproof coatings based on urethane isocyanate, alkyl-phenol-formaldehyde resin and dibutylin dilaurate using the high-resolution optical microscopy technique. Architecture and Engineering. 2018. No. 2(3). Pp. 43–47. DOI: 10.23968/2500-0055-2018-3-2-43-47
22. Andreev, V.I., Potekhin, I.A. Optimization on the strength of thick-walled shells. MGSU. 2011. 86 p.
23. Using ANSYS workbench for structural analysis. Anal. with ANSYS Softw. 2018. Pp. 511–540.

24. Yu, T. Finite element modeling of confined concrete-I: Drucker-Prager type plasticity model. Struct. Elsevier Ltd, 2010. 32(3). Pp. 665–679.
25. Malvar, L.J., Crawford, J.E., Wesevich, J.W. A plasticity concrete material model for DYNA3D. International Journal of Impact Engineering. 1997. No. 19(9-10). Pp. 847–873.
26. Lee, H.-H. Finite Element Simulations with ANSYS Workbench 18 Theory, Applications, Case Studies. 2018. CRC Press, 612 p.
27. Bao, J.Q. et al. A new generalized Drucker-Prager flow rule for concrete under compression. Engineering Structures. 2013. No. 56. Pp. 2076–2082
28. Chen, G., Hao, Y., Hao, H. 3D meso – scale modeling of concrete material in spall tests. Materials and Structures. 2015. No. 48(6). Pp. 1887–1899. DOI: 10.1617/s11527-014-0281-z
29. Babanajad, S.K., Gandomi, A.H., Alavi, A.H. New prediction models for concrete ultimate strength undertrue-triaxial stress states: An evolutionary approach. Advances in Engineering Software. 2017. No. 110. Pp. 55–68. DOI: 10.1016/j.advengsoft.2017.03.011
30. Hokeš, F., Kala, J., Hušek, M., Král, P. Parameter Identification for a Multivariable Nonlinear Constitutive Model inside ANSYS Workbench. Procedia Engineering. 2016. No. 161. Pp. 892–897.
31. Kral, P., Kala, J., Hradil, P. Verification of the elasto-plastic behavior of nonlinear concrete material models. International Journal Mechanics. 2016. No. 10. Pp. 175–181.
32. Chau, V.T., Li, C., Rahimi-Aghdam, S., Bažant, Z.P. The enigma of large-scale permeability of gas shale: Pre-existing or frac-induced? Journal of Applied Mechanics, Transactions ASME. 2017. No. 84(6). DOI: 10.1115/1.4036455
33. Shlyakhin, D.A. Forced axisymmetric vibrations of a thick circular rigidly fixed piezoceramic plate. Mechanics of Solids. 2014. No. 4(49). Pp. 435–444. DOI: 10.3103/S0025654414040086
34. Zhilin, P.A. Axisymmetric bending of a flexible circular plate with large displacements. Mechanics of Solids. 1984. No. 3(19). Pp. 128–134.
35. Wang, Y.Q., Huang, X.B., Li, J. Hydroelastic dynamic analysis of axially moving plates in continuous hot-dip galvanizing process. International Journal of Mechanical Sciences. 2016. No. 110. Pp. 201–216. DOI: 10.1016/j.ijmecsci.2016.03.010
36. Coccia, S., Imperatore, S., Rinaldi, Z. Influence of corrosion on the bond strength of steel rebars in concrete. Materials and Structures. 2016. No. 1-2(49). Pp. 537–551. DOI: 10.1617/s11527-014-0518-x
37. Huang, X., Lu, G., Yu, T. On the axial splitting and curling of circular metal tubes. International Journal of Mechanical Sciences. 2002. No. 11(44). Pp. 2369–2391. DOI: 10.1016/S0020-7403(02)00191-1
38. Zheng, W., Kwan, A.K.H., Lee, P.K.K. Direct tension test of concrete. ACI Materials Journal. 2001. No. 1(98). Pp. 63–71.
39. Stolarski, T., Nakasone, Y., Yoshimoto, S. Engineering Analysis with ANSYS Software (Second Edition). Elsevier. Amsterdam, 2018. 562 p.
40. Alekseytsev, A.V., Akhremenko, S.A. Evolutionary optimization of prestressed steel frames. Magazine of Civil Engineering. 2018. 81(5). Pp. 32–42. DOI: 10.18720/MCE.81.4.
41. Tusnina, O.A., Danilov, A.I. The stiffness of rigid joints of beam with hollow section column. Magazine of Civil Engineering. 2016. 64(4). Pp. 43–55. DOI: 10.5862/MCE.64.4
42. Tusnina, O.A. Finite element analysis of crane secondary truss. Magazine of Civil Engineering. 2018. 77(1). Pp. 68–89. DOI: 10.18720/MCE.77.7

Contacts:

Valery Morozov, +79217907963; morozov@spbgasu.ru
Eres Opbul, +79213170155; fduecnufce@mail.ru
Phan Van Phuc, +79533472586; phucprodhv@gmail.com

Инженерно-строительный журнал

ISSN 2071-0305

сайт журнала: http://engstroy.spbstu.ru/

DOI: 10.18720/MCE.86.9

Работа осесимметричных толстых плит, опертых по конической поверхности

В.И. Морозов*, Э. Опбул, Ф. Ван Фук,
Санкт-Петербургский государственный архитектурно-строительный университет, Санкт-Петербург, Россия

Ключевые слова: корпус высокого давления; торцевой элемент; осесимметричная плита; несущая способность; стенки (структурные элементы); внутреннее давление; нагрузка; шпонка; коническая поверхность.

Аннотация. Настоящая статья посвящена аналитическому и численному исследованиям работы торцовых элементов корпусов высокого давления применительно для ядерных реакторов. Поскольку реальным энергетическим выбором человечества в будущем станет широкое использование ядерной энергии, которая может вырабатываться в корпусах высокого давления, то создание методики расчета торцовых элементов в виде осесимметричных толстых плит, опертых по конической поверхности при действии равномерно распределенной нагрузки, является актуальным. С использованием известных критериев прочности бетона и принятых предпосылок в аналитическом способе расчета, а также на основе численного программного комплекса ANSYS WORKBENCH выполнены расчеты по определению величины предельной нагрузки и напряженного состояния. При этом расчеты выполнены с учетом шпоночного сопряжения толстой плиты с несущей силовой стенкой корпуса высокого давления, в том числе в зависимости от ее достаточно высокой в одном и слабой в другом случаях (переменной) жесткости. Приводится сравнительный анализ результатов расчетов, где обнаруживается адекватность предлагаемых методов расчета. Получены оригинальные способы аналитического и численного расчетов для исследования напряженного состояния торцевых элементов корпусов высокого давления в виде осесимметричных толстых плит, опертых по конической поверхности. Для работы торцевых элементов под нагрузкой свойственно образование сферического свода, где закономерно возникает напряженное состояние, характерное при трехосном сжатии бетона. Приведенные исследования показывают, что в торцевых элементах из бетона с образованием трещин в растянутой зоне не наступает внезапное разрушение, а формируется сжатый сферический свод. При этом прочность сферического свода элемента в большей степени зависит от жесткости несущей силовой стенки: чем меньше жесткость, тем меньше прочность и наоборот. Получены следующие научные результаты: – для торцовых элементов в виде толстых осесимметричных плит в предельных значениях нагрузки характерно образование сферического свода; – на основе принятых допущений, приближенным способом, получена формула по определению толщины сферического свода; – получены оригинальные способы аналитического и численного расчетов для исследования напряженного состояния торцевых элементов корпусов высокого давления в виде осесимметричных толстых плит, опертых по конической поверхности; – сравнение результатов расчетов обнаруживают незначительные расхождения аналитического и численного методов.

Литература

1. Серпик И.Н., Алексейцев А.В. Оптимизация системы стальной плоской рамы и столбчатых фундаментов // Инженерно-строительный журнал. 2016. №1(61). С. 14–24. DOI: 10.5862/MCE.61.2
2. Серпик И.Н., Алексейцев А.В., Балабин П.Ю., Курченко Н.С. Плоские стержневые системы: оптимизация с контролем общей устойчивости // Инженерно-строительный журнал. 2017. № 8(76). С. 181–192. DOI: 10.18720/MCE.76.16
3. Рыбаков В.А., Ананьева И.А., Родичева А.О., Огидан О.Т. Напряженно-деформированное состояние фрагмента сталежелезобетонного перекрытия в условиях огневого воздействия // Инженерно-строительный журнал. 2017. № 6(74). С. 161–174. DOI: 10.18720/MCE.74.13.
4. Алексейцев А.В., Курченко Н.С. Деформации стальных стропильных ферм при ударных аварийных воздействиях // Инженерно-строительный журнал. 2017. № 5(73). С. 3–13. DOI: 10.18720/MCE.73.1

5. Туснина О.А., Данилов А.И. Жесткость рамных узлов сопряжения ригеля с колонной коробчатого сечения // Инженерно-строительный журнал. 2016. № 4(64). С. 40–51. DOI: 10.5862/MCE.64.4
6. Zinkle S.J, Busby T.J. Structural materials for fission & fusion energy // Materials Today. 2009. № 11(12). Pp. 12–19. DOI: 10.1016/S1369-7021(09)70294-9
7. Klueh R.L. Reduced-activation bainitic and martensitic steels for nuclear fusion applications // Current Opinion in Solid State Materials Science. 2004. № 3-4(8). Pp. 239–250. DOI: 10.1016/j.cossms.2004.09.004
8. Klueh R.L., Hashimoto N., Maziasz P. New nano-particle-strengthened ferritic/martensitic steels by conventional thermo-mechanical treatment // Journal of Nuclear Materials. 2007. № 367–370. Pp. 48–53.
9. Kohyama A. The development of ferritic steels for DEMO blanket // Fusion Engineering and Design. 1998. № 41. Pp. 1–6.
10. Blagoeva D.T., Debarberis L., Jong M., Ten Pierick P. Stability of ferritic steel to higher doses: Survey of reactor pressure vessel steel data and comparison with candidate materials for future nuclear systems // International Journal of Pressure Vessels and Piping. 2014. № 122. Pp. 1–5. DOI: 10.1016/j.ijpvp.2014.06.001
11. Wang S. Analytical evaluation of the dome-cylinder interface of nuclear concrete containment subjected to internal pressure and thermal load // Engineering Structures. 2018. № 161. Pp. 1–7. DOI: 10.1016/j.engstruct.2018.01.063
12. Bílý P., Kohoutková A. Sensitivity analysis of numerical model of prestressed concrete containment // Nuclear Engineering and Design. 2015. № 295. Pp. 204–214. DOI: 10.1016/j.nucengdes.2015.09.027
13. Hsuan-Teh H., Jun-Xu L. Ultimate analysis of PWR prestressed concrete containment under long-term prestressing loss // Annals of Nuclear Energy. 2016. № 87. Part 2. Pp. 500–510. DOI: 10.1016/j.anucene.2015.10.005
14. Becker G., Steffen G., Notheisen C. The design of the prestressed concrete reactor vessel for gas-cooled heating reactors // Nuclear Engineering and Design. 1989. № 117. Pp. 333–340.
15. Bangash Y. Safety and reliability of prestressed concrete reactor vessels // Nuclear Engineering and Design. 1979. № 3 (51). Pp. 473–486.
16. Morozov V.I., Pbpublic., Fuk F.V. to the calculation of thick plates of conical plates on the action of uniformly distributed load // Bulletin of civil engineers. 2017. № 2 (67). Pp. 66–73. DOI: 10.23968/1999-5571-2018-15-2-66-73
17. Morozov V.I., Jurij P. Nuclear Reactor Shell of Heavy Ferrocement // World Applied Sciences Journal. № 23 (Problems of Architecture and Construction). 2013. Pp. 31–36. DOI: 10.5829/idosi.wasj.2013.23.pac.90007
18. Pukharenko Yu., Aubakirova I. Structural features of nanomodified cement stone // Architecture and Engineering. 2016. № 1(1). Pp. 66–70. DOI: 10.23968/2500-0055-2016-1-1-66-70
19. Рыбаков В.А., Ал Али М., Пантелеев А.П., Федотова К.А., Смирнов А.В. Несущая способность стропильных систем из стальных тонкостенных конструкций в чердачных крышах // Инженерно-строительный журнал. 2018. № 8(76). С. 28–39. DOI: 10.18720/MCE.76.3.
20. Jiang J., Xiao P., Ben-ben L. True-triaxial compressive behaviour of concrete under passive confinement // Construction and Building Materialsr. 2017. № 156. Pp. 584–598. DOI: 10.1016/j.conbuildmat.2017.08.143
21. Matveeva L., Efremova M., Baranets I. Studies of the morphology of waterproof coatings based on urethane isocyanate, alkyl-phenol-formaldehyde resin and dibutylin dilaurate using the high-resolution optical microscopy technique // Architecture and Engineering. 2018. № 2(3). Pp. 43–47. DOI: 10.23968/2500-0055-2018-3-2-43-47
22. Andreev V.I., Potekhin I.A. optimization on the strength of thick-walled shells. MGSU. 2011. 86 p.
23. Using ANSYS workbench for structural analysis. Anal. with ANSYS Softw. 2018. Pp. 511–540.
24. Yu T. Finite element modeling of confined concrete-I: Drucker-Prager type plasticity model // Struct. Elsevier Ltd, 2010. № 32 (3). Pp. 665–679.
25. Malvar L.J., Crawford J.E.. Wesevich J.W. A plasticity concrete material model for DYNA3D // International Journal of Impact Engineering. 1997. № 19(9-10). Pp. 847–873.
26. Lee H.-H. Finite Element Simulations with ANSYS Workbench 18 Theory // Applications, Case Studies. 2018. CRC Press. 612 p.
27. Bao J. Q. et al. A new generalized Drucker-Prager flow rule for concrete under compression // Engineering Structures. 2013. № 56. Pp. 2076–2082.
28. Chen G., Hao Y., Hao H. 3D meso – scale modeling of concrete material in spall tests // Materials and Structures. 2015. № 48(6). Pp. 1887–1899. DOI: 10.1617/s11527-014-0281-z
29. Babanajad S.K., Gandomi A.H., Alavi A.H. New prediction models for concrete ultimate strength undertrue-triaxial stress states: An evolutionary approach // Advances in Engineering Software. 2017. № 110. Pp. 55–68. DOI: 10.1016/j.advengsoft.2017.03.011
30. Hokeš F., Kala J., Hušek M., Král P. Parameter Identification for a Multivariable Nonlinear Constitutive Model inside ANSYS Workbench // Procedia Engineering. 2016. № 161. Pp. 892–897.
31. Kral P., Kala J., Hradil P. Verification of the elasto-plastic behavior of nonlinear concrete material models // International Journal Mechanics. 2016. № 10. Pp. 175–181.
32. Chau V.T., Li C., Rahimi-Aghdam S., Bažant Z.P. The enigma of large-scale permeability of gas shale: Pre-existing or frac-induced? // Journal of Applied Mechanics, Transactions ASME. 2017. № 84(6). DOI: 10.1115/1.4036455
33. Shlyakhin D.A. Forced axisymmetric vibrations of a thick circular rigidly fixed piezoceramic plate // Mechanics of Solids. 2014. № 4(49). Pp. 435–444. DOI: 10.3103/S0025654414040086
34. Zhilin P.A. Axisymmetric bending of a flexible circular plate with large displacements // Mechanics of Solids. 1984. № 3(19). Pp. 128–134.
35. Wang Y.Q., Huang X.B., Li J. Hydroelastic dynamic analysis of axially moving plates in continuous hot-dip galvanizing process // International Journal of Mechanical Sciences. 2016. № 110. Pp. 201–216. DOI: 10.1016/j.ijmecsci.2016.03.010
36. Coccia S., Imperatore S., Rinaldi, Z. Influence of corrosion on the bond strength of steel rebars in concrete // Materials and Structures. 2016. № 1-2(49). Pp. 537–551. DOI: 10.1617/s11527-014-0518-x

37. Huang X., Lu G., Yu T. On the axial splitting and curling of circular metal tubes // International Journal of Mechanical Sciences. 2002. № 11(44). Pp. 2369–2391. DOI: 10.1016/S0020-7403(02)00191-1
38. Zheng W., Kwan A.K.H., Lee P.K.K. Direct tension test of concrete // ACI Materials Journal. 2001. № 1(98). Pp. 63–71.
39. Stolarski T., Nakasone Y., Yoshimoto S. Engineering Analysis with ANSYS Software (Second Edition). Elsevier. Amsterdam, 2018. 562 p.
40. Алексейцев А.В., Ахременко С.А. Эволюционная оптимизация предварительно напряженных стальных рам // Инженерно-строительный журнал. 2018. № 5(81). С. 32–42. DOI: 10.18720/MCE.81.4.
41. Туснина О.А., Данилов А.И. Жесткость рамных узлов сопряжения ригеля с колонной коробчатого сечения // Инженерно-строительный журнал. 2016. № 4(64). С. 40–51. DOI: 10.5862/MCE.64.4
42. Туснина О.А. Конечно-элементное моделирование и расчёт подкраново-подстропильной фермы // Инженерно-строительный журнал. 2018. № 1(77). С. 68–89. DOI: 10.18720/MCE.77.7

Контактные данные:

Валерий Иванович Морозов, +79217907963; эл. почта: morozov@spbgasu.ru
Эрес Опбул, +79213170155; эл. почта: fduecnufce@mail.ru
Фан Ван Фук, +79533472586; эл. почта: phucprodhv@gmail.com

Magazine of Civil Engineering. 2019. 86(2). Pp. 105–118
Инженерно-строительный журнал. 2019. № 2(86). С. 105–118

Magazine of Civil Engineering

journal homepage: http://engstroy.spbstu.ru/

ISSN 2071-0305

DOI: 10.18720/MCE.86.10

Shear lag phenomenon in the tubular systems with outriggers and belt trusses

H. Arshadi*, A. Kheyroddin,
Semnan University, Semnan, Iran
** E-mail: hamed.arshadi@semnan.ac.ir*

Keywords: framed tube system; tube-in-tube system; trussed tube system; bundled tube system; shear lag.

Abstract. Development of technology facilitates construction of tall buildings. One of the common kinds of them is Tubular systems, divided into different types: framed tube, tube-in-tube, trussed tube and bundled tube systems. The main problem of tubular systems is the shear lag phenomenon that decreases the bending rigidity and moment resistance of the structures. In this paper, the phenomenon of shear lag in all kinds of steel tube systems is investigated analytically. In order to reach this objective, sixteen steel multi-storey tubular structures with the same plan, but a with a different number of stories and different tubular systems were designed by ETABS software based on AISC. Then the shear lags of each structure in different elevations are calculated by using the linear response spectrum analysis. The results show that nearly in the upper half of the structures the negative shear lag happens. Besides all, the formula was derived for each system with regard to the analyses data with linear regression examine by SPSS software, which showed that there is a significant relation between shear lag and three independent variables: story number, height ratio and distance from the web of the structures.

1. Introduction

For centuries, mankind have been mesmerized by the notion of building tall structures, which developments in the domain of civil engineering made this dream feasible. By passing the time, different types of lateral resistant systems for high-rise buildings were introduced, as in: tubular systems (tube-in-tube, braced tube and others), braced tall buildings, moment resisting systems, suspended tall buildings with a concrete core and so on. The lateral-resisting system is an important part of the structural system that supports the building against the lateral loads including: wind and earthquake loads. The majority of the lateral-resisting systems can be categorized into three types: 1) shear wall systems, 2) frame systems, and 3) the combination of the previous two systems. Shear wall systems are rather common choices in many earthquake-prone countries. They provide high strength and stiffness simultaneously in the direction of their placement. These structural elements are vertical ones which endure lateral loads in their plane. Core wall systems (shear walls) can reduce the lateral displacement by the core bending resistance and their displacement mode is flexural. However, these systems have a conspicuous problem which is putting the lateral resisting elements close to the neutral axes. This reduces their efficiency because they do not absorb a considerable amount of tensions and their bending rigidity index is low. Then, Fazlur Khan suggested the resisting core had to be put on the perimeter of a structure in which the normal stresses are greater, instead of being close to neutral axes [1]. Besides, their bending rigidity index increases by putting resisting elements far from the central axes. This new system was called a tubular (tube) system. The layout of this system can be rectangular, triangular or square. This system can be recognized as an evolved form of the flexural frames. By passing the time, this system changed gradually into the bundled tube, braced tube and tube-in-tube ones to get rid of the problems of the first generation system of tubular systems. In simple terms, a tube system can be defined as a three-dimensional system that utilizes the entire building perimeter to resist lateral loads [1].

One of the most important deficiencies of the tubular systems is the shear lag phenomenon. The influence of shear lag is to increase axial stresses in the corner columns and reduce the same ones in the inner columns of both the flange and the web panels [2], as shown in Figure 1. This decreases the moment resistance and

Arshadi, H., Kheyroddin, A. Shear lag phenomenon in the tubular systems with outriggers and belt trusses. Magazine of Civil Engineering. 2019. 86(2). Pp. 105–118. DOI: 10.18720/MCE.86.10.

Аршади Х., Хайруддин А. Феномен сдвигового запаздывания в трубчатых системах с вынесенными опорами и поясами ферм // Инженерно-строительный журнал. 2019. № 2(86). С. 105–118. DOI: 10.18720/MCE.86.10

bending rigidity of structures. Furthermore, the designers intend to design all the exterior columns as typically as the same as the critical one and this leads to losing materials and money. There are many strategies to overcome this problem: using bundled tube systems, mega bracings, deep spandrel beams, and mega columns at the corner of the structures. However, the most efficient is using the spandrel beams (shear rigidity index), because they distribute forces between columns more uniformly. Then the more shear rigidity index, the less shear lag is observed. It is worth mentioning that the belt trusses (along with the outriggers) can be used to prevent the rotation of the internal tube, decreasing its drift and moment, diminishing shear lag and so on, they also connect exterior columns to each other. The outriggers connect them to the columns of internal tube. These two can distribute forces among columns more uniformly.

Mazinani et al. investigated the shear lag effect of on the braced tube and framed tube systems under the wind load and the efficiency of each structure was evaluated using the linear response spectrum analysis to obtain the shear lag [3]. They show there is a relatively less shear lag in all the braced tube configurations compared to the framed tube structural system and the shear lag is not proportional to the lateral displacement. With respect to the results, optimum braced tube configuration in term of lower shear lag caused by lateral loads is presented. A simple formula for shear lag is suggested based on the cantilever method modification by Kazeminia and Khoshnudian [4]. They also realized that although by increasing the number of stories shear lag factor decreases, this index gets constant (independent of the storey number) in tall buildings more than 30 stories. Naderpour and Kheyroddin investigated the effect of increasing the stiffness of the columns and spandrel beams on decreasing the shear lag index in the concrete tubular systems, they concluded that increasing the dimension of the columns is not as effective as increasing the stiffness of spandrels [5]. Kheyroddin and Zahiri-Hashemi investigated the influence of geometric configurations of the multi-stoery bracing on the shear lag behavior of the braced tube structures and they finally proposed empirical equations to provide the optimum number of the stories that should be braced, in order to exert minimum shear lag on the structures [6]. Gaur and Goliya researched the mitigating shear lag in tall buildings [7]. Thanh Dat et al. investigated on the shear lag effect on the design of high-rise buildings [8]. Also, Sreevalli and Priya studied the effect of the shear wall area on the seismic behavior of the multi-storied building tube-in-tube structures [9]. Patels compared different types of the tubular systems in terms of different aspects such as: the time period, the lateral displacements, the base shear and the steel consumption [10]. Finally, Salehi and Khaloo studied the shear lag factor in the long structures with the pipeline system in tubes under the wind load [11].

1.1. Tube systems

The general behavior of tall buildings is similar to a cantilever column with the medium slenderness ratio. With regard to the high shear flexibility, their behavior is different from the ordinary structural columns which have flexural behavior. Then the general probabilistic buckling mode of the tall buildings is not only the flexural mode, but also shear mode or even a combination of them. Besides, not just these modes appear in the buckling modes, yet they also appear in torsion or transverse torsion modes.

One of the most challengeable issues in the domain of tall building designs is choosing the lateral resisting system. There are different types of lateral resisting systems such as: bracings, moment resisting systems, suspended tall buildings with concrete or steel braced core and so on. There are two criteria in choosing the lateral resisting tools: 1) bending rigidity index (BRI), 2) shear rigidity index (SRI). The BRI is achieved by calculation of the inertia moment of the columns about the geometric central axes, and then the farther the columns from the central axes, the more BRI is reached. The SRI asserts the amount of continuous performance between the columns, in other words, columns should be connected well with each other through the structure. An ideal SRI = 100 is shear walls without openings. Obviously, lateral resisting systems like tall buildings with central core seem inefficient in terms of having low bending rigidity indices. Besides, because of the distribution of stress through the structure, putting resistant elements near to the neutral axes which have less normal stresses leads to decreasing efficiency of them. Accordingly, for the first time, Fazlur Khan suggested the resisting core (or elements) had to be put in the perimeter of a structure in which the normal stresses and flexural rigidity indices are higher [1]. These systems called tube systems which have different kinds: framed tube system, tube-in-tub system, trussed tube systems and bundled tube systems, which will be discussed in the paragraphs below.

1.1.1. Framed tube systems

The notion behind the framed tube systems is to create a completely three-dimensional structural system that involves the entire building inertia to resist lateral loads. The main objective is to obtain higher efficiency for lateral load resistance in tall buildings. Then the suggested system for a framed tube one is closely spaced exterior columns and deep spandrel beams rigidly connected together. The closer the distribution to that of a rigid box cantilevered at the base, the more efficient the system is considered to be. The requirements necessary to create a wall-like tube structure is to place columns on the exterior approximately close to each other and to use deep spandrels joined to those columns [12]. With regard of the height and plan dimensions of the structure, the spacing of exterior columns is usually 3–4.6 m, as an example: a spacing as close as 1.0 m was used for the 110-story World Trade Center twin towers, New York. Figure 2 shows the plan and isometric views of the framed tube systems.

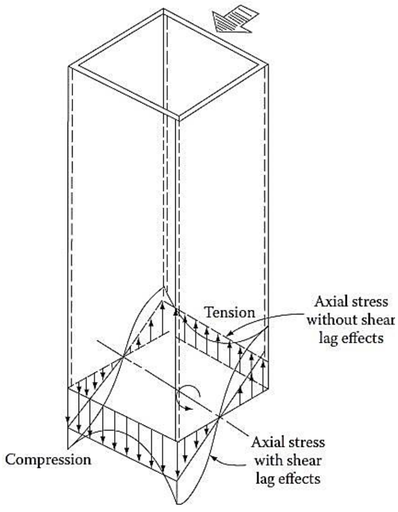

Figure 1. Axial stress distribution in a square hollow tube with and without shear lag [1].

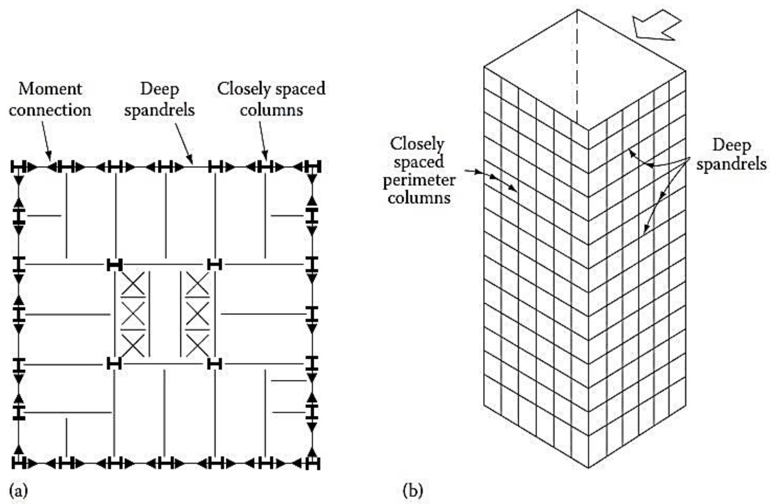

Figure 2. Framed tube: (a) schematic plan; (b) isometric view [1].

The efficiency of the system is directly related to the building height-to-width ratio, the plan dimensions, the spacing, and the size of the columns and spandrels. It is worth saying that generally the exterior columns have to bear up under the gravity and lateral loads and the contribution of the interior columns to lateral load resistance is negligible. Moreover, the interior columns should not be spaced closely to each other like the exterior ones. It is suggested that the floor system should be designed as a rigid diaphragm, distributes the loads to all elements in proportion to their stiffness. In the tube structures, usually, the strong bending axis of the columns are placed toward the face of the building to have the most efficient bending action. The frames parallel to the lateral load act as the web of the performed tube, while the frames normal to the loads act as flanges. In the case of being under bending out of the lateral forces, the framed tube acts as a cantilever beam in which the columns on the opposite sides of the neutral axis like the flanges are subjected to the normal (tensile and compressive) forces. In addition, the frames parallel to the direction of the lateral load like the webs are subjected to in-plane bending, leads to a shear rocking action associated with an independent rigid frame [13]. These systems were the first generation of the tube systems and accordingly had some disadvantages like the shear lag and closely spacing columns which limited architectural choices.

1.1.2. Tube-in-tube systems

In these systems, there are two resistant systems: two exterior and interior tubes which consist of closely spaced columns and deep spandrels that connect them. The interior tube which acts as a sort of core usually occupies 30 to 40 % of the whole area of the structural plan. This tube is the place where staircases and elevators are put in. Columns between these tubes are designed under the gravity loads, and only columns of tubes should be resistant to lateral loads. The roof should be rigid so that either of the tubes act in accordance with each other completely. The advantage of the systems is the architectural aspect because there are a few columns between the tubes and this gives vast space for many purposes [2]. The exterior tube acts like a frame and the interior tube acts like a shear wall, then they have the same interaction as the frames and shear walls. Namely, the interior tube supports the exterior tube against the lateral displacement at the bottom, and the exterior tube supports the interior one at the top. Accordingly, at the top of the structure, the interior tube has a negative effect and creates negative shear and moment which leads to a strengthening of the exterior tube so that it takes additional shear and moment. Then, the stiffness of the interior tube (the dimension of columns and spandrel beams) should be decreased to prevent this repercussion. The schematic plan of the tube-in- tube systems is demonstrated in Figure 3.

1.1.3. Trussed tube systems (*TTS*)

For super-tall buildings, the dense grid of beam and column members of a framed tube has a drastic effect on the façade architecture. Trussed tube systems have the least number of diagonals on each façade and making the diagonals intersect at the same point of the corner column (The number of spans and stories covered by diagonals should be at the same). The system is known as a tubular system because the fascia diagonals aren't just creating a truss in the plane, but also interact with the trusses on the perpendicular faces to affect the tubular behavior. In order to optimize the trussed tube action, the vertical columns should be replaced with closely spaced diagonals in both directions. The diagonally braced tube is by far the most usual method of increasing the efficiency of the framed tube [6]. The diagonals connected to the columns at each intersection, virtually eliminate the effects of shear lag in both the flange and web of frames. As a result, the structure behaves more like a braced frame, with greatly diminished bending of the exterior columns and girders. Accordingly, the columns can be spaced at larger distances and the size of the columns and spandrels get smaller than in the framed tube systems, which lead to allowing larger size windows. Moreover, in the trussed tube systems, bracings contribute to improving the performance of the tube in carrying the gravity load. Figure 4. indicates a trussed tube building.

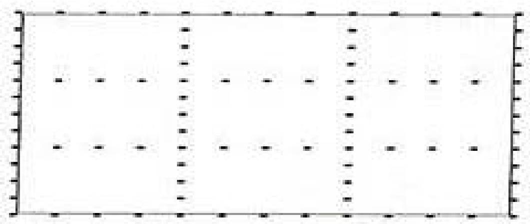

Figure 3. The schematic plan of tube-in-tube systems.

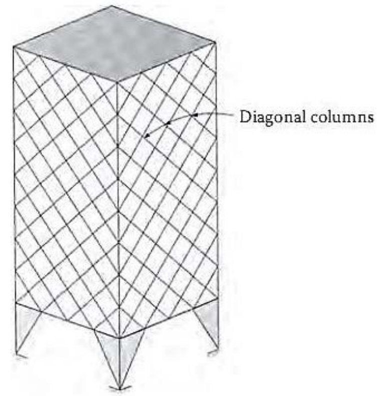

Figure 4. Trussed tube building.

1.1.4. Bundled tube systems (*BTS*)

One of the solutions to control the shear lag is to add web and flange frames as the tubular cells, which contribute to distribute forces more uniformly between columns. These systems are called bundled tubes which consist of multi tubes. Moreover, tubular systems are applicable to prismatic profiles, including a variety of non-rectilinear plans, such as circular, hexagonal, triangular, and other polygonal shapes. However, for buildings with significant vertical offsets, the discontinuity in the tubular forms introduces serious inefficiencies. A bundled tube that can be configured with the multiple cells, on the other hand, provides for vertical offsets without much loss in efficiency. Additionally, it allows for wider column spacing that would be possible with a single cell tube [12]. In principle, many building shapes can be configured using bundled tubes. The structural principle behind the bundled tube concept is that the interior rows of columns and spandrels act as interior webs minimizing the shear lag effects. Without their beneficial effect, the exterior columns in a framed tube toward the center of the building would play a negligible role in resisting the overturning moment. Figure 5. shows a bundled tube building.

1.2. Shear lag phenomenon

Although a framed tube is quite an efficient system for the tall buildings, it does have outstanding idiosyncrasies due to the shear lag effects. The shear lag phenomenon is to increase axial stresses in the corner columns and reduce them in the inner columns of both the flange and the web panels which lead to decreasing moment resistance and their efficiency [15].

The shear lag effects in tubular buildings are as similar as the solid-wall hollow tube. The major resistance comes from the web panels which deform in a manner that some columns are in tension and others are in compression. The web frames are exposed to the in-plane flexural and racking action associated with an independent rigid frame. The primary action is modified by the flexibility of the spandrel beams which increases the axial stresses in the corner columns and decreases those in the interior columns. The main interaction between the web and flange frames occurs via the axial displacements of the corner columns. The more flexible spandrel beam, the less the deformation. Every successive interior column will face a smaller deformation and hence a lower stress than the outer ones. The stresses in the corner column will be greater than those from the pure tubular action, and those in the inner columns will be less. The stresses in the inner columns lag behind those in the corner columns (shear lag). Because the column stresses are distributed less effectively than in an ideal tube, the whole capacity of the structure is not used and this makes the moment resistance and the flexural rigidity be reduced [16].

There are many strategies in order to solve this irregularity: using the bundled tube systems (increasing the number of the web and flange frames to decrease the distance of columns from them), mega bracings (they assist to distribute forces better between columns),the deep spandrel beams, the mega columns at the corner of the structures (because of having more stresses at the corners and less ones in interior columns), the belt trusses and outriggers (they assist to distribute forces better between columns) and so on. However, the most efficient solution is the spandrel beams, because they have a key role in the uniform distribution of forces between columns. The more shear rigidity index (SRI), the less the shear lag. It is worth mentioning that belt trusses (along with the outriggers) can be used to prevent the rotation of the internal tube, decreasing its moment and drift, diminishing the shear lag and so forth. The Belt trusses connect exterior columns to each other and the outrigger connect them to the columns of internal tube. These can distribute forces among columns uniformly.

It is expected that the shear lag decreases through moving to the top of the structure. Nearly, at the three-fourths of the height of structures, a shear lag index (defined as the proportion of the axial force of the tubular columns to the axial force of the central column of the tube) gets 1.0. In higher spots than the mentioned spot, this ratio gets inverted (negative shear lag happens). As will be shown in this paper, the belt trusses and outriggers draw down this point to approximately the half of the height of the structure. The positive and negative shear lag phenomena are shown in Figure 6.

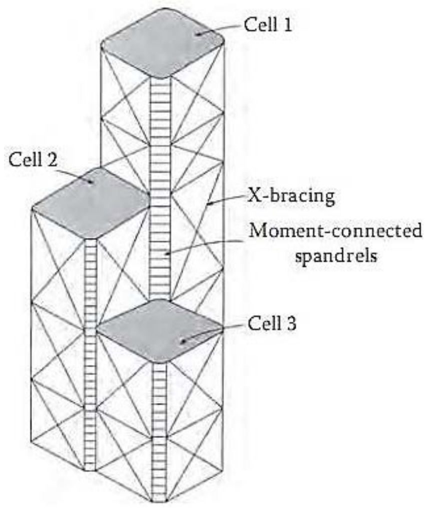

Figure 5. Trussed tube building.

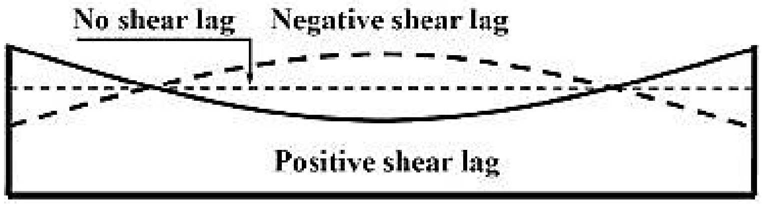

Figure 6. The positive and negative shear lags phenomena [1].

In this study the shear lag in different types of the tube systems is studied. To reach this goal, 16 models of the steel tube, tube-in-tube, bundled tube and braced tube systems (43, 54, 67, 79 stories) are designed by the ETABS software. Their geometric characteristics are regarded as the same. It is also assumed that earthquake loads are more dominant than the wind loads. By the linear dynamic analysis, the shear lag of each columns in different levels is obtained and compared with each other. The results showed that the belt trusses and outriggers drew down the point that positive shear lag turned into negative (which is at the half of the general height). Also, it is shown that by moving up to the middle of the structures, shear lag decreased and got close to 1.0, and then it progressed inversely to the top of the structures. Namely, the axial force of the central column got bigger than the others. Lastly, it was tried to investigate statistically to find a formula for each of the systems with multi-variable linear regression examines with SPSS version 23.0 software based on the results of the linear dynamic analyses (to reach a general estimation of the weight of effective variables on the shear lag phenomenon). These formulations showed that there was a significant relation between the shear lag and some dependent variables such as the story number, the height ratio and the distance from the web of the structures. The statistical analyses done in this research, indicated that the aspect ratio of the structures had not a significant role in the shear lag index.

2. Methods

2.1. Structural Modelling

In this study, 16 models: four types of tubular systems (the framed tube, tube-in-tube, trussed tube and bundled tube system) with four numbers of stories (43, 54, 67, 79 stories) have been designed based on AISC [17] to investigate on shear lag effect. Figures 7–10 demonstrate the plan view of different types of tubular models used in this study. It is worth mentioning that the green points show the location of the columns, and the blue lines with the white borders around them show the location of the outriggers which connect the tubular columns to each other. Moreover, the ordinary blue lines indicate the beams, which connect none-tubular columns to each other. The models are 60m × 60m in their plan and the overall height of the structures are 172, 216, 268 and 316 m, respectively. Therefore, the aspect ratios of structures (calculated by Eq. (1)) are much greater than 1.5π and then they are considered super tall buildings [12].

$$\frac{a}{H} \geq 1.5\pi, \tag{1}$$

where a is the dimension of the core structure and H is the overall height of the structure.

Furthermore, the belt trusses and outriggers are used in the infrastructure stories of the structures to limit their lateral displacement as discussed in the paragraphs above. The outriggers are created by connecting the exterior columns with their counterpart columns in the interior or cell tubes by bracings. Also, the belt trusses are created by connecting exterior columns with each other by bracings either. In tall buildings, usually, an infrastructure story is assigned to every 20 stories. Yet in this study, for 43, 54, 67 and 79-story structures, the belt trusses and outriggers are put respectively in every 13, 17, 21 and 25 stories. It is worth mentioning that the optimum location of the outriggers for the optimum performance is at $(1/n + 1)$, $(3/n + 1)$, $(4/n + 1)$,… and $(n/n + 1)$ height locations, where *n* is the number of outriggers. The highest floor of the structures is not an appropriate place to put the belt trusses on, because it has less efficiency in order to decrease drift and moment amounts. All of the models have only three stories with belt trusses and outriggers, so that their shear lag results can be compared with each other. The spaces between tubular columns are 3 m and between the non-tubular columns are 6 m. The former are designed under lateral and gravity loads, then they should connect rigidly with each other. The latter is designed for just the gravity loads and they should not connect rigidly to each other. The overall height of each story is 4 m. All of the tube-in-tube systems have an interior tube with the dimension of 20 m×20 m located in the middle of their plan. The cell tube dimensions in the bundled tube systems are 20 m×20 m too. In the braced tube systems, 4 pairs of mega bracings are used on each edge of exterior tubes. The floors are regarded rigid and the alternative loading is used for slabs.

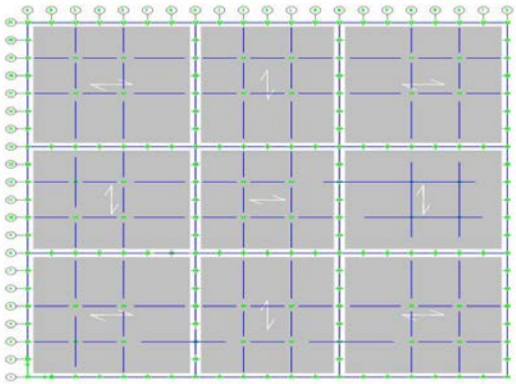

Figure 7. The plan view of bundled tube models.

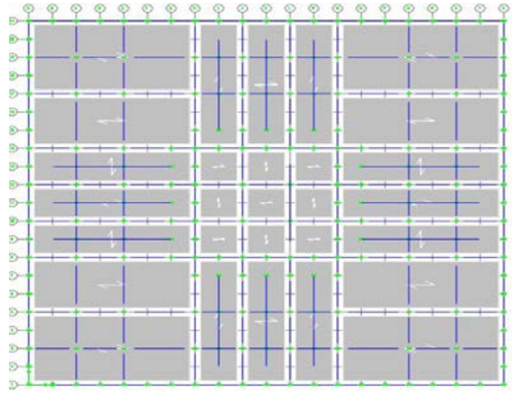

Figure 8. The plan view of trussed tube-in-tube models.

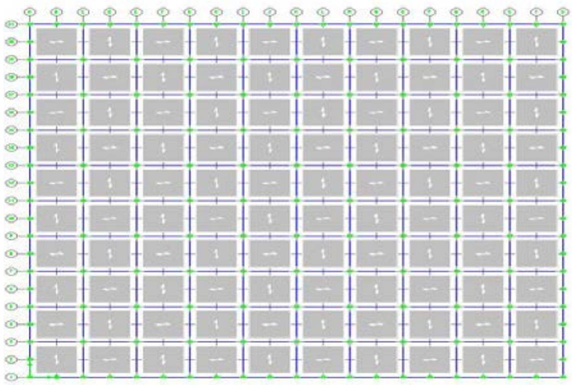

Figure 9. The plan view of framed tube models.

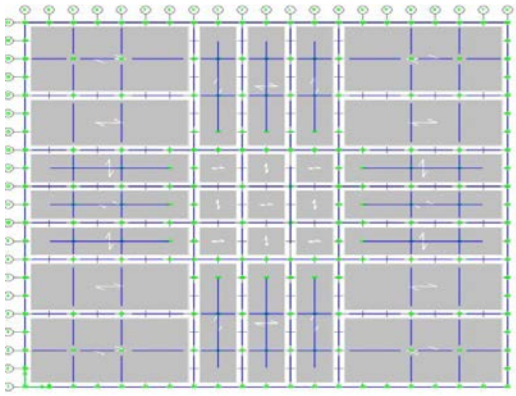

Figure 10. The plan view of tube-in-tube models.

As shown in Figures 11 and 12, the trussed tube system is considered as the tube-in-tube system which has mega braces. These mega braces are installed in the tube-in-tube systems in order to decrease their lateral displacements. Modeling and analyses are done by ETABS software based on the instructions of the AISC [17]. The shear lag factors in the first floor, the floors corresponding to a fourth and three fourths of structure height, and the highest floor is calculated, because at the bottom of the structure the positive shear lag factor and at the top of structures, the negative shear lag factor is critical. The shear lag factor (SF) is defined in Eq. (2).

$$SF = \frac{P_u}{P_c}, \tag{2}$$

where P_u is the axial force of tubular columns and P_c is the axial force of the central columns of tubes. One of the assumptions in this paper is that the earthquake loads are more critical than the wind loads. Therefore, the comparison of the models is done based on the seismic analysis in the following sections. Lastly, the stress ratios of the elements in designing are considered between 0.7 and 0.9, so that the results of models could be comparable.

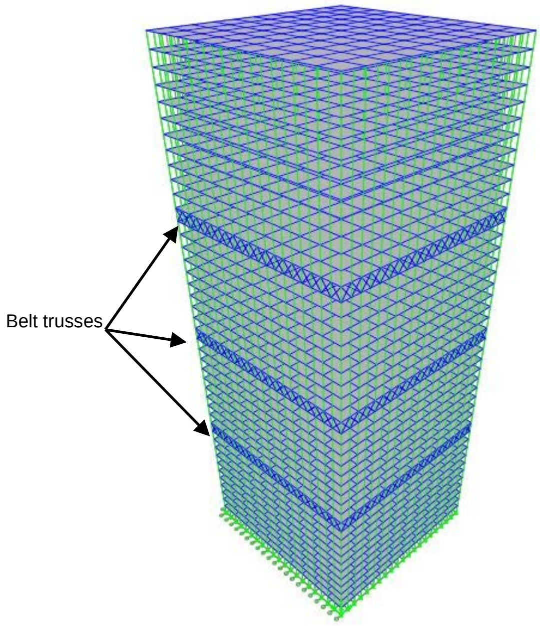

Figure 11. The 3D view of 43-story systems with belt trusses without mega braces.

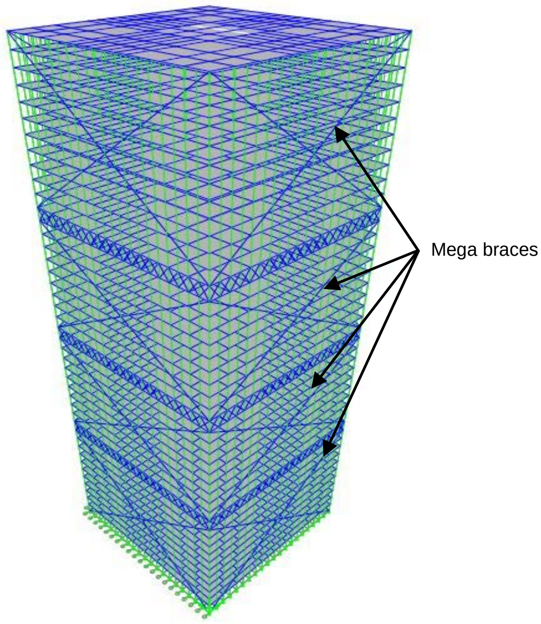

Figure 12. The 3D view of 43-storey trussed system (with mega braces and belt trusses).

2.2. Definition of parameters of analyses

The *ST37* steel with yield strength of 2400 kg/cm^2 for the elements. Gravity loads consist of 3.1 KN/m^2 as dead load and 1.5 KN/m^2 as a live load for the roof, and for all of the other floors: 4.4 KN/m^2 as dead load and 3.4 KN/m^2 as a live load.

The design-seismic load is calculated by using the Iranian Code of Practice for Seismic Resistant Design of Buildings [18]. According to this code requirement, dynamic analysis using the design spectrum of this code is necessary for buildings which are taller than 50 m height. In addition, the base shear force due to the dynamic analysis must be scaled to the base shear resulted from the linear static analysis, if that is smaller than the static base shear. The base shear force is calculated by Eq. (3).

$$V = ((ABI/R) * W), \tag{3}$$

where I is the importance factor,

R is the response modification factor,

A is the design spectral acceleration,

B is the response factor and W is the seismic weigth of the structures.

The following factors are chosen for all structures to compute the base shear force: the I factor in these structures was considered as 1.0. it is also assumed that the structures are located on a site with soil classification of type II (375 < Vs < 750 m/s, in which Vs is the velocity of shear waves) and in a region with a very high level of seismicity risk (A = 0.35). With regard to the fact that the *R* factor for tubular structures has not been mentioned in this code, in this study *R* factor set equal to 9.0 (which is similar to the response modification factor of the special steel moment-resisting frames with bracings). This amount is reasonable because the tubular systems are the developed format of the moment resisting systems. Moreover, the *R* factor of these structures obtained around 10.0 based on the research of Kim et al. [19]. Because of having outriggers and belt trusses which decrease the natural period of structures our modification factor should be less than 10.0. Besides, Zahiri-Hashemi and Kheyroddin considered the amount of *R* factor of the braced tube systems equal to 7.0 [6] which is too low based on researches of Kim et al. [19].

By the linear response spectrum analysis and static analyses, the shear lag of each column in different levels was found and compared with each other. It is worth saying that the calculation of the flange shear lag factor of levels where negative shear lag happens with the spectral dynamic analysis is meaningless, because of its negative sign, the spectral dynamic analysis could not show levels which signify the changing axial force (because of the SRSS method of modal combination). In order to verify the ETABS software and calibration, the models analyzed by Mashhadialii et al. [20] are taken into consideration.

3. Results and Discussion

In this part, it is decided to consider the geometry specifications of the plan of the structures as the same and use the same number of belt trusses and outriggers, with regard to our objective (the investigation on the trend of shear lag in different tubular systems and comparing them to each other). Firstly, the maximum amounts of the axial forces in the columns of the tubes or cell tubes were acquired by the linear dynamic (modal) analysis. Secondly, the shear lag factors are calculated by Eq. (2) and their diagrams are depicted as demonstrated in the figures below. In this study, only the shear lag factor of the tubular columns in between the web panels (flange shear lag factor) is calculated.

3.1. Studying shear lag of models

As mentioned before, one of the shortcomings of the tubular systems is shear lag, which decreases the moment resistance and efficiency of these systems against lateral loads. Generally and expectedly, the shear lag factor decreases with moving up towards the top of the structures. One of the reasons is the decreasing of the shear forces by moving up to the top of the structures. Usually, at the three-fourths of the height of the structures, the shear lag index reach to 1.0 and the distribution of forces between columns become uniform. On the other hand, higher than this point, the shear lag trend gets inverted by moving to the top of the structures. Namely, the axial force of the central column of each tube gets greater than the surrounding ones closer to the web and flange panels in that tube. As shown in Figures 13–16, this point in these structures is drawn down and located in the middle of the height of the structures. This may be out of the presence of the belt trusses and outriggers which draw down the mentioned point to that point. Accordingly, for positive shear lag factor, the more critical location is at the bottom of the structure and for the inverted on is at the top of the structures. In order to design economically, stronger columns should be put in the corners (web or flange panels) at the bottom and the central columns should be more reinforced than other ones at the half top. Figures 13-16 show the shear lag factor of the tubular columns in the flange of the structures along with the IDs of the columns. The column IDs are the number of columns in the plan from left to right.

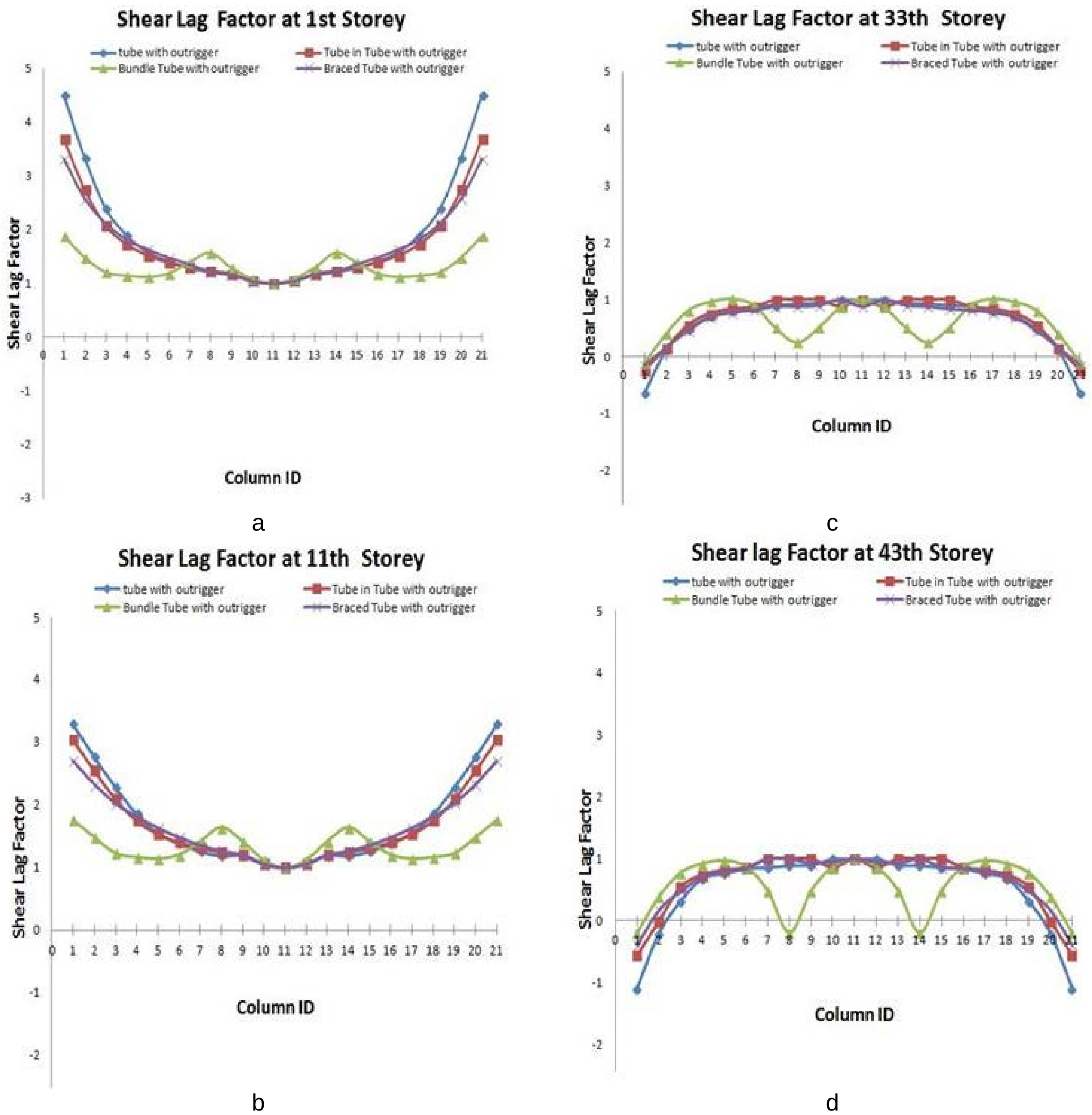

Figure 13. The flange shear lag factor in different stories of 43-story building: a) shear lag index at 1st story, b) shear lag index at 11th story, c) shear lag index at the 33rd story and d) shear lag index at 43rd story.

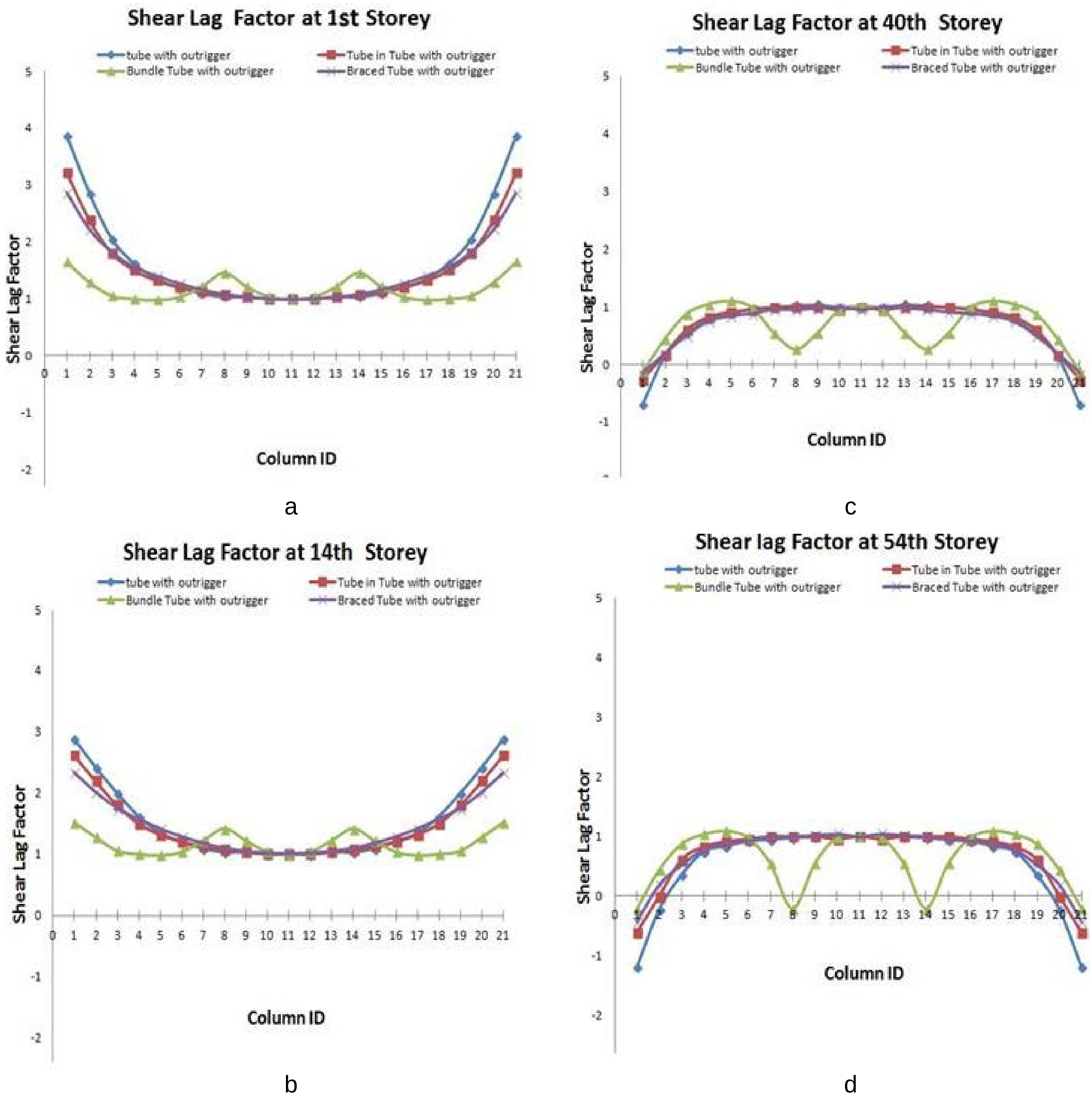

Figure 14. The flange shear lag factor in different stories of 54-story building: a) shear lag index at 1st story, b) shear lag index at 14th story, c) shear lag index at 40th story and d) shear lag index at 54th story.

As demonstrated in figures above, the trend and quantity of the shear lag indices in each type of the tubular systems remain similar to each other by increasing the number of stories. The number of stories indicates both the height and weight of structures, then the quantity of shear lag indices cannot be dependent on these two parameters. The results of the stochastic analysis with multi-variable linear regression method (as discussed in the paragraphs below) verify this fact too. It is also seen that the most uniform force distribution between columns is observed in tube-in-tube systems. In these systems, the interior and exterior tubes by the means of deep spandrels are connected and work with each other. This may be the reason for rather uniform distribution of forces. However, their distribution is not completely uniform and this uniformity is more located in the central area of the tubes. By moving towards the corners, drastic changes (increasing) in shear lag indices are seen. These differences are more at the lower stories. Generally, by increasing the number of the stories, a negligible improvement is seen in force distributions of the tube-in-tube systems. This phenomenon is expected, because increasing the number of the stories in buildings with more stories than 30 is ineffective on the shear lag improvement [4].

On the other hand, the worst force distribution among columns is observed in the framed tube systems. However, this system along with the trussed tube and tube-in-tube systems has similar amounts in the middle of the tubes and their amounts diverge by moving toward the corners. It is also observed that adding mega-braces to the tube-in-tube systems improves the uniform distribution of forces a little and the difference between them is more located at the corner of the tubes. Strengthening of mega-braces and using an effective number of mega braces may end up better improvement. The most irregular shape is shown in the bundled tube systems. In these systems, columns closer to the web panels have shear lag factor close to 1.0, but by getting distant, drastic changes happen. Except for the framed tube systems, the (positive) shear lag has more uniform distribution at the bottom of the structures than the shear lag factor at the top of them.

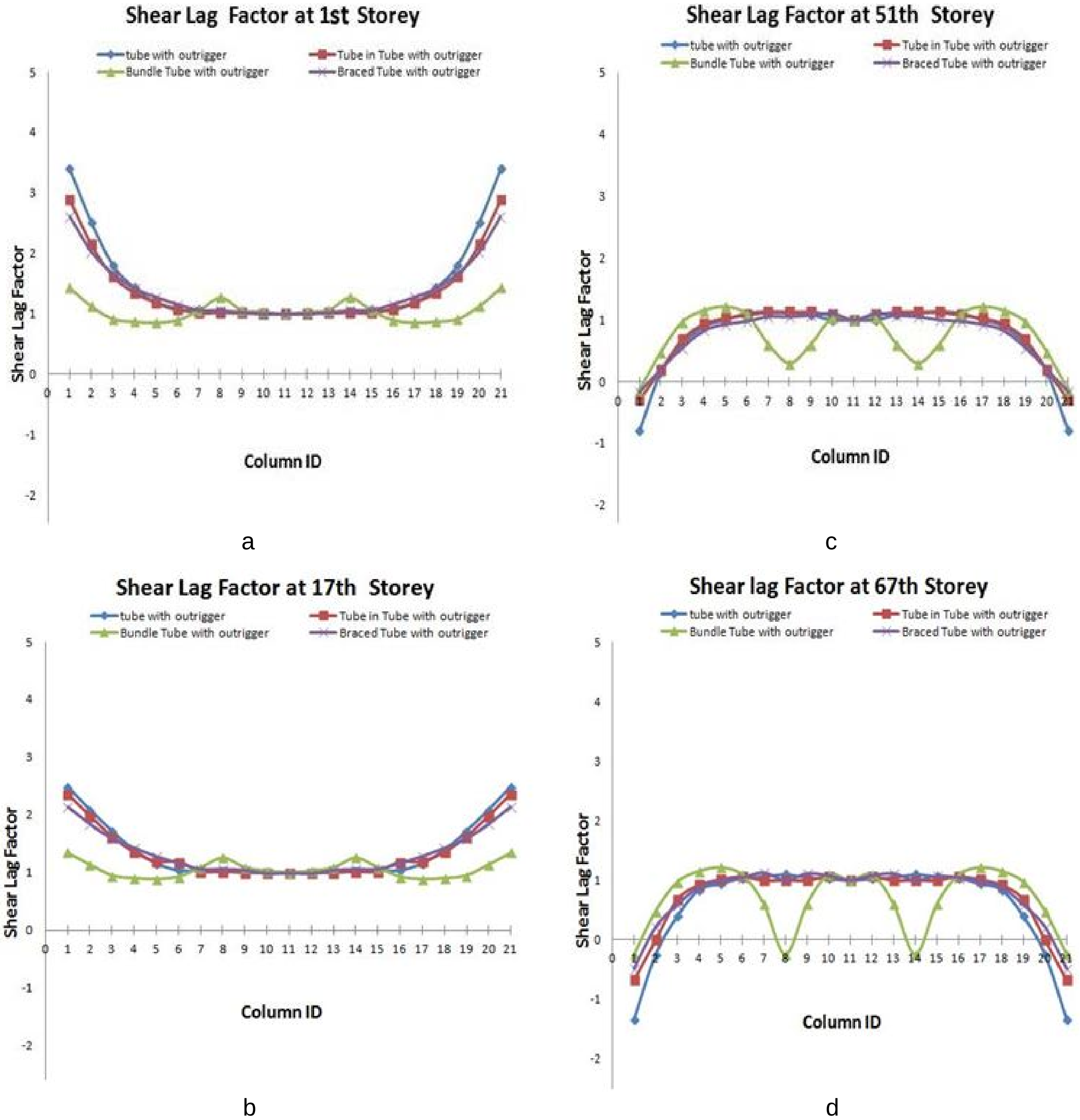

Figure 15. The flange shear lag factor in different stories of 67-story building: a) shear lag index at 1st story, b) shear lag index at 17th story, c) shear lag index at 51st story and d) shear lag index at 67th story.

1.2. Formulation of the shear lag factor for different tubular systems

In this section, it is tried to find a relation between independent variables (the story number, the height ratio-the ratio of the height of section cuts to the overall height, the aspect ratio and distance from the web of the structures) and the shear lag index with multi-variable linear-regression examine by SPSS software. This examine tells us if there is a significant relationship between the independent (predictor) variables and it also can give weights (coefficients) to the variables to reach a linear formulation. In other words, it says how much the output is explained by the independent variables.

Firstly, the linear regressions indicated that there is a significant relationship between the mentioned variables (except for the aspect ratio, which was excluded from the regression). Because the significance area (*Sig.* factor) is nearly 0.0001 (less than 5 %) in all types of the tubular systems. The *Sig.* factor shows whether there is a significant relationship between the variables or not. If the *Sig.* factor is less than 0.0001, there is a significant relationship. The *Sig.* factor is equivalent to the P-values in the linear regression. The p-value is the level of marginal significance within a statistical hypothesis test representing the probability of the occurrence of a given event. The p-value is used as an alternative to reject points to provide the smallest level of significance at which the null hypothesis would be rejected. The linear regressions demonstrated that the *Sig.* factor of aspect ratio (*a*) is 0.744 then the software excludes this variable from the regression, because it hasn't a significant role in the shear lag amount.

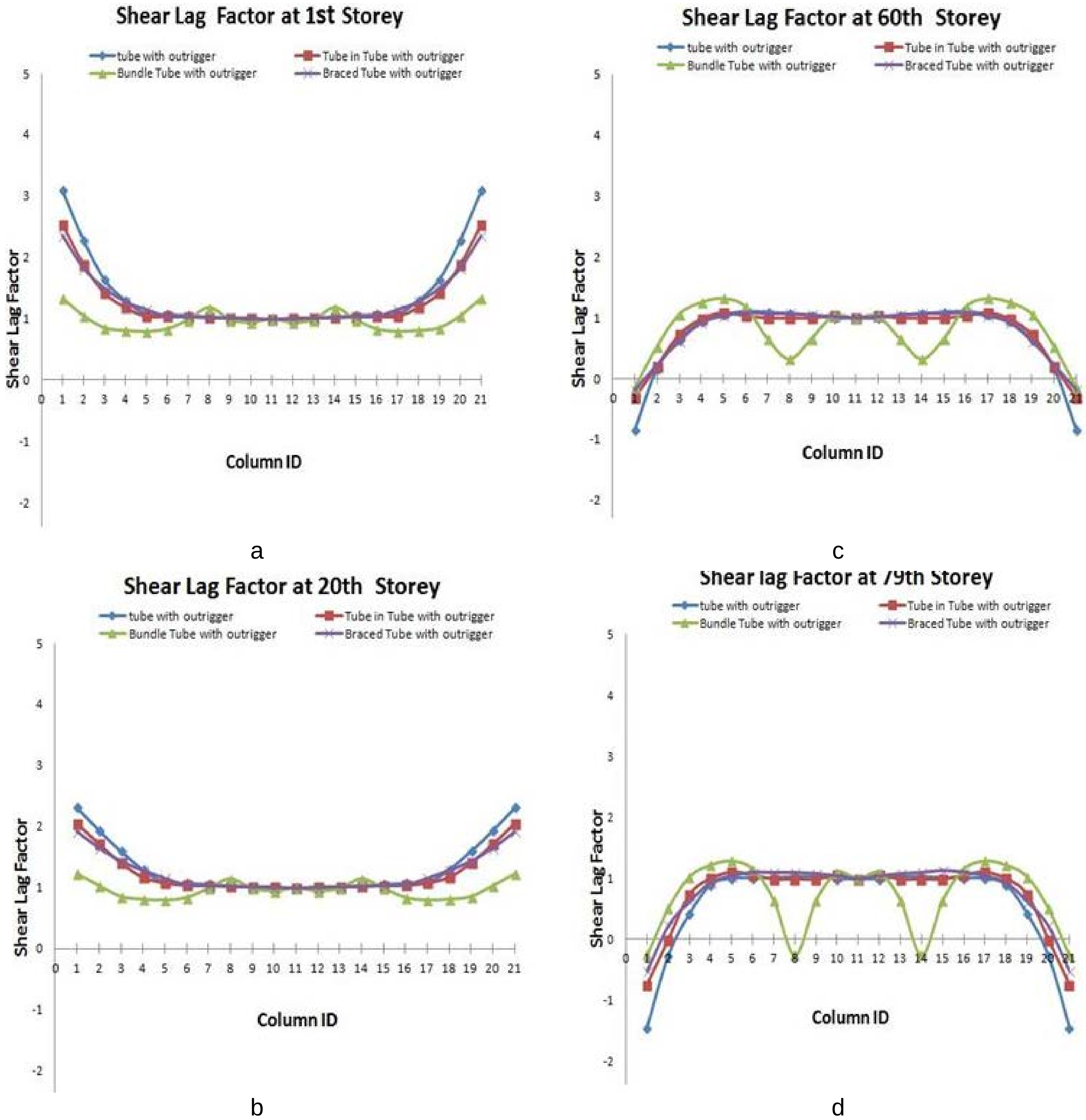

Figure 16. The flange shear lag factor in different stories of 79-story building: a) shear lag index at 1st story, b) shear lag index at 20th story, c) shear lag index at 60th story and d) shear lag index at 79th story

Secondly, the linear regressions showed that the dependence percentage of shear lag on these variables is about 30 % (R^2 factor), it means that nearly 70 % of the shear lag index are dependent on other factors that should be regarded in the regression such as the shear rigidity indices (rigidity of spandrels), the slenderness, the span lengths and so on. The R^2 factor shows how many percentages of shear lag as a dependent variable are explained by these independent variables (predictor variables).It is worth saying that R^2 is a statistical measure of how the data are close to to the fitted regression line. It is also considered as the coefficient of determination, or the coefficient of multiple determination for multiple regression.

Finally, it is tried to find formulations for the shear lag indices with the linear regression for each type of the tubular systems. These formulas can give us a general view about the effect of the mentioned factors on the shear lag amounts. As shown in the regressions, the storey number (the overall height of the structures) has the least influence on the shear lag (which verifies the research of Kazeminia and Khoshnudian [4], that asserts this parameter effect on the shear lag decreases in the structures with more than 30 stories). The number of stories is the representative of the height and weight of structures, and then the amount of the shear lag indices cannot be dependent on these two parameters. Figures 17-20 verify this issue too. Table 1 shows *Sig.* and R^2 factors for each kind of tubular systems. Moreover, although it was expected that by increasing the aspect ratio and changing the displacement mode of the structures from shear to flexural, the shear lag increases, it was seen that the aspect ratio does not have any effect on the shear lag index and it was excluded from the linear regressions by the software based on the results. The bundled tube systems have the greatest R^2 factor and the tube systems have the least one, namely, the effect of the mentioned independent variables on the shear lag index of the bundled tube systems is the most and on the tube systems is the least.

Table 1. The parameters of tubular systems.

Tubular systems	R^2 **(*R*-squared)**	***Sig.***
Framed tube buildings	0.294	**0/0001
Braced tube-in-tube buildings	0.325	**0/0001
Tube-in-tube buildings	0.307	**0/0001
Bundled tube buildings	0.307	**0/0001

The Eq. (4) shows the linear formulations for the framed tube systems:

$$L_T = -0.005S - 1.13H - 0.007D + 2.07, \quad (4)$$

where L is the shear lag index amount, S is the story number, H is the height ratio (the ratio of the height of the story in which the section is cut to the overall height of the structure) and D is the distance between columns and the nearest web of the structures. The standard error of the estimate is 0.70957.

The Eq. (5) shows the linear formulations for the braced tube systems:

$$L_{BT} = -0.004S - 0.83H - 0.004D + 1.78, \quad (5)$$

where L, S, H, and D are as the same as the ones defined in Eq. (4). The standard error of this estimate is 0.47781.

The Eq. (6) shows the linear formulations for the tube-in-tube systems:

$$L_{TT} = -0.005S - 0.9H - 0.006D + 1.9, \quad (6)$$

where L, S, H, and D are as the same as the ones defined in Eq. (4). The standard error of this estimate is 0.55040.

The Eq. (7) shows the linear formulations for the bundled tube systems:

$$L_{BuT} = -0.003S - 0.534H + 0.04D + 1.15, \quad (7)$$

where L, S, H, and D are as the same as the ones defined in Eq. (4). The standard error of this estimate is 0.34643.

As shown in Eq. (7), the role of the storey number and the column distances (from the web of the structures) in the braced tube systems is very negligible, which the amount of their *Sig.* factor verifies it. Because they are 0.054 and 0.612 respectively, which is too low, so they can be excluded from the formulation. There is another factor in the linear regression named β-effective which shows the approximate effect of each independent variable on the shear lag amounts. Figures 17–20 show the β-effective factor of the effective variables on the shear lag amounts. It is observed in Figure 20 that β-effective factor of the distance and storey number in the braced tube system is negligible, this phenomenon can be because of the more uniform distribution of forces among columns in these systems. Also, due to the presence of the numerous webs and decreasing the distance of the columns from the webs, the role of D (the distance from the nearest webs of the structures) in the bundled tube system gets more considerable than the other tubular systems.

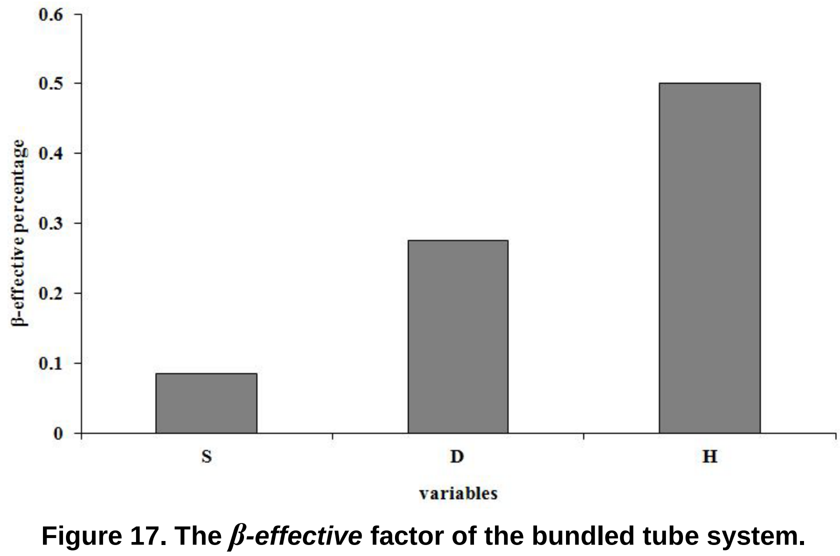

Figure 17. The *β-effective* factor of the bundled tube system.

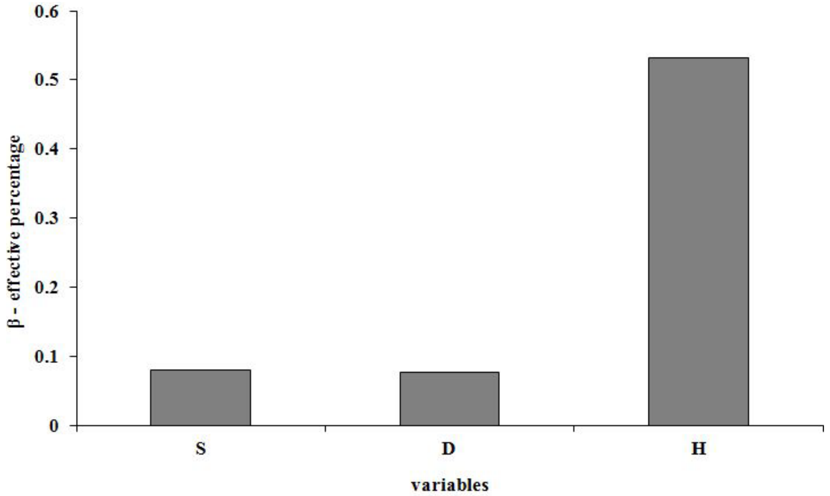

Figure 18. The *β-effective* factor of the tube system.

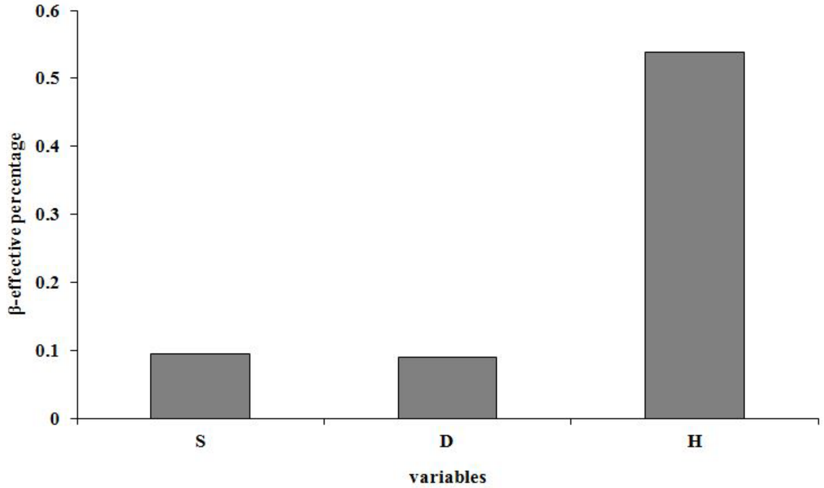

Figure 19. The *β-effective* factor of the tube-in-tube system.

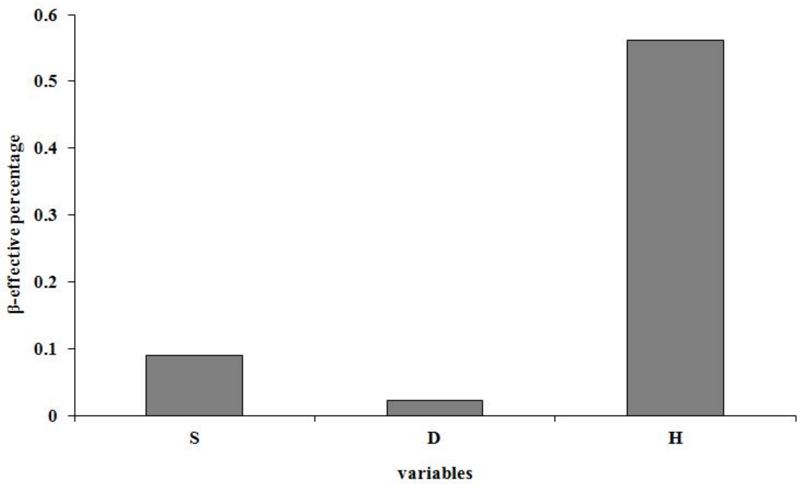

Figure 20. The *β-effective* factor of the braced tube system.

It is worth saying that regressions in order to have more inclusive results need more data. These formulas can be regarded as approximate criteria to estimate the effects of the mentioned independent variables on the shear lag index.

4. Conclusion

In this paper, the shear lag indices in different types of the tube systems are perused and statistically analyzed. To reach this goal, 16 models of steel tube, tube-in-tube, bundled tube and braced tube systems (with 43, 54, 67, 79 stories) are created by the ETABS software. Their geometric characteristics are as the same. It was also assumed that earthquake loads are more dominant than wind loads. By linear response spectrum analysis, the shear lag of each column in different levels was found and compared with each other. The results show that:

1) Belt trusses and outriggers draw down the point that the shear lag amounts get 1.0, to the half of the general height of the structures. By moving toward the top of the structure, shear lag decreases and gets 1.0, and then it progresses inversely to the top of the structures.

2) Then, it is tried to investigate statistically the data reached from the linear response spectrum analysis, to find formulations for all four types of tube systems by multi-variable linear regression examine with entering method (by SPSS version 23.0). This showed a significant relation between the shear lag index and the independent variables (the storey number, the aspect ratio of structures, the height ratio and the distance from the web of the structures).

3) It is observed that the most important independent variable is the height ratio and the least important one is the storey number (or the distance from the nearest web in the braced tube systems) in the linear regressions.

4) Although it was expected that by increasing the aspect ratio and changing the displacement mode of structures from the shear mode to the flexural one, the shear lag increases, it is seen that the aspect ratio does not have any effect on the shear lag index and was excluded from the linear regressions by the software.

References

1. Taranath, B. Structural analysis and design of tall buildings: steel and composite construction. FL. USA. CRC Press, Taylor & Francis Group.2011. 722 p.
2. Taranath, B. Wind, and earthquake resistant buildings: structural analysis and design. FL. USA.CRC Press. Boca Raton. 2004. 912 p.
3. Mazinani, I., Jumaat, M.Z., Ismail, Z., Chao, O.Z. Comparison of shear lag in a structural steel building with framed tube and braced tube. Journal of Structural Engineering and Mechanics. 2014. Vol. 49. No. 3. Pp. 297–309.
4. Kazeminia, H.R., Khoshnudian, F. The seismic behavior of tall buildings and the solutions to solve the shear lag problem. The 5th national congress of civil engineering, Ferdowsi University of Mashhad. 2010. Mashhad. Iran. Pp. 1–13. (Persian).
5. Naderpour, H., Kheyroddin, A. Investigation on the shear lag phenomenon in concrete tall buildings with tube systems. [Journal of modeling in engineering]. Semnan. Iran. 2010. Vol. 26. Pp. 33–48 (Persian).
6. Kheyroddin, A., Zahiri-Hashemi, R. Investigation of the shear-lag behavior in braced tubular structures. Annual Conference of Canadian Society of Civil Engineering. 2008. Quebec, Canada. Pp. 2037–2046.
7. Gaur, H., Goliya, R.K. Mitigating shear lag in tall buildings. International Journal of Advanced Structural Engineering (IJASE). 2015. Vol. 7. No. 3. Pp. 269–279.
8. Dat, B.T., Traykov, A., Traykova, M. Shear-lag effect and its effect on the design of high-rise buildings. E3S Web of Conferences 33. 2018.
9. Sreevalli, T., Priya, N.H. Effect of shear wall area on seismic beheavior of multi-storied building tube in tube structures. International Journal of Engineering Trends and Technlology (IJET). 2017. Vol. 44. No. 4. Pp. 202–210.
10. Patel, S.J., Patel, V.B. Comparison of different types of tubular systems. International Journal of Advance Research in Engineering. Science & Technology (IJAREST). 2016. Vol. 3. No. 4. Pp. 282–289.
11. Salehi, R., Khaloo, A. Investigation of shear lag factor in long structures with pipeline system in tubes under wind Load. American Journal of Engineering and Applied Sciences. 2018. Vol. 11. No. 2. Pp. 792–799.
12. Coull, A., Smith, B.S. Tall building structures: analysis and design. Texas. TX. USA. University of Texas Press. 1991. 552 p.
13. Haji-Kazemi, H., Company, M. Exact method of analysis of shear lag in framed tube structures. Journal of The Structural Design of Tall and Special Buildings. 2002. Vol. 11. No. 5. Pp. 375–388.
14. Shin, M., Kang, T.H.K., Pimentel, B. Towards the optimal design of high-rise building tube systems. Jouranl of The Structural Design of Tall and Special Buildings. 2010. Vol. 21. No. 6. Pp. 447–46.
15. Cross, P., Vesey, D., Chan, C.M. High-rise buildings, modeling complex engineering structures. American Society of Civil Engineers. 2007. Virginia, USA.
16. Ali, M.M., Moon, K.S. Advances in structural systems for tall buildings: emerging developments for contemporary urban giants. Journal of Buildings. 2018. Vol. 8. No. 104. Pp. 1–34.
17. AISC. ASD, Specification for structural steel buildings: allowable stress design and plastic design. USA. American Institute of Steel Construction. 2015. 213 p.
18. BHRC. Iranian code of practice for seismic resistant design of buildings: standard No. 2800 (4th. Edition). [Building and Housing Research Center]. 2017. Tehran. 211 p. (Persian)
19. Kim, J., Park, J., Shin, S., Min, K. Seismic performance of tubular structures with buckling restrained braces.Journal of The Structural design of tall and special buildings. 2007. Vol. 18. No. 4. Pp. 351–370.
20. Mashhadiali, N., Kheyroddin, A., Zahiri-Hashemi, R. Dynamic increase factor for investigation of progressive collapse potential in tall tube-type buildings. Journal of Performance of Constructed Facilities. 2016. Vol. 30. No. 6. Pp. 1–9.

Contacts:

Hamed Arshadi, 00989123498221; hamed.arshadi@semnan.ac.ir
Ali Kheyroddin, 00982331535200; kheyroddin@semnan.ac.ir

Федеральное государственное автономное образовательное учреждение высшего образования
Санкт-Петербургский политехнический университет Петра Великого

ПОЛИТЕХ
Санкт-Петербургский политехнический университет Петра Великого

Инженерно-строительный институт
Центр дополнительных профессиональных программ

195251, г. Санкт-Петербург, Политехническая ул., 29,
тел/факс: 552-94-60, www.stroikursi.spbstu.ru,
stroikursi@mail.ru

Приглашает специалистов проектных и строительных организаций,
не имеющих базового профильного высшего образования
на курсы профессиональной переподготовки (от 500 часов)
по направлению «Строительство» по программам:

П-01 «Промышленное и гражданское строительство»

Программа включает учебные разделы:

- ***Основы строительного дела***
- ***Инженерное оборудование зданий и сооружений***
- ***Технология и контроль качества строительства***
- ***Основы проектирования зданий и сооружений***
- ***Автоматизация проектных работ с использованием AutoCAD***
- ***Автоматизация сметного дела в строительстве***
- ***Управление строительной организацией***
- ***Управление инвестиционно-строительными проектами. Выполнение функций технического заказчика***

П-02 «Экономика и управление в строительстве»

Программа включает учебные разделы:

- ***Основы строительного дела***
- ***Инженерное оборудование зданий и сооружений***
- ***Технология и контроль качества строительства***
- ***Управление инвестиционно-строительными проектами. Выполнение функций технического заказчика и генерального подрядчика***
- ***Управление строительной организацией***
- ***Экономика и ценообразование в строительстве***
- ***Управление строительной организацией***
- ***Организация, управление и планирование в строительстве***
- ***Автоматизация сметного дела в строительстве***

П-03 «Инженерные системы зданий и сооружений»

Программа включает учебные разделы:

- ***Основы механики жидкости и газа***
- ***Инженерное оборудование зданий и сооружений***
- ***Проектирование, монтаж и эксплуатация систем вентиляции и кондиционирования***
- ***Проектирование, монтаж и эксплуатация систем отопления и теплоснабжения***
- ***Проектирование, монтаж и эксплуатация систем водоснабжения и водоотведения***
- ***Автоматизация проектных работ с использованием AutoCAD***
- ***Электроснабжение и электрооборудование объектов***

П-04 «Проектирование и конструирование зданий и сооружений»

Программа включает учебные разделы:

- ***Основы сопротивления материалов и механики стержневых систем***
- ***Проектирование и расчет оснований и фундаментов зданий и сооружений***
- ***Проектирование и расчет железобетонных конструкций***
- ***Проектирование и расчет металлических конструкций***
- ***Проектирование зданий и сооружений с использованием AutoCAD***
- ***Расчет строительных конструкций с использованием SCAD Office***

П-05 «Контроль качества строительства»

Программа включает учебные разделы:

- ***Основы строительного дела***
- ***Инженерное оборудование зданий и сооружений***
- ***Технология и контроль качества строительства***
- ***Проектирование и расчет железобетонных конструкций***
- ***Проектирование и расчет металлических конструкций***
- ***Обследование строительных конструкций зданий и сооружений***
- ***Выполнение функций технического заказчика и генерального подрядчика***

По окончании курса слушателю выдается диплом о профессиональной переподготовке установленного образца, дающий право на ведение профессиональной деятельности